Efficient Methods for Novel Passive Structures in Waveguide and Shielded Transmission Line Technology

by

Cheng Zhao

Thesis submitted for the degree of

Doctor of Philosophy

in

Electrical and Electronic Engineering,
Faculty of Engineering, Computer and Mathematical Sciences
The University of Adelaide, Australia

2016

Supervisors:

Assoc Prof Cheng-Chew Lim, School of Electrical & Electronic Engineering

Prof Christophe Fumeaux, School of Electrical & Electronic Engineering

Dr Thomas Kaufmann, School of Electrical & Electronic Engineering

THE UNIVERSITY of ADELAIDE

To my dearest father and mother,
with all my love.

Contents

Abstract

With the rapid development of microwave and millimetre-wave systems, the performance requirements for passive band-pass filters and diplexers, as essential parts in these systems, are steadily increasing. Both rectangular waveguide and substrate-integrated waveguide technologies help to satisfy various high-performance requirements. Rectangular waveguides offer the advantages of low loss and high power handling capabilities, while substrate-integrated waveguides have the advantages of low cost and easy integration into planar circuit technology. Besides, the miniaturisation of electronic devices is of great importance, especially for microwave or millimetre-wave systems whose volume is limited by system considerations. Hence, the two main aims of this thesis are firstly to develop efficient methods which can improve the design reliability and reduce the design cycle of such passive devices, and secondly to present novel structures of band-pass filters and diplexers whose dimensions are reduced.

In the first part of the thesis, a method based on the mode-matching technique is developed to rigorously and efficiently analyse the negative influence introduced by micromachining errors on the performance of band-pass H-plane iris filter. This analysis includes the effect on the centre frequency and 3 dB bandwidth caused by the round angles between waveguide walls and H-plane irises, or by the bevel angles on the H-plane irises. To remove these undesired influences, three approaches are proposed and verified with simulations performed with the finite-element method.

In the next part, efficient approximation approaches are investigated in the framework of the mode-matching method to analyse the characteristics of cylindrical posts placed in the cross-section of a rectangular waveguide or substrate-integrated waveguide. Compared with the H-plane irises in rectangular waveguides, cylindrical posts are more promising for realising band-pass rectangular waveguide filters, because the geometries are easier to manufacture and less prone to machining errors. Thus, a general design procedure for band-pass post filters in rectangular waveguides and substrate-integrated waveguides is developed and verified with finite-element simulations and measurements on prototypes. The tolerance analysis for the band-pass filters is also explored quickly and accurately with the developed method, while the influence of realistic material losses on the insertion loss of various structures, is also quantitatively

analysed with a full-wave simulation solver.

Next, the characteristics of a shielded microstrip line for single-mode operation is investigated rigorously based on the mode-matching method. The research focuses on the influence of the metal enclosure dimensions on the fundamental mode, and the relationships between the cutoff frequency of the 2^{nd}-order mode and the geometrical variables of the cross-section of the shielded transmission line. A similar method is then applied to an E-type folded substrate-integrated waveguide. The analysis demonstrates that the propagation characteristics for the first twenty modes in the E-type folded substrate-integrated waveguide and its corresponding equivalent rectangular waveguide are almost identical if the width of the middle metal vane in the E-type folded substrate-integrated waveguide is chosen reasonably. Exploiting this similarity property, a novel concept of band-pass post filter in E-type folded substrate-integrated waveguide technology is developed to reduce the band-pass filter dimension further, together with an efficient specific design procedure. The validity of the approach is verified via finite-element simulations and measurements on a fabricated prototype.

Finally, to reduce the sizes of common diplexers, four types of novel three-port junctions are proposed, including two improved Y-junctions in substrate-integrated waveguide technology, a double-layer junction in substrate-integrated waveguide technology, a Y-junction in T-type folded substrate-integrated waveguide technology, and a junction with stairs in T-type and E-type folded substrate-integrated waveguide technology. Exploiting the flexibility of the in-house developed mode-matching code or a commercial finite-element simulation solver, the characteristics for all presented junctions are shown to satisfy the constraints for optimum performance of diplexers when adjusting the relevant variables in the corresponding structures. Three types of these junctions are then utilised in realising diplexers whose performance is verified over the required operation bands with either numerical simulations or measurements on fabricated prototypes.

In summary, this thesis has introduced novel concepts and realisations of compact band-pass filters and diplexers in unfolded or folded substrate-integrated waveguide technology, as well as related structures. One of the crucial aspects emphasised throughout the research is the need for efficient and accurate modelling methods specifically tailored to support such developments. This has been demonstrated throughout the thesis with the combined use of powerful numerical methods and equivalent models based on symmetries or unfolded geometries.

Statement of Originality

I certify that this work contains no material, which has been accepted for the award of any other degree or diploma in my name, in any university or other tertiary institution and, to the best of my knowledge and belief, contains no material previously published or written by another person, except where due reference has been made in the text. In addition, I certify that no part of this work will, in the future, be used in a submission in my name, for any other degree or diploma in any university or other tertiary institution without the prior approval of the University of Adelaide and where applicable, any partner institution responsible for the joint-award of this degree.

I give consent to this copy of my thesis when deposited in the University Library, being made available for loan and photocopying, subject to the provisions of the Copyright Act 1968.

The author acknowledges that copyright of published works contained within this thesis resides with the copyright holder(s) of those works.

I also give permission for the digital version of my thesis to be made available on the web, via the University's digital research repository, the Library Search and also through web search engines, unless permission has been granted by the University to restrict access for a period of time.

23/03/2016

Signed Date

Acknowledgments

First and foremost, I would like to express my sincere gratitude to my supervisors Assoc Prof Cheng-Chew Lim, Prof Christophe Fumeaux and Dr Thomas Kaufmann for their continuous guidance and support during my candidature. My principal supervisor, Assoc Prof Cheng-Chew Lim accepted me as a PhD candidate in 2012. His immense and professional knowledge, serious and responsible attitude, patient and enthusiastic supervision, and constructive suggestions provided significant help in advancing my research. From the third year of my candidature, I was honoured to be one of Prof Christophe Fumeaux's students, who is an expert in microwave and millimetre-wave engineering and computational electromagnetics. He was always glad to share his extensive knowledge and abundant experimental experience, and welcomed scientific enquiries and discussions. My research work benefited a lot from his technical support, insightful advices, and meticulous feedback. Another co-supervisor whom I am genuinely indebted to is Dr Thomas Kaufmann. His deep theoretical knowledge, insightful comments, and encouragement were of great importance towards my research.

In addition to my supervisors, I would like to convey my gratitude to my friends and colleagues in the Adelaide Applied Electromagnetics Group in School of Electrical & Electronic Engineering at the University of Adelaide, Dr Ali Karami Horestani, Dr Zahra Shaterian, Dr Amir Ebrahimi, Mr Shengjian (Jammy) Chen, Dr Tiaoming (Echo) Niu, Mr Nghia Nguyen-Trong, Dr Withawat Withayachumnankul, Mr Chengjun Zou, Ms Wendy Suk Ling Lee, and Mr Sree Pinapati, to my advisor, Dr Yingbo Zhu, and to the professional staff, Mr Brandon F. Pullen, Mr Pavel Simcik, Mrs Rose-Marie Descalzi, and Mr David Bowler.

I would also like to express my heartfelt thanks to my best friends, Mr Ming Chen and Mr Qianwen Xia, for your warmest wishes, and your appearing in my life and keeping me company.

This thesis was made possible by an Australian Postgraduate Award Scholarship. I am sincerely indebted to the Department of Education and Training of Australian Government, which gave me the opportunity to undertake a PhD program at the University of Adelaide.

Last but not least, my endless love and appreciation goes to my parents who gave birth to me, raised and educated me with continuous love and patience, and were supporting and encouraging me infinitely.

Cheng Zhao,
March 2016,
Adelaide

Thesis Conventions

The following conventions have been adopted in this Thesis:

Typesetting

This document was compiled using LaTeX2e. Texmaker and TeXstudio were used as text editor interfaced to LaTeX2e. Inkscape and Xcircuit were used to produce schematic diagrams and other drawings.

Referencing

The Harvard style has been adopted for referencing.

System of units

The units comply with the international system of units recommended in an Australian Standard: AS ISO 1000–1998 (Standards Australia Committee ME/71, Quantities, Units and Conversions 1998).

Spelling

Australian English spelling conventions have been used, as defined in the Macquarie English Dictionary (A. Delbridge (Ed.), Macquarie Library, North Ryde, NSW, Australia, 2001).

Publications

Journal Articles

ZHAO-C., FUMEAUX-C., AND LIM-C. C. (2016b). Substrate-Integrated Waveguide (SIW) Diplexers with Improved Y-junctions, *Microwave and Optical Technology Letters*, **58**(6), pp. 1384–1388.

Conference Articles

ZHAO-C., FUMEAUX-C., AND LIM-C. C. (2016a). Folded Y-junction in Substrate-Integrated Waveguide Technology, *The 2nd Australian Microwave Symposium*.

ZHAO-C., FUMEAUX-C., KAUFMANN-T., ZHU-Y., AND LIM-C. C. (2015b). Mode Matching Analysis of Dimension for Single-Mode Operation of Shielded Microstrip Lines, *2015 Asia-Pacific Microwave Conference (APMC)*, Vol. 2, pp. 1–3.

ZHAO-C., FUMEAUX-C., AND LIM-C. C. (2015a). Losses in Substrate Integrated Waveguide Band-Pass Post Filters, *2015 Asia-Pacific Microwave Conference (APMC)*, Vol. 2, pp. 1–3.

ZHAO-C., FUMEAUX-C., KAUFMANN-T., ZHU-Y., HORESTANI-A. K., AND LIM-C.-C. (2015c). General Design Method for Band-pass Post Filters in Rectangular Waveguide and Substrate Integrated Waveguide, *International Symposium on Antennas and Propagation (ISAP2015)*, pp. 946–949.

ZHAO-C., KAUFMANN-T., ZHU-Y., AND LIM-C. C. (2014a). Approximation Methods for Cylindrical Posts in Rectangular Waveguides with Mode Matching Technique, *2014 IEEE Asia-Pacific Conference on Applied Electromagnetics (APACE)*, pp. 179–182.

ZHAO-C., KAUFMANN-T., ZHU-Y., AND LIM-C. C. (2014b). Efficient Approaches to Eliminate Influence Caused by Micro-Machining in Fabricating H-Plane Iris Band-Pass Filters, *2014 Asia-Pacific Microwave Conference (APMC)*, pp. 1306–1308.

Article in Review

ZHAO-C., FUMEAUX-C., AND LIM-C. C. (n.d.). Folded Substrate-Integrated Waveguide Band-pass Post Filter, *IEEE Microwave and Wireless Components Letters*. Accepted on 1 July 2016, Subject to revision.

List of Figures

List of Tables

Chapter 1

Introduction

THIS chapter provides the reader with introductory background on common passive microwave and millimetre-wave devices, including band-pass filters, shielded microstrip lines, three-port junctions, and diplexers. The motivations and objectives of this research work are then discussed, while the original contributions made in this thesis are highlighted. Finally, the structure and outline of this thesis are described.

1.1 Introduction

The microwave region of the electromagnetic spectrum is usually defined to be the range of frequencies from 300 MHz (1 m wavelength) to 300 GHz (1 mm wavelength), while the subset range of frequencies from 30 GHz (10 mm wavelength) to 300 GHz (1 mm wavelength) is also referred to as millimetre-wave region (Sorrentino and Bianchi 2010). Systems operating in this frequency region, that is, microwave and millimetre-wave systems, have become extremely popular in areas such as navigation, radar, remote sensing, or clinical medicine because lower radio-frequency bands are not able to cope with the increasing data rates (Wells 2010), and have become increasingly more congested by existing applications (Umar 2004).

As essential parts in microwave and millimetre-wave systems, band-pass filters and diplexers are often utilised to remove undesired frequency components and thus handle more frequency channels, while transmission lines are generally adopted to integrate the two passive components into other planar circuits. With the increase of the frequency, the performance of these passive devices are more susceptible to manufacture tolerances, and accurate dimensions for the transmission lines and the distributed elements used to form the band-pass filters and diplexers become more critical. In order to achieve the design specifications and cut fabrication costs, the precise prediction for the performance of these devices is thus intensively desired. Hence, this thesis aims to develop efficient and accurate methods to improve the design reliability and reduce the design cycle of such passive devices.

In addition, miniaturisation of these devices is also of great importance, especially for microwave or millimetre-wave systems whose volume is limited by system considerations. This thesis also aims to develop novel configurations for band-pass filters and diplexers which can reduce the dimensions. The developments of these novel structure benefits considerably from the efficient design methods mentioned above. Thus, the two main aspects of this thesis, that is, implementation of efficient design methods and novel structure developments, are intimately linked.

1.2 Objectives of the Thesis

High-performance band-pass filters are often realised in rectangular waveguide technology because this approach offers the advantages of low loss and high power handling capability (Sorrentino and Bianchi 2010, Gustrau 2012). The filtering function is

achieved with a series of coupling resonators that are formed by H-plane irises in the rectangular waveguide. However, because of the limitations of micro-machining processes, an H-plane iris band-pass filter can only be manufactured such that the corners between the waveguide walls and irises are rounded rather than at perfect right angles (Bornemann 2001, Bornemann *et al.* 2005). Thus, one objective of this thesis is to investigate the negative influence caused by these machining errors, especially when the filter operates at high frequencies. Subsequently, the thesis also explores effective methods for removing the unwanted influence.

Another promising realisation approach for band-pass filter design is to use cylindrical posts placed in the cross-section of a rectangular waveguide. This is especially attractive at higher frequencies because circular holes and cylindrical posts are easier to manufacture, and less prone to machining errors. Furthermore, in order to tie in with the requirement for smaller size, the proposed filter can be manufactured in substrate-integrated waveguide (SIW) technology as a band-pass via SIW filter. In other words, a band-pass post rectangular wavguide can be approximately realised in planar technology as a band-pass via SIW filter. However, designing the corresponding post or via filters with the finite-element method (FEM) (such as Ansys High Frequency Structural Simulator (HFSS) or Microwave Studio from Computer Simulation Technology (CST)) is time-consuming because of the large number of variables required in the tuning and optimisation procedures, especially considering the computational requirement for mesh fineness in order to obtain results with sufficient precision. Hence, another objective is to develop a fast and accurate general method for designing band-pass post or via rectangular waveguide or SIW filters.

In some cases, considering the volume restrictions of microwave or millimetre-wave systems, further width reduction is still desired. The concept of E-type folded substrate-integrated waveguide (FSIW) is a viable option to decrease the size of band-pass filters. With this technology, several band-pass filters have been designed by etching slots in the middle metal vane of the E-type FSIW (Wang *et al.* 2008, Wang *et al.* 2010a, Yang *et al.* 2013). However, the tuning of the slot dimensions requires a large number of variables. Thus, their optimisation using full-wave finite-element simulations is also time-consuming. A novel concept of band-pass post filter in E-type FSIW technology, is then considered as another objective of this thesis, and importantly, this structure is introduced together with an efficient specific design procedure.

Electronic devices, including band-pass filters, and diplexers, are often integrated into single-mode operation microwave and millimetre-wave systems through transmission lines. Shielded microstrip lines are a viable choice for the transmission lines because they offer the advantages of protecting circuits from environmental contaminants, preventing electromagnetic interference, and enhancing the mechanical strength (Maloratsky 2000). To avoid the influence of the metallic enclosures on the fundamental mode, the choice of dimensions for the housing is an important issue. Therefore, this thesis also aims at investigating the influence of housing dimensions on the fundamental mode of shielded transmission lines and the relationships between the cutoff frequency of the 2^{nd}-order mode and the geometrical variables of the transmission line cross-section.

In addition to band-pass filters, a three-port junction is another essential component to achieve a diplexer. Y-junctions and T-junctions are often adopted in designing diplexers with satisfactory performance (Vanin *et al.* 2010, Vanin *et al.* 2004, Kordiboroujeni *et al.* 2014). However, miniaturisation is again of great importance, especially for diplexers whose volume is limited by system considerations. Thus, this thesis aims to develop several novel three-port junctions whose dimensions are reduced and whose characteristics satisfy the constraints to achieve optimum performance of diplexers. The development of the related diplexers using these junctions is also an objective of this thesis.

1.3 Summary of Original Contributions

The original contributions included in this thesis can be described in two major parts. The first part of this thesis is focused on band-pass filters and shielded microstrip lines, and the second major part of this thesis is devoted to three-port junctions and diplexers. The original contributions presented throughout this thesis can be itemised as the following.

1.3.1 Band-Pass Filters and Shielded Microstrip Lines

- An efficient approach based on the mode-matching method (MMM) is developed to analyse the negative influence caused by micro-machining errors, that is, the rounding of the corners between the waveguide walls and the H-plane

irises caused by the finite size of the milling cutters. The method is also applied in analysing the influence of the isosceles bevel corners on the H-plane irises. Compared with the FEM using Ansys HFSS, the method can give accurate results in a much shorter time. Applying this method, it is found that by increasing the radii of the round angles, the centre frequency of the band-pass filter shifts to higher frequencies while the 3 dB bandwidth varies slightly. Meanwhile, in contrast, with the increase of the side lengths of the bevel angles, the centre frequency of the band-pass filter shifts to lower frequencies, while the 3 dB bandwidth widens (Zhao *et al.* 2014b).

- Three methods are then developed to remove the negative influence caused by rounded corners between the waveguide walls and the H-plane irises. These three methods include 1) revising the design parameters according to the estimated influence in order to compensate the frequency shift, 2) designing the band-pass filter without considering the influence of fabrication and then introducing reasonable bevel angles to compensate the offset of the centre frequency caused by rounded corners, and 3) mapping the realised structure of irises and resonator cavities with the impedance inverters (K inverters) and LC resonator network of a band-pass filter to accurately compute the aperture sizes and resonator lengths. According to the verification with the FEM using Ansys HFSS, all of the three methods have been demonstrated to be effective (Zhao *et al.* 2014b).

- Three classes of stair-casing approximations, including equal width method, arithmetic sequence thickness method, and equal sector method, are developed to investigate the characteristics of circular posts placed in the cross-section of a rectangular waveguide. The convergent behaviour of the scattering parameters computed using these approximation methods is explored. Meanwhile, through comparing the difference of the scattering parameters and reference values, the rate of convergence for each method is also explored. According to this study, the most efficient approximation method is recommended with verification using the full-wave finite-element simulations in Ansys HFSS (Zhao *et al.* 2014a).

- Based on the recommended approach for posts in rectangular waveguides introduced above, an efficient method is developed to design band-pass post filters in rectangular waveguide technology. The fast computations provide accurate relationships for the K factors as a function of the post radii and the distances between posts, and allow analysing the influence of machining tolerances on the

filter performance. The relationships for the K factors can be used to choose reasonable post dimensions for designing band-pass filters, while the error analysis helps to judge whether a given machining precision is sufficient. With this method, which can be extended to SIW technologies easily, a Chebyshev band-pass post rectangular waveguide filter and a band-pass SIW filter with a centre frequency of 10.5 GHz and a fractional bandwidth of 9.52% are designed. The validity of this method is verified via full-wave simulations using Ansys HFSS and measurements on manufactured prototypes (Zhao *et al.* 2015c).

- With the developed lossless mode-matching code, six Chebyshev band-pass post filters in SIW technology are designed with various orders for a centre frequency of 10.5 GHz and a fractional bandwidth of 9.52%. These filters are then simulated with a full-wave electromagnetic solver in order to quantitatively investigate how the insertion loss is influenced by the variations of the metal claddings and vias' conductivity, the dielectric loss tangent, and the thickness of the substrate. According to the analysis, it is found that for filters realised on a given substrate, smaller dimensions achieved by lower-order structures translate into smaller insertion loss but at the cost of lower out-of-band rejection performance. In contrast, it appears that reducing the dimension of the filters by adopting a substrate with larger relative permittivity cannot decrease the insertion loss. In addition, increasing the thickness of the substrate is another efficient way to reduce the insertion loss in the main body of the filter. However, since thicker substrate leads to larger radiation loss for the SIW-to-microstrip transition, a trade-off must be found for optimal design. For validation, one prototype filter is fabricated to compare the simulations to experimental results (Zhao *et al.* 2015a).

- In order to reduce the filter dimension further, a novel concept of band-pass post filter in E-type FSIW technology is developed, together with an efficient specific design procedure. The approach is based on a rigorous mode-matching analysis of the dispersion characteristics for the odd and even modes in the FSIW, which allows the definition of an accurate unfolded equivalent problem for a suitably chosen middle vane dimension. A direct comparison of the posts placed in the FSIW and in the equivalent unfolded dielectric-loaded rectangular waveguide confirms their similar characteristics. For illustration, the method is used to design a 5^{th}-order Chebyshev band-pass post FSIW filter with a centre frequency of 7 GHz and a fractional bandwidth of 5.71%. The viability and efficiency of the

design approach are successfully validated by the finite-element simulations and measurements on a fabricated prototype (Zhao *et al.* n.d.).

- For a shielded microstrip line, the influence of the dimensions on the fundamental mode is investigated rigorously using the MMM. In addition, the relationships between the cutoff frequency of the 2^{nd}-order mode and the geometrical variables of the cross-section of the shielded transmission line are explored. With these relationships, the most suitable geometry can be efficiently determined, which is important for preventing performance degradation through higher-order mode excitations, such as in waveguide transitions. The analysis results are verified with the finite-element simulations obtained with Ansys HFSS (Zhao *et al.* 2015b).

1.3.2 New Junctions and Diplexers

- Two novel improved Y-junctions are introduced in order to eliminate the performance degradation for common Y-junctions whose two output branches are bent to yield parallel outputs for dimension reduction. An efficient method based on the MMM is developed to analyse the characteristics of these two improved Y-junctions. It is found that through varying the angle between the two output branches or adjusting the positions of two inserted additional vias, both improved junctions can satisfy the constraints to achieve optimum performance of diplexers over a wide frequency range, illustrated in this thesis with an example extending from 7 GHz to 8.5 GHz (Zhao *et al.* 2016b).

- A double-layer structure is introduced for the realisation of a compact three-port junction designed for dimension reduction of diplexers. The proposed structure is convenient to design, because a single variable can adjust the reflection coefficients of the junction ports. In addition, with the developed efficient mode-matching-based method, the efficiency of the adjustment process is improved further. According to the analysis, the junction can satisfy the constraints for optimum performance of diplexers over a wider frequency range than the single-layer structure, as demonstrated in this thesis from 5.5 GHz to 9.5 GHz. The wider frequency band means that the flexibility of selection of a diplexer's up and down channels is increased.

- A novel Y-junction in T-type FSIW technology is introduced to reduce the junction dimensions. Similar propagation characteristics for the first eighteen modes

of the FSIW and the corresponding equivalent unfolded dielectric-loaded rectangular waveguide are demonstrated when a reasonable width of the middle metal vane is chosen for the FSIW. This study is performed with the FEM using Ansys HFSS. As a design example, it is found that the characteristics of the proposed Y-junction can satisfy the constraints for optimum performance of diplexers over the frequency band extending from 4.6 GHz to 8.5 GHz. Compared with diplexers using the common Y-junction, diplexers utilising the proposed novel junction can accommodate up and down channels in a wider frequency band (Zhao *et al.* 2016a).

- To further decrease the dimensions of diplexers achieved with T-type FSIW Y-junctions, a three-port junction with stairs is realised in both T-type and E-type FSIW technology. Based on the FEM using Ansys HFSS, the reflection coefficients for the junction ports of a demonstrated design can satisfy the constraints for optimum performance of diplexers over a frequency band from 5.3 GHz to 6.8 GHz.

- Three of the four proposed three-port junctions are adopted as components to realise diplexers. For the diplexers designed with the two improved Y-junctions and the double-layer junction, efficient methods are developed through combining the mode-matching codes for the junctions and band-pass post filters. Dimensions can then be obtained in a very short time, and the calculated scattering parameters $|S_{11}|$, $|S_{21}|$ and $|S_{31}|$ exhibit a good agreement with the simulation results from the FEM using Ansys HFSS or the measurements performed on fabricated prototypes (Zhao *et al.* 2016b). For the diplexer employing the junction with stairs in T-type and E-type FSIW technology, the junction part is still analysed with the FEM, while the band-pass filter part is calculated with the mode-matching code which can significantly improve the efficiency. According to the simulations, it is found that the diplexer design performs well and the specifications can be satisfied over the operation bands.

1.4 Thesis Outline

As visualised in Fig. 1.1, this thesis contains seven chapters. The detailed description for each chapter is listed in the following.

Chapter 1 provides a brief background on microwave and millimetre-wave components, including band-pass filters, shield microstrip lines, three-port junctions

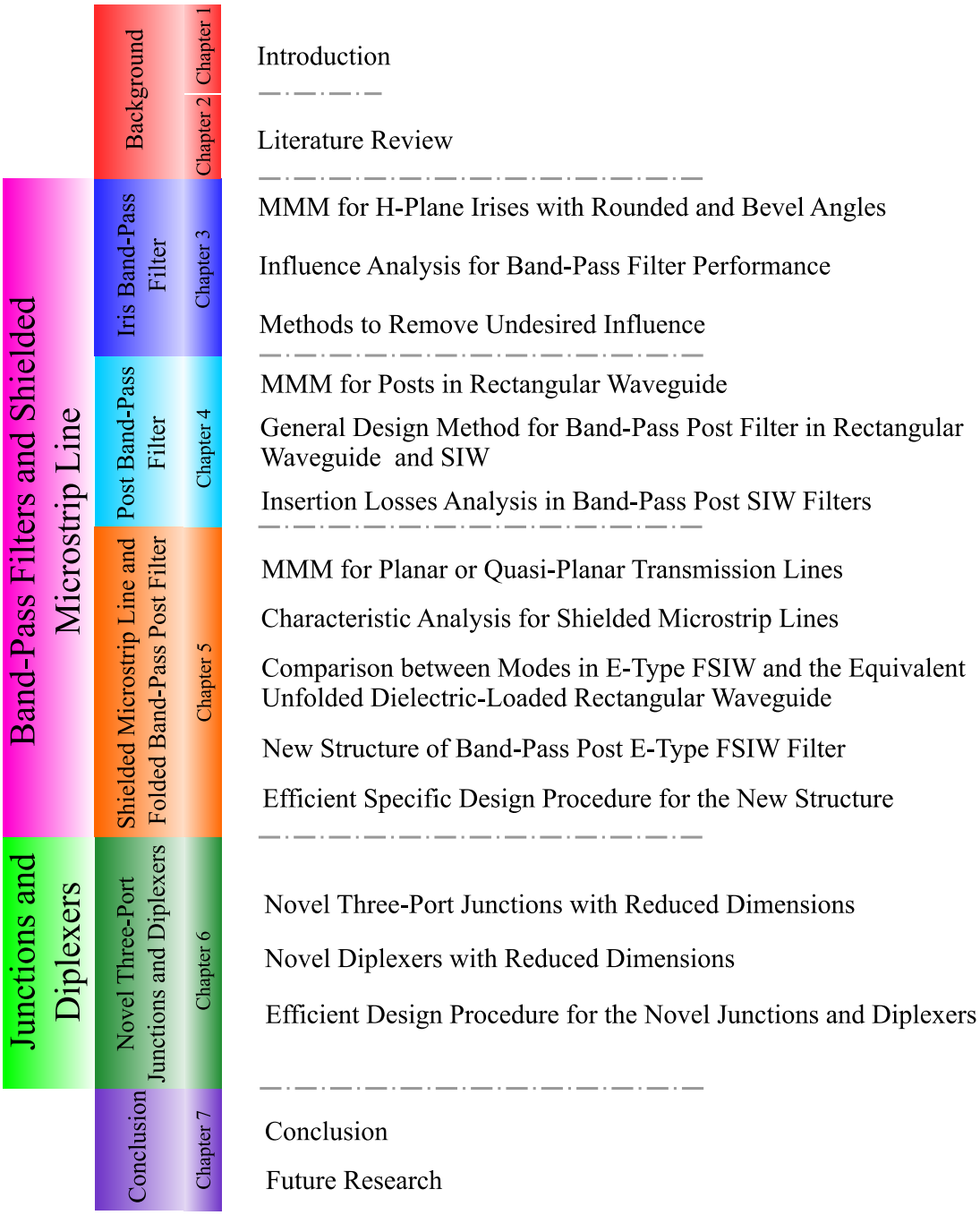

Figure 1.1. Thesis outline. The thesis is composed of 7 chapters including background and conclusion. The original contributions are distributed in Chapters 3 to 6. The thesis can be divided into two major parts. The first part that includes Chapters 3, 4 and 5 is mainly concerned with the band-pass filter and shielded microstrip lines. The second major part, which includes Chapter 6, is dedicated to the three-port junctions and diplexers. All chapters are virtually self-contained.

and diplexers. It then focuses on the objectives achieved in this thesis and summarises the original contributions. Finally, the present section describes the outline of this thesis.

Chapter 2 is a literature review. It first focuses on the historical background and theoretical development of filters, transmission lines, and multiplexers, and highlights seminal inventions and significant developments. Laying emphasis on the MMM and the FEM, this chapter then introduces the background and development of electromagnetic numerical methods applied in the rest of the thesis.

Chapter 3 explains in detail the principle of the MMM, which can be utilised to analyse the characteristics of H-plane irises placed in the cross-section of a rectangular waveguide. With high-speed and high-precision, this method is then extended to handle round corners between waveguide walls and H-plane irises, and bevel angles on H-plane irises. Using the method developed, the negative influence on band-pass iris filters caused by the rounded angles and the bevel angles is then investigated rigorously. After that, this chapter provides three efficient methods to remove the undesired influence, these being 1) revising the design parameters according to the estimated influence in order to compensate the frequency shift, 2) designing the band-pass filter without considering the influence of fabrication and then introducing reasonable bevel angles to compensate the offset of the centre frequency caused by rounded corners, and 3) mapping the realised structure of irises and resonator cavities with the K-inverter and LC resonator network of a band-pass filter to compute the aperture sizes and resonator lengths accurately.

Chapter 4 explains in detail the principle of the MMM to handle N-furcation structure in a rectangular waveguide. Three classes of approximation methods, the equal width, the arithmetic sequence thickness, and the equal sector methods, are then developed to investigate the characteristics of posts placed in the cross-section of a rectangular waveguide. By investigating the scattering parameter convergence of these approximation methods, and comparing the rate of convergence for each method, the most efficient approximation method is recommended with verification by the full-wave finite-element simulations in Ansys HFSS. Based on the recommended approach, an efficient method is developed to design band-pass post filters in rectangular waveguide technology or SIW technology. Because of the fast and precise computations, this chapter also provides accurate relationships for the K factors as a function of the post radii and the distances between

posts, and the influence of machining tolerances on the filter performance. It is noted that, the relationships for the K factors can be used to choose reasonable post dimensions for designing band-pass filters, while the error analysis helps to judge whether a given machining precision is sufficient. The method developed is applied in a Chebyshev band-pass post filter and a band-pass SIW filter, and the validity is verified via the full-wave simulations using Ansys HFSS and measurements on manufactured prototypes. In addition, this chapter also explores how the variations in the metal claddings and vias' conductivity, dielectric loss tangent, and substrate thickness influence the filter insertion loss with the Ansys HFSS full-wave simulation solver.

Chapter 5 first explains the principle of the MMM for planar or quasi-planar transmission lines. The method is then applied to a shielded microstrip line to determine how the dimensions influence the fundamental mode, while also exploring the relationships between the cutoff frequency of the 2^{nd}-order mode and the geometric variables of the cross-section of the shielded transmission line. Similar work is done to the E-type FSIW. This chapter demonstrates that a reasonable middle metal vane dimension and its equivalent unfolded dielectric-loaded rectangular waveguide have identical propagation characteristics for the first twenty modes in FSIW. A direct comparison of the posts placed in the FSIW and in the equivalent rectangular waveguide confirms their similar characteristics. This property leads to the development of a novel band-pass post filter in E-type FSIW technology, together with an efficient specific design procedure. The procedure is successfully validated by the full-wave finite-element simulations and measurements on a fabricated prototype.

Chapter 6 introduces some novel three-port junctions that can reduce the dimensions of common diplexers, including improved Y-junctions, double-layer junction, Y-junction in T-type FSIW technology and junction with stair in T-type and E-type FSIW technology. The characteristics of these proposed three-port junctions are then investigated in this chapter with the MMM or the FEM. It is found that, by adjusting corresponding variables in the configurations of these junctions, the reflection coefficients for the junction ports are able to satisfy the constraints for optimum performance of diplexers over a specified frequency band. Thus, by selecting suitable up and down channel frequency bands, three of the junctions are adopted to achieve diplexers. According to the analysis results obtained with

the MMM, the FEM using Ansys HFSS, or measurements on fabricated prototypes, all diplexer designs operate well and can satisfy the specifications over the required bands.

Chapter 7 concludes the original contributions of this thesis and recommends possible future work.

Chapter 2

Literature Review

THIS chapter provides a brief review of the historical background and theoretical development of filters, transmission lines, multiplexers, and electromagnetic numerical methods including the mode-matching and finite-element methods.

2.1 Introduction

Band-pass filters and diplexers play important roles in microwave and millimetre-wave applications, such as navigation, telecommunications, radar, remote sensing, and clinical medicine. Nowadays, the development and design of band-pass filters, diplexers, and their host transmission lines for integration into microwave and millimetre-wave systems is still challenging because of the increasingly demanding requirements for emerging applications such as higher performance and smaller dimensions. Thus, in order to shorten the design cycle and improve design accuracy, several efficient numerical methods in electromagnetics have been developed either for general-purpose applications or specifically for the design of high-quality band-pass filters, diplexers and transmission lines.

This chapter presents a short review of the historical background and fundamental developments for filters, multiplexers, and transmission lines in Section 2.2, and a description of relevant numerical methods in Section 2.3.

2.2 Filters, Transmission Lines and Multiplexers

2.2.1 Filters

A filter is a two-port building block used to control the frequency response at a certain circuit location by allowing a range of signal frequencies to be transmitted, while rejecting the others. A filter is typically classified by its frequency response as either low-pass, high-pass, band-pass, or band-reject (Pozar 2011, Hong and Lancaster 2011).

Considered as the beginning of filter theory, George Ashley Campbell created in 1910 lumped-element designs for electric wave filters using ladder networks, which included inductance introduced by loading coils and capacitance introduced by condensers (Reynolds 1991). Taking Campbell's network for low-pass filter as an example, as shown in Fig. 2.1, the ladder configuration consists of a number of sections (constant k section) with identical element values (Campbell 1917). Known as the image parameter method today, Campbell's technique was further developed by Otto Julius Zobel and others. For instance, in the 1920s and 1930s, Zobel invented the well-known m-derived filter (Belevitch 1962) and the mm'-type filter (Zobel 1932). He also improved

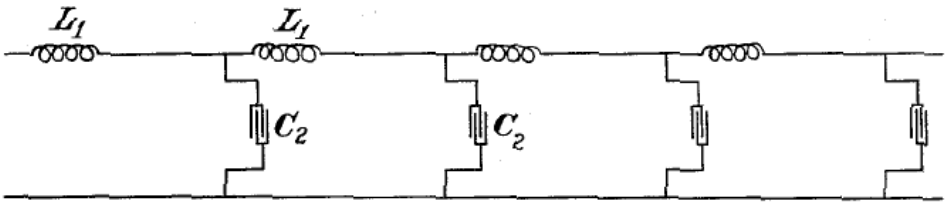

Figure 2.1. Network of Campbell's low-pass filter. This figure shows the configuration of Campbell's low-pass filter which is formed with identical sections. Source: Created by George Ashley Campbell (Campbell 1917)

the wave filter design technique to perfect the frequency characteristics in the passband by minimising reflection, and sharpening transition from the passband to the stopband (Bray 2002).

Moving away from lumped element analysis, the research on distributed element filters started before World War II (1939 - 1945). The first filter design using distributed elements was filed as a patent by W. P. Mason in 1927 (Mason 1930), and in 1937, W. P. Mason and R. A. Sykes published a paper on distributed element filters employing coaxial and balanced transmission lines (Mason and Sykes 1937). During World War II, the filtering demands of radar and electronic countermeasures led to the development of distributed element filters by the MIT Radiation Laboratory, together with many other Laboratories in the US and the UK. For example, Hans Bethe from the MIT Radiation Laboratory produced his aperture theory which plays an important role in waveguide cavity filters (Levy and Cohn 1984).

Following World War II, filter theory continued to develop. Paul Irving Richards's comprehensive theory of commensurate line circuits can be considered as the beginning of modern distributed circuit theory, while the Richards's transformation enabled the entire lumped theory to be applied in distributed element circuits, that is, a lumped element design can be converted into a distributed element design directly through the transformation relationship (Richards 1948, Levy and Cohn 1984). However, it was often inconvenient to realise distributed element filters in planar or waveguide technology, because the network resulting from the transformation always contained elements in series. Thus, to solve this problem, in 1955, K. Kuroda published identities, known today as Kuroda's identities, with which the series elements can be eliminated by impedance transformers (Ozaki and Ishii 1958, Levy and Cohn 1984). Another theoretical development was the network synthesis filter approach by Wilhelm Cauer, which

could provide a solution that accurately satisfied the design specifications. Treating network synthesis as the inverse problem of network analysis, Cauer's research was mainly developed during World War II. However, his work was not widely published until after the end of the war (Chang 2010).

Filter theory was perfected continuously in the following years. For direct-coupled cavity filters, S. B. Cohn presented in 1957 a filter design method that was based on simple equations, but generally provided poor performance for filters with low voltage standing wave ratio (VSWR) ripple tolerance and moderate bandwidths (Cohn 1957). On the contrary, in 1963, Leo Young introduced a method which could provide excellent performance for filters with low VSWR ripple tolerances and large bandwidths, however in a formalism more complicated than Cohn's (Young 1963). In order to obtain both the desirable advantages of Cohn's and Young's methods, Ralph Young presented in 1967 a new theory to handle direct-coupled cavity filters in transmission lines or waveguides (Levy 1967).

Cross-coupled filters were another area of research focus during that time, because of the improved performance and reduced dimensions achievable with fewer resonators. This was due to the additional degrees of freedom offered by coupling coefficients. The first cross-coupled filter was invented by John R. Pierce at Bell Labs in 1948. As shown in Fig. 2.2, it was formed by connecting the two parallel input and output rectangular waveguides with three circular resonant transmission lines (Pierce 1949, Pierce 1953). In the 1960s, E. C. Johnson, R. M. Kurzrok, Thomas A. Abele, Chung-Li Ren, and others became active in this field, and numerous studies about cross-coupled filters were published (Johnson 1964, Kurzrok 1966, Abele 1967, Ren 1969). Later, significant developments took place in the 1970s. Ali E. Atia and Albert E. Williams from Communications Satellite Corporation (COMSAT) presented a synthesis procedure to handle multiple couplings in a non-cascaded filter configuration (Atia and Williams 1972, Atia and Williams 1973, Atia *et al.* 1974). In the later 1990s and early 2000s, the synthesis method was further improved and extended by Richard J. Cameron (Cameron 1999, Cameron 2003).

In addition to the more compact cross-coupled filter structures, dielectric resonators are another avenue introduced for saving space. The first filter in this technology was invented by S. B. Cohn in 1965, and the dielectric material was titanium dioxide (Cohn 1965). Actually, in the 1960s, dielectrics with high permittivity were always extremely sensitive to temperature. Thus, the first temperature-stable band-pass filter

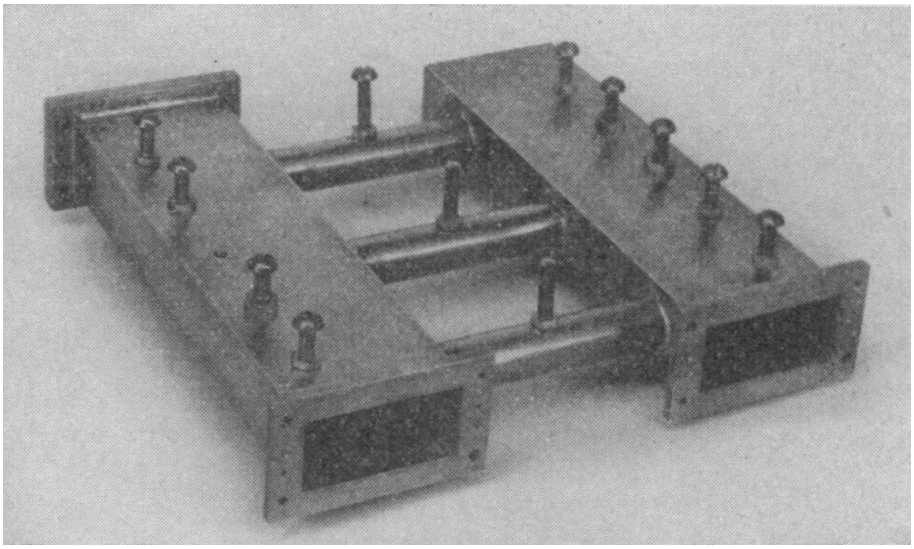

Figure 2.2. Structure of the first cross-coupled filter. This figure shows the earliest cross-coupled filter invented by John R. Pierce. It is formed by connecting the two parallel input and output rectangular waveguides with three resonators which are resonant transmission lines. Source: Created by John R. Pierce (Pierce 1949).

using dielectric resonators was reported by D. J. Massé and R. A. Pucel in 1972, following the introduction of low temperature coefficient ceramic resonators (Massé and Pucel 1972). Nowadays, with the advances in material science and technology, numerous manufacturers are able to produce temperature-stable dielectric resonators. For instance, Trans-Tech provides ceramic dielectric resonator (7300 Series) with a high relative permittivity from 72 to 75 and a low temperature coefficient of resonant frequency from -12 ppm/°C to +12 ppm/°C (Trans-Tech 2015).

Filters realised in rectangular waveguide technology are limited by the high cost, bulky volume, and difficult integration with other components. Thus, substrate-integrated waveguide (SIW) technology was proposed recently to overcome these disadvantages (Wu *et al.* 2003). An SIW is a type of waveguide/transmission line formed by placing two rows of metallised post or via-hole fences in a dielectric substrate to connect the top and the bottom metal plates electroplated onto the substrate's surfaces. The propagation characteristics of this structure, together with the leakage properties and design considerations for practical applications, was investigated in details by Dominic Deslandes and Ke Wu in 2006 (Deslandes and Wu 2006), while several empirical analytical equations were presented in several other publications (Cassivi *et al.* 2002, Yan *et al.* 2004, Xu and Wu 2005, Che *et al.* 2008a, Salehi and

Mehrshahi 2011), with which the SIW can be converted into an equivalent dielectric-loaded rectangular waveguide. Thus, in addition to the advantages of small dimensions and easy integration into planar circuits, the SIW also inherits the advantages of low loss (although larger than common rectangular waveguide loss due to the introduced dielectric losses), high quality factor, and high power handling capability from traditional rectangular waveguide. Because of these advantages, numerous filter designs in SIW technology were developed in the past decades (Zhang *et al.* 2005, Potelon *et al.* 2008, Zhang *et al.* 2010a, Shen *et al.* 2011, Chen *et al.* 2015b). However, further size reduction is still desired, especially in microwave or millimetre-wave systems whose volume is limited by system considerations. Therefore, SIW technology was later extended to half-mode substrate-integrated waveguide (HMSIW) technology whose characteristics was investigated in (Hong *et al.* 2006, Lai *et al.* 2009), and folded substrate-integrated waveguide (FSIW) technology whose characteristics were explored in (Che *et al.* 2008b, Nguyen-Trong *et al.* 2015a). These two structures formed the basis for many filter designs (Grigoropoulos *et al.* 2005, Wang *et al.* 2008, Wu *et al.* 2009, Wang *et al.* 2010b, Yang *et al.* 2013).

2.2.2 Transmission Lines

In 1827, Georg Simon Ohm described the first mathematical model of transmission lines which only contained resistance (Ohm 1827) (Fig. 2.3(a)). With this model, the resistance of a wire is proportional to the wire length, but it cannot explain the signal delay phenomenon along the wire discovered later by Josiah Latimer Clark (Hunt 1994). In 1853, Michael Faraday pointed out that there was also capacitance in the transmission line, and in the next year, taking the capacitance and its associated dispersion into account, Ohm's model was modified by Lord Kelvin by introducing shunt capacitance (Körner 1989) (Fig. 2.3(b)). In 1881, Oliver Heaviside made the model of the transmission line achieve its fullest development by inserting series inductance and shunt conductance (Fig. 2.3(c)). Heaviside's model is now known as the telegrapher's equation, while the four corresponding distributed elements are named as the primary line constants.

Ordinary electrical wires are not qualified to transmit high frequency signals such as microwaves and millimetre-waves, because with the increase of the frequency, the

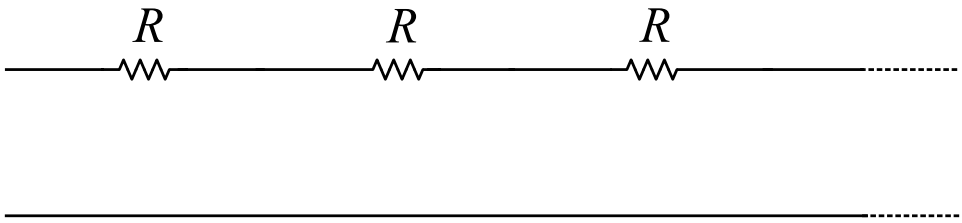

(a) Ohm's model

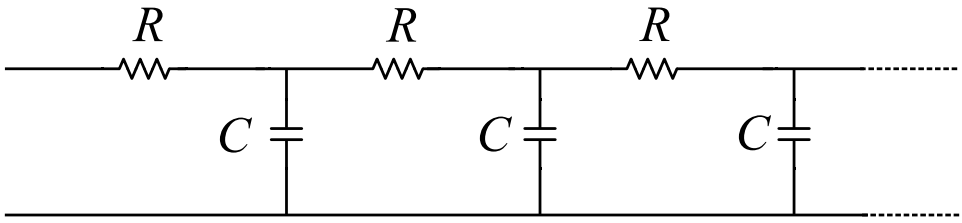

(b) Kelvin's model

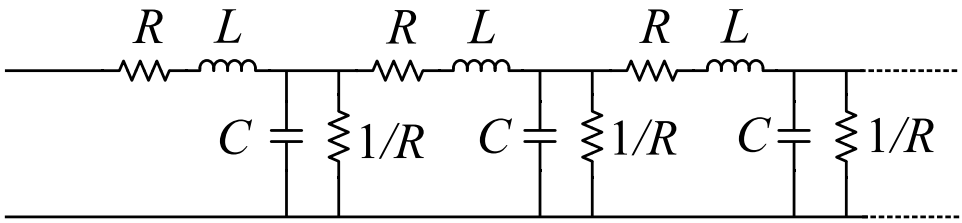

(c) Heaviside's model

Figure 2.3. Three types of transmission line models. These figures show three types of transmission line models created by (a) Georg Ohm with series resistance, (b) Lord Kelvin with series resistance and shunt capacitance, and (c) Oliver Heaviside with series resistance and inductance, and shunt capacitance and conductance. Source: Self-created using Inkscape.

lengths of the wires become comparable to or larger than the wavelengths of the electromagnetic waves. This leads to excessive power loss through radiation and the reflection from discontinuities in the wires such as connectors and joints. In order to guarantee that the signals are able to arrive at the intended destinations with the smallest power loss, transmission lines with specialised configurations, and impedance matching must be explored and developed.

In its early stages, radio frequency systems mainly relied on the two-wire lines, and coaxial lines invented by Oliver Heaviside in 1880 for transmission (Nahin 2002). Later, transmission lines in planar technology offered an alternative with advantages of being compact, low cost, and easily integrated into other planar circuits. The earliest planar transmission line, a flat-strip coaxial line, whose structure was close to a stripline, was

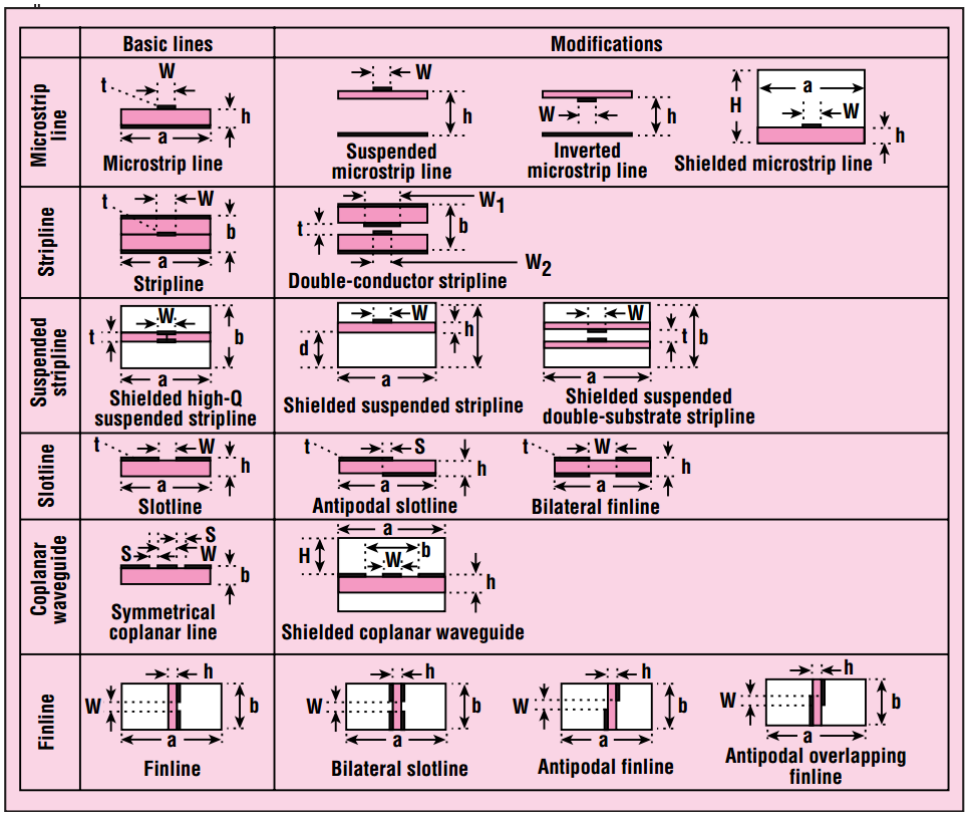

Figure 2.4. Commonly used types of printed transmission lines. This figure shows a number of transmission lines which are widely used in integrated-circuit (IC) fabrications. Source: Created by Leo G. Maloratsky (Maloratsky 2000).

applied to a production antenna and power division network by V. H. Rumsey and H. W. Jamieson during World War II (Barrett 1984). Later, the most common planar transmission line, the microstrip line, which was the competitor to the stripline, was developed by ITT laboratories around 1952 (Grieg and Engelmann 1952). Further examples of planar transmission lines are shown in Fig. 2.4 (Maloratsky 2000), with every type having its advantages and weaknesses with respect to the others. For instance, the microstrip line has a remarkable fabrication advantage over stripline due to its open structure, while the shielded microstrip line is better than the microstrip line when it comes to protecting circuits from environmental contaminants, preventing electromagnetic interference, and enhancing the circuit mechanical strength.

2.2.3 Multiplexers

A multiplexer is a device that separates a wider frequency band into a few narrower bands, or combines frequency signals from certain channels at one common port. The

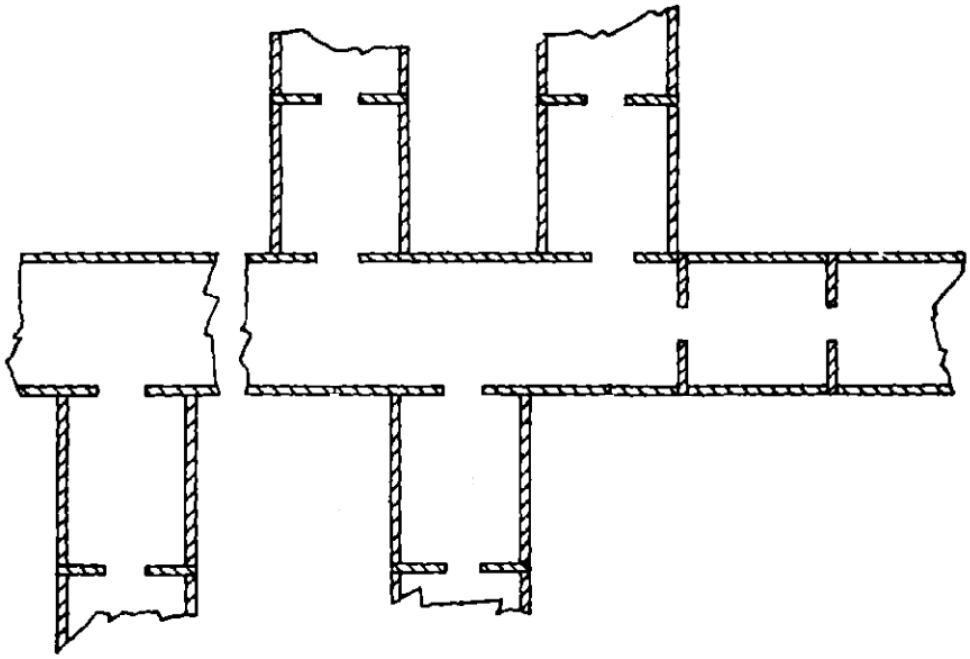

Figure 2.5. Schematic structure of a multiplexer. This figure shows the multiplexer first described by Fano and Lawson in 1948. It constists of several band-pass filters mounted in parallel into the main waveguide/transmission line. Within a particular frequency band, the corresponding filter behaves as a shunt impedance which approximately equals to the characteristic impedance of the transmission line. Source: Created by Fano and Lawson (Ragan 1948).

device can be classified into two types, contiguous multiplexers whose passbands are adjacent, and non-contiguous multiplexers whose passbands are separated by guard bands. The concept of multiplexer, whose structure is shown in Fig. 2.5, was first described in a book chapter by Fano and Lawson in 1948 (Ragan 1948), while in the same year, J. R. Pierce presented an approach for contiguous designs (Pierce 1949, Pierce 1953).

A multiplexer is generally realised by assembling various filters and eliminating their undesired mutual interactions. One of the earliest techniques for multiplexer design was proposed in the 1950s by Seymour Cohn and Frank Coale, and made use of directional filters (Matthaei *et al.* 1980). However, the technique was not popular, because it was difficult to apply modern filter technology to the directional mode. Therefore, efforts were made in assembling non-directional filters, and in the 1960s, the concept of multiplexers with compensating immittance networks at the common junction, was introduced by E. G. Cristal and G. L. Matthaei (Cristal and Matthaei 1964, Matthaei and Cristal 1967). This technique is still used sometimes, but the advances in computational

capabilities, and synthesis techniques have made it possible to produce matching filters directly without additional networks.

During the same period, E. J. Curley, from Microwave Development Laboratories, discovered that contiguous multiplexers, as well as non-contiguous multiplexers, could be realised through modifying the first few elements that were close to the common junction. The compensating networks thus could be omitted in the multiplexers. Later, in 1976, J. D. Rhodes introduced the direct design method for symmetrical interacting band-pass channel diplexers, which formalized E. J. Curley's discovery (Rhodes 1976). In 1979, J. D. Rhodes and Ralph Levy extended the method further and provided a generalised multiplexer theory (Rhodes and Levy 1979).

Another advance initiated in the 1980s is the application of planar technology in the area of multiplexers. Compared with solid coaxial constructions or waveguide structures, the printed-circuit multiplexers have the advantages of low cost, small dimensions, easy fabrication, and easy integration into other planar circuits (Levy and Cohn 1984). Recently, a new innovation occurred with the introduction of SIW structures and associated improvements of the insertion loss of printed circuit multiplexers. Numerous diplexer designs were developed in this technology in the past decades (Hao *et al.* 2005, Tang *et al.* 2007, Han *et al.* 2007, Chu *et al.* 2011, Kordiboroujeni and Bornemann 2015b, Sirci *et al.* 2015).

2.3 Numerical Methods in Electromagnetics

Computational electromagnetics refers to the numerical solution of Maxwell's equations in a process aiming at modelling the interaction of electromagnetic fields with physical objects and their environment. Because of the multitude of irregular geometries in actual components, a number of practical electromagnetic issues such as electromagnetic scattering and electromagnetic radiation, are often analytically not tractable. With the ever-increasing availability of computing power, numerical techniques implemented into computers are able to conquer the problem and obtain accurate solutions for discretised Maxwell's equations, applying various constitutive equations of material and boundary conditions. Thus, advanced numerical techniques play a crucially important role to the microwave industry nowadays, because they can provide results with sufficient precision, while reducing the development cost by shortening the design cycle.

Numerous numerical techniques were introduced in the past decades to analyse electromagnetic issues. According to the methods utilised to solve field equations, these techniques can be classified in space-domain methods represented by the finite-element method (FEM) (Silvester and Ferrari 1996) and the finite-difference method (FDM) (Davies and Muilwyk 1966), space-domain and time-domain combination methods represented by the finite-difference time-domain (FDTD) (Yee 1966) and the transmission line matrix (TLM) (Johns and Beurle 1971), and modal-domain methods represented by the mode-matching method (MMM) (Wexler 1967) and the method of moments (MoM) (Harrington 1993). This chapter only briefly reviews the historical backgrounds of the MMM and the FEM, as those two methods are used in the rest of the thesis.

Mode-Matching Method

The MMM is a rigorous and efficient technique to solve electromagnetic boundary-value problems. This method expands the electromagnetic fields that exist in the cross-section of the electronic component into a series of eigenmodes, which are solved from Maxwell's equations, and then matches all modes on the junction plane in order to get the generalised scattering matrix (GSM).

Although this technique had been applied earlier, it was not formulated as a systematic avenue to solve problems about waveguide discontinuities until 1967, by Alvin Wexler (Wexler 1967). However, because of the limitations of computer capability available at the time, the MMM was not able to realise its great potential in handling more complicated structures. The leap in computing power in the following decades changed the situation. Since the 1980s, F. Arndt, Jens Bornemann, and other pioneers invested a lot of effort to investigate the relative convergence phenomenon in the mode-matching analysis (Leroy 1983, Shih and Gray 1983, Uher and Bornemann 1993), and to weigh the advantages and disadvantages of general scattering matrix (GSM), general transmission matrix (GTM) and general admittance matrix (GAM) (Mansour and MacPhie 1986, Alessandri *et al.* 1988). They also optimised the technique and improved its efficiency through decreasing the number of required eigenvalue equations, increasing the flexibility of the procedures, and reducing the programming difficulty (Vahldieck and Bornemann 1985). Numerous devices were developed based on this technique, such as filters (Vahldieck *et al.* 1983, Papziner and Arndt 1993), multiplexers (Dittloff and Arndt 1988, Liang *et al.* 1991), power dividers (Arndt *et al.* 1987), directional couplers (Arndt *et al.* 1985, Sieverding *et al.* 1997), and so on.

Later, the MMM was extended to analyse discontinuities in circular waveguides (Accatino and Bertin 1994), ridged waveguides (Guha and Saha 1997), planar transmission lines (Shih *et al.* 1985), coaxial probes in rectangular waveguides (Yao and Zaki 1995), and others. In the past decade, the MMM has been still optimised further and applied to hot areas of research, such as frequency selective structures (FSS) (Rashid *et al.* 2012). Besides, in order to increase the generality of the MMM, the combinations with other numerical methods became another attractive aspect to researchers in relative fields (Belenguer *et al.* 2010, Pellegrini *et al.* 2014).

Finite-Element Method

The FEM is another numerical technique to obtain approximate solutions of boundary-value problems for partial differential equations. It subdivides a whole computational domain into smaller non-overlapped cells, that is, finite elements, and then assemble the simpler local element equations to model the initial complex equations of the entire problem.

This method stemmed from the demand to solve complicated elasticity and structural problems in civil and aeronautical engineering. Although its name was given by R. W. Clough in 1960 (Clough 1960), its development can be traced back to Alexander Hrennikoff and Richard Courant in the early 1940s (Hrennikoff 1941, Courant 1943). Applying the direct stiffness method, that is, the most common implementation of the FEM, for the analysis of the aircraft structures for the first time, M. J. Turner, R. W. Clough, H. C. Martin, and L. J. Topp presented a more direct process to discretise the domain by arbitrary triangular or rectangular elements (Turner *et al.* 1956). Their paper was published in 1956, and is considered as the start of the engineering FEM. In addition, in the later 1950s and early 1960s, Kang Feng presented a systematic numerical method for solving partial differential equations based on calculus, and his invention is considered as another independent invention of the FEM (Zienkiewicz 1995).

Since the early 1960s, much progress was made to the FEM in many directions. For instance, in the basis of energetic and variational considerations, the method was reformulated with weighted residuals or weak formulations; high-precision vector elements, curved elements, and isoparametric elements were created for the discretisation of the FEM (Dhatt *et al.* 2012).

As a result of the mentioned contributions, nowadays, the FEM is widely applied in many industrial and scientific fields, including electromagnetism, automobile, fluid

Table 2.1. Comparison of Numerical Methods. This table compares several numerical methods, including MMM, FEM, FDM, TLM, SDM, BEM in RAM requirement, CPU time and versatility.

Method	RAM Requirement	CPU Time	Versatility
MMM	low	low	poor
FEM	high	medium/high	good
FDTD	high	high	good
TLM	medium/high	medium/high	good
SDM	low	low	marginal
BEM	medium*	medium	good

* The RAM requirement becomes high rapidly with the problem size grows, as it is based on matrix inversion.

mechanics, and aerospace. Many commercial software applications have thus been developed for these industrial users, such as Ansys, Nastran, Fidap, and others.

To sum up, the FEM can approximate complex arbitrary geometries with a series of small cells. The generality of this technique thus is great, but sufficient precision requires a large number of mesh points which leads to large memory storage usage and low efficiency. Comparatively, the MMM is much more efficient, but this technique is limited to regular structures, such as waveguide components. A more comprehensive comparison of numerical methods, including MMM, FEM, FDM, TLM, spectral domain method (SDM), and boundary element method (BEM) is listed in Table 2.1 (Sorrentino 1989, Itoh 1989a)

2.4 Chapter Summary

This chapter introduced the historical background and theoretical development of filters, transmission lines, multiplexers, as well as the two numerical methods in electromagnetics relevant for this thesis, specifically the mode-matching method and the

finite-element method. Seminal inventions and significant developments were highlighted in this chapter.

The next chapter will explain in detail the mode-matching method for iris discontinuities in rectangular waveguides and filter theory, together with the error tolerance for iris band-pass filters.

Chapter 3

Band-Pass Iris Rectangular Waveguide Filters

THIS chapter starts by analysing electromagnetic waves in a rectangular waveguide, together with the corresponding formula derivations. It then explains the principles of the mode-matching method, with which the characteristics of irises placed in the cross-section of a rectangular waveguide can be analysed efficiently. Combining the principle of the mode-matching method and the band-pass filter theory, an efficient method to design iris band-pass filters is introduced in detail. Considering the limitations of micro-machining processes, this chapter also analyses the influence of rounded angle corners between the waveguide walls and irises. To eliminate this undesired influence, three approaches are proposed in this chapter, which consist of compensating the frequency shift, offsetting the shift with bevel angles, and taking the properties of the perturbations into account when computing the sizes. All approaches successfully correct the offset of the centre frequency caused by rounded corners and all calculated results obtained with a self-written mode-matching code are verified by the finite-element simulations.

3.1 Introduction

With the rapid development of advanced microwave and millimetre-wave systems, the performance requirements of passive band-pass filters used for removing undesired frequency components are steadily increasing. As an essential part in such systems, passive band-pass filters are often realised in waveguide technology, because of the advantages of high quality factor (Q factor), low loss, and good power handling capability (Sorrentino and Bianchi 2010, Gustrau 2012).

Metal diaphragms (irises) placed transversely in rectangular waveguides are able to generate reflected waves and store reactive energy near the discontinuities, since the excited higher-order modes are evanescent, that is, their amplitudes drop exponentially with distance from the discontinuities (Collin 1991). Thus, irises are often adopted to form cavity resonators, which are basic components for rectangular waveguide band-pass filters. For illustration, the structure of a W-band (extending from 75 GHz to 110 GHz) 5-cavity H-plane iris band-pass rectangular waveguide filter is shown in Fig. 3.1.

This chapter is organised as follows. Section 3.2 explains the principle of the mode-matching method (MMM) for irises placed transversely in a rectangular waveguide, while Section 3.3 explains briefly the principle of band-pass filters. Combining the content in Section 3.2 and Section 3.3, an efficient method to design iris band-pass rectangular waveguide filter is introduced in Subsection 3.4.1. Subsection 3.4.2 investigates the influence of rounded corners between the waveguide walls and irises due to the limitations of micro-machining processes. Three efficient approaches to eliminate the undesired influence are also presented in Subsection 3.4.3. The chapter ends in Section 3.5.

3.2 Principle of the Mode-Matching Method for Irises

Irises are often used to block a short length of waveguide at both ends in order to form a cavity resonator, in which electromagnetic waves bounce back and forth between the irises. Several common types of irises with possible geometries and their equivalent circuits are shown in Fig. 3.2. Symmetrical or asymmetrical H-plane inductive irises placed in the cross-section of a rectangular waveguide restrict its width, and have an equivalent circuit of a shunt inductance. Symmetrical or asymmetrical E-plane capacitive irises placed in the cross-section of a rectangular waveguide decrease its height,

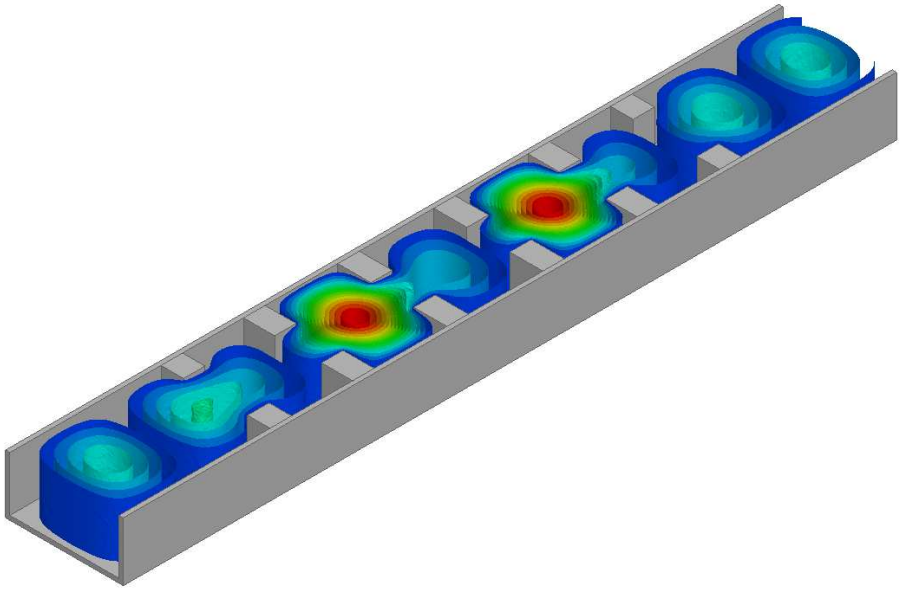

Figure 3.1. Structure of a W-band 5-cavity band-pass H-plane iris rectangular waveguide filter. This figure depicts the structure of a 5^{th}-order band-pass rectangular waveguide filter whose centre frequency is 94 GHz and passband expends from 92 GHz to 96 GHz. The filter is designed with H-plane irises and a standard WR-10 rectangular waveguide. The image shows the instantaneous field distribution at 94 GHz. Source: Self-created using Ansys High Frequency Structural Simulator (Ansys HFSS) and Inkscape.

which yields an equivalent circuit of a shunt capacitance. A rectangular resonant iris placed in the cross-section of a rectangular waveguide, which restricts both width and height, can be considered as parallel LC resonant circuit (Pozar 2011). Since the first two classes of irises (H-plane and E-plane irises) can be treated as the simplification of the third one, the following analysis shall focus on the rectangular resonant iris.

3.2.1 Fields in Rectangular Waveguide

Waveguides are metal tubes used to guide electromagnetic waves and they can be hollow or fully filled with dielectric material. The cross-section of a waveguide can be rectangular, circular, or elliptical. However, the most common waveguide cross-section is rectangular, since it presents the advantages of wide bandwidth for single-mode operation, reasonably low attenuation, and good mode stability for the fundamental mode of propagation (Collin 1991).

Since this type of waveguide is composed of a single conductor, it only supports the propagation of transverse electric modes (TE modes) and transverse magnetic modes

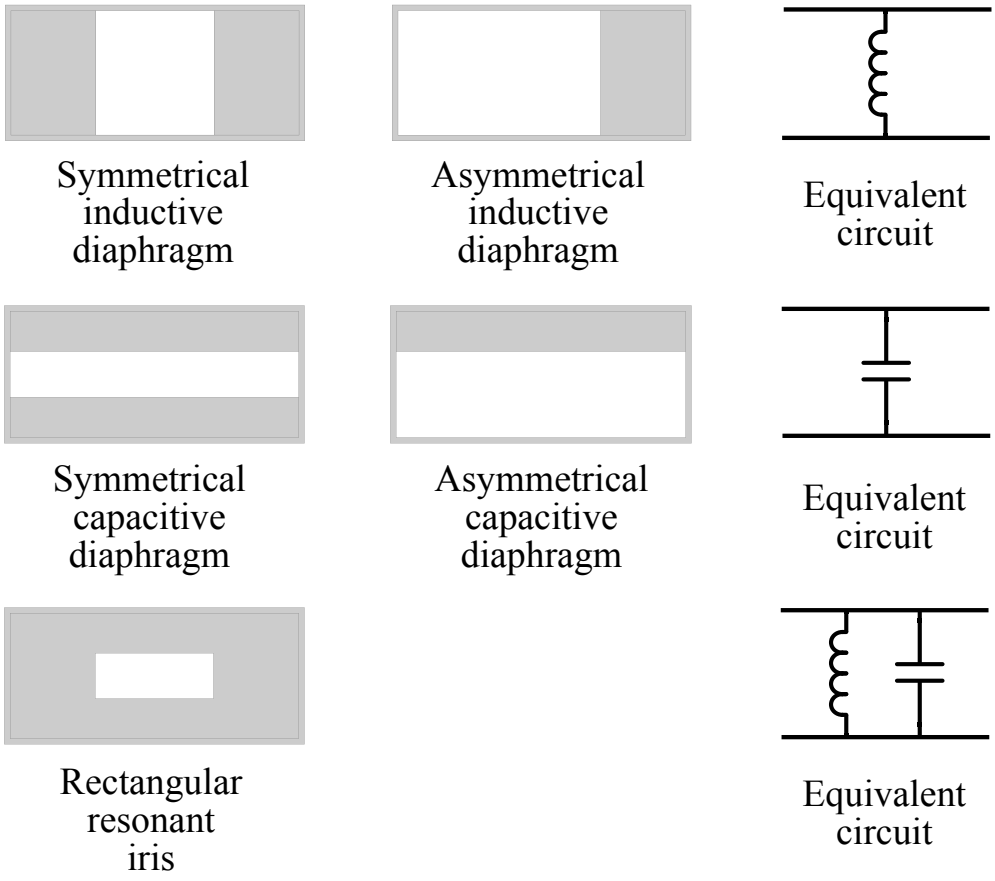

Figure 3.2. Common iris discontinuities in rectangular waveguide and their equivalent circuits. This figure shows some irises placed in the cross-section of a rectangular waveguide, including symmetrical and asymmetrical inductive irises, symmetrical and asymmetrical capacitive irises and rectangular resonant iris which are able to yield equivalent shunt inductance, capacitance, or a resonant combination. Source: Self-created using Ansys HFSS and Inkscape.

(TM modes) (Pozar 2011). The TE_{10} mode is the fundamental mode for a rectangular waveguide, and it is the preferred mode when a waveguide is used in practice. Its electric and magnetic fields are shown in Fig. 3.3.

Generally, electric and magnetic modes exist in a rectangular waveguide, including the fundamental modes and the other high-order modes. According to basic electromagnetic theory, for propagation along the z-axis, these modes can be expressed by the following equations (Collin 1991, Rothwell and Cloud 2008)

$$\vec{E} = \bigtriangledown \times (A_h \vec{z}) + \frac{1}{j\omega\varepsilon} \bigtriangledown \times \bigtriangledown \times (A_e \vec{z}), \tag{3.1}$$

$$\vec{H} = \bigtriangledown \times (A_e \vec{z}) - \frac{1}{j\omega\mu} \bigtriangledown \times \bigtriangledown \times (A_h \vec{z}), \tag{3.2}$$

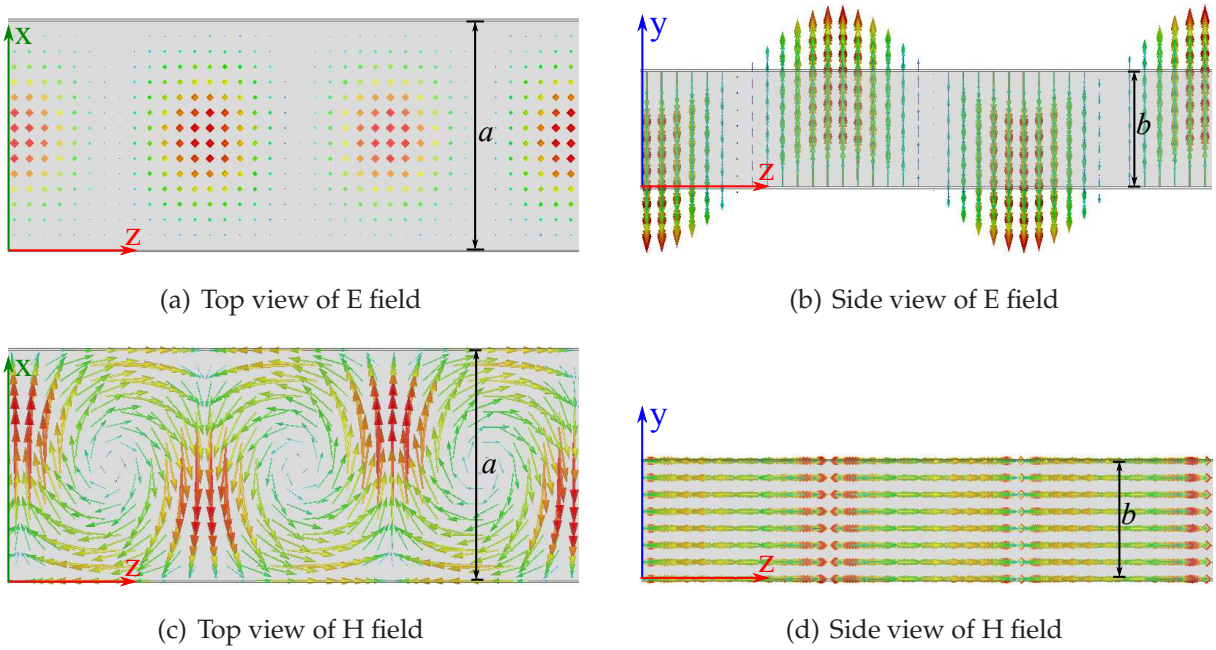

(a) Top view of E field

(b) Side view of E field

(c) Top view of H field

(d) Side view of H field

Figure 3.3. Electric and magnetic fields for the TE_{10} mode in a rectangular waveguide. These figures show the instantaneous electric and magnetic fields for the fundamental mode TE_{10} mode in a rectangular waveguide whose width is a and height is b. Source: Self-created using Ansys HFSS and Inkscape.

where A_h and A_e are the magnitudes of z-directed magnetic and electric vector potentials, ω represents angular frequency, ε and μ are the permittivity and permeability of the loaded medium in a waveguide respectively, j is the notation for complex numbers, and $\vec{z}$ is the unit vector along the z-axis.

Eq. 3.1 and 3.2 can be further derived to obtain the equations for transverse electric and magnetic fields, $\vec{E}_t$ and $\vec{H}_t$, as the following

$$\vec{E}_t = -\bigtriangledown_t A_h \times \vec{z} + \frac{1}{j\omega\varepsilon} \bigtriangledown_t \frac{\partial A_e}{\partial z}, \tag{3.3}$$

$$\vec{H}_t = \bigtriangledown_t A_e \times \vec{z} + \frac{1}{j\omega\mu} \bigtriangledown_t \frac{\partial A_h}{\partial z}, \tag{3.4}$$

where subscript t means transverse and $\bigtriangledown_t$ is the transverse gradient operator.

As known from basic electromagnetic theory, the magnitudes of z-directed magnetic and electric vector potentials, A_h and A_e, satisfy the homogeneous Helmholtz equations

$$\bigtriangledown_t^2 A_h + k_c^2 A_h = 0, \tag{3.5}$$

$$\nabla_t^2 A_e + k_c^2 A_e = 0, \tag{3.6}$$

where ∇_t^2 is the transverse Laplace operator, and k_c is the cutoff wavenumber for a waveguide.

Applying the method of separation of variables (Polyanin and Manzhirov 2006), Eq. 3.5 and 3.6 can be solved. The solutions are shown below

$$A_h = (Q_{h1}e^{-jk_{hx}x} + Q_{h2}e^{jk_{hx}x})(Q_{h3}e^{-jk_{hy}y} + Q_{h4}e^{jk_{hy}y})e^{-\Gamma_h z}, \tag{3.7}$$

$$A_e = (Q_{e1}e^{-jk_{ex}x} + Q_{e2}e^{jk_{ex}x})(Q_{e3}e^{-jk_{ey}y} + Q_{e4}e^{jk_{ey}y})e^{-\Gamma_e z}, \tag{3.8}$$

where $Q_{h1...4}$ and $Q_{e1...4}$ are amplitude coefficients, k_{hx}, k_{hy}, k_{ex} and k_{ey} are wavenumbers along the x-axis and the y-axis for different TE and TM modes, and Γ_h and Γ_e are propagation constants.

For TE modes, utilising the boundary conditions that the normal derivative of A_h on the inner surface of the waveguide is 0, that is, $\frac{\partial A_h}{\partial \vec{n}}|_{inner\ surface} = 0$ (Collin 1991), Eq. 3.7 can be further derived together with the cutoff wavenumber k_{hc} formula for TE modes

$$\begin{aligned} A_h &= Q_h T_h e^{-\Gamma_h z} \\ T_h &= \cos(k_{hx}x)\cos(k_{hy}y) = \cos(\frac{m\pi x}{a})\cos(\frac{n\pi y}{b}) \\ k_{hc} &= \sqrt{{k_{hx}}^2 + {k_{hy}}^2} = \sqrt{(\frac{m\pi}{a})^2 + (\frac{n\pi}{b})^2} \end{aligned} \tag{3.9}$$

where Q_h is the amplitude coefficient for TE modes in the rectangular waveguide, T_h is the eigenfunction for TE modes, and the non-negative integers m and n represent the index of TE modes, which cannot be zero at the same time (Pozar 2011).

For TM modes, utilising the boundary conditions that A_e on the inner surface of the waveguide is 0, that is, $A_e|_{inner\ surface} = 0$ (Collin 1991), similar equations can be obtained as the following

$$\begin{aligned} A_e &= Q_e T_e e^{-\Gamma_e z} \\ T_e &= \sin(k_{ex}x)\sin(k_{ey}y) = \sin(\frac{m\pi x}{a})\sin(\frac{n\pi y}{b}) \\ k_{ec} &= \sqrt{{k_{ex}}^2 + {k_{ey}}^2} = \sqrt{(\frac{m\pi}{a})^2 + (\frac{n\pi}{b})^2} \end{aligned} \tag{3.10}$$

where Q_e is the amplitude coefficient for TM modes in the rectangular waveguide, T_e is the eigenfunction for TM modes, k_{ec} is the cutoff wavenumber, and m and n also represent the index of TM modes. It is noted that m and n here are non-negative and non-zero integers (Pozar 2011).

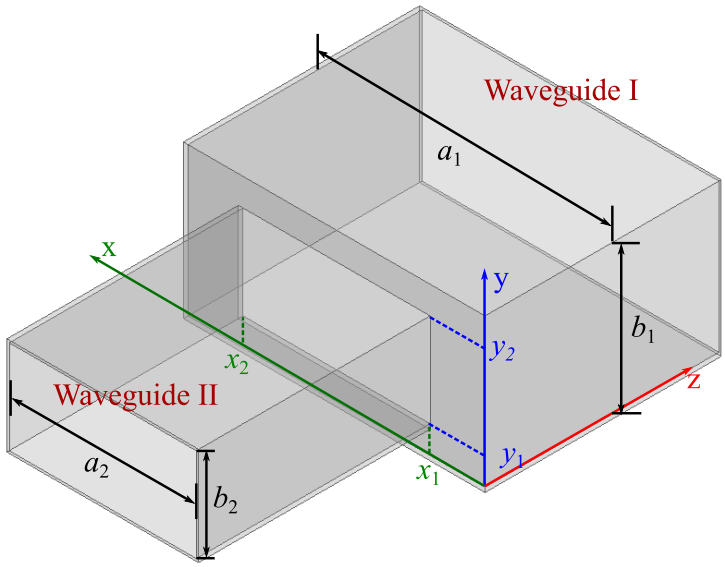

Figure 3.4. A double-plane step discontinuity in rectangular waveguide. This figure shows the configuration of a double-plane step discontunity, which is formed by two rectangular waveguides. Waveguide I has a width of a_1 and a height of b_1, while waveguide II has a width of a_2 and a height of b_2. Variables including x_1, x_2, y_1 and y_2 determine the position of the aperture on the junction surface, that is, $z = 0$ plane. Source: Self-created using Ansys HFSS and Inkscape.

3.2.2 Mode-Matching Analysis of Rectangular Waveguide Double-Plane Step Discontinuities

The structure of a double-plane step discontinuity formed by two rectangular waveguides is shown in Fig. 3.4. Because of the discontinuity at the junction plane, there will be forward and backward electromagnetic waves in both waveguides as shown in Fig. 3.5, including the fundamental mode TE_{10} mode and the other excited high-order TE_{mn} and TM_{mn} modes. High-order modes below their cut-off frequency can exist in the vicinity of the discontinuity, and have an exponential attenuation with distance from the $z = 0$ plane. However, the influence caused by these evanescent modes is not negligible, since they are reasons for the energy storage (Collin 1991).

Taking these excited modes into account, the MMM can be applied to analyse quickly and accurately the double-plane step discontinuity placed in a rectangular waveguide (Patzelt and Arndt 1982, Uher and Bornemann 1993, Jarry and Beneat 2008). The energy on each side of the discontinuity is required to be conserved. Thus, the equations for the magnitudes of z-directed magnetic and electric vector potentials A_h

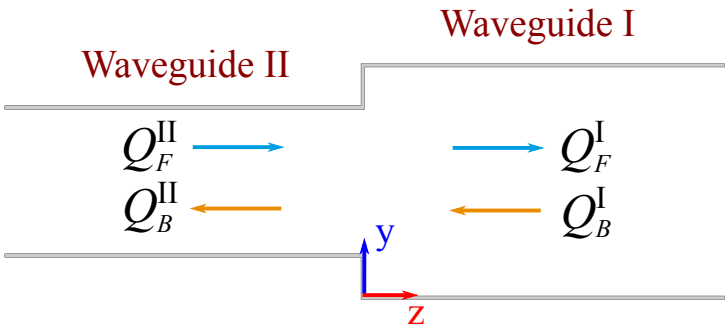

Figure 3.5. Wave amplitude coefficients at the junction between waveguide I and II. This figure shows the electromagnetic waves at the discontinuity of the two waveguides. Q_F^{I} and Q_F^{II} represent the amplitude coefficients for modes propagating along z-direction, while Q_B^{I} and Q_B^{II} represent the amplitude coefficients for modes propagating along opposite direction from z-direction. Source: Self-created using Ansys HFSS and Inkscape.

and A_e in Eq. 3.9 and 3.10 should be modified as below

$$A^i_{hm^i_h n^i_h} = Q^i_{hm^i_h n^i_h} G^i_{hm^i_h n^i_h} T^i_{hm^i_h n^i_h} e^{-\Gamma^i_{hm^i_h n^i_h} z}, \tag{3.11}$$

$$A^i_{em^i_e n^i_e} = Q^i_{em^i_e n^i_e} G^i_{em^i_e n^i_e} T^i_{em^i_e n^i_e} e^{-\Gamma^i_{em^i_e n^i_e} z}, \tag{3.12}$$

where i represents the regions in Waveguide I and II, $G^i_{hm^i_h n^i_h}$ and $G^i_{em^i_e n^i_e}$ represent normalised coefficients which limit the average power carried by each mode to 1 W.

For TE modes, $A^i_{em^i_e n^i_e} = 0$, thus, the transverse electric and magnetic fields can be obtained through simplifying Eq. 3.3 and 3.4

$$\vec{E}^i_{thm^i_h n^i_h} = -\bigtriangledown_t A^i_{hm^i_h n^i_h} \times \vec{z}, \tag{3.13}$$

$$\vec{H}^i_{thm^i_h n^i_h} = \frac{1}{j\omega\mu^i} \bigtriangledown_t \frac{\partial A^i_{hm^i_h n^i_h}}{\partial z}. \tag{3.14}$$

The power carried by TE modes is

$$P^i_{hm^i_h n^i_h} = \frac{1}{2} \iint_{\mathcal{S}} (\vec{E}^i_{thm^i_h n^i_h} \times \vec{H}^{i*}_{thm^i_h n^i_h}) d\vec{\mathcal{S}}, \tag{3.15}$$

where $\mathcal{S}$ represents the closed cross-section surface of the rectangular waveguide.

Substituting Eq. 3.11, 3.13 and 3.14 into Eq. 3.15 yields

$$\begin{aligned} P^i_{hm^i_h n^i_h} &= -\frac{1}{2}\iint_S \frac{\Gamma^{i*}_{hm^i_h n^i_h}}{j\omega\mu^i}(\bigtriangledown_t A^i_{hm^i_h n^i_h} \times \vec{z}) \times A^{i*}_{hm^i_h n^i_h} \cdot \vec{z}\mathrm{d}S \\ &= -\frac{\Gamma^{i*}_{hm^i_h n^i_h}}{2j\omega\mu^i}|Q^i_{hm^i_h n^i_h}|^2 {G^i_{hm^i_h n^i_h}}^2 \iint_S (\bigtriangledown_t T^i_{hm^i_h n^i_h} \times \vec{z}) \times \bigtriangledown_t T^{i*}_{hm^i_h n^i_h} \cdot \vec{z}\mathrm{d}S \\ &= -\frac{\Gamma^{i*}_{hm^i_h n^i_h}}{2j\omega\mu^i}|Q^i_{hm^i_h n^i_h}|^2 {G^i_{hm^i_h n^i_h}}^2 \iint_S \bigtriangledown_t T^i_{hm^i_h n^i_h} \cdot \bigtriangledown_t T^{i*}_{hm^i_h n^i_h}\mathrm{d}S. \end{aligned} \tag{3.16}$$

Normalising the power expressed in Eq. 3.16, the formula for the normalised coefficient can be expressed as

$$G^i_{hm^i_h n^i_h} = \sqrt{\frac{j\omega\mu^i}{\Gamma^i_{hm^i_h n^i_h}\iint_S \bigtriangledown_t T^i_{hm^i_h n^i_h} \cdot \bigtriangledown_t T^{i*}_{hm^i_h n^i_h}\mathrm{d}S}} = \frac{\sqrt{Z^i_{hm^i_h n^i_h}}}{\sqrt{\iint_S \bigtriangledown_t T^i_{hm^i_h n^i_h} \cdot \bigtriangledown_t T^{i*}_{hm^i_h n^i_h}\mathrm{d}S}}, \tag{3.17}$$

where $Z^i_{hm^i_h n^i_h} = j\omega\mu^i/\Gamma^i_{hm^i_h n^i_h}$ is the wave impedance for TE modes.

Meanwhile, substituting eigenfunctions $T^i_{hm^i_h n^i_h}$ (Eq. 3.9) into Eq. 3.17, the normalised coefficients for TE modes can be expressed as

$$G^i_{hm^i_h n^i_h} = \frac{2}{\sqrt{a_i b_i}}\frac{\sqrt{Z^i_{hm^i_h n^i_h}}}{k^i_{hcm^i_h n^i_h}}. \tag{3.18}$$

In the same manner, the equations for power carried by the TM modes and the formula for the normalised coefficient can be described as below

$$P^i_{em^i_e n^i_e} = -\frac{\Gamma^{i*}_{em^i_e n^i_e}}{2j\omega\varepsilon^i}|Q^i_{em^i_e n^i_e}|^2 {G^i_{em^i_e n^i_e}}^2 \iint_S \bigtriangledown_t T^i_{em^i_e n^i_e} \cdot \bigtriangledown_t T^{i*}_{em^i_e n^i_e}\mathrm{d}S, \tag{3.19}$$

$$G^i_{em^i_e n^i_e} = \frac{\sqrt{Y^i_{em^i_e n^i_e}}}{\sqrt{\iint_S \bigtriangledown_t T^i_{em^i_e n^i_e} \cdot \bigtriangledown_t T^{i*}_{em^i_e n^i_e}\mathrm{d}S}}, \tag{3.20}$$

where $Y^i_{em^i_e n^i_e} = j\omega\varepsilon^i/\Gamma^i_{em^i_e n^i_e}$ represents the wave admittance for TM modes.

Substituting eigenfunctions $T^i_{em^i_e n^i_e}$ (Eq. 3.10) into Eq. 3.20, the normalised coefficients for TM modes can be expressed as

$$G^i_{em^i_e n^i_e} = \frac{2}{\sqrt{a_i b_i}}\frac{\sqrt{Y^i_{em^i_e n^i_e}}}{k^i_{ecm^i_e n^i_e}}. \tag{3.21}$$

All modes in the double-plane waveguide step can now be fully described with the equations above (3.9, 3.10 3.11, 3.12, 3.18, 3.21). As shown in Fig. 3.5, each rectangular waveguide contains reflected and transmitted electromagnetic waves. Considering backward and forward waves together, the magnitudes of z-directed magnetic and electric vector potentials, A_h^i and A_e^i can be expressed below

$$A_h^i = \sum_{m_h^i=0}^{\infty}\sum_{n_h^i=0}^{\infty} G^i_{hm_h^i n_h^i} T^i_{hm_h^i n_h^i} (Q^i_{hm_h^i n_h^i F} e^{-\Gamma^i_{hm_h^i n_h^i} z} + Q^i_{hm_h^i n_h^i B} e^{+\Gamma^i_{hm_h^i n_h^i} z}), \tag{3.22}$$

$$A_e^i = \sum_{m_e^i=1}^{\infty}\sum_{n_e^i=1}^{\infty} G^i_{em_e^i n_e^i} T^i_{em_e^i n_e^i} (Q^i_{em_e^i n_e^i F} e^{-\Gamma^i_{em_e^i n_e^i} z} + Q^i_{em_e^i n_e^i B} e^{+\Gamma^i_{em_e^i n_e^i} z}), \tag{3.23}$$

where $Q^i_{hm_h^i n_h^i F}$ and $Q^i_{em_e^i n_e^i F}$ represent the amplitude coefficients for modes propagating along z-direction, while $Q^i_{hm_h^i n_h^i B}$ and $Q^i_{em_e^i n_e^i B}$ represent the amplitude coefficients for modes propagating along opposite direction from z-direction.

In the double-plane waveguide step, transverse electric and magnetic fields on the junction plane are continuous. Thus, substituting Eq. 3.22 and 3.23 into Eq. 3.3 and 3.4, and matching the obtained transverse electric and magnetic fields on the $z = 0$ plane respectively, two equations can be derived as below

$$\begin{aligned}
&\sum_{m_h^{\mathrm{I}}=0}^{\infty}\sum_{n_h^{\mathrm{I}}=0}^{\infty} G^{\mathrm{I}}_{hm_h^{\mathrm{I}} n_h^{\mathrm{I}}} (\bigtriangledown_t T^{\mathrm{I}}_{hm_h^{\mathrm{I}} n_h^{\mathrm{I}}} \times \vec{z})(Q^{\mathrm{I}}_{hm_h^{\mathrm{I}} n_h^{\mathrm{I}} F} + Q^{\mathrm{I}}_{hm_h^{\mathrm{I}} n_h^{\mathrm{I}} B}) \\
&+\frac{1}{j\omega\varepsilon^{\mathrm{I}}} \sum_{m_e^{\mathrm{I}}=0}^{\infty}\sum_{n_e^{\mathrm{I}}=0}^{\infty} G^{\mathrm{I}}_{em_e^{\mathrm{I}} n_e^{\mathrm{I}}} \Gamma^{\mathrm{I}}_{em_e^{\mathrm{I}} n_e^{\mathrm{I}}} \bigtriangledown_t T^{\mathrm{I}}_{em_e^{\mathrm{I}} n_e^{\mathrm{I}}} (Q^{\mathrm{I}}_{em_e^{\mathrm{I}} n_e^{\mathrm{I}} F} + Q^{\mathrm{I}}_{em_e^{\mathrm{I}} n_e^{\mathrm{I}} B}) \\
&= \sum_{m_h^{\mathrm{II}}=0}^{\infty}\sum_{n_h^{\mathrm{II}}=0}^{\infty} G^{\mathrm{II}}_{hm_h^{\mathrm{II}} n_h^{\mathrm{II}}} (\bigtriangledown_t T^{\mathrm{II}}_{hm_h^{\mathrm{II}} n_h^{\mathrm{II}}} \times \vec{z})(Q^{\mathrm{II}}_{hm_h^{\mathrm{II}} n_h^{\mathrm{II}} F} + Q^{\mathrm{II}}_{hm_h^{\mathrm{II}} n_h^{\mathrm{II}} B}) \\
&+\frac{1}{j\omega\varepsilon^{\mathrm{II}}} \sum_{m_e^{\mathrm{II}}=0}^{\infty}\sum_{n_e^{\mathrm{II}}=0}^{\infty} G^{\mathrm{II}}_{em_e^{\mathrm{II}} n_e^{\mathrm{II}}} \Gamma^{\mathrm{II}}_{em_e^{\mathrm{II}} n_e^{\mathrm{II}}} \bigtriangledown_t T^{\mathrm{II}}_{em_e^{\mathrm{II}} n_e^{\mathrm{II}}} (Q^{\mathrm{II}}_{em_e^{\mathrm{II}} n_e^{\mathrm{II}} F} + Q^{\mathrm{II}}_{em_e^{\mathrm{II}} n_e^{\mathrm{II}} B}),
\end{aligned} \tag{3.24}$$

$$\begin{aligned}
&\frac{1}{j\omega\mu^{\mathrm{I}}} \sum_{m_h^{\mathrm{I}}=1}^{\infty}\sum_{n_h^{\mathrm{I}}=1}^{\infty} G^{\mathrm{I}}_{hm_h^{\mathrm{I}} n_h^{\mathrm{I}}} \Gamma^{\mathrm{I}}_{hm_h^{\mathrm{I}} n_h^{\mathrm{I}}} \bigtriangledown_t T^{\mathrm{I}}_{hm_h^{\mathrm{I}} n_h^{\mathrm{I}}} (Q^{\mathrm{I}}_{hm_h^{\mathrm{I}} n_h^{\mathrm{I}} F} - Q^{\mathrm{I}}_{hm_h^{\mathrm{I}} n_h^{\mathrm{I}} B}) \\
&- \sum_{m_e^{\mathrm{I}}=1}^{\infty}\sum_{n_e^{\mathrm{I}}=1}^{\infty} G^{\mathrm{I}}_{em_e^{\mathrm{I}} n_e^{\mathrm{I}}} (\bigtriangledown_t T^{\mathrm{I}}_{em_e^{\mathrm{I}} n_e^{\mathrm{I}}} \times \vec{z})(Q^{\mathrm{I}}_{em_e^{\mathrm{I}} n_e^{\mathrm{I}} F} - Q^{\mathrm{I}}_{em_e^{\mathrm{I}} n_e^{\mathrm{I}} B}) \\
&= \frac{1}{j\omega\mu^{\mathrm{II}}} \sum_{m_h^{\mathrm{II}}=1}^{\infty}\sum_{n_h^{\mathrm{II}}=1}^{\infty} G^{\mathrm{II}}_{hm_h^{\mathrm{II}} n_h^{\mathrm{II}}} \Gamma^{\mathrm{II}}_{hm_h^{\mathrm{II}} n_h^{\mathrm{II}}} \bigtriangledown_t T^{\mathrm{II}}_{hm_h^{\mathrm{II}} n_h^{\mathrm{II}}} (Q^{\mathrm{II}}_{hm_h^{\mathrm{II}} n_h^{\mathrm{II}} F} - Q^{\mathrm{II}}_{hm_h^{\mathrm{II}} n_h^{\mathrm{II}} B}) \\
&- \sum_{m_e^{\mathrm{II}}=1}^{\infty}\sum_{n_e^{\mathrm{II}}=1}^{\infty} G^{\mathrm{II}}_{em_e^{\mathrm{II}} n_e^{\mathrm{II}}} (\bigtriangledown_t T^{\mathrm{II}}_{em_e^{\mathrm{II}} n_e^{\mathrm{II}}} \times \vec{z})(Q^{\mathrm{II}}_{em_e^{\mathrm{II}} n_e^{\mathrm{II}} F} - Q^{\mathrm{II}}_{em_e^{\mathrm{II}} n_e^{\mathrm{II}} B}).
\end{aligned} \tag{3.25}$$

From Eq. 3.24, we dot-multiply both sides by $\bigtriangledown_t T^{\mathrm{I}}_{em_e^{\mathrm{I}'} n_e^{\mathrm{I}'}}$ and $\bigtriangledown_t T^{\mathrm{I}}_{hm_h^{\mathrm{I}'} n_h^{\mathrm{I}'}} \times \vec{z}$ respectively, and then compute the integral on the junction plane. Utilising the orthogonality of electromagnetic fields (Collin 1991), two matrix equations can be obtained

$$\left[Q^{\mathrm{I}}_{eF}\right] + \left[Q^{\mathrm{I}}_{eB}\right] = J_{EH}\left(\left[Q^{\mathrm{II}}_{hF}\right] + \left[Q^{\mathrm{II}}_{hB}\right]\right) + J_{EE}\left(\left[Q^{\mathrm{II}}_{eF}\right] + \left[Q^{\mathrm{II}}_{eB}\right]\right), \tag{3.26}$$

$$\left[Q^{\mathrm{I}}_{hF}\right] + \left[Q^{\mathrm{I}}_{hB}\right] = J_{HH}\left(\left[Q^{\mathrm{II}}_{hF}\right] + \left[Q^{\mathrm{II}}_{hB}\right]\right) + J_{HE}\left(\left[Q^{\mathrm{II}}_{eF}\right] + \left[Q^{\mathrm{II}}_{eB}\right]\right), \tag{3.27}$$

where J_{EH}, J_{EE}, J_{HH} and J_{HE} are coupling coefficients which can be expressed as

$$\begin{aligned} J_{EH} &= Y^{\mathrm{I}}_{em_e^{\mathrm{I}'} n_e^{\mathrm{I}'}} \frac{G^{\mathrm{II}}_{hm_h^{\mathrm{II}} n_h^{\mathrm{II}}} \iint_S \bigtriangledown_t T^{\mathrm{I}}_{em_e^{\mathrm{I}'} n_e^{\mathrm{I}'}} \cdot (\bigtriangledown_t T^{\mathrm{II}}_{hm_h^{\mathrm{II}} n_h^{\mathrm{II}}} \times \vec{z}) \mathrm{d}\mathcal{S}}{G^{\mathrm{I}}_{em_e^{\mathrm{I}'} n_e^{\mathrm{I}'}} \iint_S \bigtriangledown_t T^{\mathrm{I}}_{em_e^{\mathrm{I}'} n_e^{\mathrm{I}'}} \cdot \bigtriangledown_t T^{\mathrm{I}}_{em_e^{\mathrm{I}'} n_e^{\mathrm{I}'}} \mathrm{d}\mathcal{S}} \\ &= \frac{4\pi^2}{\sqrt{a_1 a_2 b_1 b_2}} \frac{\sqrt{Y^{\mathrm{I}}_{em_e^{\mathrm{I}'} n_e^{\mathrm{I}'}} Z^{\mathrm{II}}_{hm_h^{\mathrm{II}} n_h^{\mathrm{II}}}}}{k^{\mathrm{I}}_{ecm_e^{\mathrm{I}'} n_e^{\mathrm{I}'}} k^{\mathrm{II}}_{hcm_h^{\mathrm{II}} n_h^{\mathrm{II}}}} \frac{1}{\sqrt{(1+\delta_{0m_h^{\mathrm{II}}})(1+\delta_{0n_h^{\mathrm{II}}})}} \int_{x_1}^{x_2} \int_{y_1}^{y_2} \\ &\quad \Big\{ -\frac{m_e^{\mathrm{I}} n_h^{\mathrm{II}}}{a_1 b_2} \cos\left(\frac{m_e^{\mathrm{I}} \pi x}{a_1}\right) \sin\left(\frac{n_e^{\mathrm{I}} \pi y}{b_1}\right) \cos\left(\frac{m_h^{\mathrm{II}} \pi (x-x_1)}{a_2}\right) \sin\left(\frac{n_h^{\mathrm{II}} \pi (y-y_1)}{b_2}\right) + \\ &\quad \frac{m_h^{\mathrm{II}} n_e^{\mathrm{I}}}{a_2 b_1} \sin\left(\frac{m_e^{\mathrm{I}} \pi x}{a_1}\right) \cos\left(\frac{n_e^{\mathrm{I}} \pi y}{b_1}\right) \sin\left(\frac{m_h^{\mathrm{II}} \pi (x-x_1)}{a_2}\right) \cos\left(\frac{n_h^{\mathrm{II}} \pi (y-y_1)}{b_2}\right) \Big\} \mathrm{d}x\mathrm{d}y, \end{aligned} \tag{3.28}$$

$$\begin{aligned} J_{EE} &= \frac{\Gamma^{\mathrm{II}}_{em_e^{\mathrm{II}} n_e^{\mathrm{II}}} G^{\mathrm{II}}_{em_e^{\mathrm{II}} n_e^{\mathrm{II}}} \iint_S \bigtriangledown_t T^{\mathrm{I}}_{em_e^{\mathrm{I}'} n_e^{\mathrm{I}'}} \cdot \bigtriangledown_t T^{\mathrm{II}}_{em_e^{\mathrm{II}} n_e^{\mathrm{II}}} \mathrm{d}\mathcal{S}}{\Gamma^{\mathrm{I}}_{em_e^{\mathrm{I}'} n_e^{\mathrm{I}'}} G^{\mathrm{I}}_{em_e^{\mathrm{I}'} n_e^{\mathrm{I}'}} \iint_S \bigtriangledown_t T^{\mathrm{I}}_{em_e^{\mathrm{I}'} n_e^{\mathrm{I}'}} \cdot \bigtriangledown_t T^{\mathrm{I}}_{em_e^{\mathrm{I}'} n_e^{\mathrm{I}'}} \mathrm{d}\mathcal{S}} \\ &= \frac{4}{\sqrt{a_1 a_2 b_1 b_2}} \frac{k^{\mathrm{I}}_{ecm_e^{\mathrm{I}'} n_e^{\mathrm{I}'}}}{k^{\mathrm{II}}_{ecm_e^{\mathrm{II}} n_e^{\mathrm{II}}}} \sqrt{\frac{\Gamma^{\mathrm{II}}_{em_e^{\mathrm{II}} n_e^{\mathrm{II}}}}{\Gamma^{\mathrm{I}}_{em_e^{\mathrm{I}'} n_e^{\mathrm{I}'}}}} \int_{x_1}^{x_2} \int_{y_1}^{y_2} \\ &\quad \Big\{ \sin\left(\frac{m_e^{\mathrm{I}} \pi x}{a_1}\right) \sin\left(\frac{n_e^{\mathrm{I}} \pi y}{b_1}\right) \sin\left(\frac{m_e^{\mathrm{II}} \pi (x-x_1)}{a_2}\right) \sin\left(\frac{n_e^{\mathrm{II}} \pi (y-y_1)}{b_2}\right) \Big\} \mathrm{d}x\mathrm{d}y. \end{aligned} \tag{3.29}$$

$$\begin{aligned} J_{HH} &= \frac{G^{\mathrm{II}}_{hm_h^{\mathrm{II}} n_h^{\mathrm{II}}} \iint_S \bigtriangledown_t T^{\mathrm{I}}_{hm_h^{\mathrm{I}'} n_h^{\mathrm{I}'}} \cdot \bigtriangledown_t T^{\mathrm{II}}_{hm_h^{\mathrm{II}} n_h^{\mathrm{II}}} \mathrm{d}\mathcal{S}}{G^{\mathrm{I}}_{hm_h^{\mathrm{I}'} n_h^{\mathrm{I}'}} \iint_S \bigtriangledown_t T^{\mathrm{I}}_{hm_h^{\mathrm{I}'} n_h^{\mathrm{I}'}} \cdot \bigtriangledown_t T^{\mathrm{I}}_{hm_h^{\mathrm{I}'} n_h^{\mathrm{I}'}} \mathrm{d}\mathcal{S}} \\ &= \frac{4}{\sqrt{a_1 a_2 b_1 b_2}} \frac{k^{\mathrm{II}}_{hcm_h^{\mathrm{II}} n_h^{\mathrm{II}}}}{k^{\mathrm{I}}_{hcm_h^{\mathrm{I}'} n_h^{\mathrm{I}'}}} \sqrt{\frac{\Gamma^{\mathrm{I}}_{hm_h^{\mathrm{I}'} n_h^{\mathrm{I}'}}}{\Gamma^{\mathrm{II}}_{hm_h^{\mathrm{II}} n_h^{\mathrm{II}}}}} \int_{x_1}^{x_2} \int_{y_1}^{y_2} \\ &\quad \Big\{ \frac{\cos\left(\frac{m_h^{\mathrm{I}} \pi x}{a_1}\right) \cos\left(\frac{n_h^{\mathrm{I}} \pi y}{b_1}\right) \cos\left(\frac{m_h^{\mathrm{II}} \pi (x-x_1)}{a_2}\right) \cos\left(\frac{n_h^{\mathrm{II}} \pi (y-y_1)}{b_2}\right)}{\sqrt{(1+\delta_{0m_h^{\mathrm{I}}})(1+\delta_{0n_h^{\mathrm{I}}})(1+\delta_{0m_h^{\mathrm{II}}})(1+\delta_{0n_h^{\mathrm{II}}})}} \Big\} \mathrm{d}x\mathrm{d}y, \end{aligned} \tag{3.30}$$

$$J_{HE} = \frac{G^{\mathrm{II}}_{em_e^{\mathrm{II}}n_e^{\mathrm{II}}} \iint_{\mathcal{S}} (\bigtriangledown_t T^{\mathrm{I}}_{hm_h^{\mathrm{I}'}n_h^{\mathrm{I}'}} \times \vec{z}) \cdot \bigtriangledown_t T^{\mathrm{II}}_{em_e^{\mathrm{II}}n_e^{\mathrm{II}}} \mathrm{d}\mathcal{S}}{Y^{\mathrm{II}}_{em_e^{\mathrm{II}}n_e^{\mathrm{II}}} G^{\mathrm{I}}_{hm_h^{\mathrm{I}'}n_h^{\mathrm{I}'}} \iint_{\mathcal{S}} \bigtriangledown_t T^{\mathrm{I}}_{hm_h^{\mathrm{I}'}n_h^{\mathrm{I}'}} \cdot \bigtriangledown_t T^{\mathrm{I}}_{hm_h^{\mathrm{I}'}n_h^{\mathrm{I}'}} \mathrm{d}\mathcal{S}}. \tag{3.31}$$

It is noted that, according to the property of vector cross product and the identity that the curl of the gradient of any twice-differentiable scalar field is always the zero vector (Matthews 2000), the integral part of the numerator in the J_{HE} equation (3.31) can be expressed as

$$\begin{aligned} &\iint_{\mathcal{S}} (\bigtriangledown_t T^{\mathrm{I}}_{hm_h^{\mathrm{I}'}n_h^{\mathrm{I}'}} \times \vec{z}) \cdot \bigtriangledown_t T^{\mathrm{II}}_{em_e^{\mathrm{II}}n_e^{\mathrm{II}}} \mathrm{d}\mathcal{S} = \iint_{\mathcal{S}} (\bigtriangledown_t \times T^{\mathrm{I}}_{hm_h^{\mathrm{I}'}n_h^{\mathrm{I}'}} \vec{z}) \cdot \bigtriangledown_t T^{\mathrm{II}}_{em_e^{\mathrm{II}}n_e^{\mathrm{II}}} \mathrm{d}\mathcal{S} \\ = &\iint_{\mathcal{S}} [\bigtriangledown_t \cdot (T^{\mathrm{I}}_{hm_h^{\mathrm{I}'}n_h^{\mathrm{I}'}} \vec{z} \times \bigtriangledown_t T^{\mathrm{II}}_{em_e^{\mathrm{II}}n_e^{\mathrm{II}}}) + T^{\mathrm{I}}_{hm_h^{\mathrm{I}'}n_h^{\mathrm{I}'}} \vec{z} \cdot (\bigtriangledown_t \times \bigtriangledown_t T^{\mathrm{II}}_{em_e^{\mathrm{II}}n_e^{\mathrm{II}}})] \mathrm{d}\mathcal{S} \\ = &\iint_{\mathcal{S}} \bigtriangledown_t \cdot (T^{\mathrm{I}}_{hm_h^{\mathrm{I}'}n_h^{\mathrm{I}'}} \vec{z} \times \bigtriangledown_t T^{\mathrm{II}}_{em_e^{\mathrm{II}}n_e^{\mathrm{II}}}) \mathrm{d}\mathcal{S}. \end{aligned} \tag{3.32}$$

Based on the two-dimension divergence theorem (Gauss's theorem) and the geometric definition of dot product (Matthews 2000), Eq.3.32 can be further derived as

$$\begin{aligned} &\iint_{\mathcal{S}} \bigtriangledown_t \cdot (T^{\mathrm{I}}_{hm_h^{\mathrm{I}'}n_h^{\mathrm{I}'}} \vec{z} \times \bigtriangledown_t T^{\mathrm{II}}_{em_e^{\mathrm{II}}n_e^{\mathrm{II}}}) \mathrm{d}\mathcal{S} = \int_{\mathcal{L}} (T^{\mathrm{I}}_{hm_h^{\mathrm{I}'}n_h^{\mathrm{I}'}} \vec{z} \times \bigtriangledown_t T^{\mathrm{II}}_{em_e^{\mathrm{II}}n_e^{\mathrm{II}}}) \cdot \vec{n} \mathrm{d}\mathcal{L} \\ = &\int_{\mathcal{L}} \bigtriangledown_t T^{\mathrm{II}}_{em_e^{\mathrm{II}}n_e^{\mathrm{II}}} \cdot (T^{\mathrm{I}}_{hm_h^{\mathrm{I}'}n_h^{\mathrm{I}'}} \vec{n} \times \vec{z}) \mathrm{d}\mathcal{L} = \int_{\mathcal{L}} \bigtriangledown_t T^{\mathrm{II}}_{em_e^{\mathrm{II}}n_e^{\mathrm{II}}} \cdot T^{\mathrm{I}}_{hm_h^{\mathrm{I}'}n_h^{\mathrm{I}'}} \vec{l} \mathrm{d}\mathcal{L} \\ = &0, \end{aligned} \tag{3.33}$$

where $\mathcal{L}$ is a closed contour enclosing surface $\mathcal{S}$, $\vec{l}$ represents the unit tangent vector of the closed contour $\mathcal{L}$, and $\vec{n}$ is a unit vector normal to the closed contour $\mathcal{L}$. Hence, the coupling coefficient J_{HE} is always equal to 0, that is, $J_{HE} \equiv 0$, can be demonstrated.

Handling Eq. 3.25 in a similar manner, another two matrix equations can be obtained as the following

$$J^{\mathrm{tr}}_{HE}(\left[Q^{\mathrm{I}}_{hF}\right] - \left[Q^{\mathrm{I}}_{hB}\right]) + J^{\mathrm{tr}}_{EE}(\left[Q^{\mathrm{I}}_{eF}\right] - \left[Q^{\mathrm{I}}_{eB}\right]) = \left[Q^{\mathrm{II}}_{eF}\right] - \left[Q^{\mathrm{II}}_{eB}\right], \tag{3.34}$$

$$J^{\mathrm{tr}}_{HH}(\left[Q^{\mathrm{I}}_{hF}\right] - \left[Q^{\mathrm{I}}_{hB}\right]) + J^{\mathrm{tr}}_{EH}(\left[Q^{\mathrm{I}}_{eF}\right] - \left[Q^{\mathrm{I}}_{eB}\right]) = \left[Q^{\mathrm{II}}_{hF}\right] - \left[Q^{\mathrm{I}}_{hB}\right]. \tag{3.35}$$

where coupling coefficients J^{tr}_{HE}, J^{tr}_{EE}, J^{tr}_{HH} and J^{tr}_{EH} are transposed matrices of J_{HE}, J_{EE}, J_{HH} and J_{EH}.

Rearranging the positions of those amplitude coefficients, Eq. 3.26, 3.27, 3.34 and 3.35 can be expressed as

$$\begin{bmatrix} Q^{\mathrm{I}}_{hB} \\ Q^{\mathrm{I}}_{eB} \\ Q^{\mathrm{II}}_{hF} \\ Q^{\mathrm{II}}_{eF} \end{bmatrix} = S \begin{bmatrix} Q^{\mathrm{I}}_{hF} \\ Q^{\mathrm{I}}_{eF} \\ Q^{\mathrm{II}}_{hB} \\ Q^{\mathrm{II}}_{eB} \end{bmatrix} = \begin{bmatrix} S_{11} & S_{12} \\ S_{21} & S_{22} \end{bmatrix} \begin{bmatrix} Q^{\mathrm{I}}_{hF} \\ Q^{\mathrm{I}}_{eF} \\ Q^{\mathrm{II}}_{hB} \\ Q^{\mathrm{II}}_{eB} \end{bmatrix} \tag{3.36}$$

where S is the scattering matrix for the double-plane waveguide step, which can be calculated as the following equations (Bornemann *et al.* 2011)

$$\begin{aligned} S_{11} &= -(U + \mathcal{M}\mathcal{M}^{\mathrm{tr}})^{-1}(U - \mathcal{M}\mathcal{M}^{\mathrm{tr}}), \\ S_{12} &= 2(U + \mathcal{M}\mathcal{M}^{\mathrm{tr}})^{-1}\mathcal{M}, \\ S_{21} &= \mathcal{M}^{\mathrm{tr}}[U - S_{11}], \\ S_{22} &= U - 2\mathcal{M}(U + \mathcal{M}\mathcal{M}^{T})^{-1}\mathcal{M}^{\mathrm{tr}}, \\ \mathcal{M} &= \begin{bmatrix} J_{HH} & J_{HE} \\ J_{EH} & J_{EE} \end{bmatrix}, \end{aligned} \tag{3.37}$$

where U is the unit matrix, and $\mathcal{M}$ is the coupling coefficient matrix.

3.2.3 Scattering Matrices of Irises Placed in Rectangular Waveguides

As shown in Fig. 3.6, a rectangular waveguide is divided into three regions including Waveguide I, Waveguide II, and Waveguide III. The resonant iris placed in the cross-section of a rectangular waveguide can be considered as consisting of Waveguide II and two discontinuities formed by the transition from Waveguide I to Waveguide II and from Waveguide II to Waveguide III. Therefore, the scattering matrix of the resonant iris structure can be calculated by cascading the scattering matrices of the discontinuities and Waveguide II.

The scattering matrices S_{I} and S_{III} for the discontinuities, that is, the double-plane waveguide steps on $z = 0$ and $z = c$ planes, can be calculated with the MMM explained in last section and expressed as Eq. 3.38. Meanwhile, the scattering matrix for the Waveguide II can be obtained easily through Eq. 3.39 (Arndt *et al.* 1986)

$$S_{\mathrm{I}} = \begin{bmatrix} S_{11} & S_{12} \\ S_{21} & S_{22} \end{bmatrix}, \qquad S_{\mathrm{III}} = \begin{bmatrix} S_{22} & S_{21} \\ S_{12} & S_{11} \end{bmatrix}. \tag{3.38}$$

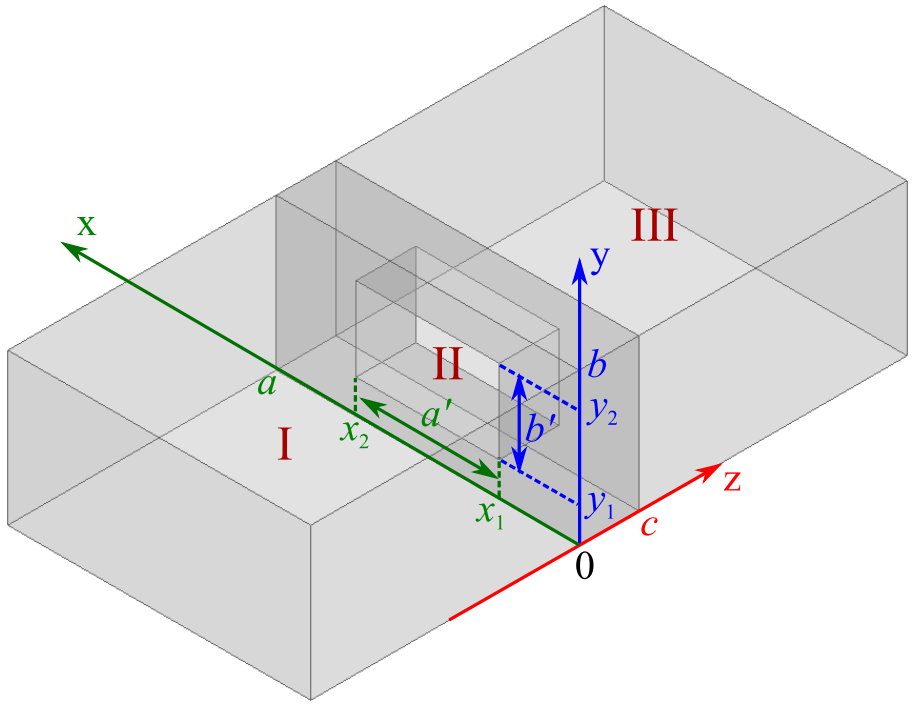

Figure 3.6. A resonant iris placed in the cross-section of a rectangular waveguide. This figure depicts the structure of a resonant iris placed in a rectangular waveguide. The rectangular waveguide is divided into Waveguide I ($z \leq 0$), Waveguide II ($0 \leq z \leq c$), and Waveguide III ($z \geq c$). Waveguide I and Waveguide III have the same cross-section with a width a and a height b, while Waveguide II has a width a', a height b' and a thickness c. Source: Self-created using Ansys HFSS and Inkscape.

$$S_{\mathrm{II}} = \begin{bmatrix} 0 & V \\ V & 0 \end{bmatrix}, \qquad V = \begin{bmatrix} e^{-\Gamma_{hm_hn_h}c} & 0 \\ 0 & e^{-\Gamma_{em_en_e}c} \end{bmatrix}, \tag{3.39}$$

where $e^{-\Gamma_{hm_hn_h}c}$ and $e^{-\Gamma_{em_en_e}c}$ represent the exponential factors of TE and TM modes in Waveguide II.

As a consequence, the scattering matrix for the whole resonant iris structure can be computed through the following equations (Dobrowolski 2010)

$$\begin{aligned} S_{11}^{iris} &= S_{11} + S_{12}V\left(U - (S_{22}V)^2\right)^{-1} S_{22}VS_{21}, \\ S_{12}^{iris} &= S_{12}V\left(U - (S_{22}V)^2\right)^{-1} S_{21}, \\ S_{21}^{iris} &= S_{12}\left(U - (VS_{22})^2\right)^{-1} VS_{21}, \\ S_{22}^{iris} &= S_{11} + S_{12}\left(U - (VS_{22})^2\right)^{-1} VS_{22}VS_{21}. \end{aligned} \tag{3.40}$$

For the capacitive irises (E-plane irises, $a' = a$, as shown in Fig. 3.2) placed in rectangular waveguides operating in the fundamental mode TE_{10} mode, high-order $TE_{m_h n_h}$ and $TM_{m_e n_e}$ modes are both excited because of the discontinuities. Thus, the scattering matrix can be calculated with the same coupling coefficient matrix derived for the resonant iris structures. However, for the inductive irises (H-plane irises, $b' = b$, as shown in Fig. 3.2) arranged in the rectangular waveguide and operated in the TE_{10} mode, only $TE_{m_h 0}$ modes can be excited. Therefore, the scattering matrix should be computed with modified corresponding coupling coefficient matrix shown below

$$\mathcal{M} = [J_{HH}] = \frac{2}{\sqrt{aa'}} \sqrt{\frac{\Gamma^{\mathrm{I}}_{hm_h^{\mathrm{I}'}0}}{\Gamma^{\mathrm{II}}_{hm_h^{\mathrm{II}}0}}} \int_{x_1}^{x_2} \sin\left(\frac{m_h^{\mathrm{I}'}\pi x}{a}\right) \sin\left(\frac{m_h^{\mathrm{II}}\pi(x - x_1)}{a'}\right) \mathrm{d}x. \tag{3.41}$$

Since the structure of band-pass filter in this chapter is based on inductive diaphragms, an H-plane iris structure is taken as an example in order to investigate the relationship between the convergence and the number of modes, and to verify the validity and efficiency of the MMM. As shown in Fig. 3.7, a symmetrical iris is placed in the cross-section of a standard W-band (extending from 75 GHz to 110 GHz) WR-10 waveguide with a width of $a = 2.54$ mm and a height of $b = 1.27$ mm. The width a' of the aperture is 1.2 mm, while the thickness c of the irises is 0.5 mm.

With these dimensions for the H-plane iris rectangular waveguide structure, the relationship between the convergence and the number of modes is explored at 94 GHz in the following. As shown in Fig. 3.8, by increasing the number of modes, either $|S_{11}|$ or $|S_{21}|$ stabilises to a value, and when the number of modes is larger than 10, the changes for $|S_{11}|$ and $|S_{21}|$ are insignificant.

By setting the number of modes to 15, in W-Band (extending from 75 GHz to 110 GHz), the calculated mode-matching results for the H-plane iris structure are verified by the finite-element method (FEM) simulations performed with Ansys HFSS as shown in Fig. 3.9. Obviously, without taking losses into account, the calculated mode-matching results for the amplitude and phase of $|S_{11}|$ and $|S_{21}|$ have a good match with the results simulated with the FEM using Ansys HFSS. It is noted that, to ensure that the simulated results have sufficient precision, the maximum length of elements for the mesh setting in Ansys HFSS is chosen as 0.1 mm. Thus, for a standard computer with a 3.40 GHz i7-2600 CPU and 14.0 GB RAM, it takes 264 s to simulate one frequency point (94 GHz). In contrast, the MMM shows a remarkable advantage in efficiency for it takes only 0.17 s to calculate one frequency point (94 GHz).

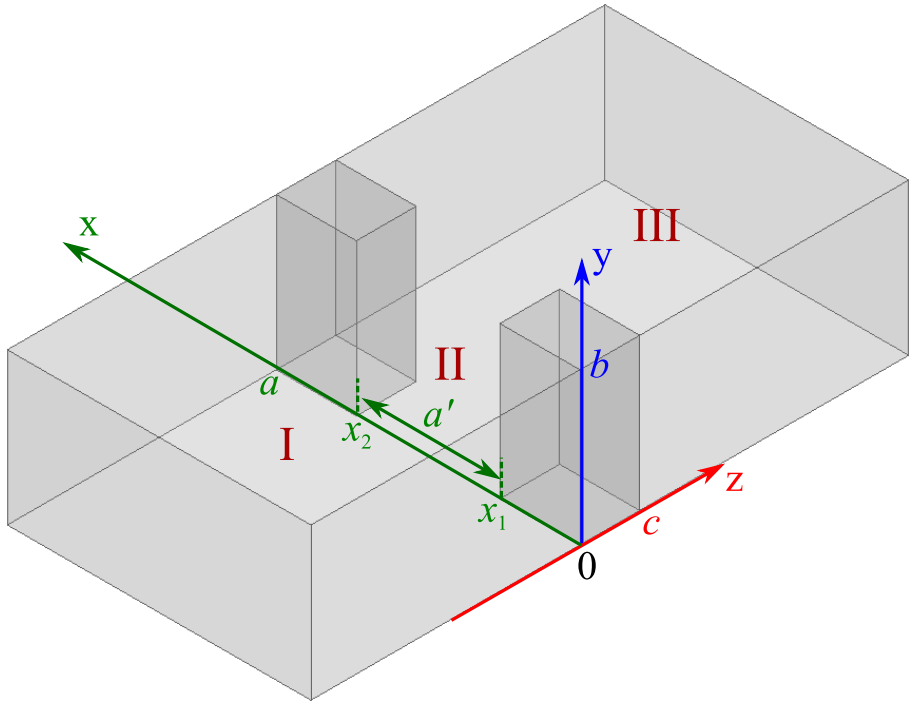

Figure 3.7. Symmetric H-plane iris placed in the cross-section of a rectangular waveguide. This figure depicts the structure of a symmetrical inductive iris placed in a rectangular waveguide. The rectangular waveguide is divided into Waveguide I ($z \leq 0$), Waveguide II ($0 \leq z \leq c$), and Waveguide III ($z \geq c$) by the iris. Waveguide I and Waveguide III have the same cross-section with a width a and a height b, while Waveguide II has a width a', a height b, and a thickness c. Source: Self-created using Ansys HFSS and Inkscape.

3.3 Principle of Band-Pass Filter

As an essential part in microwave and millimetre-wave systems, a filter is often utilised to control the frequency response at a certain point by providing transmission at frequencies within the passband and attenuation in the stopband.

Two common methods, the image parameter method and the insertion loss method using network synthesis techniques, can be applied to design filters. In order to remove undesired frequency components, the first approach cascades a series of two-port filter sections such as constant-k section, m-derived section, and mm'-type section. However, this simple method does not support the specification of a particular frequency response over the whole operation frequency band. Therefore, this method has to be iterated many times to satisfy the design requirements. The second approach is based on the design specifications and begins with the needed transfer function and

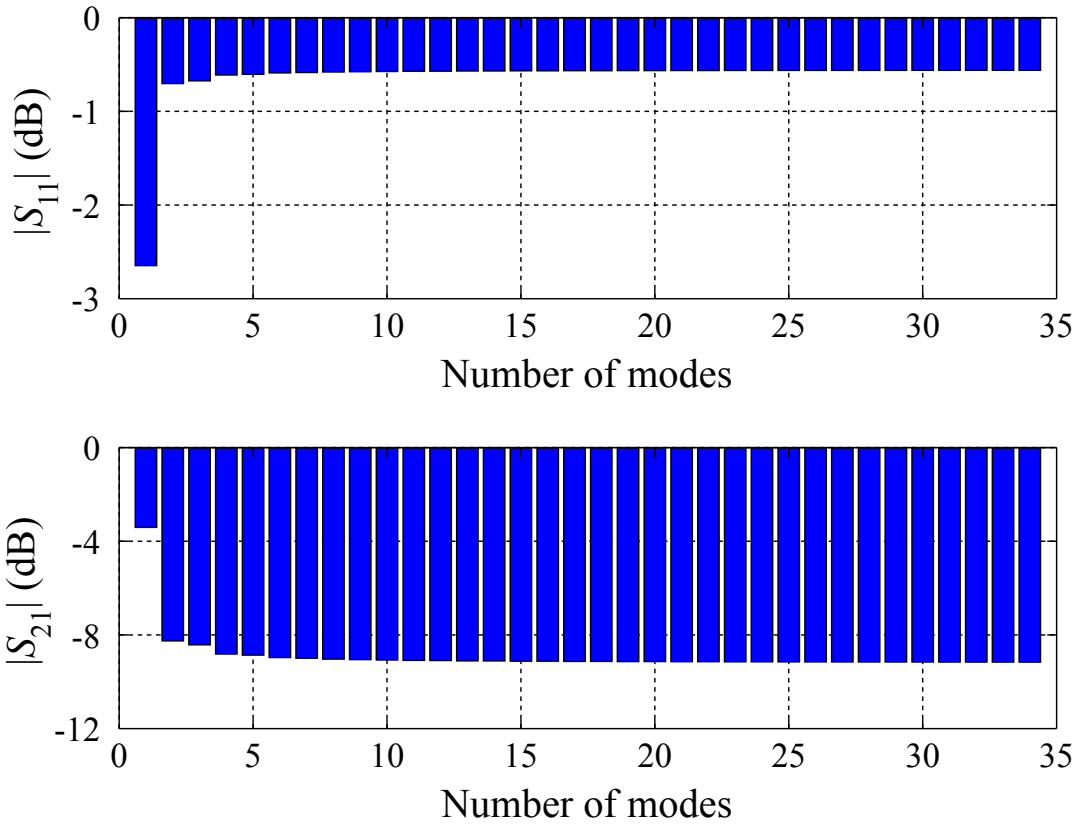

Figure 3.8. Relationship between the convergence and the number of adopted modes at 94 GHz. This figure shows that with the increase of the number of modes, the scattering parameters $|S_{11}|$ and $|S_{21}|$ at 94 GHz trend to stable values. Source: Self-created using Matlab.

then determines the required sections to form the corresponding filter which can meet or approximate the desired frequency response. This method provides a methodical manner of filter design and has a high degree of control over amplitude and phase characteristics in passband and stopband. Hence, it is often adopted in designing filters in microwave and millimetre-wave systems.

In this perspective, only the principle of the insertion loss method is explained in this thesis. In addition, typical frequency responses for filters include low-pass, high-pass, band-pass, and band-reject characteristics. For brevity, the explanation here starts from low-pass filters, while the considerations are then focussed on the transformation for band-pass filters. Extending the transformation, the other response types can be obtained in a similar manner.

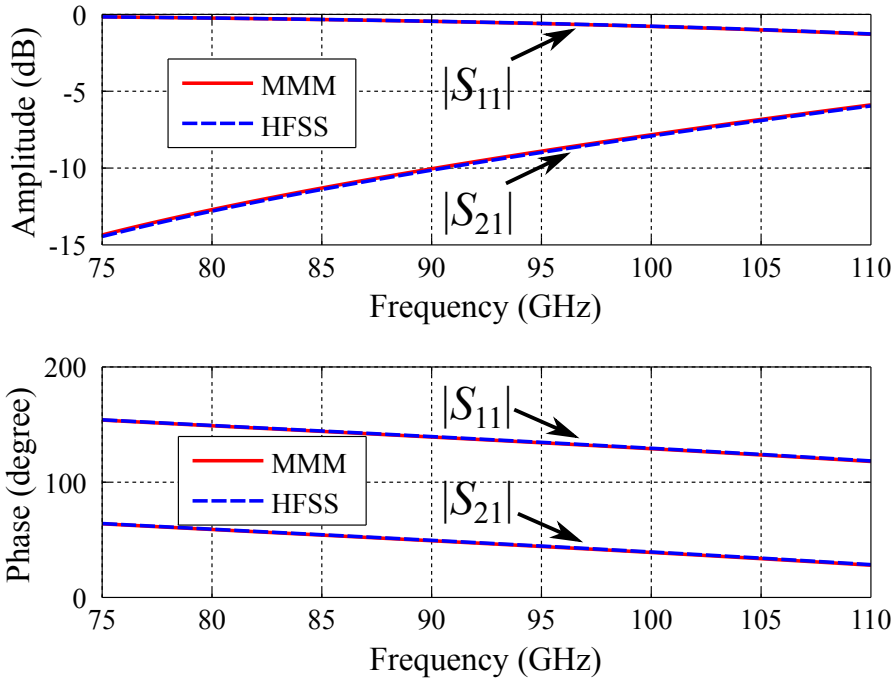

Figure 3.9. Comparison for the amplitude and phase of scattering parameters obtained through the MMM with 15 modes and the FEM using Ansys HFSS in W-Band. This figure shows that the calculated mode-matching results for the amplitude and phase of $|S_{11}|$ and $|S_{21}|$ match well with those simulated with Ansys HFSS. Source: Self-created using Ansys HFSS and Matlab.

3.3.1 Principle of the Insertion Loss Method

For an ideal filter, the insertion loss in the passband should be zero, while the transmitted power in the stopband should attenuate infinitely. However, such filters cannot be realised in practice. Existing filters can be considered as the approximations of the ideal ones. To approximate the frequency response of the ideal filters, the first step is to decide the transfer function which is defined for a low-pass filter as the following (Pozar 2011, Hong and Lancaster 2011)

$$\begin{aligned} |S_{21}(j\omega)|^2 &= \frac{1}{1+\epsilon^2 F_N^2(\omega/\omega_c)}, \\ P_{LR} &= \frac{P_{inc}}{P_{load}} = \frac{1}{|S_{21}(j\omega)|^2}, \end{aligned} \tag{3.42}$$

where $|S_{21}|^2$ is the amplitude-squared transmission coefficient, ω is the radian frequency, ω_c is the cutoff radian frequency, ϵ is the ripple constant, F_N is the filtering function, N is the order of the filter, P_{LR} is the power loss ratio, and P_{inc} and P_{load}

represent the power available from the source and the power delivered to the load respectively.

Furthermore, for a given transfer function, the insertion loss for a filter can be expressed in dB by the following equation

$$IL = 10\log P_{LR} = 10\log\frac{1}{|S_{21}(j\omega)|^2}. \tag{3.43}$$

Obviously, the characteristics of the insertion loss over the operation frequency band for a filter is described by the transfer functions. Namely, the practical filter responses can be determined by different transfer functions, including the classical ones such as Butterworth (maximally flat) response, Chebyshev (equal ripple) response, elliptic function response, and Gaussian (maximally flat group-delay) response.

Taking the Chebyshev response as an example, the particular response for such a filter can be described by the amplitude-squared transfer function

$$|S_{21}(j\omega)|^2| = \frac{1}{1+\epsilon^2\mathcal{T}_N^2(\omega)}, \tag{3.44}$$

where the ripple constant ϵ can be computed with a given passband ripple A_r in dB by equation

$$\epsilon = \sqrt{10^{A_r/10}-1}, \tag{3.45}$$

while the Chebyshev function $\mathcal{T}_N$ can be expressed as the following

$$\mathcal{T}_N(\omega) = \begin{cases} \cos\left(N\cos^{-1}(\frac{\omega}{\omega_c})\right), & \text{if } \omega \le \omega_c \\ \cosh\left(N\cosh^{-1}(\frac{\omega}{\omega_c})\right), & \text{if } \omega \ge \omega_c. \end{cases} \tag{3.46}$$

Based on Eq. 3.43 to 3.46, the Chebyshev low-pass responses for filters with different orders are plotted in Fig. 3.10. In the figure, it can be seen that the Chebyshev responses exhibit equal ripples with a magnitude A_r in dB in the passband extending from 0 rad/s to w_c rad/s. In addition, with the increase of the order of the filter, the insertion loss IL shows a more dramatic rise.

3.3.2 Low-Pass Filter Prototype

An all-pole low-pass filter, such as Butterworth low-pass filter, Chebyshev low-pass filter, or Gaussian low-pass filter, can be realised with both types of N^{th}-order ladder

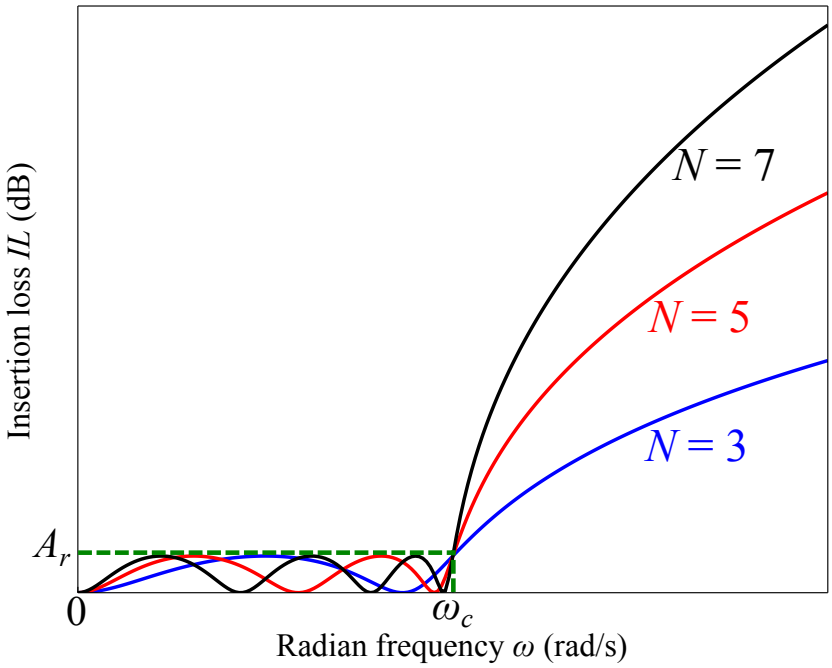

Figure 3.10. Chebyshev (equal ripple) low-pass response for filters with $N = 3$, $N = 5$, and $N = 7$ orders. This figure shows that, in the passband of a Chebyshev low-pass filter, the Chebyshev response has equal ripples which are defined by A_r. In addition, a filter with larger order has a sharper stopband performance. Source: Self-created using Matlab.

networks shown in Fig. 3.11. As shown in the figure, g_0 represents source resistance or conductance, g_{n+1} represents load resistance or conductance, and g_1 to g_n are the values for electronic elements which can be considered as shunt capacitors or series inductors (Hong and Lancaster 2011).

For a low-pass filter realised with either of these two networks, if the values for electronic elements g_1 to g_n, are normalised to make the source resistance or conductance g_0 and the cutoff radian frequency ω_c be 1, this filter is defined as a low-pass prototype filter.

Many practical filters, including low-pass filters, high-pass filters, band-pass filters, and band-stop filters, can be designed through the frequency and element transformations on the basis of this low-pass prototype filter. In addition, because numerous tables of element values for low-pass prototype filters with various frequency responses have already been tabulated, the filter synthesis procedures can be skipped. Therefore, the design efficiency can be improved significantly.

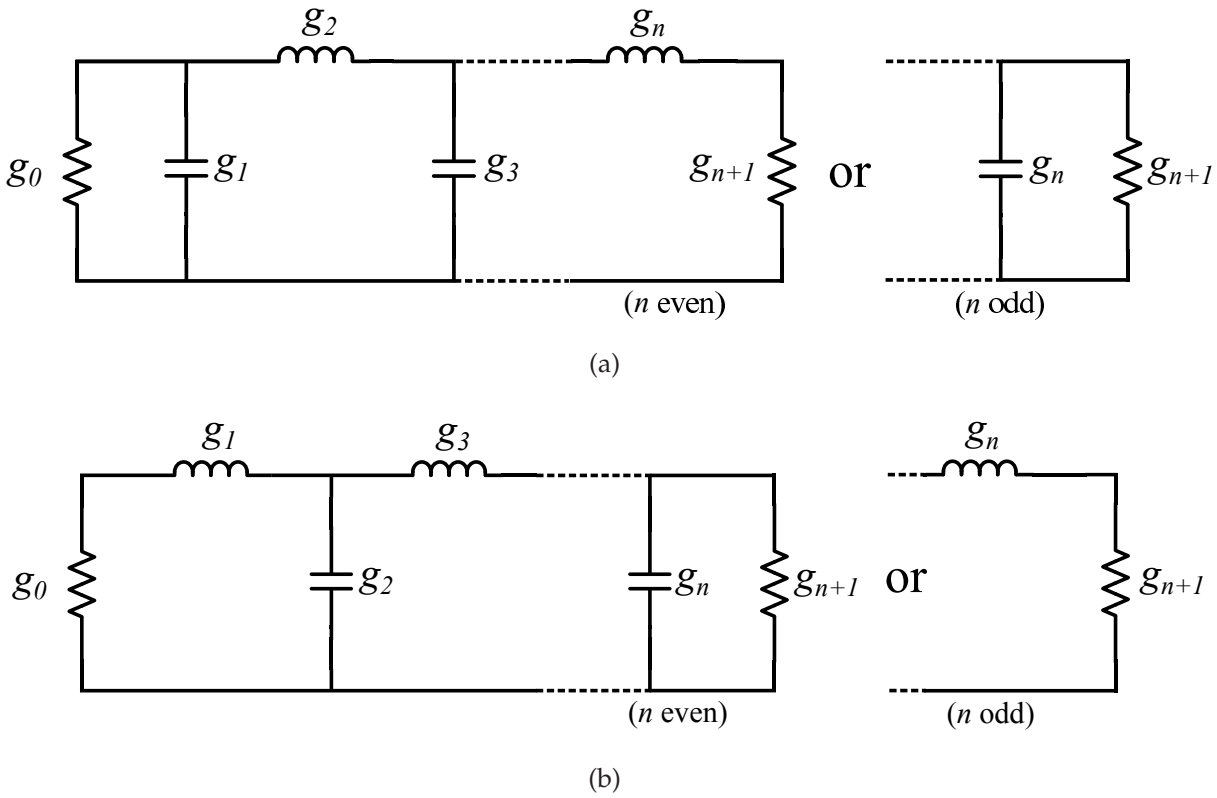

Figure 3.11. Two types of ladder networks for all-pole low-pass filters. This figure shows two ladder networks which can be utilised to realise low-pass filters. The network in (a) begins with a shunt element, while the network in (b) begins with a series element. Source: Self-created using Inkscape.

Equations for calculating the values for electronic elements are still necessary, since element value tables sometimes cannot satisfy specific design requirements. For a Chebyshev low-pass prototype filter, with equal ripple A_r in passband and cutoff radian frequency $\omega_c = 1\,\text{rad/s}$, the formulae for element values are listed below (Hong and Lancaster 2011)

$$
\begin{aligned}
g_0 &= 1, \\
g_1 &= \frac{2}{\gamma}\sin\left(\frac{\pi}{2n}\right), \\
g_i &= \frac{1}{g_{i-1}}\frac{4\sin\left(\frac{(2i-1)\pi}{2n}\right)\sin\left(\frac{(2i-3)\pi}{2n}\right)}{\gamma^2+\sin^2\left(\frac{(i-1)\pi}{n}\right)} \quad \text{for } i = 2,3,...,n, \\
g_{n+1} &= \begin{cases} 1, & \text{for n odd,} \\ \coth^2\left(\frac{\eta}{4}\right), & \text{for n even,} \end{cases}
\end{aligned}
\tag{3.47}
$$

where

$$\begin{aligned} \eta &= \ln\Big(\coth\big(\frac{A_r}{17.37}\big)\Big), \\ \gamma &= \sinh\Big(\frac{\eta}{2n}\Big). \end{aligned} \tag{3.48}$$

As a typical specification, the stop-band attenuation for a Chebyshev low-pass prototype at a radian frequency ω_s is required to be larger than a constant A_s in dB. Adopting a suitably high order for a filter is an option to achieve this, since, as demonstrated in Subsection 3.3.1, a sharper stop-band performance can be obtained by increasing the order. Thus, to meet the specification, the required order n of the filter can be found through the following equation (Hong and Lancaster 2011)

$$n \geq \frac{\cosh^{-1}\sqrt{\frac{10^{\frac{A_s}{10}}-1}{10^{\frac{A_r}{10}}-1}}}{\cosh^{-1}\omega_s}. \tag{3.49}$$

3.3.3 Band-Pass Transformation

A low-pass prototype filter is defined as a filter which has a normalised source resistance or conductance, and an unity cutoff radian frequency. Based on this low-pass prototype filter, a practical filter, whose frequency response may be low-pass, high-pass, band-pass, or band-stop, can be designed through the frequency and element transformations.

To achieve the band-pass transformation based on a low-pass prototype filter, the electronic elements in the ladder network for the low-pass filter as shown in Fig. 3.11 should be converted into LC resonators. In other words, the shunt elements should be replaced by parallel LC resonators, while the series element should be replaced by series LC resonators. Thus, the networks for band-pass filters are obtained as shown in Fig. 3.12.

For a Chebyshev band-pass filter, whose passband edge radian frequencies are ω_1' and ω_2', the transformation can be achieved through mapping the radian frequency ω' for the band-pass filter to the radian frequency ω for the low-pass prototype filter with the following frequency substitution (Pozar 2011)

$$\omega \Leftarrow \frac{1}{FBW}\Big(\frac{\omega'}{\omega_0'} - \frac{\omega_0'}{\omega'}\Big), \tag{3.50}$$

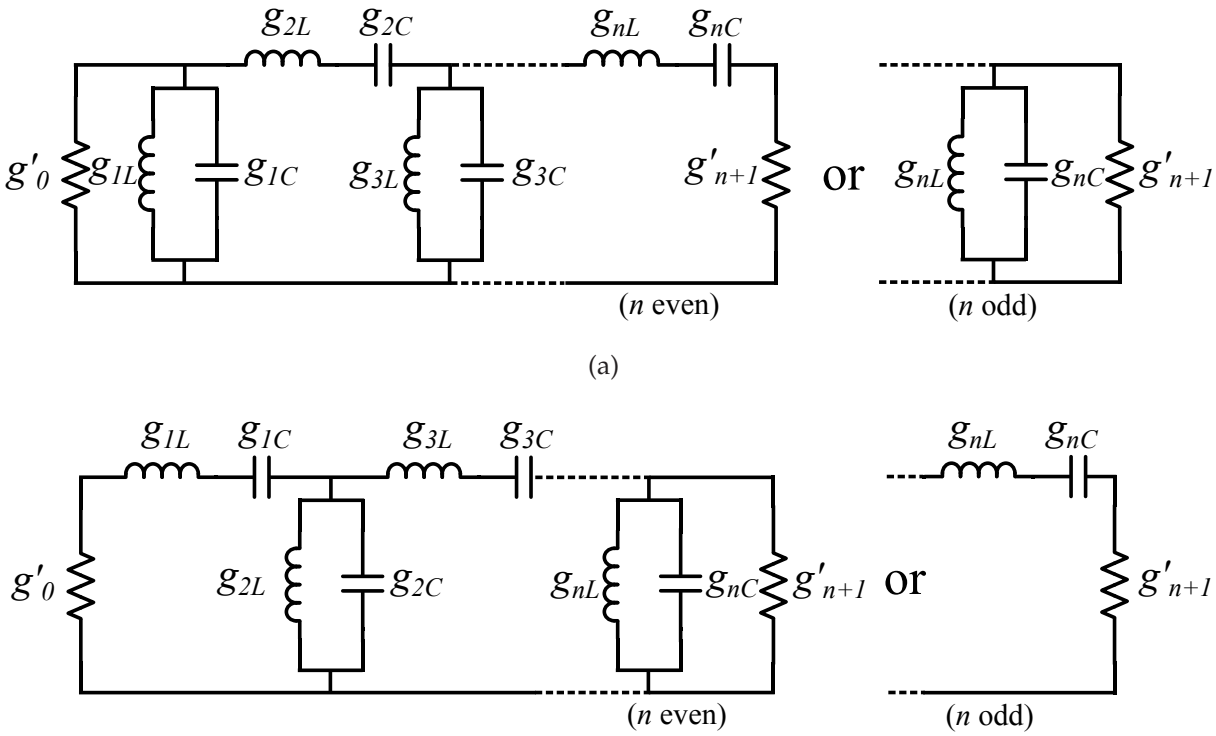

Figure 3.12. Two types of networks for band-pass filters transformed from ladder networks for low-pass filters. This figure shows two networks which can be utilised to realise band-pass filters. The networks are transformed from ladder networks for low-pass filters shown in Fig. 3.11 by replacing the electronic elements with LC resonators. Source: Self-created using Inkscape.

where the fractional bandwidth FBW is defined as

$$FBW = \frac{\omega'_2 - \omega'_1}{\omega'_0}, \tag{3.51}$$

and the centre radian frequency is defined as

$$\omega'_0 = \sqrt{\omega'_1 \omega'_2}. \tag{3.52}$$

Further, the equations of the inductive and capacitive electronic elements in the series and parallel LC resonators for the transformed band-pass filters can be derived in Eq. 3.53 and 3.54 respectively

$$\begin{aligned} g_{nL} &= \frac{1}{FBW\omega'_0}\vartheta g_n, \\ g_{nC} &= \frac{FBW}{\omega'_0}\frac{1}{\vartheta g_n}, \end{aligned} \tag{3.53}$$

$$g_{nC} = \frac{1}{FBW\omega_0'}\frac{g_n}{\vartheta}, \qquad g_{nL} = \frac{FBW}{\omega_0'}\frac{\vartheta}{g_n}, \tag{3.54}$$

where ϑ represents the impedance scaling factor, which can be expressed as the following equation

$$\vartheta = \begin{cases} \frac{g_0'}{g_0}, & \text{for } g_0' \text{ and } g_0 \text{ being the resistance,} \\ \frac{g_0}{g_0'}, & \text{for } g_0' \text{ and } g_0 \text{ being the conductance,} \end{cases} \tag{3.55}$$

where g_0' is the practical source resistance or conductance as shown in Fig. 3.12.

3.4 Band-Pass Iris Filter

Thus far, the design procedures for a band-pass filter realised with lumped elements has been explained in detail. However, with the increase of frequency, lumped elements become inapplicable, since the wavelengths of the electromagnetic waves, for example microwave and millimetre-wave, become comparable to or even smaller than the physical sizes of the circuits. Therefore, distributed elements should be introduced in order to handle this issue.

3.4.1 Realisation of Band-Pass Iris Filter

As shown in Fig. 3.12, the networks for a band-pass filter realised with alternate series resonators and parallel resonators are difficult to be achieved with distributed elements. Thus, in order to make those resonators in series, the networks should be transformed again by introducing impedance inverters (K inverters) or admittance inverters (J inverters). Here, only the network for band-pass filter using impedance inverters are drawn in Fig. 3.13 (Hong and Lancaster 2011).

As shown in the figure, the network consists of series resonators and shunt impedance inverters. The resonant frequency of these resonators should be located at the centre radian frequency ω_0' of the band-pass filter, while the theoretical normalised value

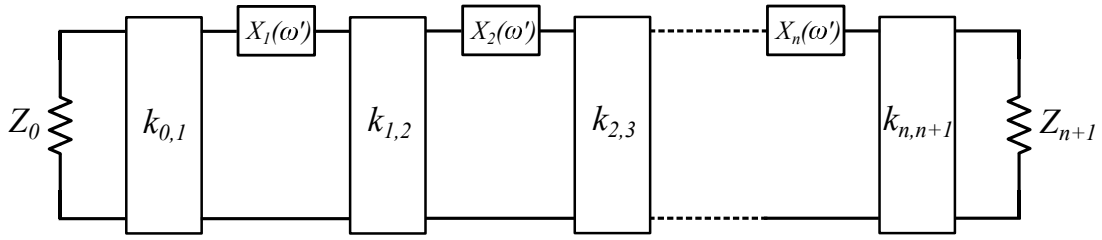

Figure 3.13. Network for generalised band-pass filter using impedance inverters. This figure shows the configuration of a band-pass filter using shunt impedance inverters and series resonators. Both the impedance inverters and the resonators can be realised with distributed elements. Z represents the source impedance, k is the value for the K inverter, and $X(\omega')$ is the reactance of the distributed resonator. Source: Self-created using Inkscape.

$k_{n,n+1}$ of the impedance inverters can be calculated through equations below

$$k_{n,n+1} = \begin{cases} \sqrt{\frac{\pi FBW}{2g_0 g_1}}, & \text{for } n = 0, \\ \frac{\pi FBW}{2\sqrt{g_n g_{n+1}}}, & \text{for } n = 1, 2, ..., N-1, \\ \sqrt{\frac{\pi FBW}{2g_n g_{n+1}}}, & \text{for } n = N. \end{cases} \tag{3.56}$$

It is noted that, for dispersive medium, the FBW in above equations should be replaced by fractional guide wavelength FGW which can be computed through the formula (Cameron *et al.* 2007)

$$FGW = \frac{\lambda_{g1} - \lambda_{g2}}{\lambda_{g0}}, \tag{3.57}$$

where λ_{g1} and λ_{g2} are the guide wavelengths at the passband edge frequencies, while λ_{g0} is the guide wavelengths at the centre frequency.

The network for a 5^{th}-order Chebyshev band-pass filter using impedance inverters and series LC resonators can be realised by placing irises in the cross-sections of a rectangular waveguide, that is, the symmetric rectangular waveguide structure shown in Fig. 3.14, since the irises placed in the cross-sections of the rectangular waveguide can work as impedance inverters, while the cavity resonators formed by these irises can behave like LC resonators.

A symmetrical iris placed in the cross-section of a rectangular waveguide and its equivalent circuit for the impedance inverter are shown in Fig. 3.15. With the MMM introduced previously, the scattering parameters for the two-port iris network, that is, $|S_{11}|$, $|S_{12}|$, $|S_{21}|$, and $|S_{22}|$, can be calculated quickly and accurately. The corresponding

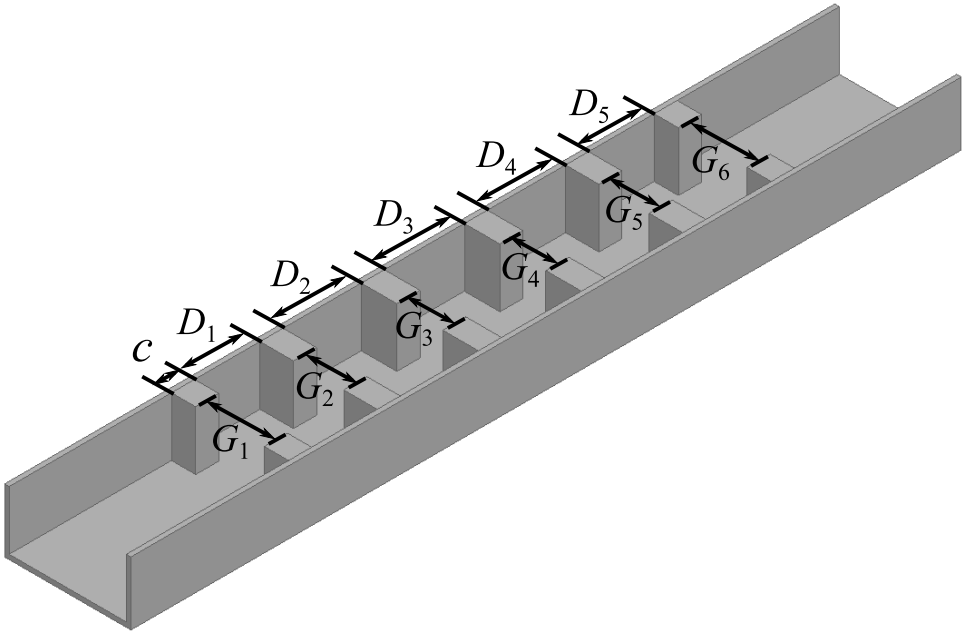

Figure 3.14. Structure of a 5^{th}-order Chebyshev band-pass iris filter. This figure shows the configuration of a Chebyshev band-pass filter achieved by placing irises in the cross-sections of a rectangular waveguide. c is the thickness of the iris, G represents the gap between the iris plates, and D is the length of the resonant cavity. Source: Self-created using Ansys HFSS and Inkscape.

impedance inverter value, denoted as k', can then be obtained through

$$k' = \sqrt{\frac{1 - |S_{11}|}{1 + |S_{11}|}}, \tag{3.58}$$

or

$$k' = |\tan\left(\frac{\theta}{2} + \tan^{-1}\left(\frac{X_s}{2}\right)\right)|, \tag{3.59}$$

where the electrical length θ, the normalised element values of the equivalent circuit for the impedance inverter X_s and X_p can be computed through (Park *et al.* 2003)

$$\begin{aligned} \theta &= -tan^{-1}(2X_p + X_s) - tan^{-1}(X_s), \\ jX_s &= \frac{1 + S_{11} - S_{21}}{1 - S_{11} + S_{21}}, \\ jX_p &= \frac{2S_{21}}{(1 - S_{11})^2 - S_{21}^2}. \end{aligned} \tag{3.60}$$

Furthermore, to design this type of band-pass filter, the first step is to map the practical impedance inverter values $k'_{n,n+1}$ of the iris to the calculated theoretical values $k_{n,n+1}$.

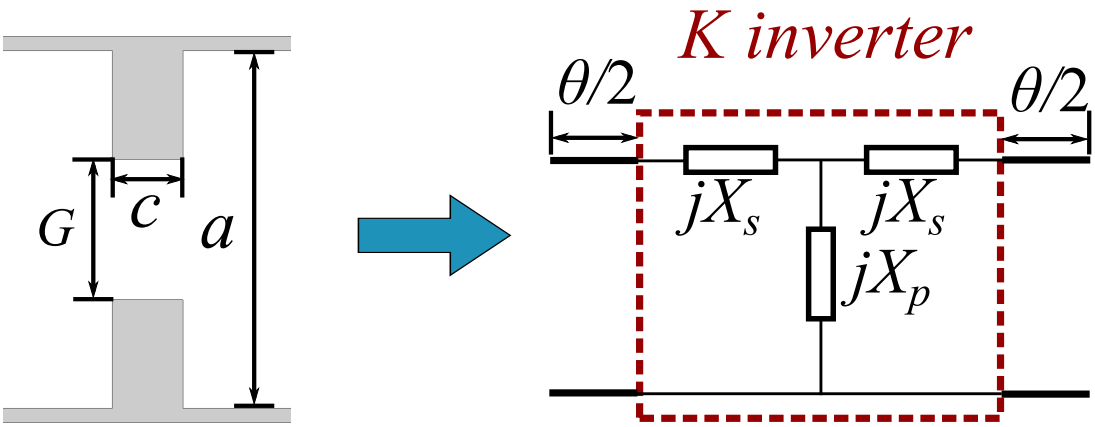

Figure 3.15. An iris placed in the cross-section of a rectangular waveguide and the equivalent circuit for the impedance inverter. The left figure shows the top view of a symmetrical iris in a rectangular waveguide. This structure can behave as an impedance inverter, and thus the equivalent circuit for the impedance inverter is also provided in the right figure. Source: Self-created using Ansys HFSS and Inkscape.

In the other words, an equation about two variables, including the inner gaps G_n of the irises and the thicknesses c_n of the irises, should be solved.

$$f(G,c) = k'_{n,n+1}(G,c) - k_{n,n+1} = 0. \tag{3.61}$$

For convenience, usually the thicknesses c of all irises are fixed as one constant. Thus, the Eq. 3.61 can be simplified as an equation with one unknown quantity, and this equation can be solved efficiently with various methods, such as the bisection method or Newton's method (Burden *et al.* 2015).

After this step, the lengths of the half-wavelength resonator cavities formed by iris pairs can be calculated through the following equation (Park *et al.* 2003, Pozar 2011)

$$D_n = \frac{\lambda_{g0}}{2\pi}\left(\pi - \frac{1}{2}(\theta_n + \theta_{n+1})\right). \tag{3.62}$$

Based on a standard W-band (extending from 75 GHz to 110 GHz) WR-10 waveguide whose width and height are 2.54 mm and 1.27 mm respectively, the design method is applied to a 5^{th}-order Chebyshev band-pass iris filter with a centre frequency of 94 GHz and a fractional bandwidth of 4.25% (passband extending from 92 GHz to 96 GHz). For a standard computer with a 3.40 GHz i7-2600 CPU and 14.0 GB RAM, the gaps G between the iris plates and the lengths D of the resonant cavities illustrated in Fig. 3.14 can be determined in just 0.08 seconds. With the dimensions listed in Table 3.1, the

Table 3.1. Dimensions of a 5^{th}-order Chebyshev band-pass iris filter (Units: mm). The table gives the dimensions, including the iris thicknesses c, the gaps G between iris plates, and the lengths D of the resonant cavities, used to realise a 5^{th}-order Chebyshev band-pass iris filter whose structure is illustrated in Fig. 3.14.

c	G_1, G_6	G_2, G_5	G_3, G_4	D_1, D_5	D_2, D_4	D_3
0.5	1.488	1.091	0.996	1.421	1.694	1.736

calculated mode-matching results are verified by simulation results with the FEM using Ansys HFSS. As shown in Fig. 3.16, the calculated mode-matching results have a good match with the results of the full-wave simulation. It is noted that both the mode-matching calculation and the finite-element simulation do not take losses into account.

3.4.2 Influence of Fabrication Inaccuracies

In view of the limitations of micro-machining processes, in a manufactured H-plane iris band-pass filter, the corners between the waveguide walls and irises are round angles rather than perfect right angles. Namely, the ideal structure illustrated in Fig. 3.14 is actually realised as the structure shown in Fig. 3.17 instead. The resulting differences between ideal design and realisable geometries do influence the performance of the band-pass filter, especially when it operates at high frequency bands (Bornemann 2001, Bornemann *et al.* 2005). Because of the high performance requirements for a band-pass filter, the undesired influence caused by rounded angles should be removed. Therefore, the influence introduced by round angles together with bevel angles shall be analysed with the MMM in this subsection, in order to provide references for the next section to solve the influence problem.

With the MMM, it is difficult to analyse an iris with round angles or bevel angles directly. Fortunately, round angles or bevel angles (as an isosceles right triangle) can be approximated as M steps of double-plane discontinuities as shown in Fig. 3.18.

The number of steps M depends on the radius r of a round angle or the side ls of a bevel angle. Thus, the convergence has been investigated with two approximation examples at 94 GHz. One is an iris with a thickness of 0.5 mm, a gap of 1.0 mm, and

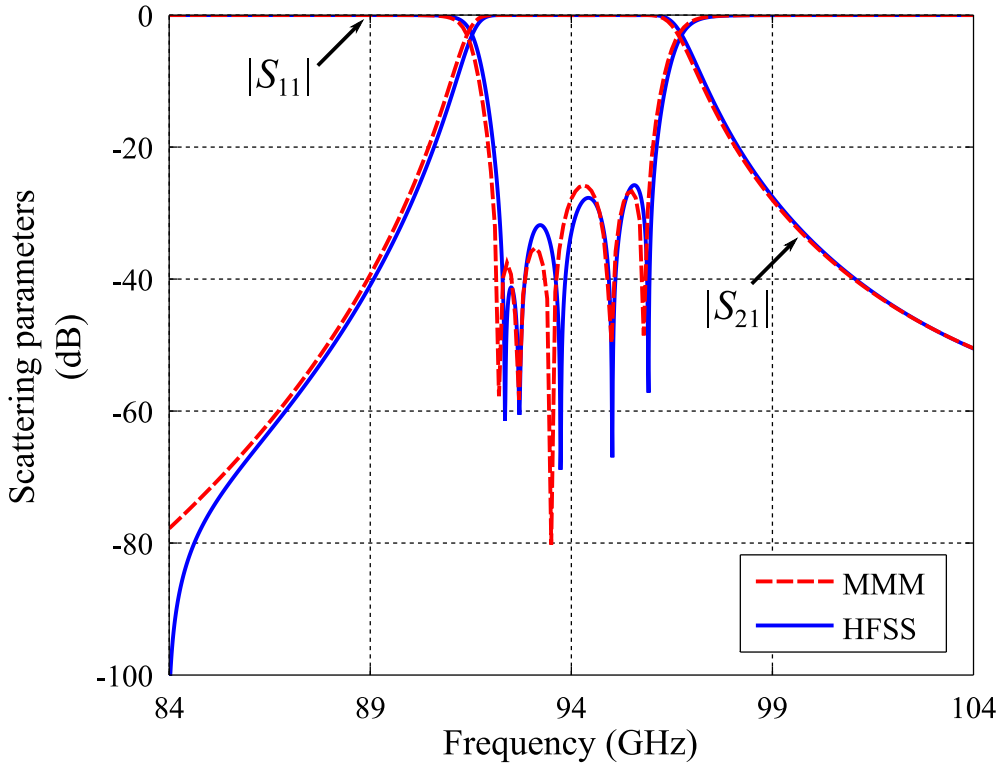

Figure 3.16. Comparison of scattering parameters obtained using MMM and the FEM using Ansys HFSS. This figure shows the frequency response of a 5^{th}-order Chebyshev band-pass iris filter obtained through the MMM and the FEM. The comparison verifies the validity of the self-developed mode-matching code. Source: Self-created using Ansys HFSS and Matlab.

round angles with a radius of 0.5 mm, while the other is an iris with a thickness of 0.5 mm, a gap of 1.0 mm, and bevel angles with a side of 0.1 mm. It is noted that both examples are based on a standard W-Band (extending from 75 GHz to 110 GHz) WR-10 waveguide. As shown in Fig. 3.19(a), with the increase of the number of steps, the scattering parameters $|S_{11}|$ and $|S_{21}|$ of the first round angle approximation converges gradually. Obviously, when the number of steps M is larger than 10, the variations for $|S_{11}|$ and $|S_{21}|$ can be ignored. Similarly, as shown in Fig. 3.19(b), a 5-step staircase actually is sufficient to approximate a bevel angle with 0.1 mm side lengths.

Up to now, based on the dimensions listed in Table 3.1 and the principle introduced above, the influence resulted from the round angles or bevel angles is able to be analysed.

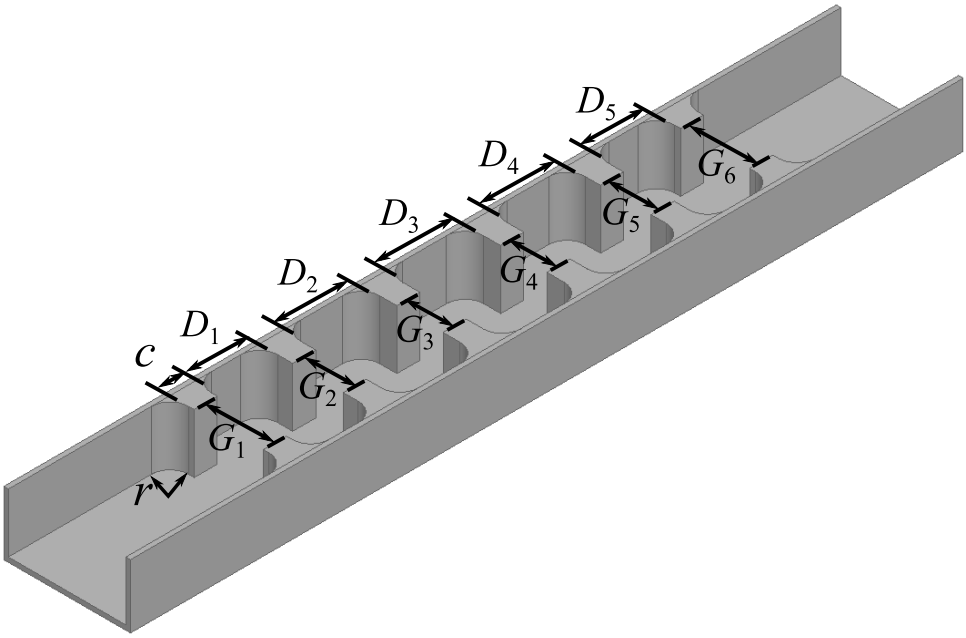

Figure 3.17. Structure of a 5^{th}-order Chebyshev band-pass iris filter with round angles. This figure shows the realised configuration of a Chebyshev band-pass filter achieved by fabricating irises in the cross-sections of a rectangular waveguide with a milling machine. c is the thickness of the iris, G represents the gap between the iris plates, D is the length of the resonant cavity, and r is the radius of the rounded corner. Source: Self-created using Ansys HFSS and Inkscape.

For the structure in Fig. 3.17, by increasing the radii of the round angles, the centre frequency (94 GHz originally) of the band-pass filter shifts to higher frequencies while the 3 dB bandwidth varies slightly. The relationship among the radius, the offset, and the variation of bandwidth is shown in Fig. 3.20(a). Clearly, up to a radius of 0.1 mm, no significant influence on the centre frequency is visible while up to a radius of 0.35 mm, the variation of the bandwidth fluctuates around 0 with a small amplitude. As the radius increases, the centre frequency shifts exponentially upward. For a radius of 0.5 mm, the offset is 0.76 GHz and the variation of bandwidth is 0.03 GHz.

For the band-pass iris filter which is formed by Fig. 3.18(b), by increasing the side lengths of the bevel angles, on the contrary, the centre frequency (94 GHz originally) of the band-pass filter shifts to lower frequencies. Meanwhile, the 3 dB bandwidth widens as the side lengths increase. The relationship between the side length, the offset, and the increment of the bandwidth is shown in Fig. 3.20(b). Compared with round angles, both the centre frequency and bandwidth are more susceptible to the change of bevel angles. The centre frequency shifts by 0.76 GHz when the side length

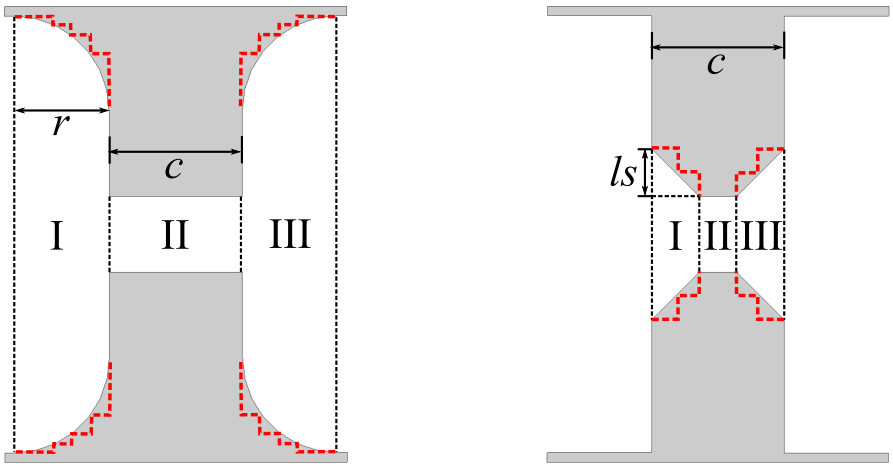

Figure 3.18. Irises with different types of fabrication effects taken into account: (a) round angles, (b) bevel angles. These two figures show irises with rounded angles and bevel angles. The rounded angles are formed because the milling cutter has a given radius, while the bevel angles are introduced to eliminate undesired fabrication influence. Source: Self-created using Ansys HFSS and Inkscape.

is around 0.06 mm while the bandwidth expands by 0.2 GHz when the side length is only 0.03 mm.

3.4.3 Approaches to Remove Undesired Influence

To eliminate the undesired influence, in previous work (Bornemann 2001), the resonator lengths have been adjusted first, and then both the aperture sizes and resonator lengths have been optimised according to fabrication limitations. The disadvantages of this method are that it requires the adjustment of several variables, and the optimisation space significantly grows with the order of the band-pass filter.

In order to improve the optimisation efficiency, three efficient approaches are proposed. Approach A: revise the design parameters according to the estimated influence in order to compensate the frequency shift; Approach B: design the band-pass filter without considering the influence of fabrication and then introduce reasonable bevel angles to correct the offset of the centre frequency; Approach C: map the realised structure of irises and resonator cavities with the impedance inverter and LC resonator network of a band-pass filter to directly and accurately compute the aperture sizes and resonator lengths.

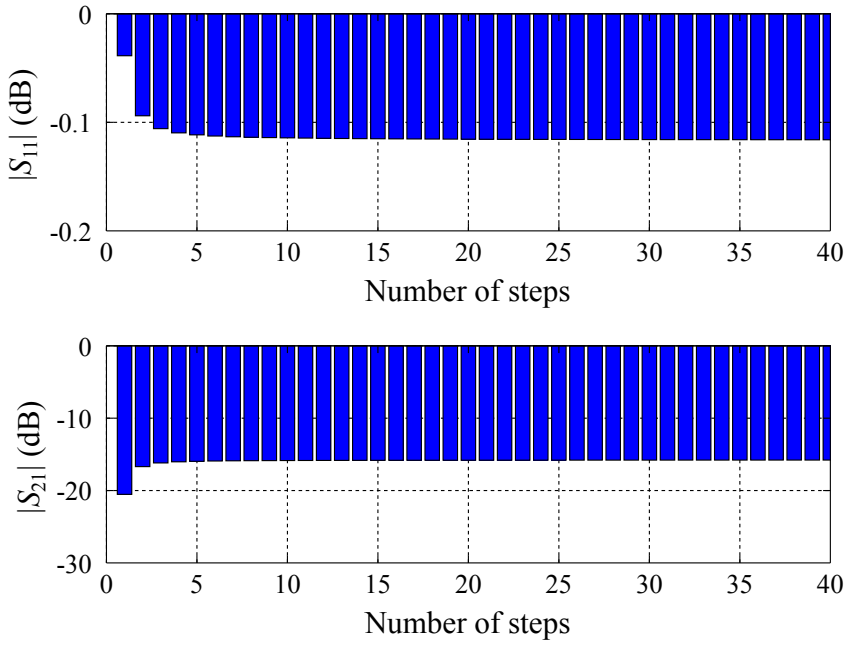

(a)

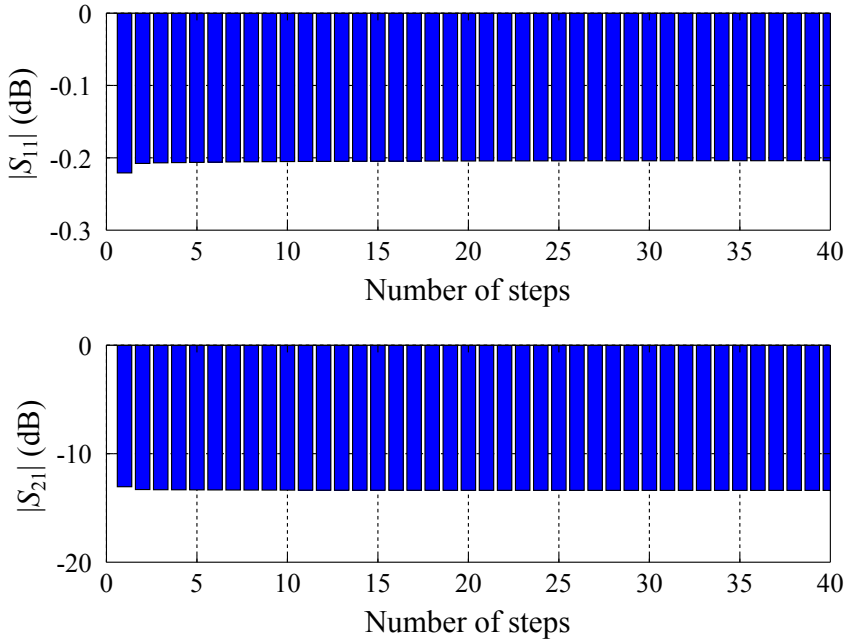

(b)

Figure 3.19. Relationship between the convergence and the number of steps for an iris with (a) round angles and (b) bevel angles at 94 GHz. These figures show the scattering parameters $|S_{11}|$ and $|S_{21}|$ trend to constants with the increase of the number of steps for approximating round angles and bevel angles. Source: Self-created using Matlab.

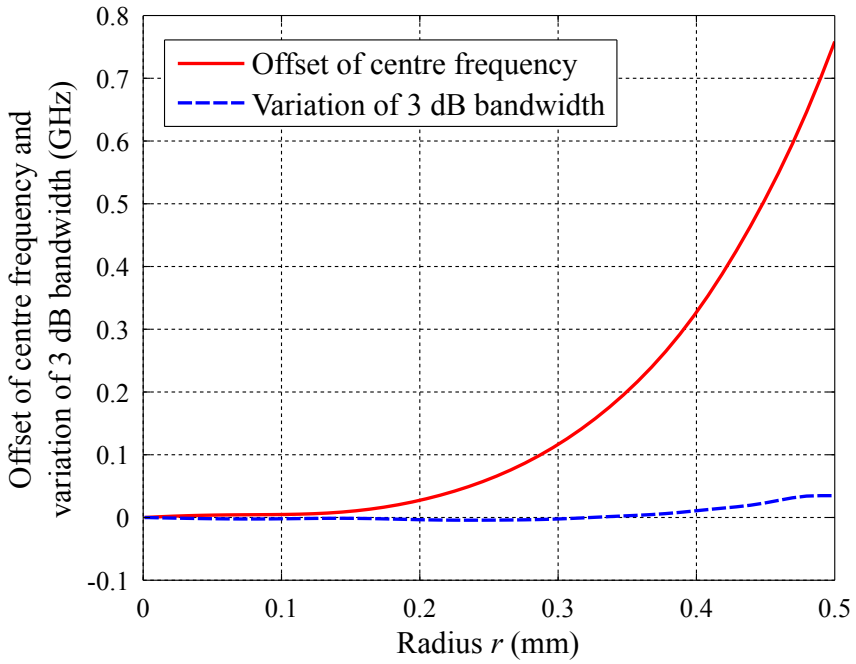

(a) Round angles

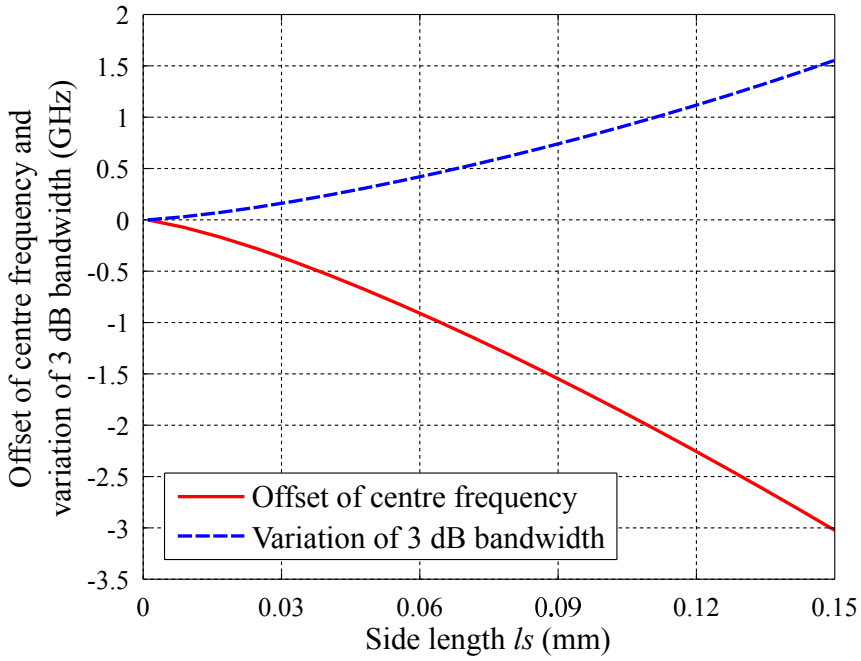

(b) Bevel angles

Figure 3.20. Relationship between the radius or side length, the offset of the centre frequency, and the variation of bandwidth. These figures show that how the round angles and bevel angles affect the centre frequency and 3 dB bandwidth for the 5^{th}-order Chebyshev band-pass iris filter. Source: Self-created using Matlab.

Table 3.2. Dimensions of a 5^{th}-order Chebyshev band-pass iris filter with round angles (Units: mm). The table gives the dimensions, including the iris thicknesses c, the gaps G between iris plates and the lengths D of the resonant cavities, used to realise a 5^{th}-order Chebyshev band-pass iris filter whose structure is illustrated in Fig. 3.17. This filter is designed to be fabricated with a milling machine with a cutter radius r.

c	r	G_1, G_6	G_2, G_5	G_3, G_4	D_1, D_5	D_2, D_4	D_3
0.5	0.4	1.493	1.095	0.999	1.429	1.704	1.746

The following analysis is based on a 5^{th}-order Chebyshev band-pass iris filter with a centre frequency of 94 GHz and a fractional bandwidth of 4.25%. This filter is designed to be fabricated with a milling machine with a cutter radius of 0.4 mm.

Approach A: Compensation of Frequency Shift

For Approach A, according to Fig. 3.20(a), the 0.4 mm radius round angles lead to a 0.34 GHz offset for the centre frequency. Thus, in order to shift the centre frequency back to the specified value (94 GHz), a band-pass filter with a centre frequency of 93.66 GHz needs to be designed instead. One aspect to note is that the fractional bandwidth also can be revised based on Fig. 3.20(a). However, because the bandwidth increment caused by a radius of 0.4 mm is limited, this influence is ignored here.

The computation time for the modified filter using the MMM is around 0.2 seconds on a standard computer with a 3.40 GHz i7-2600 CPU and 14.0 GB RAM. The optimised values are given in Table 3.2. The calculated results are in a good match with the simulation results of the FEM using Ansys HFSS as shown in Fig. 3.21.

Approach B: Counteract Frequency Shift with Bevel Angle

Approach B is another way to adjust the centre frequency. It employs the structure which is formed by Fig. 3.22, that is, the combination structure of Fig. 3.18(a) and (b), and utilises the opposite influence on centre frequency caused by bevel angles to balance out the frequency shift caused by round angles.

Based on the initial design given in Table 3.1, to counteract the 0.34 GHz offset, the initial side length can be set to 0.026 mm according to Fig. 3.20(b). We compute the

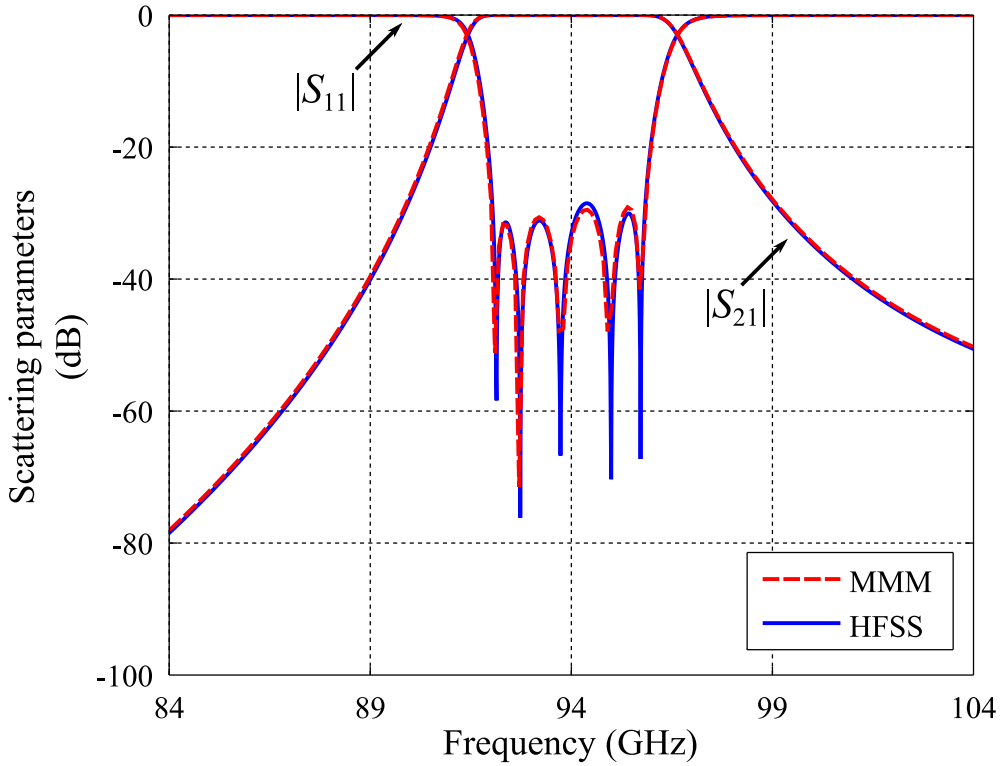

Figure 3.21. Comparison of scattering parameters obtained using the MMM and the FEM using Ansys HFSS. This figure shows the frequency response of a 5^{th}-order Chebyshev band-pass iris filter with round angles obtained through the MMM and the FEM. The design requirements are satisfied well with Approach A. Source: Self-created using Ansys HFSS and Matlab.

centre frequency with the initial side length and compare it with 94 GHz. If they do not match well, the side length needs to be adjusted around 0.026 mm until the calculated centre frequency satisfies the design requirement. The side length is here finalised as 0.025 mm.

To deal with this case, with the method introduced in (Bornemann 2001), six variables (G_1, G_2, G_3, D_1, D_2, D_3) are required to be optimised. This second method greatly reduces the amount of variables required to be adjusted. However, a side length of 0.025 mm also introduces a 0.13 GHz increment of the 3 dB bandwidth. Thus, it is necessary to check whether the bandwidth is still acceptable in the end.

The simulation result comparison between this method and the FEM using Ansys HFSS is shown in Fig. 3.23. The frequency response curves are almost in coincidence, thus, a good agreement between the two methods can be confirmed.

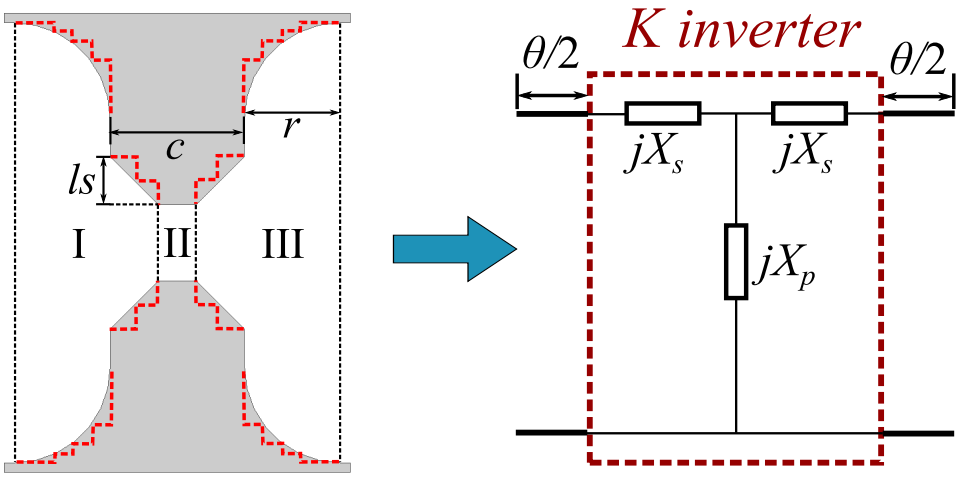

Figure 3.22. An iris with both rounded angles and bevel angles and its equivalent circuit for the impedance inverter. The left figure shows a combination of the structures of Fig. 3.18(a) and (b). This structure can behave as an impedance inverter, and thus the equivalent circuit for the impedance inverter is also provided in the right figure. Source: Self-created using Ansys HFSS and Inkscape.

Approach C: Direct Mapping Method

Compared with Approach B, in the third method, all sizes are designed with the perturbations taken into account directly without subsequent adjustment. This is achieved by mapping irises shown in Fig. 3.18 or 3.22, and resonant cavities formed by iris pairs with the network for generalised band-pass filter using impedance inverters shown in Fig. 3.13.

Here, the iris shown in Fig. 3.22 with both round angles (radius: 0.4 mm) and bevel angles (side length: 0.1 mm) is chosen. If the thickness c is fixed as 0.5 mm, by matching the calculated values for the equivalent impedance inverters to the theoretical ones, the gaps G between iris plates can then be determined. Moreover, the lengths D of the resonant cavities also can be computed with the wavelength at the centre frequency and the electrical lengths using Eq. 3.62.

Based on the MMM, all dimensions listed in Table 3.3 can be calculated. As shown in Fig. 3.24, the calculated mode-matching results also match well with the FEM simulations using Ansys HFSS.

According to the analysis above, clearly, all of the three approaches can be applied to eliminate the undesired influence caused by micro-machining errors, that is, the round angles between waveguide walls and irises. In addition, due to the high-speed and

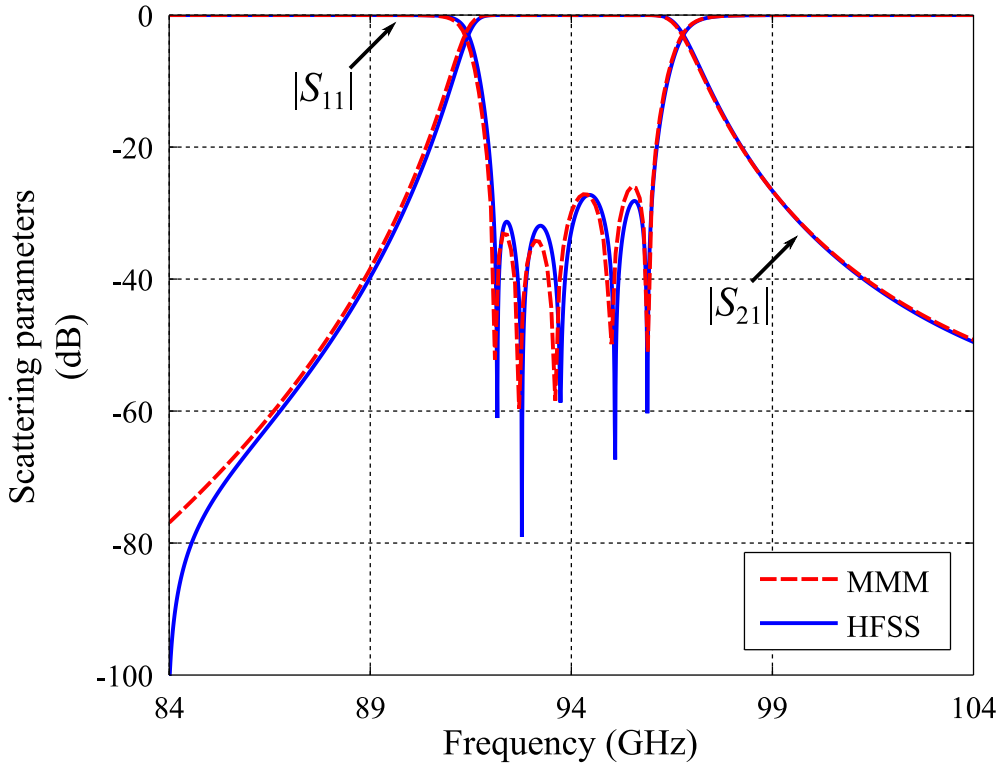

Figure 3.23. Comparison of scattering parameters obtained using the MMM and the FEM using Ansys HFSS. This figure shows the frequency response of a 5^{th}-order Chebyshev band-pass iris filter with both round and bevel angles obtained through the MMM and the FEM. The undesired influence caused by round angles is removed through Approach B. Source: Self-created using Ansys HFSS and Matlab.

high-precision of the MMM, the iris band-pass filter design and the tolerance analysis can be handled efficiently.

3.5 Chapter Summary

In this chapter, the electromagnetic waves propagating in a rectangular waveguide have been analysed and some corresponding equations have been derived. Based on these equations, the principle of the mode-matching method has been explained in detail for the analysis of waveguide discontinuities. Thus, the characteristics of irises with or without rounded or bevel angles, placed in the cross-section of a rectangular waveguide, can be analysed efficiently.

Combining the principle of the mode-matching method and the band-pass filter theory, a Chebyshev 5^{th}-order band-pass iris filter has been designed rapidly and accurately.

Table 3.3. Dimensions of a 5^{th}-order Chebyshev band-pass iris filter with both round angles and bevel angles (Units: mm). This table gives the dimensions, including the iris thicknesses c, the gaps G between iris plates and the lengths D of the resonant cavities, used to realise a 5^{th}-order Chebyshev band-pass iris filter formed with iris geometries shown in Fig. 3.22. The iris has both round angles with a radius r and bevel angles with a side ls.

c	r	ls	G_1, G_6	G_2, G_5	G_3, G_4	D_1, D_5	D_2, D_4	D_3
0.5	0.4	0.1	1.434	1.035	0.941	1.413	1.682	1.723

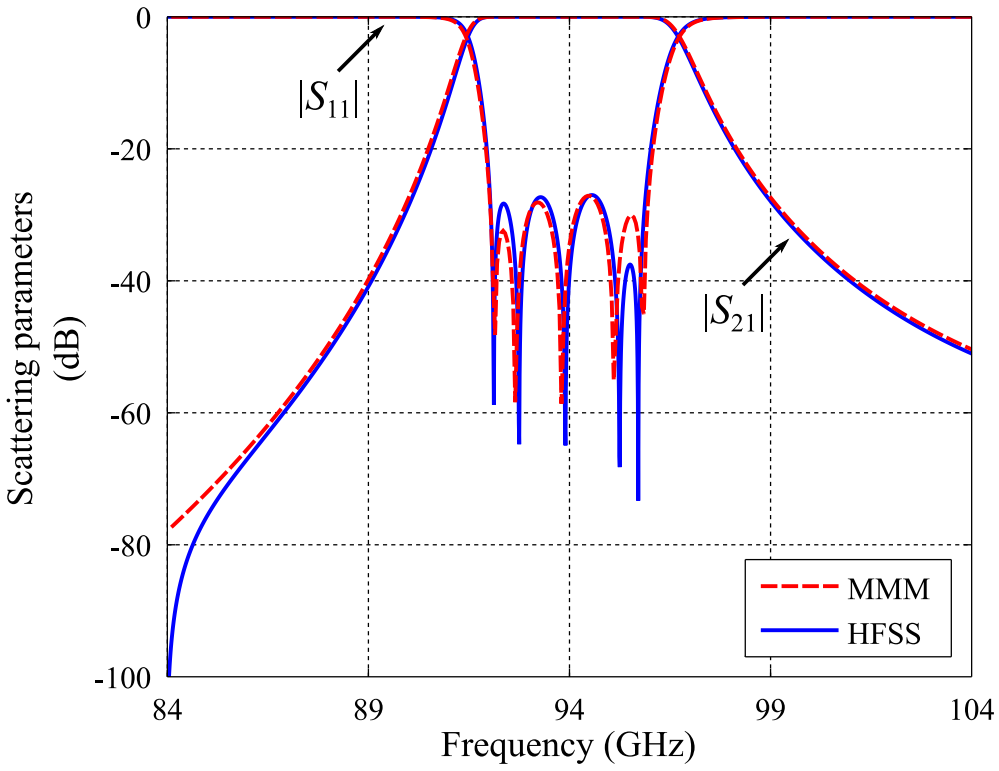

Figure 3.24. Comparison of scattering parameters obtained using the MMM and the FEM using Ansys HFSS. This figure shows the frequency response of a 5^{th}-order Chebyshev band-pass iris filter with both round and bevel angles, which is designed with Approach C. The calculated mode-matching results agree well with the simulations performed with Ansys HFSS. Source: Self-created using Ansys HFSS and Matlab.

In addition, considering the limitations of micro-machining processes, an analysis of

the influence caused by rounded angles has been presented. On this basis, this chapter also proposed three efficient approaches to eliminate the undesired influence of rounded corners: compensating the frequency shift, offsetting the shift with bevel angles, and taking the properties of the perturbations into account when computing the sizes. All approaches successfully corrected the offset of the centre frequency caused by rounded corners and all calculated results obtained with a self-developed mode-matching code have been verified by full-wave finite-element simulations using Ansys HFSS.

In the next chapter, the principle of analysing the characteristics of posts placed in the cross-section of a rectangular waveguide will be explained. Based on this method, a general design method for band-pass post filters in rectangular waveguide and substrate-integrated waveguide will be introduced. In addition, the next chapter will also analyse losses in substrate-integrated waveguide band-pass post filters with the finite-element method using Ansys HFSS.

Chapter 4

Band-Pass Post Rectangular Waveguide Filters

THIS chapter starts by explaining the principle of the mode-matching method for analysing N-furcation structures placed in a rectangular waveguide. It then introduces nine approaches to approximate posts placed in the cross-section of a rectangular waveguide based on a series of N-furcation structures. Through comparing the difference between the scattering parameters and accurate reference solutions for the post structures and the rate of convergence for each approach, the most efficient approximation is also recommended. On that basis, we combine the principle of the mode-matching method for analysing posts assigned in a rectangular waveguide with band-pass filter theory, and introduce an efficient general method for band-pass post filters in rectangular waveguides and substrate-integrated waveguides. It is followed by the investigation of the influence on the performance of band-pass filters caused by manufacture-induced filter dimension errors. Since the mode-matching method is based on lossless simulations, while insertion loss is an important specification to judge the quality of a band-pass post filter, the last part of this chapter also explores the insertion losses in band-pass post substrate-integrated waveguide filters.

4.1 Introduction

A high-performance band-pass filter can be realised by placing various irises in the cross-section of a rectangular waveguide. However, as introduced in Chapter 3, because of the limitations of micro-machining processes, the corners of the various discontinuity features, such as between waveguide walls and irises, are rounded rather than perfect right angles. The resulting differences between ideal designs and realisable geometries do influence the performance of the band-pass filters, especially when they operate at high frequencies (Bornemann 2001, Bornemann *et al.* 2005).

Compared with the above mentioned discontinuities in waveguides, cylindrical posts placed in the cross-section of a rectangular waveguide or circular holes are intrinsically easier to manufacture with standard technology. Thus, posts are less prone to machining errors and are promising for realising band-pass waveguide filters at higher frequency bands. Due to the high-speed and high-accuracy, an efficient method based on the mode-matching method (MMM) is still one of the most powerful options for the design of band-pass waveguide post filters. It is noted that the method is applicable to post filters in waveguides but can be extended to substrate-integrated waveguide (SIW) technology, which is able to reduce the dimension of the band-pass filters greatly. For illustration, the structures of two X-band 5-cavity band-pass post filters in a rectangular waveguide and an SIW are shown in Fig. 4.1.

This chapter is organised as follows. Section 4.2 explains the principle of the MMM for double-plane discontinuities with multiple apertures, and investigates the most efficient approach to approximate cylindrical posts placed in a rectangular waveguide. In section 4.3, a general design method for band-pass post filters in rectangular waveguides and SIWs is introduced, while the validity of the method is verified via full-wave simulations using Ansys High Frequency Structural Simulator (Ansys HFSS) and measurements on manufactured prototypes. Chapter 4.4 then explores the influence on the performance of band-pass filters caused by dimension errors. The characterisation of the ohmic and dielectric losses in band-pass post SIW filters is then analysed with Ansys HFSS in Section 4.5. The chapter ends in Section 4.6.

4.2 Principle of the Mode-Matching Method for Posts

A band-pass filter can be realised by placing posts in the cross-section of a rectangular waveguide instead of irises, since posts are another option to block a short length of

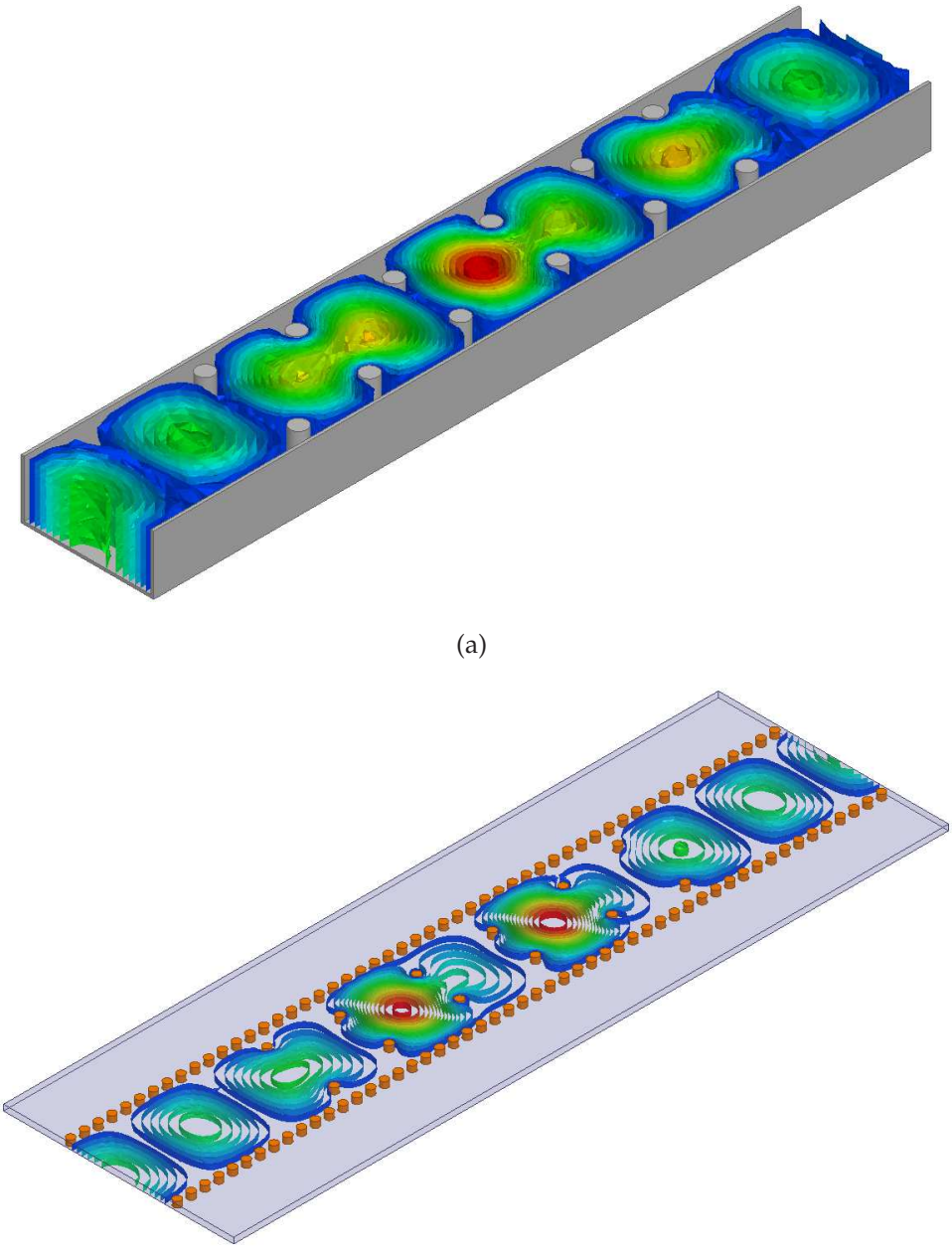

(a)

(b)

Figure 4.1. Structures of X-band 5-cavity band-pass (a) post rectangular waveguide filter, and (b) via SIW filter. These figures depict the structures of 5^{th}-order band-pass post rectangular waveguide filter and via SIW filter. In both cases, the centre frequency is 10.5 GHz and passband extends from 10 GHz to 11 GHz. The top filter is designed based on a standard X-Band WR-90 rectangular waveguide, while the bottom filter employs an SIW having the similar propagation characteristics to the WR-90 rectangular waveguide. The images show the instantaneous field distributions at 10.5 GHz. Source: Self-created using Ansys HFSS.

waveguide in order to form a cavity resonator. The characteristics of this type of band-pass filter, whose structure is shown in Fig. 4.1(a), can be analysed with full-wave simulation tools such as Ansys HFSS or Microwave Studio from Computer Simulation Technology (CST). However, this process is quite time-consuming because of the large number of variables, especially considering the requirement on mesh fineness in order to obtain results with sufficient precision. In contrast, the MMM shows a distinct advantage in analysing the characteristics of posts placed in the cross-section of a rectangular waveguide, because of the demonstrated high speed and high accuracy (Patzelt and Arndt 1982, Bornemann and Arndt 1987, Papziner and Arndt 1993).

It is noted that the characteristics analysis for posts placed in the cross-section of a rectangular waveguide and vias assigned in the cross-section of an SIW can be merged, since an SIW can be transformed into an equivalent dielectric-loaded rectangular waveguide. Several empirical analytical equations can be used to realise this equivalent modelling (Cassivi *et al.* 2002, Yan *et al.* 2004, Xu and Wu 2005, Che *et al.* 2008a, Salehi and Mehrshahi 2011), and this thesis employs the equation introduced by Cassivi (Cassivi *et al.* 2002), which expresses the equivalent width W_e as:

$$W_e = W_i - \frac{d^2}{0.95p}, \tag{4.1}$$

where d is the via diameter, p is the interval between two adjacent vias, and W_i is the physical width of the SIW, measured as the distance between the centres of the two via rows.

4.2.1 Mode-Matching Analysis of Double-Plane Discontinuity with Multiple Apertures

The characteristics of a double-plane discontinuity with multiple apertures can be analysed with the MMM. In order to explain the principle, a double-plane discontinuity with two apertures is taken as an example. Extending the explanation below, a discontinuity with more windows can be handled in the similar way.

As shown in Fig. 4.2, the discontinuity is formed at the junction plane ($z = 0$ plane) by three rectangular waveguides. Because of this discontinuity, high-order modes, including TE_{mn} and TM_{mn} modes, are excited from the fundamental mode TE_{10}. These modes, existing in the vicinity of the discontinuity, are continuous on the junction plane, that is, the transverse electric and magnetic fields on $z = 0$ plane satisfy the

following equations

$$\begin{aligned}
\vec{E}^{\mathrm{I}}_{th} + \vec{E}^{\mathrm{I}}_{te} &= \vec{E}^{\mathrm{II}}_{th} + \vec{E}^{\mathrm{II}}_{te} + \vec{E}^{\mathrm{III}}_{th} + \vec{E}^{\mathrm{III}}_{te}, \\
\vec{H}^{\mathrm{I}}_{th} + \vec{H}^{\mathrm{I}}_{te} &= \vec{H}^{\mathrm{II}}_{th} + \vec{H}^{\mathrm{II}}_{te}, \\
\vec{H}^{\mathrm{I}}_{th} + \vec{H}^{\mathrm{I}}_{te} &= \vec{H}^{\mathrm{III}}_{th} + \vec{H}^{\mathrm{III}}_{te},
\end{aligned} \tag{4.2}$$

where $\vec{E}_{th}$, $\vec{E}_{te}$, $\vec{H}_{th}$, and $\vec{H}_{te}$ in different waveguides can be fully described with the magnitudes of z-directed magnetic and electric vector potentials A_h and A_e, normalised coefficients G_h and G_e, and amplitude coefficients for forward and backward waves Q_{hF}, Q_{eF}, Q_{hB}, and Q_{eB}.

In the similar manner introduced in Chapter 3, an equation relating amplitude coefficients and scattering matrix can be expressed as

$$\begin{bmatrix} Q^{\mathrm{I}}_{hB} \\ Q^{\mathrm{I}}_{eB} \\ Q^{\mathrm{II}}_{hF} \\ Q^{\mathrm{II}}_{eF} \\ Q^{\mathrm{III}}_{hF} \\ Q^{\mathrm{III}}_{eF} \end{bmatrix} = \left[\begin{array}{c|cc} S_{11} & S_{12} & S_{13} \\ \hline S_{21} & S_{22} & S_{23} \\ S_{31} & S_{32} & S_{33} \end{array}\right] \begin{bmatrix} Q^{\mathrm{I}}_{hF} \\ Q^{\mathrm{I}}_{eF} \\ Q^{\mathrm{II}}_{hB} \\ Q^{\mathrm{II}}_{eB} \\ Q^{\mathrm{III}}_{hB} \\ Q^{\mathrm{III}}_{eB} \end{bmatrix} = \begin{bmatrix} S'_{11} & S'_{12} \\ S'_{21} & S'_{22} \end{bmatrix} \begin{bmatrix} Q^{\mathrm{I}}_{hF} \\ Q^{\mathrm{I}}_{eF} \\ Q^{\mathrm{II}}_{hB} \\ Q^{\mathrm{II}}_{eB} \\ Q^{\mathrm{III}}_{hB} \\ Q^{\mathrm{III}}_{eB} \end{bmatrix}. \tag{4.3}$$

The equation (3.37) still can be utilised to compute the scattering parameters. However, since these equations are derived to handle two-port networks, the three-port discontinuity network should be first transformed into two-port network. Namely, it is necessary to merge S_{12} and S_{13} as S'_{12}, to merge S_{21} and S_{31} as S'_{21}, and to unite S_{22}, S_{23}, S_{32}, and S_{33} as S'_{22}. Importantly, the coupling matrix M required in Eq. 3.37 should also be modified as the following

$$\mathcal{M}' = \left[\begin{array}{cc|cc} J^{\mathrm{I,II}}_{HH} & J^{\mathrm{I,II}}_{HE} & J^{\mathrm{I,III}}_{HH} & J^{\mathrm{I,III}}_{HE} \\ J^{\mathrm{I,II}}_{EH} & J^{\mathrm{I,II}}_{EE} & J^{\mathrm{I,III}}_{EH} & J^{\mathrm{I,III}}_{EE} \end{array}\right], \tag{4.4}$$

where $J^{\mathrm{I,II}}_{HH}$, $J^{\mathrm{I,II}}_{HE}$, $J^{\mathrm{I,II}}_{EH}$, and $J^{\mathrm{I,II}}_{EE}$ are coupling coefficients between waveguide I and waveguide II, while $J^{\mathrm{I,III}}_{HH}$, $J^{\mathrm{I,III}}_{HE}$, $J^{\mathrm{I,III}}_{EH}$, and $J^{\mathrm{I,III}}_{EE}$ represent coupling coefficients between waveguide I and waveguide III. All of these coupling coefficients can be obtained through Eq. 3.28 to 3.31.

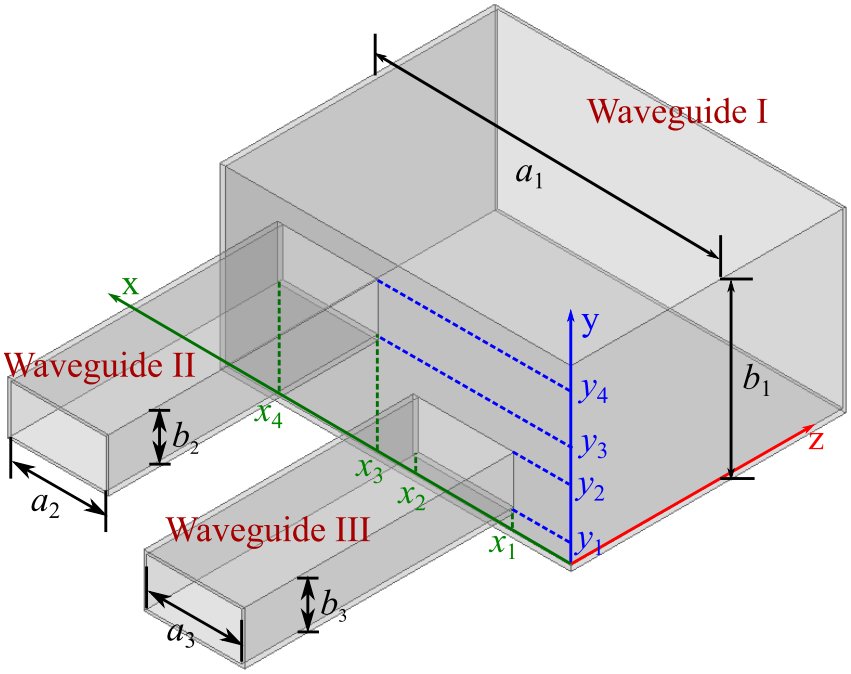

Figure 4.2. A double-plane step discontinuity with two apertures. This figure shows the configuration of a double-plane discontunity with two apertures, which is formed by three rectangular waveguides. Waveguide I has a width of a_1 and a height of b_1, waveguide II has a width of a_2 and a height of b_2, while waveguide III has a width of a_3 and a height of b_3. Variables including x_1, x_2, x_3, x_4, y_1, y_2, y_3, and y_4 determine the positions of the apertures on the junction surface, that is, $z = 0$ plane. Source: Self-created using Ansys HFSS and Inkscape.

4.2.2 Scattering Matrices of N-furcations Placed in Rectangular Waveguides

As shown in Fig. 4.3, a rectangular waveguide is divided into three regions by two H-plane inserts. Region I and III are full-size waveguides, while region II consists of three small waveguides. Obviously, the scattering parameters of this 3-furcation structure can be obtained by cascading the scattering matrix of the discontinuity formed by region I and II (S_I), the scattering matrices of small rectangular waveguides in region II (S_{II1}, S_{II2}, S_{II3}), and the scattering matrices of the discontinuity formed by region II and III (S_{III}). For illustration, a schematic diagram is presented in Fig. 4.4(a), where the discontinuity on the $z = 0$ or $z = c$ plane is considered as a 4-port network, while the small waveguides in between are considered as 2-port networks.

The discontinuity formed by region I and II or region II and III can be treated as a special case of a double-plane discontinuity with three apertures, whose heights are the

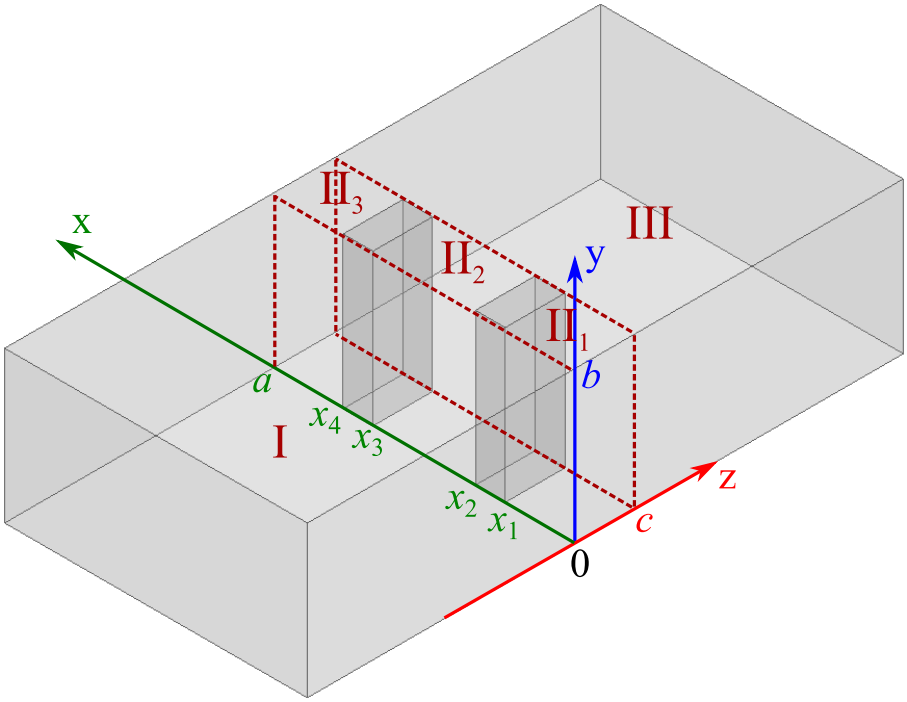

Figure 4.3. Two H-plane inserts placed in the cross-section of a rectangular waveguide. This figure shows that a rectangular waveguide is divided into three regions by two H-plane inserts. Region I ($z \leq 0$) and III ($z \geq c$) are big waveguides, while region II ($0 \leq z \leq c$) consists of three small waveguides. Rectangular waveguides in all regions have the same height. Source: Self-created using Ansys HFSS and Inkscape.

same as the host rectangular waveguide. The discontinuity exists along the x-direction, not along the y-direction. Thus, only the TE_{m0} modes are excited from the fundamental mode TE_{10}. The scattering parameter calculation can then be further simplified based on Eq. 3.28 to 3.31, because the required coupling matrix only contains coupling coefficients $J_{HH}^{\mathrm{I,II_1}}$, $J_{HH}^{\mathrm{I,II_2}}$, and $J_{HH}^{\mathrm{I,II_3}}$, which can be expressed as

$$
\begin{aligned}
J_{HH}^{\mathrm{I,II_1}} &= \frac{2}{\sqrt{ax_1}} \sqrt{\frac{\Gamma^{I}_{hm_h^{\mathrm{I}'}0}}{\Gamma^{\mathrm{II_1}}_{hm_h^{\mathrm{II_1}}0}}} \int_0^{x_1} \sin\left(\frac{m_h^{\mathrm{I}'}\pi x}{a}\right) \sin\left(\frac{m_h^{\mathrm{II_1}}\pi x}{x_1}\right) \mathrm{d}x, \\
J_{HH}^{\mathrm{I,II_2}} &= \frac{2}{\sqrt{a(x_3-x_2)}} \sqrt{\frac{\Gamma^{\mathrm{I}}_{hm_h^{\mathrm{I}'}0}}{\Gamma^{\mathrm{II_2}}_{hm_h^{\mathrm{II_2}}0}}} \int_{x_2}^{x_3} \sin\left(\frac{m_h^{\mathrm{I}'}\pi x}{a}\right) \sin\left(\frac{m_h^{\mathrm{II_2}}\pi (x-x_2)}{x_3-x_2}\right) \mathrm{d}x, \\
J_{HH}^{\mathrm{I,II_3}} &= \frac{2}{\sqrt{a(a-x_4)}} \sqrt{\frac{\Gamma^{\mathrm{I}}_{hm_h^{\mathrm{I}'}0}}{\Gamma^{\mathrm{II_3}}_{hm_h^{\mathrm{II_3}}0}}} \int_{x_4}^{a} \sin\left(\frac{m_h^{\mathrm{I}'}\pi x}{a}\right) \sin\left(\frac{m_h^{\mathrm{II_3}}\pi (x-x_4)}{a-x_4}\right) \mathrm{d}x.
\end{aligned}
\tag{4.5}
$$

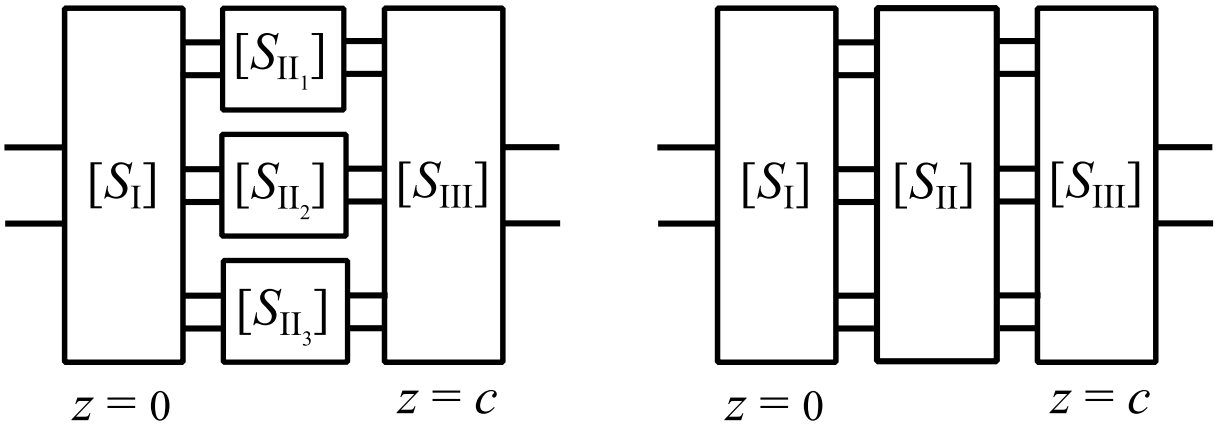

Figure 4.4. Schematic diagrams of an N-furcation rectangular waveguide structure. These figures shows an N-furcation structure (Fig. 4.3) schematically. The first considers the discontinuity on $z = 0$ and $z = c$ plane as 4-port networks and the three small waveguides in between as 2-port networks. The second considers the three small waveguides as a 6-port network. Source: Self-created using Inkscape.

The scattering parameters for the three small waveguides in region II can be obtained through Eq. 3.39. However, in order to simplify the cascade process and improve the calculation efficiency, as shown in Fig. 4.4(b), the three 2-port networks are merged as one 6-port network. Thus, the corresponding equation for the scattering parameters should be modified as

$$S_{\mathrm{II}} = \begin{bmatrix} 0 & V \\ V & 0 \end{bmatrix}, \qquad V = \begin{bmatrix} e^{-\Gamma^{\mathrm{II}_1}_{hm_h0}c} & 0 & 0 \\ 0 & e^{-\Gamma^{\mathrm{II}_2}_{hm_h0}c} & 0 \\ 0 & 0 & e^{-\Gamma^{\mathrm{II}_3}_{hm_h0}c} \end{bmatrix}, \tag{4.6}$$

where $e^{-\Gamma^{\mathrm{II}_1}_{hm_h0}c}$, $e^{-\Gamma^{\mathrm{II}_2}_{hm_h0}c}$, and $e^{-\Gamma^{\mathrm{II}_3}_{hm_h0}c}$ represent the exponential factors of TE_{m_h0} modes of waveguides in region II.

Thus far, the scattering matrices for the discontinuities on the $z = 0$ and $z = c$ plane, and the waveguides in regions II can all be obtained. The scattering matrix for the whole 3-furcation structure can then be computed by following Eq. 3.40 with the three scattering matrices.

To verify the validity of the implemented MMM code for N-furcations, a 3-furcation structure based on a standard W-Band (extending from 75 GHz to 110 GHz) WR-10 waveguide with a width of $a = 2.54$ mm and a height of $b = 1.27$ mm is taken as an

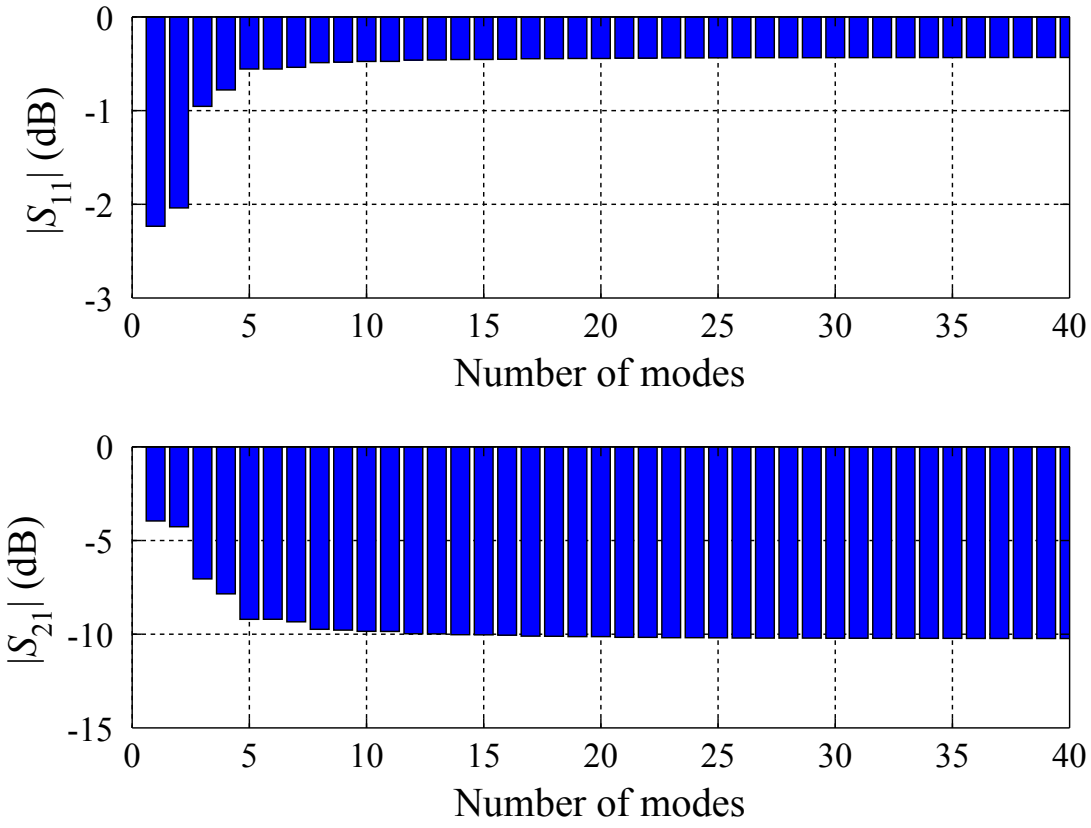

Figure 4.5. Relationship between the convergence and the number of adopted modes at 94 GHz. This figure shows that with the increase of the number of modes, the scattering parameters $|S_{11}|$ and $|S_{21}|$ trend to stable values. Source: Self-created using Matlab.

example. As defined in Fig. 4.3, the H-plane inserts have a thickness of $c = 0.4\,\text{mm}$, while the variables x_1, x_2, x_3, and x_4 used to determine the positions and thicknesses of the inserts are 0.5 mm, 0.6 mm, 1.7 mm, and 2.0 mm respectively.

With the dimensions provided above for the 3-furcation waveguide structure, the relationship between the convergence and the number of modes (for simplicity, numbers of modes in different waveguides are chosen the same) has been investigated at 94 GHz. As shown in Fig. 4.5, by increasing the number of modes, both $|S_{11}|$ and $|S_{21}|$ converge to a stable value. In addition, when the number of modes is larger than 25, the changes for $|S_{11}|$ and $|S_{21}|$ are insignificant.

By setting the number of modes to 25, the calculated mode-matching results for the 3-furcation waveguide structure are verified by the finite-element method (FEM) simulations performed with Ansys HFSS as shown in Fig. 4.6. Obviously, without taking

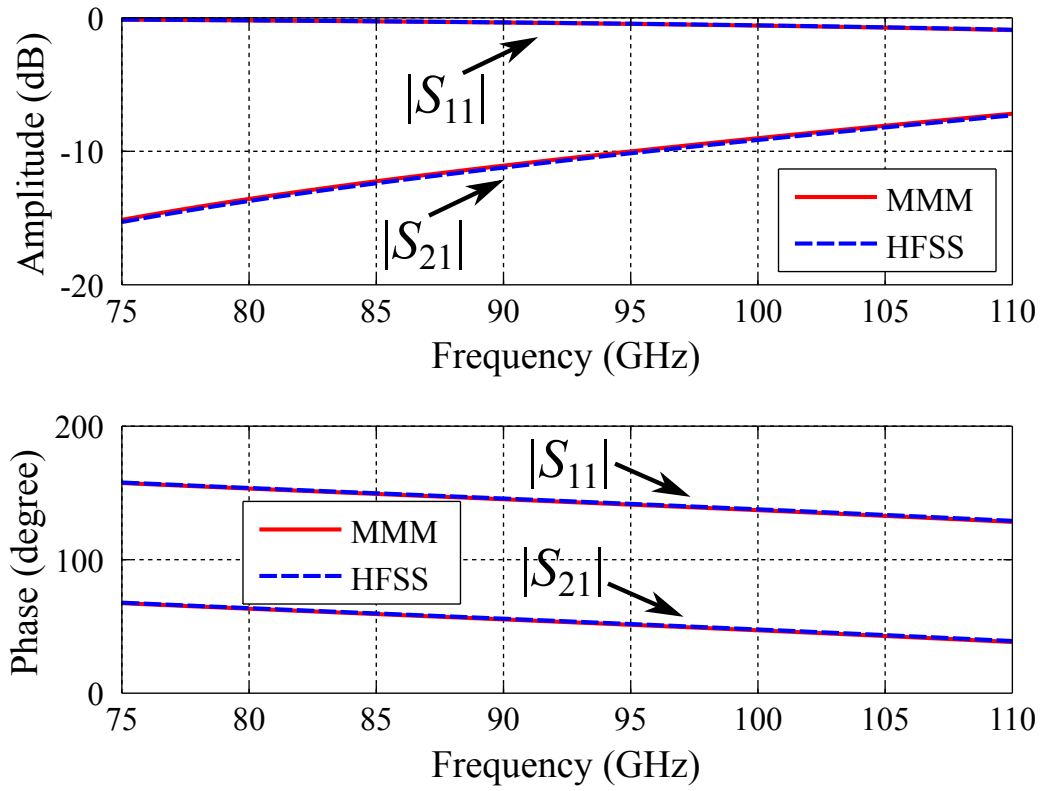

Figure 4.6. Comparison for the amplitude and phase of scattering parameters obtained through the MMM with 25 modes and the FEM using Ansys HFSS in W-Band. These figures show that the calculated mode-matching results for the amplitude and phase of $|S_{11}|$ and $|S_{21}|$ match well with those simulated with Ansys HFSS. Source: Self-created using Matlab.

losses into account, the calculated mode-matching results for the amplitude and phase of $|S_{11}|$ and $|S_{21}|$ have a good match with the results simulated with the FEM using Ansys HFSS. It is noted that, to ensure simulated results with sufficient precision, the maximum length of elements for the mesh setting in Ansys HFSS is chosen as 0.1 mm. Thus, for a standard computer with a 3.40 GHz i7-2600 CPU and 14.0 GB RAM, it takes 258 s to simulate one frequency point (94 GHz). However, the MMM shows a clear advantage in efficiency, since it takes only 0.034 s for one frequency point (94 GHz).

For a symmetric 3-furcation structure, a magnetic wall can be exploited at the centre of the waveguide as shown in Fig. 4.7. Thus, the calculation time can be further reduced since the symmetry reduces the number of coupling matrices. Importantly, because of the magnetic wall, the boundary conditions for waveguide I, waveguide II_2 and waveguide III have been changed. As a consequence, excited high-order even modes

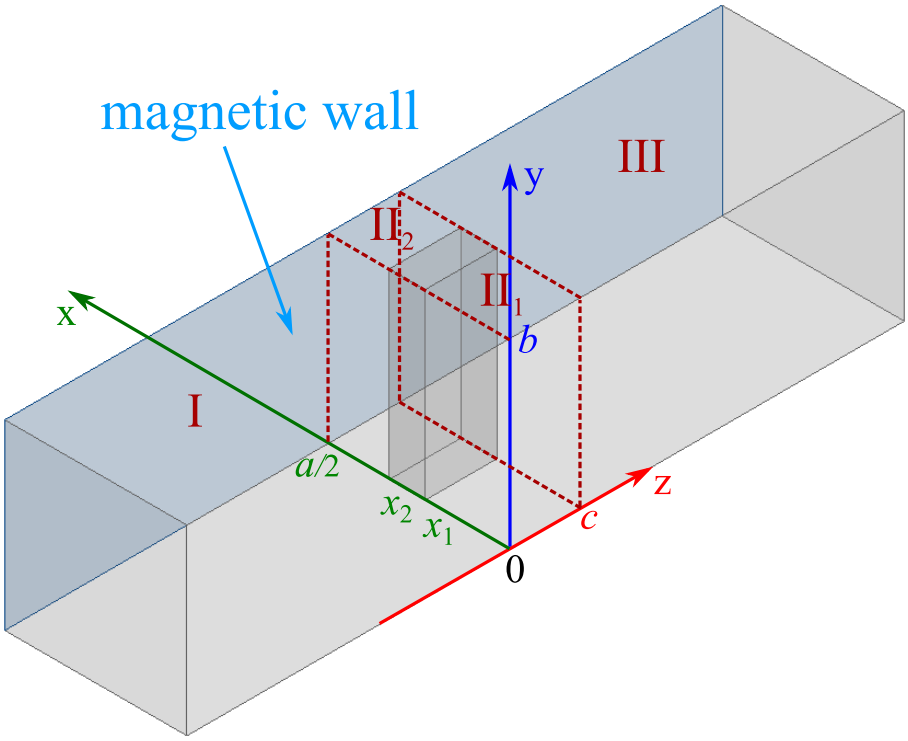

Figure 4.7. Half part of a symmetric 3-furcation structure shown in Fig. 4.3. This figure shows half part of a symmetric 3-furcation structure modelled with a magnetic wall at the centre of the waveguide. The half waveguide is divided into three regions. Region I ($z \leq 0$) and III ($z \geq c$) are full-size waveguides, while region II ($0 \leq z \leq c$) consists of two small waveguides. Source: Self-created using Ansys HFSS and Inkscape.

such as TE_{20} and TE_{40}, which are not symmetric with respect to the magnetic wall, are precluded and can be discarded.

4.2.3 Mode-Matching Analysis of Posts Placed in a Rectangular Waveguide

With the MMM, it is difficult to analyse cylindrical posts placed in the cross-section of a rectangular waveguide directly. However, the posts can be approximated as $2 \times M$ steps of waveguide N-furcations.

Based on the method introduced in Section 4.2.2, the scattering matrix of each waveguide N-furcation can be calculated. Thus, the scattering matrix of the posts can be obtained through cascading the scattering matrices of all N-furcations. One important aspect to note is that, because of the symmetry of the cylindrical posts, only half the N-furcation steps need to be considered. According to the different calculations

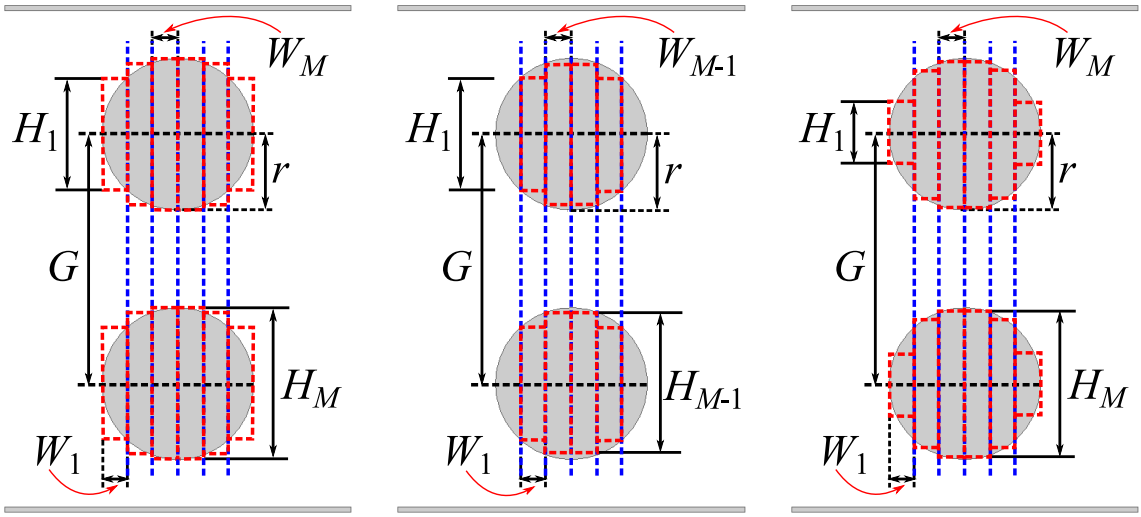

(a) Approach 1 (b) Approach 2 (c) Approach 3

Figure 4.8. Method A (equal width method): approximation of cross-section by (a) over-estimating, (b) under-estimating the circle and (c) averaging the previous two approaches. These figures show three post approximation approaches with equal widths including over-estimating the circles (angles of the N-furcations exceed the cross-section of the posts), under-estimating the circles (angles of the N-furcations are on the surfaces of the posts), and average the first two approximations. Source: Self-created using Ansys HFSS and Inkscape.

of the widths (W) and thicknesses (H) of the N-furcations, three approximation methods, including the equal width, the arithmetic sequence thickness and the equal sector methods, are introduced below.

Method A: Equal Width Method

As shown in Fig. 4.8, the horizontal diameters are divided into $2 \times M$ parts by vertical reference lines of equal spacing W. Any vertical reference line has two intersections with the cross-section, and the distance between the two intersections is the thickness H of the corresponding N-furcations. Thus, the posts can be approximated by three stair-cased approaches as shown in Fig. 4.8(a) to 4.8(c). First, the staircases of the N-furcations are completely outside the cross-section of the posts (Fig. 4.8(a)); second, the staircases of the N-furcations are completely inside the surfaces of the posts (Fig. 4.8(b)); third, the staircases are built as average of the first two approximations (that is, the thicknesses are the mean of the two previous values).

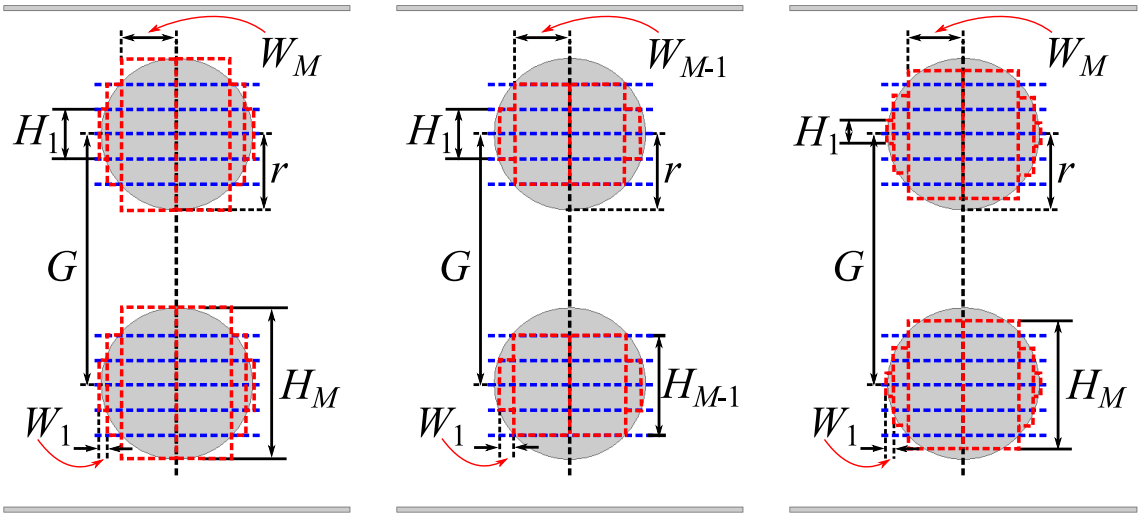

(a) Approach 1 (b) Approach 2 (c) Approach 3

Figure 4.9. Method B (arithmetic sequence thickness method): approximation of cross-section by (a) over-estimating, (b) under-estimating the circle and (c) averaging the previous two approaches. These figures show three post approximation approaches with arithmetic sequence thicknesses including over-estimating the circles (angles of the N-furcations exceed the cross-section of the posts), under-estimating the circles (angles of the N-furcations are on the surfaces of the posts), and average the first two approximations. Source: Self-created using Ansys HFSS and Inkscape.

Method B: Arithmetic Sequence Thickness Method

The vertical diameters are separated into $2 \times M$ parts equally by horizontal reference lines as shown in Fig. 4.9. Each horizontal reference line has two intersections with a circle. The distance between any two intersections that are symmetric to the horizontal diameter is the thickness H of the corresponding bifurcation. Obviously, the half thickness series is an arithmetic sequence. Similar to the previous method, the posts can be approximated by three stair-casing approaches as shown in Fig. 4.9(a) to 4.9(c) using over-estimation, under-estimation of the shape and taking the average of the two previous approaches.

Method C: Equal Sector Method

The cross-section is divided into equal sectors by reference lines as shown in Fig. 4.10. In term of trigonometric functions, both the thickness H and width W of each bifurcation step can be calculated. Similarly, the posts also can be approximated by three

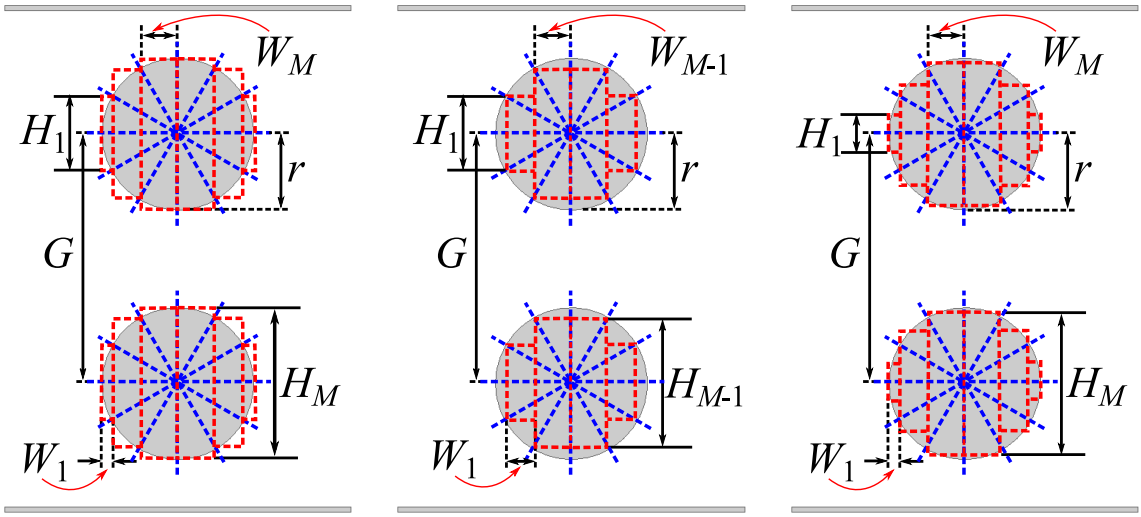

(a) Approach 1 (b) Approach 2 (c) Approach 3

Figure 4.10. Method C (equal sector method): approximation of cross-section by (a) over-estimating, (b) under-estimating the circle and (c) averaging the previous two approaches. These figures show three post approximation approaches based on equal sectors including over-estimating the circles (angles of the N-furcations exceed the cross-section of the posts), under-estimating the circles (angles of the N-furcations are on the surfaces of the posts), and average the first two approximations. Source: Self-created using Ansys HFSS and Inkscape.

stair-casing approaches as shown in Fig. 4.10(a) to 4.10(c) using over-estimation, under-estimation of the shape and taking the average of the two previous approaches.

Evaluation of the Post Approximation Methods

Numerical experiments have been performed at 94 GHz on a symmetric post structure. It is based on a standard W-Band (extending from 75 GHz to 110 GHz) WR-10 waveguide, whose width is 2.54 mm and height is 1.27 mm. The radii r of the posts are 0.25 mm, while the distance G between the centres of the two posts is 1.6 mm.

The relationship between the number of steps M and the scattering parameters $|S_{11}|$, $|S_{21}|$ of the dominant mode TE_{10} for the three approximation methods are plotted in Fig. 4.11 respectively. The three convergence figures show that for all of the approximation methods, with the increase of the number of steps M, the values of $|S_{11}|$ and $|S_{21}|$ tend towards constants. More detailed data when the number of steps is 10, 50, and 5000 are listed in Table 4.1. Clearly, when the number of steps M reaches 5000, the values of $|S_{11}|$ and $|S_{21}|$ for different approximation methods are nearly converged. In

Table 4.1. Scattering parameters at 94 GHz (Units: dB). The table gives the scattering parameters $|S_{11}|$ and $|S_{21}|$ of posts which are approximated with $2 \times M$ steps of 3-furcation structures. M is set as 10, 50 and 5000.

Method		$M = 10$		$M = 50$		$M = 5000$	
		S_{11}	S_{21}	S_{11}	S_{21}	S_{11}	S_{21}
A	Over	-0.5465	-9.272	-0.5956	-8.923	-0.6082	-8.838
	Under	-0.6804	-8.386	-0.6223	-8.745	-0.6085	-8.836
	Average	-0.6123	-8.811	-0.6088	-8.834	-0.6084	-8.837
B	Over	-0.5270	-9.4200	-0.5891	-8.967	-0.6082	-8.838
	Under	-0.7360	-8.072	-0.6300	-8.696	-0.6086	-8.835
	Average	-0.6243	-8.732	-0.6093	-8.831	-0.6084	-8.837
C	Over	-0.5451	-9.283	-0.5952	-8.925	-0.6082	-8.838
	Under	-0.6747	-8.420	-0.6213	-8.752	-0.6085	-8.836
	Average	-0.6086	-8.835	-0.6082	-8.838	-0.6084	-8.837

fact, if the number of steps M is increased to 10000, the values of $|S_{11}|$ and $|S_{21}|$ are almost identical to the fourth significant digit. Thus, it is reasonable to consider that -0.6084 dB and -8.837 dB are the constants to which the $|S_{11}|$ and $|S_{21}|$ tend at 94 GHz, that is, the accurate reference values.

The relationships between the difference of the scattering parameters and the accurate reference values ΔS_{11}, ΔS_{21} and the number of steps M for each approximation methods are plotted next. As shown in Fig. 4.12, with the increase of the number of steps M, all curves tend to zero with different rates of convergence. Since the errors of $|S_{11}|$ achieve zero quickly, here, the analysis only focuses on the differences of $|S_{21}|$. The required minimum number of steps to limit the errors of $|S_{21}|$ in the range of ± 0.1 dB or ± 0.05 dB are listed in Table 4.2. According to the table, the needed quantities of steps for those approximation methods differ significantly. Furthermore, the equal sector method (Approach 3) with averaged stair-casing shows the best performance compared to the others. Since fewer steps mean faster speed, it is the recommended method to approximate cylindrical posts in rectangular waveguides.

The structure has been simulated with the FEM using Ansys HFSS, and the numerical results are shown in Fig. 4.13. The variables in the software, *maximum delta s*, *maximum number of passes* and *mesh operations* are set as 0.01, 20, and default respectively. In such

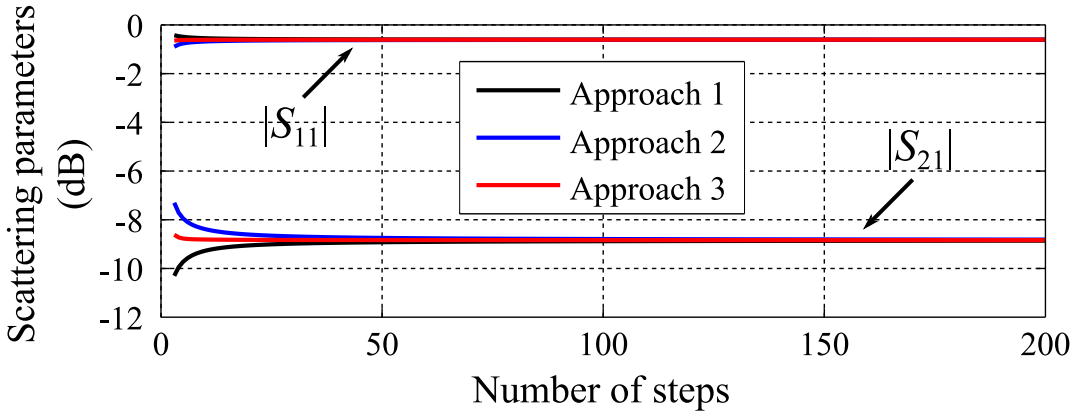

(a) Method A

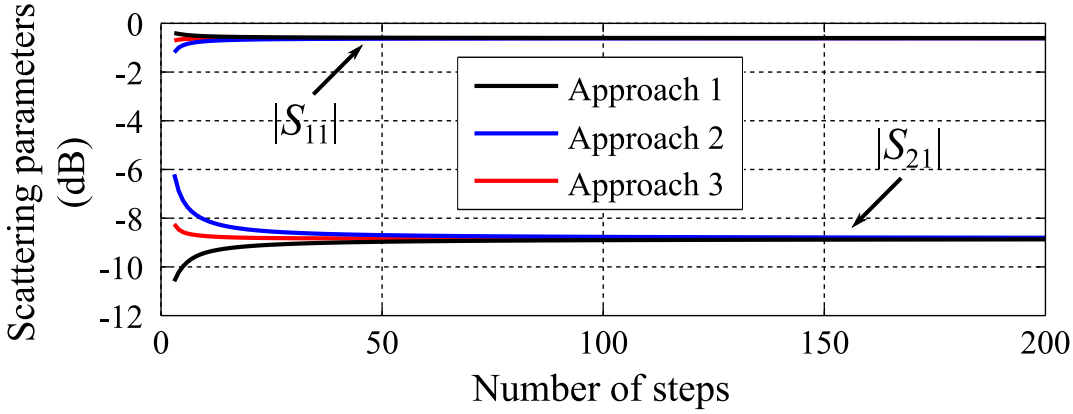

(b) Method B

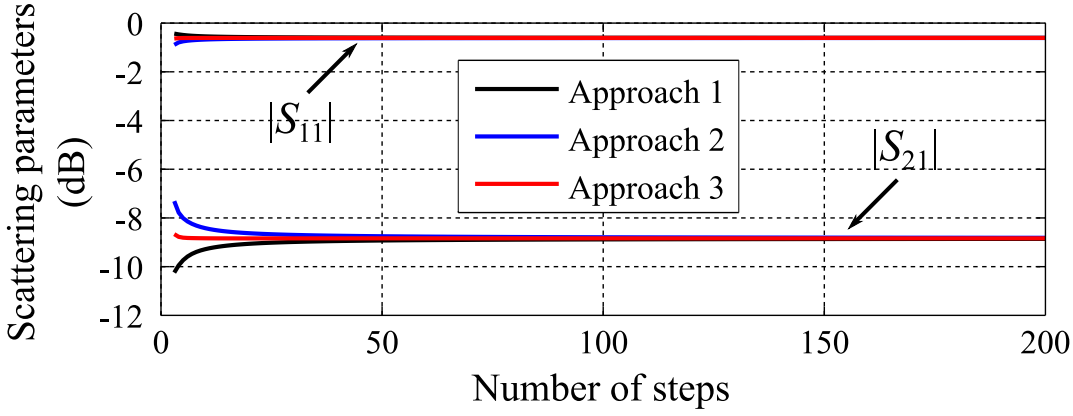

(c) Method C

Figure 4.11. Scattering parameter convergences: (a) equal width method, (b) arithmetic sequence thickness method and (c) equal sector method. These figures show that for all of the approximation methods, with the increase of the number of steps M, the values of $|S_{11}|$ and $|S_{21}|$ tend towards constants. Source: Self-created using Matlab.

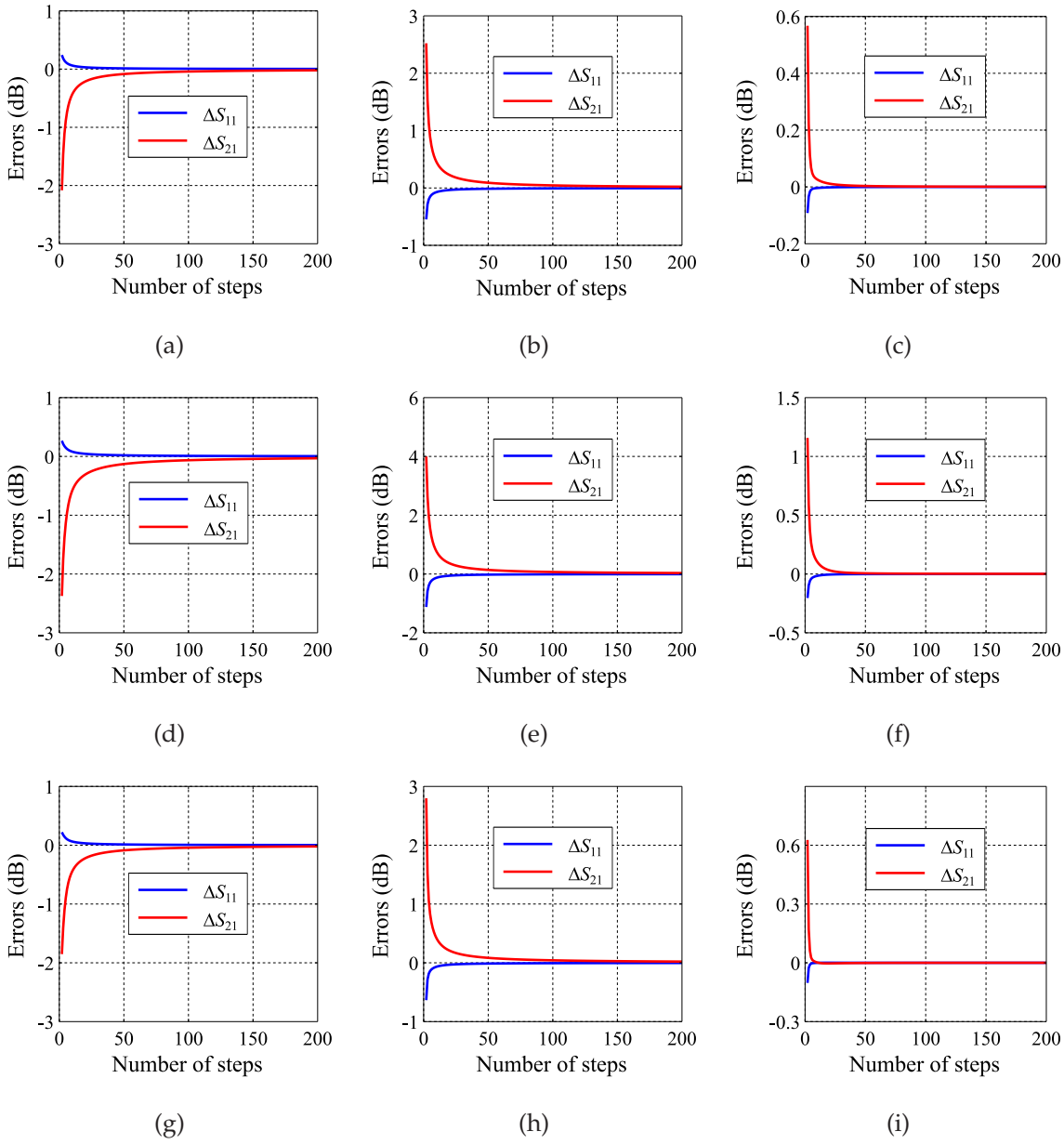

Figure 4.12. Difference between scattering parameters and accurate reference values: (a) equal width method (over), (b) equal width method (under), (c) equal width method (average), (d) arithmetic sequence thickness method (over), (e) arithmetic sequence thickness method (under), (f) arithmetic sequence thickness method (average), (g) equal sector method (over), (h) equal sector method (under), and (i) equal sector method (average). These figures show that for all of the approximation methods, with the increase of the number of steps M, the difference of the scattering parameters and the accurate values ΔS_{11}, ΔS_{21} tend towards zero. However, the rates of convergence for these approximation approaches are different, namely different approaches lead to different efficiencies. Source: Self-created using Matlab.

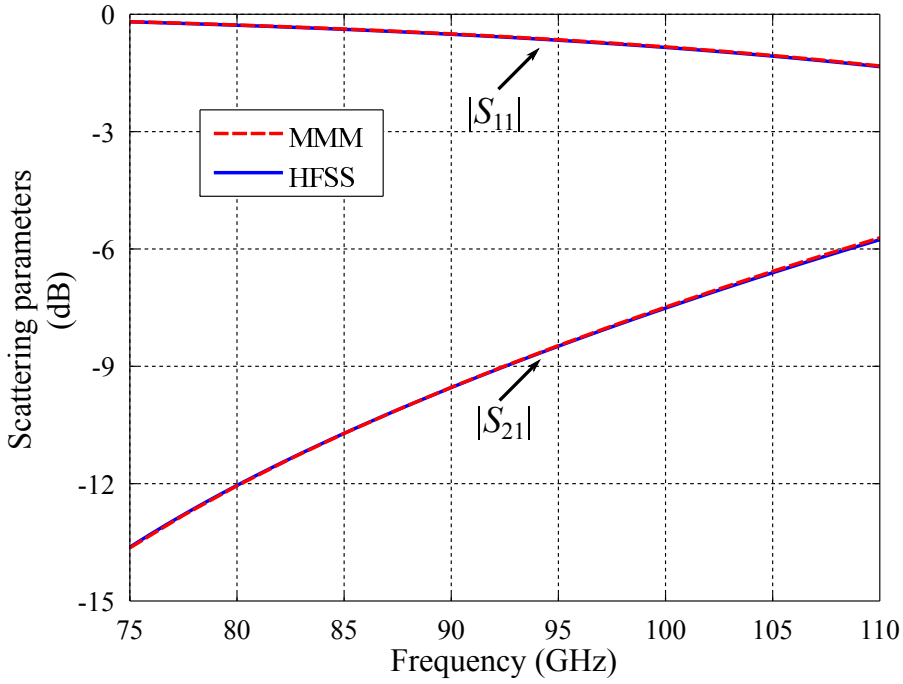

Figure 4.13. Comparison between the MMM and the FEM using Ansys HFSS. This figure shows that, for a rectangular waveguide structure in which posts are inserted, if the number of approximation steps is set to 3, the calculated mode-matching results based on equal sector method (average) have a good match with the simulation results of Ansys HFSS at 94 GHz. Source: Self-created using Ansys HFSS and Matlab.

setups, for a standard computer with a 3.40 GHz i7-2600 CPU and 14.0 GB RAM, it takes 8 seconds to simulate a frequency point (94 GHz).

To achieve the same precision as Ansys HFSS, based on the recommended approximation method, the required number of steps is only 3. As shown in Fig. 4.13, the calculated results have a good match with the simulation results of Ansys HFSS. In addition, with the MMM, it only takes 0.1 seconds to calculate at a frequency point (94 GHz) using the same computer. More detailed computation time *ti* and scattering parameters comparisons are listed in Table 4.3. It is noted that, Case (i) is for the above structure, while Case (ii) and Case (iii) are for the cases where the distance G is changed to 1 mm and the radii r are decreased to 0.15 mm respectively.

By decreasing the *maximum delta s* and increasing *maximum number of passes*, Ansys HFSS can obtain more accurate simulation results. However, more time is needed. Thus, to deal with this kind of problem, the MMM is significantly more efficient.

Table 4.2. Minimum number of steps M to limit the errors of $|S_{21}|$ in ± 0.1 dB or ± 0.05 dB (Units: dB). This table gives the number of steps M with which the difference between scattering parameters and accurate values can be restricted in ± 0.1 dB or ± 0.05 dB.

Method		M (± 0.1 dB)	M (± 0.05 dB)
A	Over	43	85
	Under	46	90
	Average	5	6
B	Over	66	129
	Under	70	136
	Average	11	16
C	Over	44	86
	Under	43	85
	Average	4	5

Table 4.3. Computation time and scattering parameters comparisons. This table compares the computation time and the scattering parameters at different frequency points using the MMM and the FEM (Ansys HFSS). Three structures are considered in this table.

CASE		HFSS			MMM		
		ti (s)	S_{11} (dB)	S_{21} (dB)	ti (s)	S_{11} (dB)	S_{21} (dB)
i	75 GHz	8	-0.1928	-13.6217	0.082	-0.1924	-13.6307
	94 GHz	8	-0.6314	-8.6868	0.104	-0.6348	-8.6648
	110 GHz	8	-1.3397	-5.7605	0.091	-1.3582	-5.7095
ii	75 GHz	8	-0.0007	-37.6927	0.125	-0.0007	-37.6821
	94 GHz	9	-0.0021	-33.0649	0.094	-0.0022	-33.0404
	110 GHz	9	-0.0040	-30.3187	0.108	-0.0041	-30.2780
iii	75 GHz	5	-1.0415	-6.7116	0.084	-1.0470	-6.6913
	94 GHz	5	-2.6845	-3.3625	0.094	-2.7016	-3.3426
	110 GHz	5	-4.4696	-1.9200	0.092	-4.5034	-1.9013

4.3 General Design for Band-Pass Post Filters in Rectangular Waveguides and Substrate-Integrated Waveguides

Microwave and millimetre-wave systems are widely used in many areas such as telecommunications, radar, remote sensing and clinical medicine. With the rapid development of these fields, the performance requirements of passive band-pass filters, as an essential part in these systems, have been steadily increasing to reject undesired frequency components and thus mitigate interferences between coexisting systems. Both waveguide and SIW filters are able to satisfy various high-performance requirements, with the waveguide filters offering the advantages of low loss and high power handling capabilities, while the SIW filters have the advantages of low cost and easy integration into planar circuit technology.

4.3.1 Structures of Band-Pass Post Filters

The MMM has been developed as a highly accurate and efficient technique to analyse discontinuities in waveguides. Therefore, it also has been extensively applied in designing band-pass waveguide filters realised through irises (Park *et al.* 2003, Zhang and Lu 2010, Subramanyam *et al.* 2014), E-plane metal inserts (Ofli *et al.* 2005, Zhao and Fan 2011, Zhang *et al.* 2010b), broadside oriented strip obstacles and multiple quadratic posts (Arndt *et al.* 1986). However, as mentioned, because of the limitations of micromachining processes, for these types of waveguide filter designs, the corners of the various discontinuity features, such as between waveguide walls and irises, or for the rectangular holes of an E-plane metal insert, are rounded rather than perfect right angles. The resulting differences between ideal designs and realisable geometries do influence the performance of the band-pass filters, especially when they operate at high frequencies (Bornemann 2001, Bornemann *et al.* 2005). Compared with the above discontinuities in waveguides, cylindrical posts placed in one cross-section of a rectangular waveguide or circular holes are easier to manufacture. Thus, posts are less prone to machining errors and are promising for realising band-pass waveguide filters at higher frequencies, e.g. in the millimetre-wave bands.

In order to minimise the dimensions of band-pass filters in rectangular waveguide technology, numerous band-pass SIW filters were developed (Qiu *et al.* 2008, Zou *et al.*

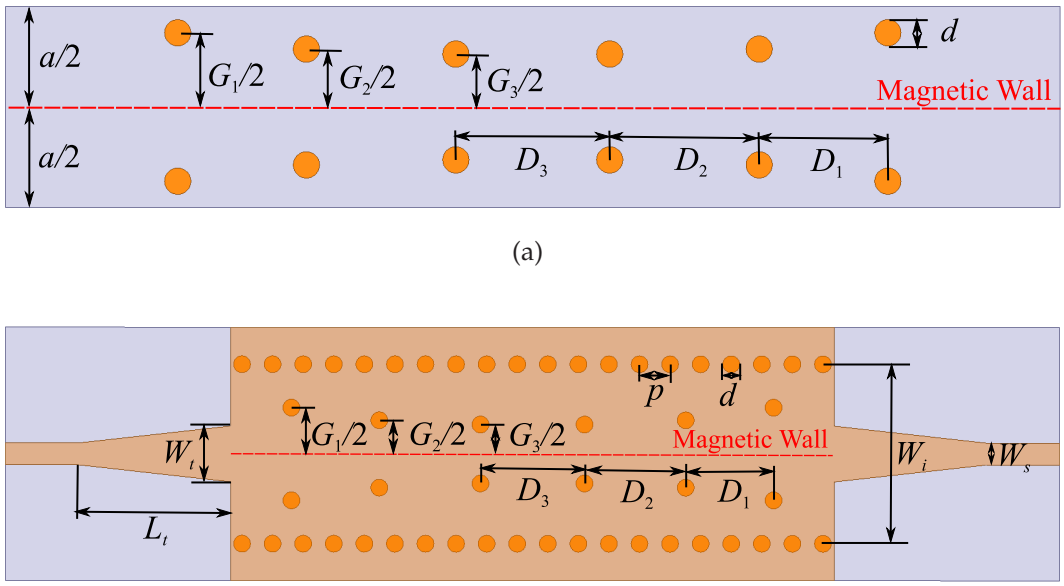

Figure 4.14. Realisations of 5-cavity band-pass filters: (a) post rectangular waveguide filter, (b) via SIW filter. These figures show the configurations of post filters realised in rectangular waveguide and SIW technology. It is noted that an SIW-to-microstrip transition is required in order to test or integrate the SIW filter with the other planar circuits. Source: Self-created using Ansys HFSS and Inkscape.

2011), in which rows of vias were used to approximate irises or E-plane inserts. In addition to increasing simulation time, these via rows may also introduce undesired effects on the performance of the band-pass filters because of the distances and displacements between adjacent vias. Therefore, to improve the analysis and reduce processing difficulties, it is advantageous to model the vias as posts instead of approximating them as irises or E-plane inserts.

In this perspective, the designs of band-pass post rectangular waveguide filters and band-pass via SIW filters are merged as one issue in this chapter. Meanwhile, the dimensions deciding the performance of band-pass filters are shown in Fig. 4.14. It is noted that, in order to test the band-pass SIW filter, a transition structure is required to match the SIW to a feeding 50 Ω microstrip line. The width W_t and length L_t of the taper can be designed with the MMM, where the taper is modelled as a sequence of microstrip step discontinuities (Bornemann *et al.* 2011). Alternatively, it can be designed by the method introduced in (Deslandes 2010, Miralles *et al.* 2011).

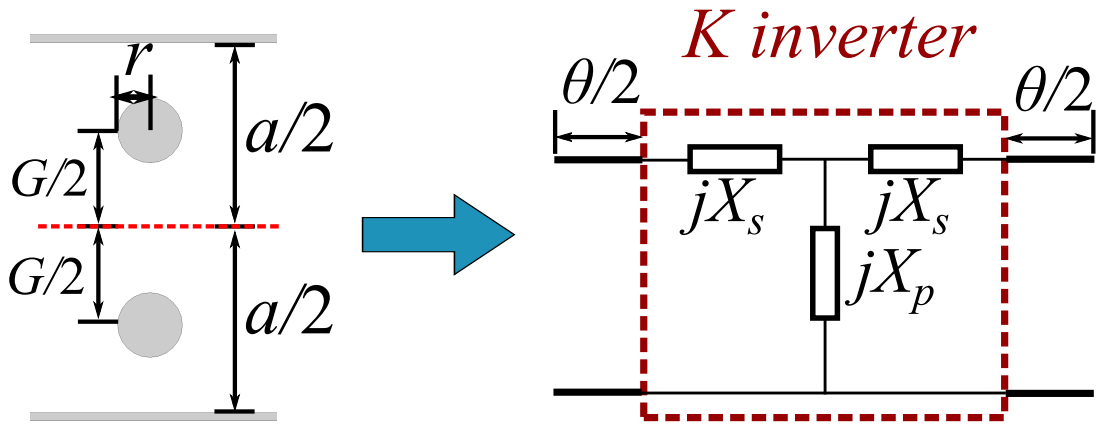

Figure 4.15. Posts placed in the cross-section of a rectangular waveguide and the equivalent circuit for the impedance inverter. The left figure shows the top view of a post pair in a rectangular waveguide. This structure can behave as an impedance inverter. Thus, the equivalent circuit for the impedance inverter is also provided in the right figure. Source: Self-created using Ansys HFSS and Inkscape.

4.3.2 K Inverter Values Analysis of Posts or Vias

According to the description in Section 4.3.1, the network for band-pass filters using impedance inverters presented in Chapter 3 also can be realised by placing post pairs in the cross-section of a rectangular waveguide, since post pairs can behave as K-inverters as shown in Fig. 4.15, while half wavelength waveguide cavities formed by post pairs can work as LC resonators.

The K factors of post pairs in rectangular waveguides depend on their dimensions, namely the radii r of the posts and distances $G/2$ to the magnetic wall. Therefore, to match K factors with theoretical values, it is possible to use the following three approaches: (a) fix the radii and adjust the distances, (b) fix the distances and adjust the radii, and (c) adjust both the radii and the distances.

From a simulation view, the third option should be discarded, since it contains twice the number of variables, which increases the complexity of the design. From the fabrication view, it is a better choice to adopt the first option, because it is more convenient to manufacture with the same posts, in particular for the fabrication of SIW filters using rivets with standard sizes. Therefore, Approach (a) is selected in the following analysis.

During the design and realisation of a band-pass filter based on post pairs with different distances, starting from a blind choice for the post radius may waste time and

lead to design failure. Thus, it is important to first ensure that, with the fixed radius, the K factors of the structures can yield all the required theoretical K values. Based on the proposed MMM for post pair configurations, the dependence of the K factors on the radii r and the distances $G/2$ are analysed in Fig. 4.16(a) for a standard X-band (extending from 8 GHz to from 12 GHz) WR-90 rectangular waveguide and in Fig. 4.16(b) for an SIW implemented in a Rogers 6002 substrate with a thickness of 0.762 mm and a relative permittivity of 2.94.

In general, the K factors for a pair of posts in a rectangular waveguide and a pair of vias in an SIW have similar variation trends. For a fixed radius, when progressively increasing the distance $G/2$, the K values drop first and then increase gradually. Besides, lower K values are obtained for thicker posts, when they are moved from the centre of the waveguide (magnetic wall) to the electrical side wall. From the computed curves as shown in Fig. 4.16, a reasonable post size can be selected conveniently. For example, to design a 5-cavity Chebyshev band-pass post rectangular waveguide filter with a centre frequency of 10.5 GHz and a fractional bandwidth of 9.52% (passband extending from 10 GHz to 11 GHz), the theoretical K values calculated through equations presented in Chapter 3 are 0.5702, 0.2475, 0.1714, 0.1714, 0.2475, and 0.5702, that is, between 0.1714 and 0.5702. According to Fig. 4.16(a), obviously, posts with a radius of 1.5 mm are suitable to implement the design.

4.3.3 Design Examples

In this section, the presented technique is applied to design a 5-cavity band-pass post rectangular waveguide filter and a 5-cavity band-pass via SIW filter shown in Fig. 4.17. Both symmetric Chebyshev filters are required to have a centre frequency at 10.5 GHz and a fractional band-width of 9.52%.

By utilising posts with a radius of 1.5 mm and vias with a radius of 0.5 mm, the dimensions of each filter can be obtained within 1 second by a standard computer with a 3.40 GHz i7-2600 CPU and 14.0 GB RAM, if 25 modes and 10-step approximation of the post are adopted. The calculated dimensions can be further optimised through space mapping technique or comparing the extracted coupling matrix with the theoretical one in order to have closer frequency responses to ideal ones (Cameron *et al.* 2007). However, since the calculated values already give satisfactory results, no optimisation

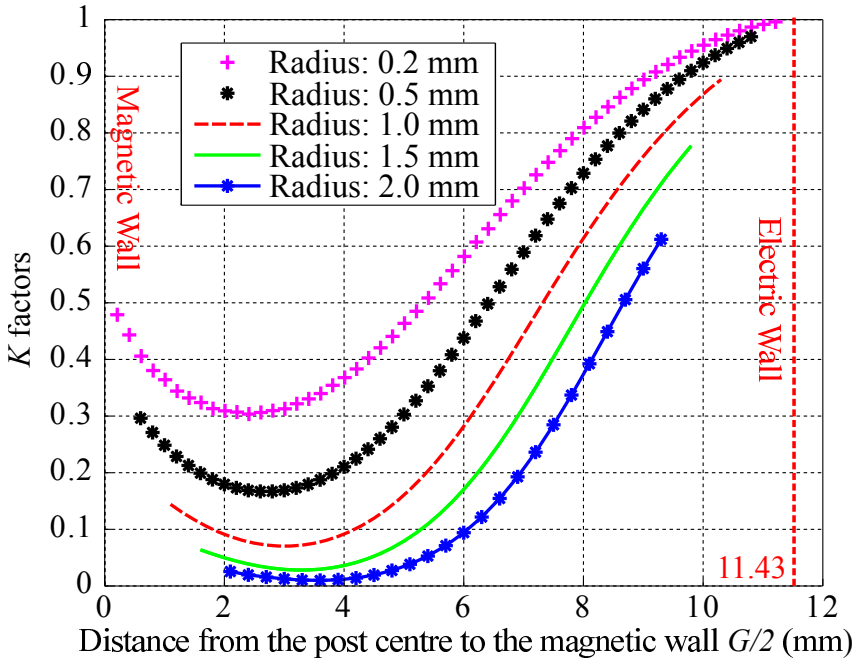

(a)

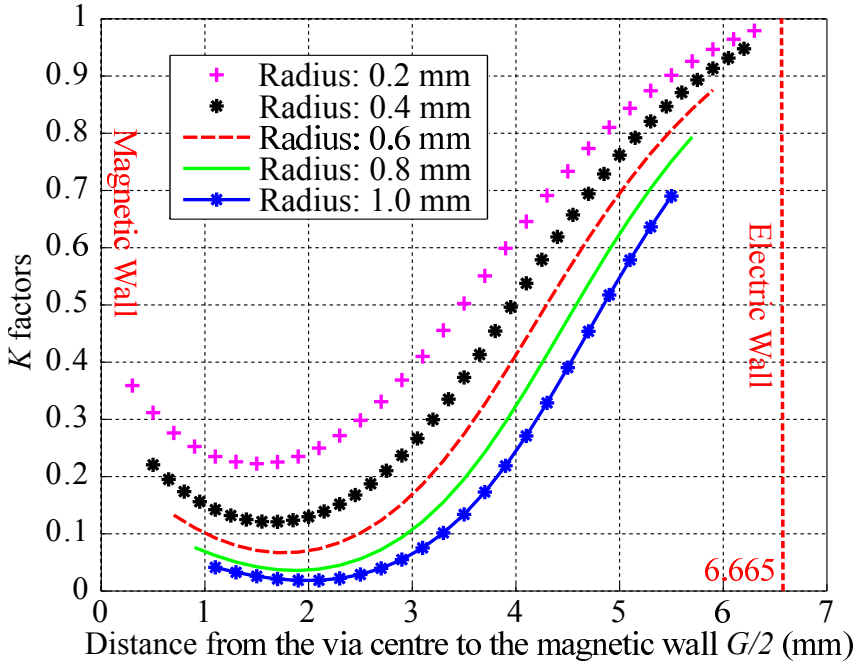

(b)

Figure 4.16. Relationships of K factors, radii r and distances $G/2$ to the magnetic wall. These figures show relationships of K factors, radii and distances to the magnetic wall, where (a) is based on a standard X-band WR-90 rectangular waveguide whose width $a = 22.86\,\text{mm}$ and height $b = 10.16\,\text{mm}$, and (b) is based on an SIW with effective width $W_e = 13.33\,\text{mm}$ and height $b = 0.762\,\text{mm}$. Source: Self-created using Matlab.

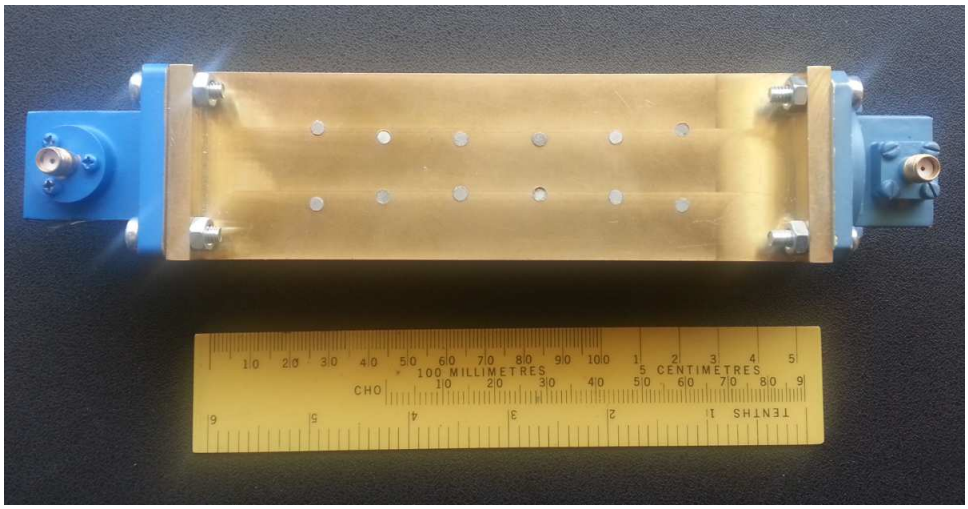

(a)

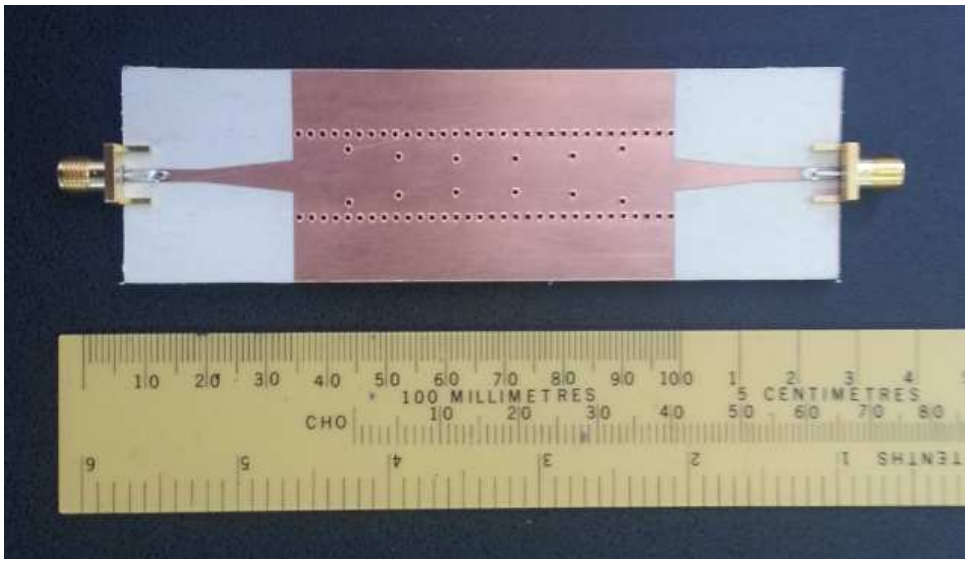

(b)

Figure 4.17. Fabricated 5-cavity Chebyshev band-pass post filters. These figures show two fabricated 5-cavity Chebyshev band-pass post filters, where (a) is based on rectangular waveguide technology, while (b) is based on SIW technology. Source: Self-photographed.

is applied in this chapter. The obtained values for the geometry variables of Fig. 4.14(a) and (b) are listed in Tables 4.4 and 4.5 respectively.

The calculated results for both filters are first verified by the finite-element simulations performed with Ansys HFSS as shown in Fig. 4.18(a) and 4.18(b). Obviously, the calculated mode-matching results have a good match with the simulation results of the

Table 4.4. Dimensions of a 5^{th}-order Chebyshev band-pass post filter in rectangular waveguide technology (Units: mm). The table gives the dimensions, including the width a and height b of the rectangular waveguide, the post diameter d, the gaps G between posts and the lengths D of the resonant cavities, used to realise a 5^{th}-order Chebyshev band-pass post filter whose structure is illustrated in Fig. 4.14(a).

G_1, G_6	G_2, G_5	G_3, G_4	D_1, D_5	D_2, D_4	D_3
16.84	13.14	12.01	14.64	17.00	17.50

a	b	d
22.86	10.16	3.00

full-wave finite-element simulation. It is noted that, both the mode-matching calculation and the finite-element simulation do not take losses into account.

A second validation of the method is provided with experimental results. For the post rectangular waveguide filter, the measured passband agrees well with the calculation results. The measured insertion loss at 10.5 GHz is about 0.87 dB including losses in the two coaxial-to-waveguide adapters, while the return loss in the passband is better than 18 dB. A test of the two adapters in back-to-back configuration shows that in passband the $|S_{21}|$ is around -0.28 dB and the $|S_{11}|$ is below -18 dB, hence, the higher $|S_{11}|$ parameter can be explained through the non-ideal transitions. Besides, unaccounted losses are also caused by the visible surface roughness of the inner waveguide and posts. For the via SIW filter, the testing results also match well with the calculation results. The measured insertion loss at 10.5 GHz is about 1.51 dB including losses in the two SMA connectors, while the return loss in the passband is better than 15 dB. Clearly, compared with the post rectangular waveguide filter, the SIW filter has relatively high insertion losses since more losses are introduced by the dielectric, the transition structures and the microstrip lines. However, the SIW filter is much lighter and easier to integrate into other planar circuits from a practical perspective.

To sum up, the results of both validations for the two filters agree well with the calculation results. Thus, the efficiency and the accuracy of the design approach are successfully validated.

Table 4.5. Dimensions of a 5^{th}-order Chebyshev band-pass via filter in SIW technology (Units: mm). The table gives the dimensions, including the length L_t and the width W_t of the taper, the via diameter d, the gaps G between posts and the lengths D of the resonant cavities and so on, used to realise a 5^{th}-order Chebyshev band-pass post filter whose structure is illustrated in Fig. 4.14(b).

G_1, G_6	G_2, G_5	G_3, G_4	D_1, D_5	D_2, D_4	D_3
8.78	6.39	5.58	8.33	9.60	9.87

W_i	W_t	L_t	W_s	d	p	b
13.91	5.29	14.12	2.08	1.00	1.80	0.762

4.4 Tolerance Analysis

The performance of a band-pass post rectangular waveguide filter or a band-pass via SIW filter is affected by manufacture-induced errors on the width a of the waveguide or the equivalent width W_e of the SIW, on the radii r of the posts, on the gaps $G/2$ from the post centres to the magnetic wall, on the lengths D of the resonant cavities as well as by the relative position of the posts. For the SIW filter, the equivalent width W_e also can be influenced by errors on the radius r of the via, on the space W_i between the two via rows, and on the pitch p between the two adjacent vias. Owing to the larger number of arbitrary combinations and for the sake of brevity, only the influence of the major sources of errors is described here, that is, waveguide widths, post radii, gap dimensions, and the cavity lengths.

As shown in Fig. 4.19(a) and (e), by increasing the width or equivalent width with an error from -0.5 mm to +0.5 mm, the centre frequencies for both filters shift to lower frequencies. However, the variations of the 3 dB bandwidths change in different ways, that is, the 3 dB bandwidth of the post filter turns narrower, while that of the SIW filter becomes wider. The offset and variation of the centre frequency and the 3 dB bandwidth caused by the other manufacture tolerances have very similar trends in the post filter and SIW filter. Therefore, the comments in the following focus on the band-pass via SIW filter (Fig. 4.19(f), (g) and (h)).

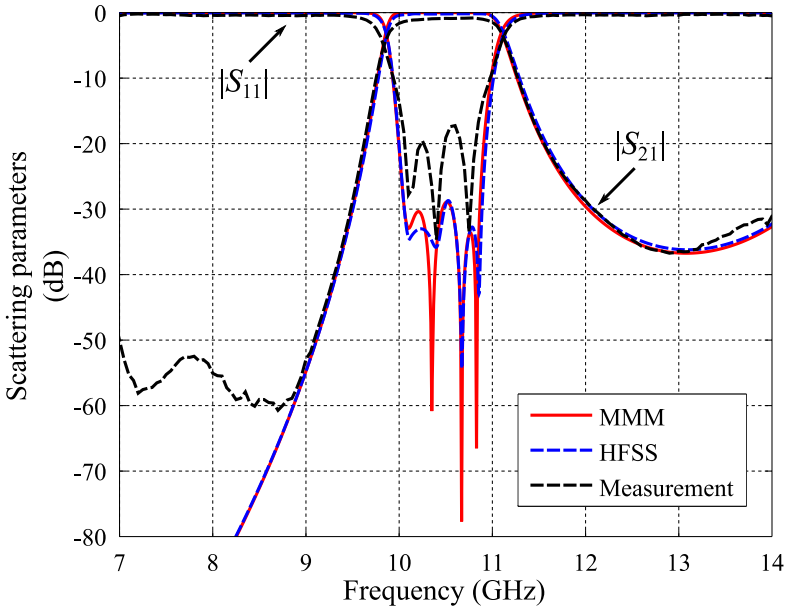

(a) Band-pass post rectangular waveguide filter

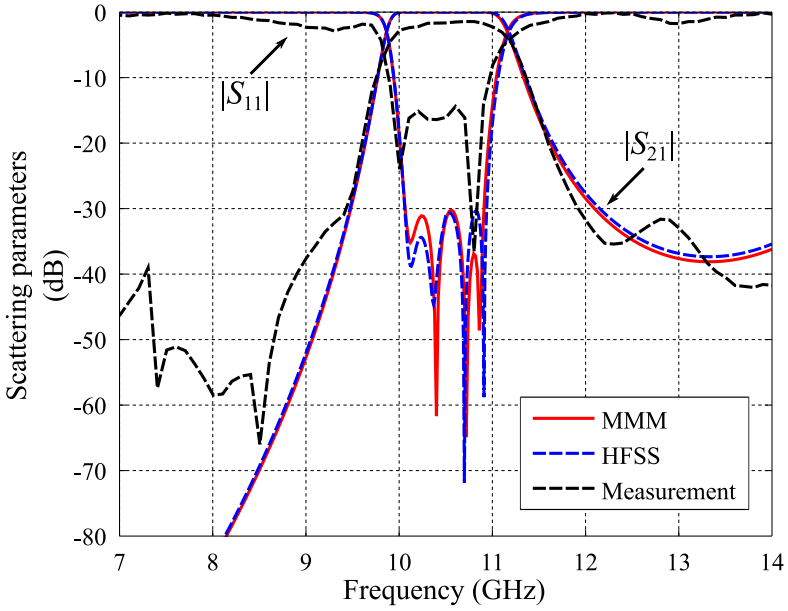

(b) Band-pass via SIW filter

Figure 4.18. Comparison of scattering parameters obtained using the MMM, the FEM (Ansys HFSS), and measurements. These figures compare the scattering parameters of the two band-pass post filters, obtained using the MMM, the FEM (Ansys HFSS), and measurements. It is noted that both the mode-matching calculation and the finite-element simulation do not take losses into account. Source: Self-created using Ansys HFSS and Matlab.

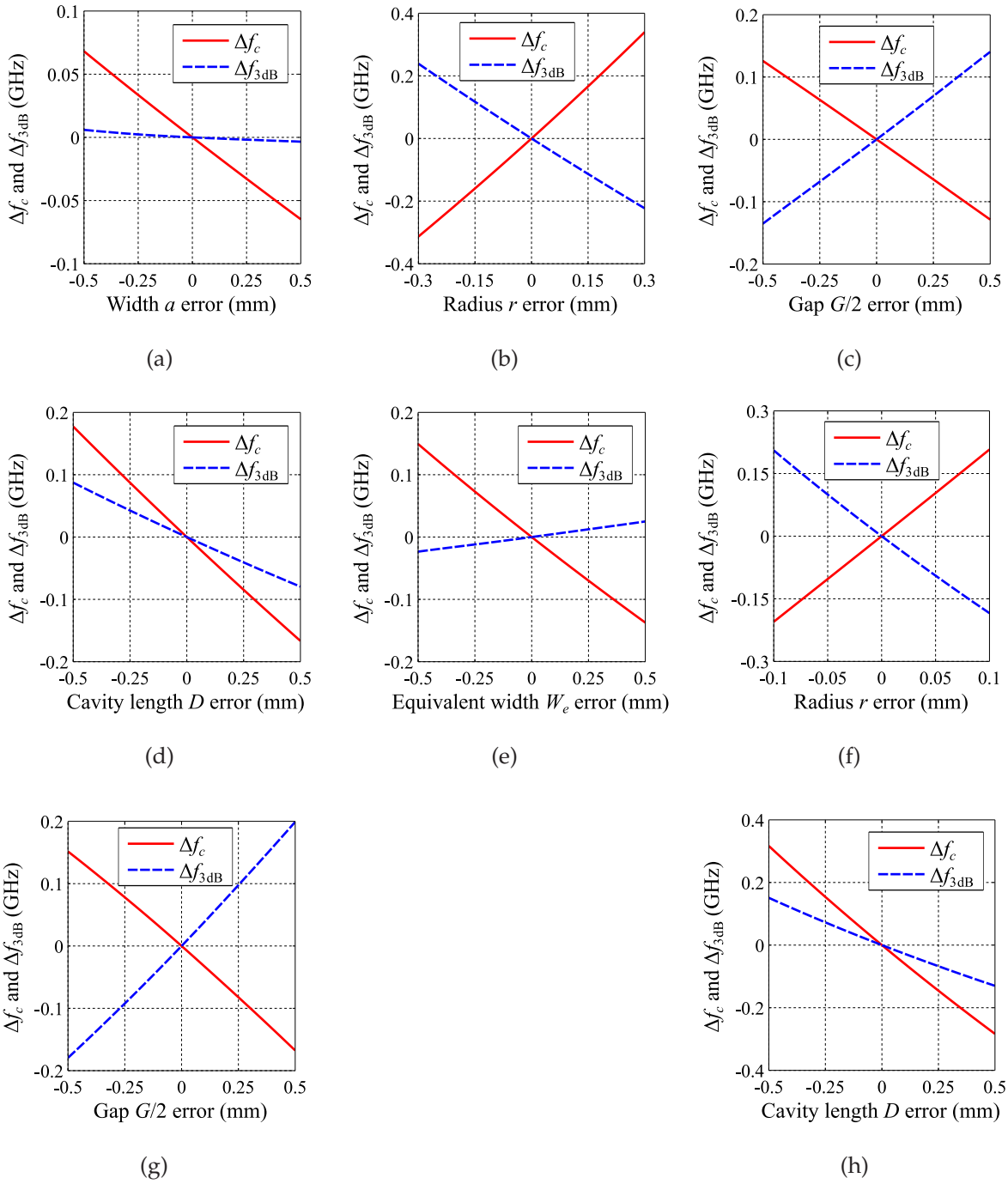

Figure 4.19. Offset Δf_c of centre frequency and variation $\Delta f_{3\,\mathrm{dB}}$ of 3 dB bandwidth caused by machining errors. These figures show the influence of machining errors on the performance of the two filters, where (a), (b), (c), and (d) show the influence introduced by width errors, radius errors, gap errors, and distance errors in the band-pass post rectangular waveguide filter, while (e), (f), (g), and (h) show the influence caused by equivalent width errors, radius errors, gap errors, and distance errors in the band-pass via SIW filter. Source: Self-created using Matlab.

Fig. 4.19(f) shows that by increasing all radii with an error between -0.1 mm and 0.1 mm, the centre frequency of the band-pass filter shifts to higher frequencies, while the 3 dB bandwidth is becoming narrower. In contrast, Fig. 4.19(g) shows that by increasing all gaps with errors between -0.5 mm and 0.5 mm, the centre frequency moves to lower frequencies, while the 3 dB bandwidth becomes wider. Other than in the previous two cases, the distance errors lead to changes of the centre frequency and bandwidth in the same direction as shown in Fig. 4.19(h). By increasing the distance with an error from -0.5 mm to +0.5 mm, both the centre frequency and the 3 dB bandwidth decrease. In addition, for the SIW filter, the offset and variation also can be caused by the error of the relative permittivity, which is specified by the manufacturer as ± 0.04 (Rogers Corporation 2015). However, tests of this material parameter tolerance indicate that the impact of this error can be ignored.

4.5 Insertion Losses Analysis

As demonstrated in Section 4.3, a band-pass post filters in rectangular waveguide or SIW can be designed with the MMM, which provides fast and reliable results. The method is based on lossless simulations, however insertion loss is a crucial specification to judge the quality of a band-pass post filter. Thus, it is necessary to explore the losses in the band-pass filter independently. In addition, since the designs of band-pass post rectangular waveguide filters and band-pass via SIW filters are able to be combined into one issue and the insertion losses in band-pass post rectangular waveguide filters are much smaller than those in band-pass via SIW filters, only the insertion losses in band-pass via SIW filters are analysed.

To investigate the losses in the SIW filters, firstly, based on the MMM, two sets of Chebyshev band-pass via SIW filters have been designed in Rogers RT/duroid 6002 (with relative permittivity $\varepsilon_r = 2.94$ and loss tangent $\tan\delta = 0.0012$) and RT/duroid 6006 (with $\varepsilon_r = 6.15$ and $\tan\delta = 0.0027$). The thickness of both selected substrates is the same, namely $b = 0.762$ mm. All filters are designed for a centre frequency of 10.5 GHz and a bandwidth extending from 10 GHz to 11 GHz. In the present investigation, band-pass filters in each set are realised as 3^{rd}-, 5^{th}- and 7^{th}-order structures. As mentioned, the SIW-to-microstrip transitions are also designed according to the method introduced in (Deslandes 2010). The dimensions for the six band-pass via SIW filters are given in Table 4.6 and Table 4.7.

Table 4.6. Filters designed with RT/duroid 6002 (Units: mm). The table gives the dimensions, including the length L_t and the width W_t of the transition taper, the via diameter d, the gaps G between posts, and the lengths D of the resonant cavities and similar, used to realise 3^{rd}-, 5^{th}-, 7^{th}-order Chebyshev band-pass via SIW filters.

N	G_1, G_{N+1}	G_2, G_N	G_3, G_{N-1}	G_4, G_{N-2}	D_1, D_N	D_2, D_{N-1}	D_3, D_{N-2}
3	9.18	6.96	∅	∅	7.95	8.87	∅
5	8.78	6.39	5.58	∅	8.33	9.60	9.87
7	8.68	6.26	5.39	5.21	8.41	9.70	10.01

N	D_4, D_{N-3}	b	d	p	W_i	W_s	W_t	L_t
3	∅	0.762	1.00	1.80	13.91	2.08	5.29	14.12
5	∅	0.762	1.00	1.80	13.91	2.08	5.29	14.12
7	10.06	0.762	1.00	1.80	13.91	2.08	5.29	14.12

To analyse the losses in the SIW filters, it is necessary to analyse the designs using a different simulation method which includes realistic losses. Thus, secondly, the finite-element simulations using Ansys HFSS are adopted to complete the analysis. Considering first the top and bottom cladding and vias as copper, the simulated results obtained for the via filters including losses in the transition structures and the SMA connectors are presented in Fig. 4.20. As shown in the figure, the simulated return coefficients $|S_{11}|$ in the specified passband (10 GHz to 11 GHz) are all below -20 dB. The transmission coefficients $|S_{21}|$ at the centre frequency (10.5 GHz) of the filters realised in RT/duroid 6002 lead to insertion losses of 1.09 dB, 1.48 dB, and 1.89 dB, while that of the filters realised in RT/duroid 6006 lead to insertion losses of 1.43 dB, 2.01 dB, and 2.67 dB respectively.

To ensure that the simulations are realistic, the 5^{th}-order filter on copper-clad RT/-duroid 6002 substrate has been fabricated and measured. As shown in Fig. 4.21, the testing results have a good match with the simulation results. The measured reflection coefficient in the passband is below -15 dB, while the measured insertion loss at 10.5 GHz is about 1.51 dB which is close to the simulated insertion loss 1.48 dB. Thus,

Table 4.7. Filters designed with RT/duroid 6006 (Units: mm). The table gives the dimensions, including the length L_t and the width W_t of the transition taper, the via diameter d, the gaps G between posts, and the lengths D of the resonant cavities and similar, used to realise 3^{rd}-, 5^{th}-, 7^{th}-order Chebyshev band-pass via SIW filters.

N	G_1, G_{N+1}	G_2, G_N	G_3, G_{N-1}	G_4, G_{N-2}	D_1, D_N	D_2, D_{N-1}	D_3, D_{N-2}
3	6.80	6.80	∅	∅	5.57	6.23	∅
5	6.53	4.98	4.50	∅	5.84	6.76	6.96
7	6.46	4.90	4.40	4.30	5.90	6.83	7.06

N	D_4, D_{N-3}	b	d	p	W_i	W_s	W_t	L_t
3	∅	0.762	1.00	1.80	9.80	1.15	2.97	5.26
5	∅	0.762	1.00	1.80	9.80	1.15	2.97	5.26
7	7.10	0.762	1.00	1.80	9.8	1.15	2.97	5.26

the analysis based on the simulation results can be considered as accurate description of the filters including losses.

For a Chebyshev band-pass via SIW filter as shown in Fig. 4.22, the losses exist in the SMA connectors, SIW-to-microstrip transitions, and the main body of the filter. Since the transitions can be achieved through various structures with different sizes (Nam *et al.* 2005, Ding and Wu 2007, Caballero *et al.* 2013), they are dependent on their specific realisation and should not be considered in the filter analysis. Thus, the following analysis only focuses on the insertion losses at the centre frequency (10.5 GHz) in the main body of the filter.

To start the analysis, it is noted that the filter designs provided previously satisfy the vias' geometry conditions elaborated in (Deslandes and Wu 2002, Deslandes and Wu 2006), such that the leakage loss is negligible: the via diameter d is smaller than one fifth of the guide wavelength and the interval p is less than or equal to twice the via diameter. Therefore, the insertion losses in the main body of the filter consist of three components: (i) ohmic losses in the claddings of the laminate, (ii) ohmic losses

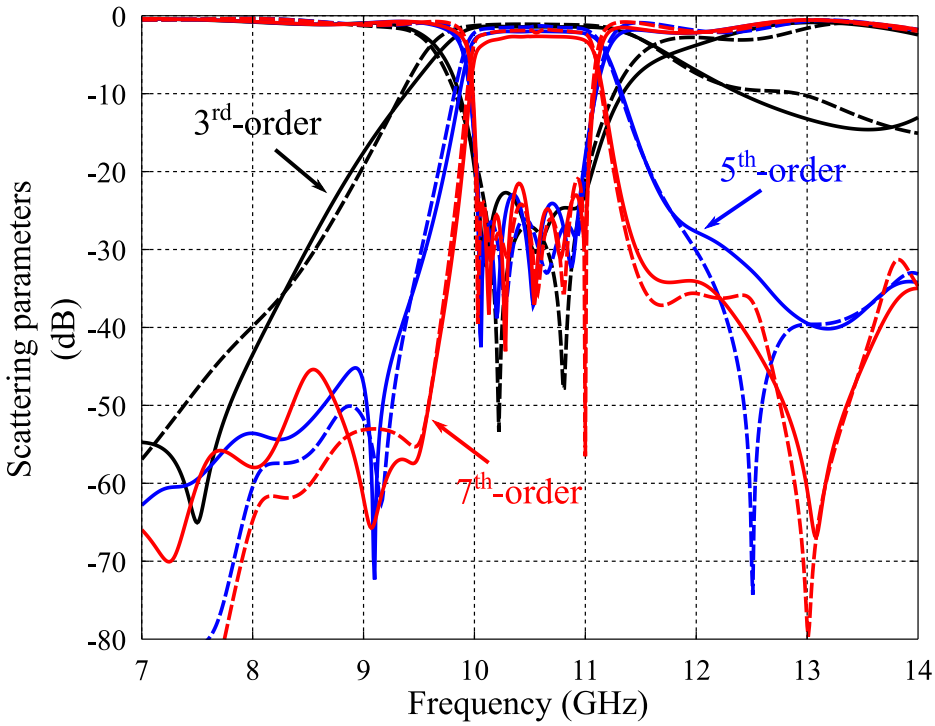

Figure 4.20. Comparison of scattering parameters between the simulation results for two sets of band-pass SIW filters. This figure compares scattering parameters between the simulation results for two sets of band-pass SIW filters of various orders realised in RT/duroid 6002 (dashed lines) and RT/duroid 6006 (solid lines). Source: Self-created using Ansys HFSS and Matlab.

in the metallic vias, and (iii) dielectric losses in the substrate. By assigning one of these components to lossy material in simulations, and setting the other two to lossless materials, the contributions to insertion loss at the centre frequency for the two sets of band-pass filters can be individually attributed to different lossy components. The simulated results for the filters realised in RT/duroid 6002 and RT/duroid 6006 are listed in Tables 4.8 and 4.9 respectively. It is noted that the percentages listed in the tables are based on the loss contributions expressed in dB. As mentioned, since the two types of laminates are available with a thick metal lower side cladding, that is, brass, aluminium, and copper, and a thin copper cladding on top, while the vias also can be manufactured with these materials, the insertion losses have been analysed by setting the top cladding as copper, and the bottom cladding and the vias as brass, aluminium, and copper respectively.

The results from the Tables 4.8 and 4.9 are first considered from the point of view of ohmic losses. As observed from the tables, a higher conductivity can result in markedly

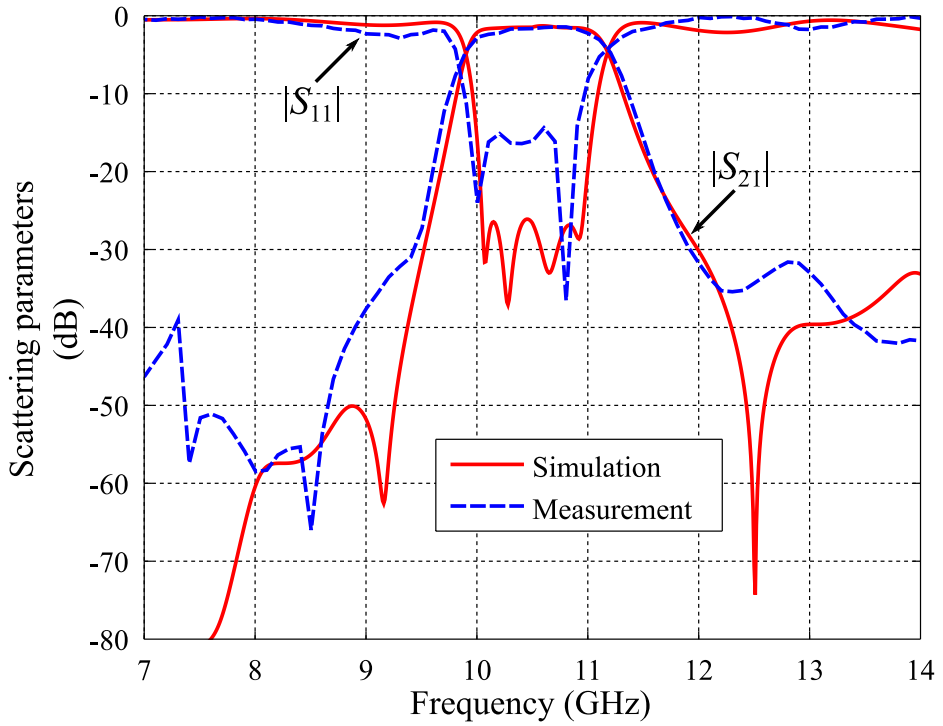

Figure 4.21. Comparison of scattering parameters obtained using the FEM (Ansys HFSS) and measurements. This figure compares the scattering parameters between the simulation results and measurements of a band-pass SIW filters. This band-pass SIW filter is fabricated with RT/duroid 6002 substrate, whose top and bottom metal is copper. Source: Self-created using Ansys HFSS and Matlab.

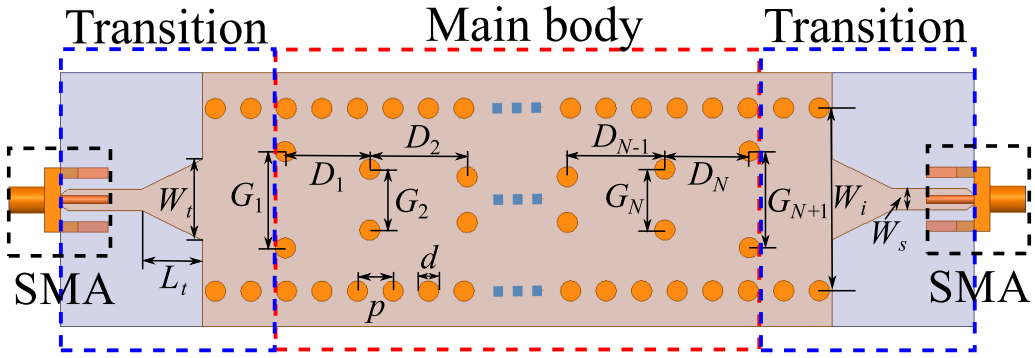

Figure 4.22. Generic structure of an N^{th}-order Chebyshev band-pass post SIW filter. This figure shows the generic structure of an N^{th}-order Chebyshev band-pass post SIW filter. This filter is divided into three components, including SMA connectors, SIW-to-microstrip transitions, and the main body of the filter. Source: Self-created using Ansys HFSS and Inkscape.

Table 4.8. Insertion losses at 10.5 GHz introduced by different components of the N^{th}-order filters realised in RT/duroid 6002. The table gives the insertion losses at 10.5 GHz introduced by different components of the N^{th}-order filters, including ohmic losses in the claddings of the laminate, ohmic losses in the metallic vias, and dielectric losses in the substrate.

6002	N	Cladding		Vias		Dielectric		Sum
		S_{21} (dB)	%	S_{21} (dB)	%	S_{21} (dB)	%	S_{21} (dB)
Brass	3	0.139	44.8	0.042	13.5	0.129	41.7	0.310
	5	0.341	44.9	0.103	13.6	0.316	41.5	0.760
	7	0.557	45.1	0.162	13.1	0.516	41.8	1.235
Aluminium	3	0.105	40.2	0.027	10.3	0.129	49.5	0.261
	5	0.258	40.3	0.066	10.3	0.316	49.4	0.640
	7	0.420	40.5	0.102	9.8	0.516	49.7	1.038
Copper	3	0.095	38.6	0.022	8.9	0.129	52.5	0.246
	5	0.232	38.5	0.055	9.1	0.316	52.4	0.603
	7	0.376	38.6	0.083	8.5	0.516	52.9	0.975

lower insertion losses. For example, for a 7^{th}-order band-pass filter realised in RT/-duroid 6002, when the material of the bottom cladding and vias is changed from brass to copper, the insertion loss decreases from 1.24 dB to 0.97 dB. Distinguishing the two ohmic loss contributions, it is observed that the losses introduced by the vias are relatively small, regardless of the kind of metal used. Furthermore, for a given metal used for the bottom cladding and vias, the percentage of loss contributions remains nearly unchanged with increasing filter order.

Further investigations have been done in order to obtain a more detailed relationship between the insertion loss and the conductivity. This is achieved by fixing the conductivity of the top cladding to 5.8×10^7 S/m (copper) and the substrate loss tangent to 0.0012, and varying the conductivity of the bottom claddings and vias from

Table 4.9. Insertion losses at 10.5 GHz introduced by different components of the N^{th}-order filters realised in RT/duroid 6006. The table gives the insertion losses at 10.5 GHz introduced by different components of the N^{th}-order filters, including ohmic losses in the claddings of the laminate, ohmic losses in the metallic vias, and dielectric losses in the substrate.

6006	N	Cladding		Vias		Dielectric		Sum
		S_{21} (dB)	%	S_{21} (dB)	%	S_{21} (dB)	%	S_{21} (dB)
Brass	3	0.142	28.7	0.057	11.5	0.296	59.8	0.495
	5	0.345	28.8	0.135	11.3	0.718	59.9	1.198
	7	0.561	28.8	0.215	11.0	1.172	60.2	1.948
Aluminium	3	0.108	24.5	0.036	8.2	0.296	67.3	0.440
	5	0.262	24.6	0.087	8.2	0.718	67.2	1.067
	7	0.423	24.4	0.136	7.9	1.172	67.7	1.731
Aluminium	3	0.097	22.9	0.030	7.1	0.296	70.0	0.423
	5	0.235	22.9	0.071	6.9	0.718	70.2	1.024
	7	0.379	22.8	0.110	6.6	1.172	70.6	1.661

1.5×10^7 S/m (brass) to 5.8×10^7 S/m (copper). As shown in Fig. 4.23(a), the dependence of the insertion loss (expressed in dB) on conductivity for each filter at 10.5 GHz indicates the expected decrease, but with a gradually declining rate of descent. The decrease is more marked for the filters with higher orders, that is, larger size.

Considering now the effect of dielectric losses, the top and bottom cladding and the vias are set as copper, and the loss tangent is swept from 0.0012 to 0.0027. The relationship between the insertion loss at 10.5 GHz for each filter and the variation of the loss tangent is obtained through simulations as shown in Fig. 4.23(b). It is observed that with the increase of the loss tangent, the insertion loss (expressed in dB) grows linearly, and the rate of increase is larger for a filter with higher orders.

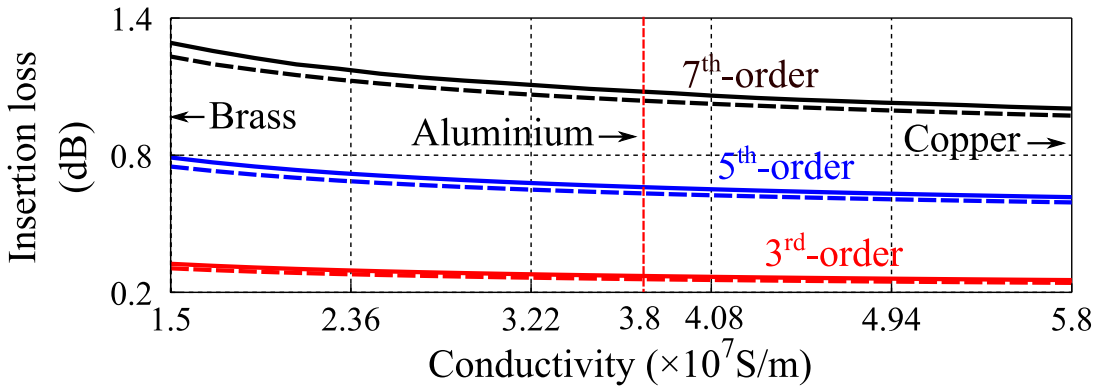

(a)

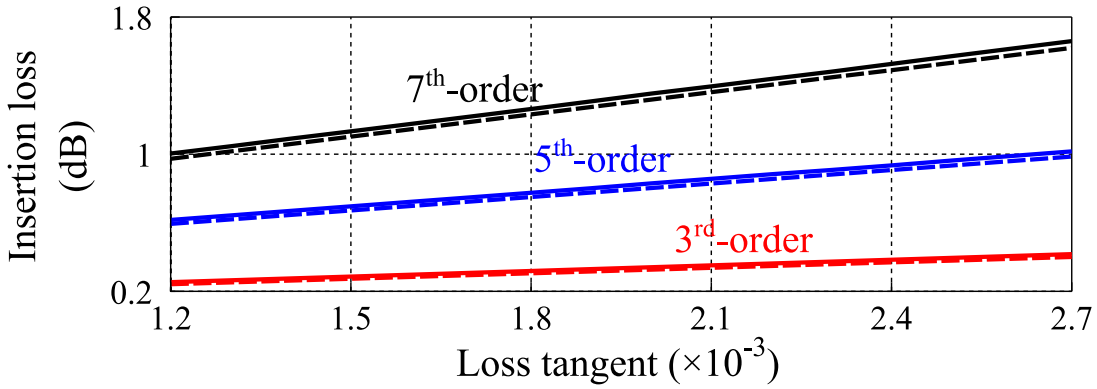

(b)

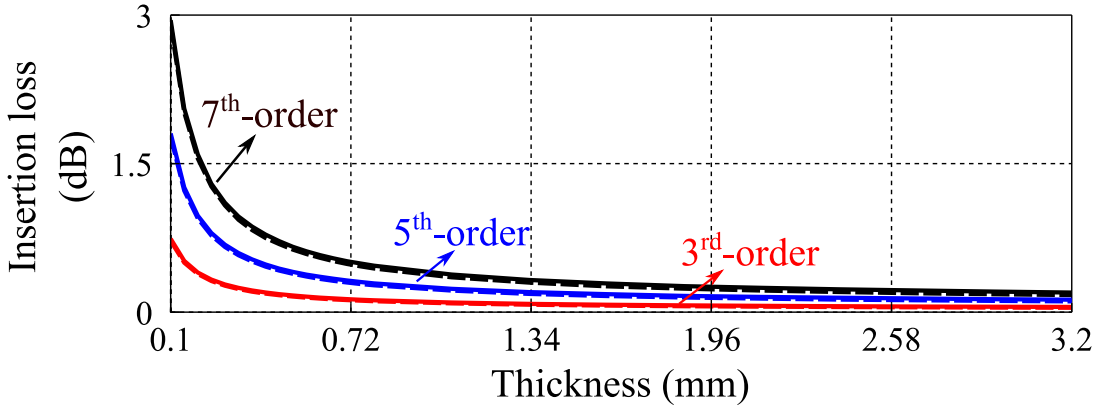

(c)

Figure 4.23. Influence caused by the metal conductivity, the dielectric loss tangent, and the thickness of the substrate on the insertion losses of band-pass SIW filters realised in RT/duroid 6002 (dashed lines) and RT/duroid 6006 (solid lines) at 10.5 GHz. These figures show relationships between the insertion losses at 10.5 GHz and (a) the metal conductivity, (b) the dielectric loss tangent, and (c) the thickness of the substrate. Source: Self-created using Ansys HFSS and Matlab.

Moreover, the influence of the substrate thickness on the insertion loss has also been considered. The performed simulations (not included here for brevity) show that, with different thicknesses, the dielectric loss remains almost the same, while the ohmic loss is affected significantly. Thus, the investigation is completed through fixing the conductivity of the top and bottom cladding and the vias to 5.8×10^7 S/m (copper), setting the dielectric as lossless material and varying the thickness from 0.1 mm to 3.2 mm. As shown in Fig. 4.23(c), with the increase of the thickness, the insertion loss drops quickly first and then gradually stabilises. The rate of descent is particularly remarkable for filters with higher orders.

Obviously, for filters realised on a given substrate, smaller dimensions achieved by lower-order structures translate into smaller insertion loss, but at the cost of lower out-of-band rejection performance. In contrast, it appears that reducing the dimension of the filters by adopting a substrate with larger relative permittivity cannot decrease the insertion loss. In addition, increasing the thickness of the substrate is another efficient way to reduce the insertion loss in the main body of the filter. However, since a thicker substrate leads to a larger radiation loss for the SIW-to-microstrip transition, a trade-off must be found for optimal design.

4.6 Chapter Summary

In this chapter, the principle of the mode-matching method to analyse the N-furcation rectangular waveguide structure has been explained first. Based on this framework, nine approaches to approximate posts placed in the cross-section of a rectangular waveguide have then been introduced. Furthermore, by comparing the difference of the scattering parameters from accurate reference values of the post structure, and the rate of convergence for each method, the most efficient approximation method has been recommended.

Combining the principle of the mode-matching method to analyse the characteristics of posts placed in rectangular waveguide and the band-pass filter theory presented in Chapter 3, a general design method for band-pass post filters in rectangular waveguide and substrate-integrated waveguide has been introduced. The approach has been verified via the full-wave finite-element simulations using Ansys HFSS and measurements on manufactured band-pass filters. In addition, since the mode-matching method is based on lossless simulations, but insertion loss is an important specification

to judge the quality of a band-pass filter, it has been therefore necessary to conduct the insertion loss analysis using a different simulation method that includes realistic losses. This study was performed using Ansys HFSS.

In the next chapter, the principle of the mode-matching method for planar or quasi-planar transmission lines will be explained. Based on this method, the characteristics of shielded microstrip lines for single-mode operation, and that of the folded substrate-integrated waveguide, will be analysed. A novel concept of band-pass post filter in folded substrate-integrated waveguide technology, together with an efficient specific design procedure will then be presented.

Chapter 5

Shielded Transmission Lines and Band-Pass Folded Substrate-Integrated Waveguide Filters

THIS chapter starts by explaining the principle of the mode-matching method to specifically analyse the characteristics of planar and quasi-planar transmission lines. It then applies the method to single-mode operation shielded microstrip lines, in order to firstly investigate the influence of the shielded line dimensions on the fundamental mode, and secondly explore the relationships between the cut-off frequency of the 2^{nd}-order mode and the geometrical variables of the cross-section of the shielded transmission line. This study is then followed by an investigation of the characteristics of the folded substrate-integrated waveguide. It is found that the first twenty modes in a folded substrate-integrated waveguide can have nearly the same dispersion characteristics as a corresponding unfolded dielectric-loaded rectangular waveguide if the length of the middle vane for the folded substrate-integrated waveguide is chosen appropriately. From this observation, the novel concept of band-pass post filter in folded substrate-integrated waveguide technology is presented at the end of this chapter, together with an efficient and specific design procedure.

5.1 Introduction

Planar and quasi-planar transmission lines are widely used in microwave and millimetre-wave systems. Apart from the common and simple structures such as microstrip lines, striplines, or slotlines, transmission lines can be realised with multiple materials in complex geometries. For instance, the quality factor and the slow-wave mode propagation characteristics in metal-insulator-semiconductor (MIS) transmission lines improved by using inhomogeneous semiconductor substrates was investigated in several publications (Kiang 1996, Chen *et al.* 1996, Kucera and Gutmann 1997).

Nowadays, monolithic microwave integrated circuits (MMICs) and optoelectronic integrated circuits (OEICs) are extensively applied in fields such as military, global positioning, and civil communication. Because of their complex multilayer structures, components in MMIC or OEIC systems are often integrated by quasi-planar transmission lines such as shielded microstrip lines, finlines, or suspended striplines, since they allow a high-degree of integration, direct implementation of semiconductors, and easy fabrication employing photolithographic techniques (Schmidt 1981). They also offer

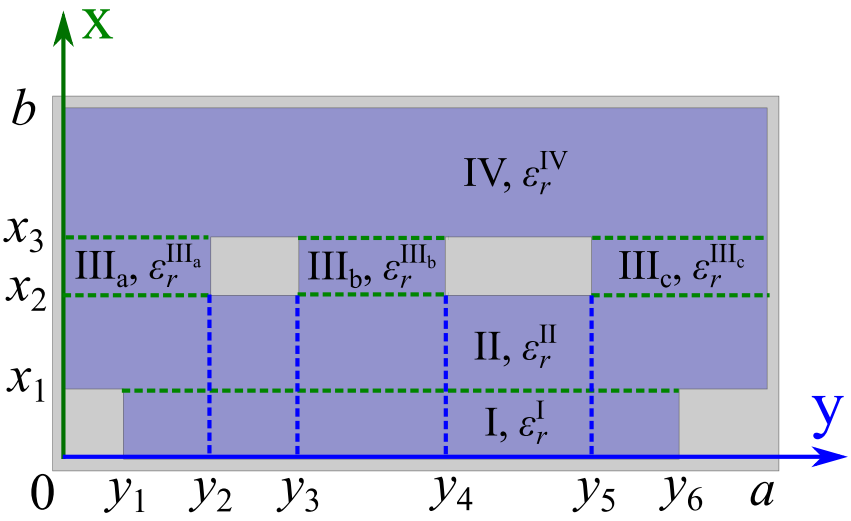

Figure 5.1. Structure of a planar or quasi-planar transmission line for microwave, millimetre-wave and optoelectronic applications. This figure shows a planar or quasi-planar transmission line which can be utilised in MMIC and OEIC systems. The cross-section is divided into several regions and subregions by metal strips. The regular geometries are suitable for analysis using the MMM. Source: Self-created using Ansys HFSS and Inkscape.

advantages of low dispersion, wide single-mode operation bandwidth, reduced attenuation from the dielectric, and increased mechanical tolerance (Itoh 1989b).

Considering the requirements for accurate, realistic, and reliable models for planar or quasi-planar transmission lines, the mode-matching method (MMM) obviously is a reasonable option because of its advantages of high speed, accuracy, and straightforward extension to various planar or quasi-planar transmission lines. Thus, this chapter first extends the description of the MMM to specifically analyse the characteristics of planar or quasi-planar transmission lines (Section 5.2). Based on this method, the characteristics of a shielded microstrip line for single-mode operation is analysed in Section 5.3, while the characteristics of a folded substrate-integrated waveguide (FSIW) are analysed in Section 5.4. Most importantly, it is found that a FSIW can be designed to have quite similar characteristics with a substrate-integrated waveguide (SIW). This is conveniently achieved by adjusting the size of the middle metal vane in the FSIW. Thus, building on this property, a novel concept of band-pass post filter in FSIW technology is presented in the same section, together with an efficient specific design procedure. The findings in this chapter are then summarised in Section 5.5.

5.2 Mode-Matching Method for Planar and Quasi-Planar Transmission Lines

MMIC and OEIC systems utilise various types of planar and quasi-planar transmission lines to realise the connections among different devices. However, analysing these transmission lines individually (one by one) is time-consuming, unnecessary, and often even unrealistic. Thus, this section only explains the principle of the MMM based on a given planar or quasi-planar transmission line. It is noted that the principle can be easily extended to other more complicated planar or quasi-planar transmission lines.

As shown in Fig. 5.1, the cross-section of a planar or quasi-planar transmission line for microwave, millimetre-wave, and optoelectronic applications is divided into four regions, namely Region I, II, III, and IV. Region III is further divided into three subregions by two metal strips. In addition, the relative permittivity of the dielectric in each region or subregions are assumed to be $\varepsilon_r^{\mathrm{I}}$, $\varepsilon_r^{\mathrm{II}}$, $\varepsilon_r^{\mathrm{III_a}}$, $\varepsilon_r^{\mathrm{III_b}}$, $\varepsilon_r^{\mathrm{III_c}}$, and $\varepsilon_r^{\mathrm{IV}}$ as shown in the figure. According to the equations presented in Chapter 3, Hybrid modes, including TE and TM modes, can exist in each region or subregion of the planar and quasi-planar transmission lines. These modes can be described with the magnitudes of z-directed

magnetic and electric vector potentials. Thus, according to the boundary conditions along x-direction shown in Fig. 5.1, the eigenfunctions for magnetic and electric vector potentials in each region or subregion can be derived as Eq. 5.1 and 5.2 respectively.

$$
\begin{aligned}
T_h^{\mathrm{I}} &= \sum_{n_h=0}^{\infty} \frac{\cos(\frac{n_h\pi}{y_6-y_1}y)}{\sqrt{1+\delta_{0n_h}}}(A_{m_h}^{\mathrm{I}} e^{jk_{xm_h}^{\mathrm{I}}x} + B_{m_h}^{\mathrm{I}} e^{-jk_{xm_h}^{\mathrm{I}}x}),\\
T_h^{\mathrm{II}} &= \sum_{n_h=0}^{\infty} \frac{\cos(\frac{n_h\pi}{a}y)}{\sqrt{1+\delta_{0n_h}}}(A_{m_h}^{\mathrm{II}} e^{jk_{xm_h}^{\mathrm{II}}x} + B_{m_h}^{\mathrm{II}} e^{-jk_{xm_h}^{\mathrm{II}}x}),\\
T_h^{\mathrm{III_a}} &= \sum_{n_h=0}^{\infty} \frac{\cos(\frac{n_h\pi}{y_2}y)}{\sqrt{1+\delta_{0n_h}}}(A_{m_h}^{\mathrm{III_a}} e^{jk_{xm_h}^{\mathrm{III_a}}x} + B_{m_h}^{\mathrm{III_a}} e^{-jk_{xm_h}^{\mathrm{III_a}}x}),\\
T_h^{\mathrm{III_b}} &= \sum_{n_h=0}^{\infty} \frac{\cos(\frac{n_h\pi}{y_4-y_3}y)}{\sqrt{1+\delta_{0n_h}}}(A_{m_h}^{\mathrm{III_b}} e^{jk_{xm_h}^{\mathrm{III_b}}x} + B_{m_h}^{\mathrm{III_b}} e^{-jk_{xm_h}^{\mathrm{III_b}}x}),\\
T_h^{\mathrm{III_c}} &= \sum_{n_h=0}^{\infty} \frac{\cos(\frac{n_h\pi}{a-y_5}y)}{\sqrt{1+\delta_{0n_h}}}(A_{m_h}^{\mathrm{III_c}} e^{jk_{xm_h}^{\mathrm{III_c}}x} + B_{m_h}^{\mathrm{III_c}} e^{-jk_{xm_h}^{\mathrm{III_c}}x}),\\
T_h^{\mathrm{IV}} &= \sum_{n_h=0}^{\infty} \frac{\cos(\frac{n_h\pi}{a}y)}{\sqrt{1+\delta_{0n_h}}}(A_{m_h}^{\mathrm{IV}} e^{jk_{xm_h}^{\mathrm{IV}}x} + B_{m_h}^{\mathrm{IV}} e^{-jk_{xm_h}^{\mathrm{IV}}x}),
\end{aligned}
\tag{5.1}
$$

and

$$
\begin{aligned}
T_e^{\mathrm{I}} &= \sum_{n_e=1}^{\infty} \sin(\frac{n_e\pi}{y_6-y_1}y)\frac{1}{jk_{xm_e}^{\mathrm{I}}}(C_{m_e}^{\mathrm{I}} e^{jk_{xm_e}^{\mathrm{I}}x} - D_{m_e}^{\mathrm{I}} e^{-jk_{xm_e}^{\mathrm{I}}x}),\\
T_e^{\mathrm{II}} &= \sum_{n_e=1}^{\infty} \sin(\frac{n_e\pi}{a}y)\frac{1}{jk_{xm_e}^{\mathrm{II}}}(C_{m_e}^{\mathrm{II}} e^{jk_{xm_e}^{\mathrm{II}}x} - D_{m_e}^{\mathrm{II}} e^{-jk_{xm_e}^{\mathrm{II}}x}),\\
T_e^{\mathrm{III_a}} &= \sum_{n_e=1}^{\infty} \sin(\frac{n_e\pi}{y_2}y)\frac{1}{jk_{xm_e}^{\mathrm{III_a}}}(C_{m_e}^{\mathrm{III_a}} e^{jk_{xm_e}^{\mathrm{III_a}}x} - D_{m_e}^{\mathrm{III_a}} e^{-jk_{xm_e}^{\mathrm{III_a}}x}),\\
T_e^{\mathrm{III_b}} &= \sum_{n_e=1}^{\infty} \sin(\frac{n_e\pi}{y_4-y_3}y)\frac{1}{jk_{xm_e}^{\mathrm{III_b}}}(C_{m_e}^{\mathrm{III_b}} e^{jk_{xm_e}^{\mathrm{III_b}}x} - D_{m_e}^{\mathrm{III_b}} e^{-jk_{xm_e}^{\mathrm{III_b}}x}),\\
T_e^{\mathrm{III_c}} &= \sum_{n_e=1}^{\infty} \sin(\frac{n_e\pi}{a-y_5}y)\frac{1}{jk_{xm_e}^{\mathrm{III_c}}}(C_{m_e}^{\mathrm{III_c}} e^{jk_{xm_e}^{\mathrm{III_c}}x} - D_{m_e}^{\mathrm{III_c}} e^{-jk_{xm_e}^{\mathrm{III_c}}x}),\\
T_e^{\mathrm{IV}} &= \sum_{n_e=1}^{\infty} \sin(\frac{n_e\pi}{a}y)\frac{1}{jk_{xm_e}^{\mathrm{IV}}}(C_{m_e}^{\mathrm{IV}} e^{jk_{xm_e}^{\mathrm{IV}}x} - D_{m_e}^{\mathrm{IV}} e^{-jk_{xm_e}^{\mathrm{IV}}x}),
\end{aligned}
\tag{5.2}
$$

where m_h, n_h, m_e, and n_e represent the index of magnetic and electric modes in the regions or subregions, δ_{0,n_h} is the Kronecker delta, k_{xm_h} and k_{xm_e} are unknown wavenumbers along the x-direction, and A, B, C, and D represent unknown amplitude coefficients for different modes.

Eq. 5.1 and 5.2 can be simplified by setting

$$\begin{aligned} \mathcal{Q}^i_{hm_h} &= A^i_{m_h} e^{jk^i_{xm_h}x} + B^i_{m_h} e^{-jk^i_{xm_h}x}, \\ \mathcal{P}^i_{em_e} &= \frac{1}{jk^i_{xm_e}} (C^i_{m_e} e^{jk^i_{xm_e}x} - D^i_{m_e} e^{-jk^i_{xm_e}x}), \end{aligned} \tag{5.3}$$

and

$$\begin{aligned} \mathcal{Q}^i_{em_e} &= \frac{\partial \mathcal{P}^i_{em_e}}{\partial x} = C^i_{m_e} e^{jk^i_{xm_e}x} + D^i_{m_e} e^{-jk^i_{xm_e}x}, \\ \mathcal{P}^i_{hm_h} &= \frac{\partial \mathcal{Q}^i_{hm_h}}{\partial x} = jk^i_{xm_h} (A^i_{m_h} e^{jk^i_{xm_h}x} - B^i_{m_h} e^{-jk^i_{xm_h}x}), \end{aligned} \tag{5.4}$$

where the superscript i represents the divided regions and subregions.

For Eq. 5.3, we can obtain

$$\begin{aligned} \mathcal{Q}^i_{hm_h}(x_{i-1}) &= A^i_{m_h} e^{jk^i_{xm_h}(x_i - \Delta x_i)} + B^i_{m_h} e^{-jk^i_{xm_h}(x_i - \Delta x_i)} \\ &= \cos(k^i_{xm_h}\Delta x_i)(A^i_{m_h} e^{jk^i_{xm_h}x_i} + B^i_{m_h} e^{-jk^i_{xm_h}x_i}) \\ &\quad + j\sin(k^i_{xm_h}\Delta x_i)(A^i_{m_h} e^{jk^i_{xm_h}x_i} - B^i_{m_h} e^{-jk^i_{xm_h}x_i}) \\ &= \cos(k^i_{xm_h}\Delta x_i)\mathcal{Q}^i_{hm_h}(x_i) + \frac{1}{k^i_{xm_h}} \sin(k^i_{xm_h}\Delta x_i)\mathcal{P}^i_{hm_h}(x_i), \end{aligned} \tag{5.5}$$

and

$$\begin{aligned} \mathcal{P}^i_{em_e}(x_{i-1}) &= \frac{1}{jk^i_{xm_e}} (C^i_{m_e} e^{jk^i_{xm_e}(x_i - \Delta x_i)} - D^i_{m_e} e^{-jk^i_{xm_e}(x_i - \Delta x_i)}) \\ &= \frac{1}{jk^i_{xm_e}} [\cos(k^i_{xm_e}\Delta x_i)(C^i_{m_e} e^{jk^i_{xm_e}x_i} - D^i_{m_e} e^{-jk^i_{xm_e}x_i}) \\ &\quad + j\sin(k^i_{xm_e}\Delta x_i)(C^i_{m_e} e^{jk^i_{xm_e}x_i} + D^i_{m_e} e^{-jk^i_{xm_e}x_i})] \\ &= \cos(k^i_{xm_e}\Delta x_i)\mathcal{P}^i_{em_e}(x_i) + \frac{1}{k^i_{xm_e}} \sin(k^i_{xm_e}\Delta x_i)\mathcal{Q}^i_{em_e}(x_i), \end{aligned} \tag{5.6}$$

where Δx_i represents the thickness of the regions or subregions.

Similarly, for Eq. 5.4, we can obtain

$$\begin{aligned} \mathcal{P}^i_{hm_h}(x_{i-1}) &= jk^i_{xm_h} (A^i_{m_h} e^{jk^i_{xm_h}(x_i - \Delta x_i)} - B^i_{m_h} e^{-jk^i_{xm_h}(x_i - \Delta x_i)}) \\ &= jk^i_{xm_h} [\cos(k^i_{xm_h}\Delta x_i)(A^i_{m_h} e^{jk^i_{xm_h}x_i} - B^i_{m_h} e^{-jk^i_{xm_h}x_i}) \\ &\quad + j\sin(k^i_{xm_h}\Delta x_i)(A^i_{m_h} e^{jk^i_{xm_h}x_i} + B^i_{m_h} e^{-jk^i_{xm_h}x_i})] \\ &= \cos(k^i_{xm_h}\Delta x_i)\mathcal{P}^i_{hm_h}(x_i) - k^i_{xm_h} \sin(k^i_{xm_h}\Delta x_i)\mathcal{Q}^i_{hm_h}(x_i), \end{aligned} \tag{5.7}$$

and

$$\begin{aligned}\mathcal{Q}^i_{em_e}(x_{i-1}) &= C^i_{m_e} e^{jk^i_{xm_e}(x_i-\Delta x_i)} + D^i_{m_e} e^{-jk^i_{xm_e}(x_i-\Delta x_i)} \\ &= \cos(k^i_{xm_e}\Delta x_i)(C^i_{m_e} e^{jk^i_{xm_e}x_i} + D^i_{m_e} e^{-jk^i_{xm_e}x_i}) \\ &\quad + j\sin(k^i_{xm_e}\Delta x_i)(C^i_{m_e} e^{jk^i_{xm_e}x_i} - D^i_{m_e} e^{-jk^i_{xm_e}x_i}) \\ &= \cos(k^i_{xm_e}\Delta x_i)\mathcal{Q}^i_{em_e}(x_i) + k^i_{xm_e}\sin(k^i_{xm_e}\Delta x_i)\mathcal{P}^i_{em_e}(x_i).\end{aligned} \tag{5.8}$$

Obviously, $\mathcal{Q}^i_{hm_h}$ and $\mathcal{P}^i_{em_e}$ can be considered as representing electromagnetic waves propagating along the $\pm$ x-direction. Thus, based on Eq. 5.5, 5.6, 5.7, and 5.8, for a given region or subregion, the relationship between the $\mathcal{P}^i_{hm_h}$, $\mathcal{P}^i_{em_e}$, $\mathcal{Q}^i_{hm_h}$, and $\mathcal{Q}^i_{em_e}$ of the bottom of the dielectric and those of the top of the dielectric can be derived as the following matrix equation

$$\begin{bmatrix}\mathcal{P}^i_{hm_h}(x_{i-1}) \\ \mathcal{P}^i_{em_e}(x_{i-1}) \\ \mathcal{Q}^i_{hm_h}(x_{i-1}) \\ \mathcal{Q}^i_{em_e}(x_{i-1})\end{bmatrix} = \mathcal{R}^i \begin{bmatrix}\mathcal{P}^i_{hm_h}(x_i) \\ \mathcal{P}^i_{em_e}(x_i) \\ \mathcal{Q}^i_{hm_h}(x_i) \\ \mathcal{Q}^i_{em_e}(x_i)\end{bmatrix} = \begin{bmatrix}\mathcal{D}_1 & 0 & \mathcal{D}_2 & 0 \\ 0 & \mathcal{D}_3 & 0 & \mathcal{D}_4 \\ \mathcal{D}_5 & 0 & \mathcal{D}_1 & 0 \\ 0 & \mathcal{D}_6 & 0 & \mathcal{D}_3\end{bmatrix} \begin{bmatrix}\mathcal{P}^i_{hm_h}(x_i) \\ \mathcal{P}^i_{em_e}(x_i) \\ \mathcal{Q}^i_{hm_h}(x_i) \\ \mathcal{Q}^i_{em_e}(x_i)\end{bmatrix}, \tag{5.9}$$

where $\mathcal{R}^i$ represents the transmission matrix and

$$\begin{aligned}\mathcal{D}_1 &= \mathrm{diag}\{\cos(k^i_{xm_h}\Delta x_i)\}, \\ \mathcal{D}_2 &= \mathrm{diag}\{-k^i_{xm_h}\sin(k^i_{xm_h}\Delta x_i)\}, \\ \mathcal{D}_3 &= \mathrm{diag}\{\cos(k^i_{xm_e}\Delta x_i)\}, \\ \mathcal{D}_4 &= \mathrm{diag}\{\frac{1}{k^i_{xm_e}}\sin(k^i_{xm_e}\Delta x_i)\}, \\ \mathcal{D}_5 &= \mathrm{diag}\{\frac{1}{k^i_{xm_h}}\sin(k^i_{xm_h}\Delta x_i)\}, \\ \mathcal{D}_6 &= \mathrm{diag}\{-k^i_{xm_e}\sin(k^i_{xm_e}\Delta x_i)\}.\end{aligned} \tag{5.10}$$

The total electromagnetic fields derived from the magnetic or electric potentials should satisfy the following interface conditions, that is, Eq. 5.11 to 5.14, since the fields on the interfaces along y-direction and z-direction are continuous.

$$\begin{aligned}E^i_z &= E^{i+1}_z, \\ \frac{1}{j\omega\varepsilon_0\varepsilon^i_r}{k^i_c}^2 T^i_e &= \frac{1}{j\omega\varepsilon_0\varepsilon^{i+1}_r}{k^{i+1}_c}^2 T^{i+1}_e, \\ T^i_e &= \frac{\varepsilon^i_r}{\varepsilon^{i+1}_r}\frac{{k^{i+1}_c}^2}{{k^i_c}^2} T^{i+1}_e, \\ T^i_e &= \frac{\varepsilon^i_r}{\varepsilon^{i+1}_r}\frac{\varepsilon^{i+1}_r - (k_z/k_0)^2}{\varepsilon^i_r - (k_z/k_0)^2} T^{i+1}_e,\end{aligned} \tag{5.11}$$

where k_c^i is the cutoff wavenumber in regions or subregions, k_0 represents the wavenumber in free space, k_z is the propagation constant, and ε_0 and ε_r^i are the permittivity in free space and relative permittivity respectively. Similarly,

$$\begin{aligned} E_y^i &= E_y^{i+1}, \\ \frac{\partial T_h^i}{\partial x} + \frac{1}{j\omega\varepsilon_0\varepsilon_r^i}(-jk_z)\frac{\partial T_e^i}{\partial y} &= -\frac{\partial T_h^{i+1}}{\partial x} + \frac{1}{j\omega\varepsilon_0\varepsilon_r^{i+1}}(-jk_z)\frac{\partial T_e^{i+1}}{\partial y}, \\ \frac{\partial T_h^i}{\partial x} &= \frac{\partial T_h^{i+1}}{\partial x} - \frac{k_z}{\omega\varepsilon_0\varepsilon_r^i}\frac{\partial T_e^i}{\partial y} + \frac{k_z}{\omega\varepsilon_0\varepsilon_r^{i+1}}\frac{\partial T_e^{i+1}}{\partial y}, \\ \frac{\partial T_h^i}{\partial x} &= \frac{\partial T_h^{i+1}}{\partial x} + \frac{k_z}{\omega\varepsilon_0}\frac{\varepsilon_r^i/\varepsilon_r^{i+1} - 1}{\varepsilon_r^i - (k_z/k_0)^2}\frac{\partial T_e^{i+1}}{\partial y}, \end{aligned} \tag{5.12}$$

$$\begin{aligned} H_z^i &= H_z^{i+1}, \\ \frac{1}{j\omega\mu}{k_c^i}^2 T_h^i &= \frac{1}{j\omega\mu}{k_c^{i+1}}^2 T_h^{i+1}, \\ T_h^i &= \frac{{k_c^{i+1}}^2}{{k_c^i}^2} T_h^{i+1}, \\ T_h^i &= \frac{\varepsilon_r^{i+1} - (k_z/k_0)^2}{\varepsilon_r^i - (k_z/k_0)^2} T_h^{i+1}, \quad or \\ T_h^{i+1} &= \frac{\varepsilon_r^i - (k_z/k_0)^2}{\varepsilon_r^{i+1} - (k_z/k_0)^2} T_h^i, \end{aligned} \tag{5.13}$$

$$\begin{aligned} H_y^i &= H_y^{i+1}, \\ \frac{\partial T_e^i}{\partial x} + \frac{1}{j\omega\mu}(-jk_z)\frac{\partial T_h^i}{\partial y} &= \frac{\partial T_e^{i+1}}{\partial x} + \frac{1}{j\omega\mu}(-jk_z)\frac{\partial T_h^{i+1}}{\partial y}, \\ \frac{\partial T_e^i}{\partial x} &= \frac{\partial T_e^{i+1}}{\partial x} + \frac{k_z}{\omega\mu}\frac{\partial T_h^i}{\partial y} - \frac{k_z}{\omega\mu}\frac{\partial T_h^{i+1}}{\partial y}, \\ \frac{\partial T_e^i}{\partial x} &= \frac{\partial T_e^{i+1}}{\partial x} + \frac{k_z}{\omega\mu}\frac{\varepsilon_r^{i+1} - \varepsilon_r^i}{\varepsilon_r^i - (k_z/k_0)^2}\frac{\partial T_h^{i+1}}{\partial y}, \quad or \\ \frac{\partial T_e^{i+1}}{\partial x} &= \frac{\partial T_e^i}{\partial x} + \frac{k_z}{\omega\mu}\frac{\varepsilon_r^i - \varepsilon_r^{i+1}}{\varepsilon_r^{i+1} - (k_z/k_0)^2}\frac{\partial T_h^i}{\partial y}. \end{aligned} \tag{5.14}$$

Furthermore, substituting the derived eigenfunctions for magnetic and electric potentials in different regions or subregions (Eq. 5.1 and 5.2) into interface condition equations (5.11 to 5.14), the corresponding coupling matrices for different interfaces can then be obtained. The interfaces between Regions II and III are taken an example to illustrate the derivation, while the other interfaces can be analysed with similar method.

Firstly, we consider the electric fields on the interfaces between Regions II and III. According to Eq. 5.12, y-direction electric fields at $x = x_2$ in Regions II and III have the

following relationships,

$$
\begin{aligned}
E_y^{\mathrm{II}} &= E_y^{\mathrm{III_a}} + E_y^{\mathrm{III_b}} + E_y^{\mathrm{III_c}}, \\
\frac{\partial T_h^{\mathrm{II}}}{\partial x} &= \frac{\partial T_h^{\mathrm{III_a}}}{\partial x} + \frac{\partial T_h^{\mathrm{III_b}}}{\partial x} + \frac{\partial T_h^{\mathrm{III_c}}}{\partial x} + \frac{k_z}{\omega\varepsilon_0}\frac{\varepsilon_r^{\mathrm{II}}/\varepsilon_r^{\mathrm{III_a}} - 1}{\varepsilon_r^{\mathrm{II}} - (k_z/k_0)^2}\frac{\partial T_e^{\mathrm{III_a}}}{\partial y} \\
&\quad + \frac{k_z}{\omega\varepsilon_0}\frac{\varepsilon_r^{\mathrm{II}}/\varepsilon_r^{\mathrm{III_b}} - 1}{\varepsilon_r^{\mathrm{II}} - (k_z/k_0)^2}\frac{\partial T_e^{\mathrm{III_b}}}{\partial y} + \frac{k_z}{\omega\varepsilon_0}\frac{\varepsilon_r^{\mathrm{II}}/\varepsilon_r^{\mathrm{III_c}} - 1}{\varepsilon_r^{\mathrm{II}} - (k_z/k_0)^2}\frac{\partial T_e^{\mathrm{III_c}}}{\partial y}, \\
\sum_{n_h=0}^{\infty}\frac{\cos(\frac{n_h\pi}{a}y)}{\sqrt{1+\delta_{0n_h}}}P_{hm_h}^{\mathrm{II}} &= \sum_{n_{h\mathrm{a}}=0}^{\infty}\frac{\cos(\frac{n_{h\mathrm{a}}\pi}{y_2}y)}{\sqrt{1+\delta_{0n_{h\mathrm{a}}}}}\mathcal{P}_{hm_{h\mathrm{a}}}^{\mathrm{III_a}} + \sum_{n_{h\mathrm{b}}=0}^{\infty}\frac{\cos(\frac{n_{h\mathrm{b}}\pi}{y_4-y_3}y)}{\sqrt{1+\delta_{0n_{h\mathrm{b}}}}}\mathcal{P}_{hm_{h\mathrm{b}}}^{\mathrm{III_b}} \\
&\quad + \sum_{n_{h\mathrm{c}}=0}^{\infty}\frac{\cos(\frac{n_{h\mathrm{c}}\pi}{a-y_5}y)}{\sqrt{1+\delta_{0n_{h\mathrm{c}}}}}\mathcal{P}_{hm_{h\mathrm{c}}}^{\mathrm{III_c}} + e_{1\mathrm{a}}\sum_{n_{e\mathrm{a}}=1}^{\infty}\frac{n_{e\mathrm{a}}\pi}{y_2}\cos(\frac{n_{e\mathrm{a}}\pi}{y_2}y)\mathcal{P}_{em_{e\mathrm{a}}}^{\mathrm{III_a}} \\
&\quad + e_{1\mathrm{b}}\sum_{n_{e\mathrm{b}}=1}^{\infty}\frac{n_{e\mathrm{b}}\pi}{y_4-y_3}\cos(\frac{n_{e\mathrm{b}}\pi}{y_4-y_3}y)\mathcal{P}_{em_{e\mathrm{b}}}^{\mathrm{III_b}} \\
&\quad + e_{1\mathrm{c}}\sum_{n_{e\mathrm{c}}=1}^{\infty}\frac{n_{e\mathrm{c}}\pi}{a-y_5}\cos(\frac{n_{e\mathrm{c}}\pi}{a-y_5}y)\mathcal{P}_{em_{e\mathrm{c}}}^{\mathrm{III_c}},
\end{aligned}
\tag{5.15}
$$

where

$$
\begin{aligned}
e_{1\mathrm{a}} &= \frac{k_z}{\omega\varepsilon_0}\frac{\varepsilon_r^{\mathrm{II}}/\varepsilon_r^{\mathrm{III_a}} - 1}{\varepsilon_r^{\mathrm{II}} - (k_z/k_0)^2}, \\
e_{1\mathrm{b}} &= \frac{k_z}{\omega\varepsilon_0}\frac{\varepsilon_r^{\mathrm{II}}/\varepsilon_r^{\mathrm{III_b}} - 1}{\varepsilon_r^{\mathrm{II}} - (k_z/k_0)^2}, \\
e_{1\mathrm{c}} &= \frac{k_z}{\omega\varepsilon_0}\frac{\varepsilon_r^{\mathrm{II}}/\varepsilon_r^{\mathrm{III_c}} - 1}{\varepsilon_r^{\mathrm{II}} - (k_z/k_0)^2}.
\end{aligned}
\tag{5.16}
$$

For Eq. 5.15, we multiply both sides by $\sum_{n_h'=0}^{\infty}\frac{\cos(\frac{n_h'\pi}{a}y)}{\sqrt{1+\delta_{0,n_h'}}}$, and then compute the integral on the interfaces. Utilising the orthogonality of electromagnetic fields, one equation can be obtained as below

$$
\left[\mathcal{P}_{hm_h}^{\mathrm{II}}\right] = \begin{bmatrix} J_{n_h',n_{h\mathrm{a}}}^{\mathrm{II,III_a}} & J_{n_h',n_{h\mathrm{b}}}^{\mathrm{II,III_b}} & J_{n_h',n_{h\mathrm{c}}}^{\mathrm{II,III_c}} & J_{n_h',n_{e\mathrm{a}}}^{\mathrm{II,III_a}} & J_{n_h',n_{e\mathrm{b}}}^{\mathrm{II,III_b}} & J_{n_h',n_{e\mathrm{c}}}^{\mathrm{II,III_c}} \end{bmatrix} \begin{bmatrix} \mathcal{P}_{hm_{h\mathrm{a}}}^{\mathrm{III_a}} \\ \mathcal{P}_{hm_{h\mathrm{b}}}^{\mathrm{III_b}} \\ \mathcal{P}_{hm_{h\mathrm{c}}}^{\mathrm{III_c}} \\ \mathcal{P}_{em_{e\mathrm{a}}}^{\mathrm{III_a}} \\ \mathcal{P}_{em_{e\mathrm{b}}}^{\mathrm{III_b}} \\ \mathcal{P}_{em_{e\mathrm{c}}}^{\mathrm{III_c}} \end{bmatrix},
\tag{5.17}
$$

where coupling coefficients $J^{\mathrm{II,III_a}}_{n'_h,n_{h\mathrm{a}}}$, $J^{\mathrm{II,III_b}}_{n'_h,n_{h\mathrm{b}}}$, $J^{\mathrm{II,III_c}}_{n'_h,n_{h\mathrm{c}}}$, $J^{\mathrm{II,III_a}}_{n'_h,n_{e\mathrm{a}}}$, $J^{\mathrm{II,III_b}}_{n'_h,n_{e\mathrm{b}}}$ and $J^{\mathrm{II,III_c}}_{n'_h,n_{e\mathrm{c}}}$ can be expressed as

$$
\begin{aligned}
J^{\mathrm{II,III_a}}_{n'_h,n_{h\mathrm{a}}} &= \frac{2}{a}\sum_{n_{h\mathrm{a}}=0}^{\infty}\int_0^{y_2}\frac{\cos(\frac{n'_h\pi}{a}y)}{\sqrt{1+\delta_{0n'_h}}}\frac{\cos(\frac{n_{h\mathrm{a}}\pi}{y_2}y)}{\sqrt{1+\delta_{0n_{h\mathrm{a}}}}}\mathrm{d}y,\\
J^{\mathrm{II,III_b}}_{n'_h,n_{h\mathrm{b}}} &= \frac{2}{a}\sum_{n_{h\mathrm{b}}=0}^{\infty}\int_{y_3}^{y_4}\frac{\cos(\frac{n'_h\pi}{a}y)}{\sqrt{1+\delta_{0n'_h}}}\frac{\cos(\frac{n_{h\mathrm{b}}\pi}{y_4-y_3}y)}{\sqrt{1+\delta_{0n_{h\mathrm{b}}}}}\mathrm{d}y,\\
J^{\mathrm{II,III_c}}_{n'_h,n_{h\mathrm{c}}} &= \frac{2}{a}\sum_{n_{h\mathrm{c}}=0}^{\infty}\int_{y_5}^{a}\frac{\cos(\frac{n'_h\pi}{a}y)}{\sqrt{1+\delta_{0n'_h}}}\frac{\cos(\frac{n_{h\mathrm{c}}\pi}{a-y_5}y)}{\sqrt{1+\delta_{0n_{h\mathrm{c}}}}}\mathrm{d}y,\\
J^{\mathrm{II,III_a}}_{n'_h,n_{e\mathrm{a}}} &= \frac{2e_{1\mathrm{a}}}{a}\sum_{n_{e\mathrm{a}}=1}^{\infty}\frac{n_{e\mathrm{a}}\pi}{y_2}\int_0^{y_2}\frac{\cos(\frac{n'_h\pi}{a}y)}{\sqrt{1+\delta_{0n'_h}}}\cos(\frac{n_{e\mathrm{a}}\pi}{y_2}y)\mathrm{d}y,\\
J^{\mathrm{II,III_b}}_{n'_h,n_{e\mathrm{b}}} &= \frac{2e_{1\mathrm{b}}}{a}\sum_{n_{e\mathrm{b}}=1}^{\infty}\frac{n_{e\mathrm{b}}\pi}{y_4-y_3}\int_{y_3}^{y_4}\frac{\cos(\frac{n'_h\pi}{a}y)}{\sqrt{1+\delta_{0n'_h}}}\cos(\frac{n_{e\mathrm{b}}\pi}{y_4-y_3}y)\mathrm{d}y,\\
J^{\mathrm{II,III_c}}_{n'_h,n_{e\mathrm{c}}} &= \frac{2e_{1\mathrm{c}}}{a}\sum_{n_{e\mathrm{c}}=1}^{\infty}\frac{n_{e\mathrm{c}}\pi}{a-y_5}\int_{y_5}^{a}\frac{\cos(\frac{n'_h\pi}{a}y)}{\sqrt{1+\delta_{0n'_h}}}\cos(\frac{n_{e\mathrm{c}}\pi}{a-y_5}y)\mathrm{d}y.
\end{aligned}
\tag{5.18}
$$

For the z-direction electric fields at $x = x_2$ in Regions II and III, according to Eq. 5.11, similarly, we can have

$$
\begin{aligned}
E_z^{\mathrm{II}} &= E_z^{\mathrm{III_a}} + E_z^{\mathrm{III_b}} + E_z^{\mathrm{III_c}},\\
T_e^{\mathrm{II}} &= \frac{\varepsilon_r^{\mathrm{II}}}{\varepsilon_r^{\mathrm{III_a}}}\frac{\varepsilon_r^{\mathrm{III_a}}-(k_z/k_0)^2}{\varepsilon_r^{\mathrm{II}}-(k_z/k_0)^2}T_e^{\mathrm{III_a}} + \frac{\varepsilon_r^{\mathrm{II}}}{\varepsilon_r^{\mathrm{III_b}}}\frac{\varepsilon_r^{\mathrm{III_b}}-(k_z/k_0)^2}{\varepsilon_r^{\mathrm{II}}-(k_z/k_0)^2}T_e^{\mathrm{III_b}}\\
&\quad + \frac{\varepsilon_r^{\mathrm{II}}}{\varepsilon_r^{\mathrm{III_c}}}\frac{\varepsilon_r^{\mathrm{III_c}}-(k_z/k_0)^2}{\varepsilon_r^{\mathrm{II}}-(k_z/k_0)^2}T_e^{\mathrm{III_c}},\\
\begin{bmatrix}\mathcal{P}^{\mathrm{II}}_{em_e}\end{bmatrix} &= \begin{bmatrix}0 & 0 & 0 & J^{\mathrm{II,III_a}}_{n'_e,n_{e\mathrm{a}}} & J^{\mathrm{II,III_b}}_{n'_e,n_{e\mathrm{b}}} & J^{\mathrm{II,III_c}}_{n'_e,n_{e\mathrm{c}}}\end{bmatrix}
\begin{bmatrix}\mathcal{P}^{\mathrm{III_a}}_{hm_{h\mathrm{a}}}\\ \mathcal{P}^{\mathrm{III_b}}_{hm_{h\mathrm{b}}}\\ \mathcal{P}^{\mathrm{III_c}}_{hm_{h\mathrm{c}}}\\ \mathcal{P}^{\mathrm{III_a}}_{em_{e\mathrm{a}}}\\ \mathcal{P}^{\mathrm{III_b}}_{em_{e\mathrm{b}}}\\ \mathcal{P}^{\mathrm{III_c}}_{em_{e\mathrm{c}}}\end{bmatrix},
\end{aligned}
\tag{5.19}
$$

where

$$
\begin{aligned}
J^{\mathrm{II,III_a}}_{n'_e,n_{ea}} &= \frac{2}{ae_{2a}} \sum_{n_{ea}=1}^{\infty} \int_0^{y_2} \sin(\frac{n'_e\pi}{a}y)\sin(\frac{n_{ea}\pi}{y_2}y)\mathrm{d}y, \\
J^{\mathrm{II,III_b}}_{n'_e,n_{eb}} &= \frac{2}{ae_{2b}} \sum_{n_{eb}=1}^{\infty} \int_{y_3}^{y_4} \sin(\frac{n'_e\pi}{a}y)\sin(\frac{n_{eb}\pi}{y_4-y_3}y)\mathrm{d}y, \\
J^{\mathrm{II,III_c}}_{n'_e,n_{ec}} &= \frac{2}{ae_{2c}} \sum_{n_{ec}=1}^{\infty} \int_{y_5}^{a} \sin(\frac{n'_e\pi}{a}y)\sin(\frac{n_{ec}\pi}{a-y_5}y)\mathrm{d}y, \\
e_{2a} &= \frac{\varepsilon_r^{\mathrm{II}}}{\varepsilon_r^{\mathrm{III_a}}} \frac{\varepsilon_r^{\mathrm{III_a}} - (k_z/k_0)^2}{\varepsilon_r^{\mathrm{II}} - (k_z/k_0)^2}, \\
e_{2b} &= \frac{\varepsilon_r^{\mathrm{II}}}{\varepsilon_r^{\mathrm{III_b}}} \frac{\varepsilon_r^{\mathrm{III_b}} - (k_z/k_0)^2}{\varepsilon_r^{\mathrm{II}} - (k_z/k_0)^2}, \\
e_{2c} &= \frac{\varepsilon_r^{\mathrm{II}}}{\varepsilon_r^{\mathrm{III_c}}} \frac{\varepsilon_r^{\mathrm{III_c}} - (k_z/k_0)^2}{\varepsilon_r^{\mathrm{II}} - (k_z/k_0)^2}.
\end{aligned}
\tag{5.20}
$$

Eq. 5.17 and 5.19 can then be written in matrix form, as

$$
\begin{bmatrix} \mathcal{P}^{\mathrm{II}}_{hm_h} \\ \mathcal{P}^{\mathrm{II}}_{em_e} \end{bmatrix} = \begin{bmatrix} J^{\mathrm{II,III_a}}_{n'_h,n_{ha}} & J^{\mathrm{II,III_b}}_{n'_h,n_{hb}} & J^{\mathrm{II,III_c}}_{n'_h,n_{hc}} & J^{\mathrm{II,III_a}}_{n'_h,n_{ea}} & J^{\mathrm{II,III_b}}_{n'_h,n_{eb}} & J^{\mathrm{II,III_c}}_{n'_h,n_{ec}} \\ 0 & 0 & 0 & J^{\mathrm{II,III_a}}_{n'_e,n_{ea}} & J^{\mathrm{II,III_b}}_{n'_e,n_{eb}} & J^{II,\mathrm{III_c}}_{n'_e,n_{ec}} \end{bmatrix} \begin{bmatrix} \mathcal{P}^{\mathrm{III_a}}_{hm_{ha}} \\ \mathcal{P}^{\mathrm{III_b}}_{hm_{hb}} \\ \mathcal{P}^{\mathrm{III_c}}_{hm_{hc}} \\ \mathcal{P}^{\mathrm{III_a}}_{em_{ea}} \\ \mathcal{P}^{\mathrm{III_b}}_{em_{eb}} \\ \mathcal{P}^{\mathrm{III_c}}_{em_{ec}} \end{bmatrix} = \mathcal{C}_1^{\mathrm{II,III}} \begin{bmatrix} \mathcal{P}^{\mathrm{III_a}}_{hm_{ha}} \\ \mathcal{P}^{\mathrm{III_b}}_{hm_{hb}} \\ \mathcal{P}^{\mathrm{III_c}}_{hm_{hc}} \\ \mathcal{P}^{\mathrm{III_a}}_{em_{ea}} \\ \mathcal{P}^{\mathrm{III_b}}_{em_{eb}} \\ \mathcal{P}^{\mathrm{III_c}}_{em_{ec}} \end{bmatrix}
\tag{5.21}
$$

where $\mathcal{C}_1^{\mathrm{II,III}}$ is the coupling matrix for y-direction and z-direction electric fields on interfaces between region II and III.

Secondly, we focus on the magnetic fields on the interfaces. For y-direction magnetic fields at $x = x_2$ in Regions II and $\mathrm{III_a}$, according to Eq. 5.14, we have

$$
\begin{aligned}
\frac{k_z}{\omega\mu} \frac{\varepsilon_r^{\mathrm{II}} - \varepsilon_r^{\mathrm{III_a}}}{\varepsilon_r^{\mathrm{III_a}} - (k_z/k_0)^2} \frac{\partial T_h^{\mathrm{II}}}{\partial y} + \frac{\partial T_e^{\mathrm{II}}}{\partial x} &= \frac{\partial T_e^{\mathrm{III_a}}}{\partial x}, \\
\begin{bmatrix} J^{\mathrm{II,III_a}}_{n'_{ea},n_h} & J^{\mathrm{II,III_a}}_{n'_{ea},n_e} \end{bmatrix} \begin{bmatrix} \mathcal{Q}^{\mathrm{II}}_{hm_h} \\ \mathcal{Q}^{\mathrm{II}}_{em_e} \end{bmatrix} &= \begin{bmatrix} \mathcal{Q}^{\mathrm{III_a}}_{em_{ea}} \end{bmatrix},
\end{aligned}
\tag{5.22}
$$

where

$$
\begin{aligned}
J^{\mathrm{II,III_a}}_{n'_{ea},n_h} &= -\frac{2e_{3a}}{y_2}\sum_{n_h=0}^{\infty}\frac{n_h\pi}{a}\int_0^{y_2}\sin(\frac{n'_{ea}\pi}{y_2}y)\frac{\sin(\frac{n_h\pi}{a}y)}{\sqrt{1+\delta_{0n_h}}}\mathrm{d}y,\\
J^{\mathrm{II,III_a}}_{n'_{ea},n_e} &= \frac{2}{y_2}\sum_{n_e=1}^{\infty}\int_0^{y_2}\sin(\frac{n'_{ea}\pi}{y_2}y)\sin(\frac{n_e\pi}{a}y)\mathrm{d}y,\\
e_{3a} &= \frac{k_z}{\omega\mu}\frac{\varepsilon_r^{\mathrm{II}}-\varepsilon_r^{\mathrm{III_a}}}{\varepsilon_r^{\mathrm{III_a}}-(k_z/k_0)^2}.
\end{aligned}
\tag{5.23}
$$

For y-direction magnetic fields at $x = x_2$ in Regions II and $\mathrm{III_b}$, we have

$$
\begin{aligned}
\frac{k_z}{\omega\mu}\frac{\varepsilon_r^{\mathrm{II}}-\varepsilon_r^{\mathrm{III_b}}}{\varepsilon_r^{\mathrm{III_b}}-(k_z/k_0)^2}\frac{\partial T_h^{\mathrm{II}}}{\partial y}+\frac{\partial T_e^{\mathrm{II}}}{\partial x} &= \frac{\partial T_e^{\mathrm{III_b}}}{\partial x},\\
\begin{bmatrix} J^{\mathrm{II,III_b}}_{n'_{eb},n_h} & J^{\mathrm{II,III_b}}_{n'_{eb},n_e}\end{bmatrix}\begin{bmatrix} Q^{\mathrm{II}}_{hm_h}\\ Q^{\mathrm{II}}_{em_e}\end{bmatrix} &= \begin{bmatrix} Q^{\mathrm{III_b}}_{em_{eb}}\end{bmatrix},
\end{aligned}
\tag{5.24}
$$

where

$$
\begin{aligned}
J^{\mathrm{II,III_b}}_{n'_{eb},n_h} &= -\frac{2e_{3b}}{y_4-y_3}\sum_{n_h=0}^{\infty}\frac{n_h\pi}{a}\int_{y_3}^{y_4}\sin(\frac{n'_{eb}\pi}{y_4-y_3}y)\frac{\sin(\frac{n_h\pi}{a}y)}{\sqrt{1+\delta_{0n_h}}}\mathrm{d}y,\\
J^{\mathrm{II,III_b}}_{n'_{eb},n_e} &= \frac{2}{y_4-y_3}\sum_{n_e=1}^{\infty}\int_{y_3}^{y_4}\sin(\frac{n'_{eb}\pi}{y_4-y3}y)\sin(\frac{n_e\pi}{a}y)\mathrm{d}y,\\
e_{3b} &= \frac{k_z}{\omega\mu}\frac{\varepsilon_r^{\mathrm{II}}-\varepsilon_r^{\mathrm{III_b}}}{\varepsilon_r^{\mathrm{III_b}}-(k_z/k_0)^2}.
\end{aligned}
\tag{5.25}
$$

For y-direction magnetic fields at $x = x_2$ in Regions II and $\mathrm{III_c}$, we have

$$
\begin{aligned}
\frac{k_z}{\omega\mu}\frac{\varepsilon_r^{\mathrm{II}}-\varepsilon_r^{\mathrm{III_c}}}{\varepsilon_r^{\mathrm{III_c}}-(k_z/k_0)^2}\frac{\partial T_h^{\mathrm{II}}}{\partial y}+\frac{\partial T_e^{\mathrm{II}}}{\partial x} &= \frac{\partial T_e^{\mathrm{III_c}}}{\partial x},\\
\begin{bmatrix} J^{\mathrm{II,III_c}}_{n'_{ec},n_h} & J^{\mathrm{II,III_c}}_{n'_{ec},n_e}\end{bmatrix}\begin{bmatrix} Q^{\mathrm{II}}_{hm_h}\\ Q^{\mathrm{II}}_{em_e}\end{bmatrix} &= \begin{bmatrix} Q^{\mathrm{III_c}}_{em_{ec}}\end{bmatrix},
\end{aligned}
\tag{5.26}
$$

where

$$
\begin{aligned}
J^{\mathrm{II,III_c}}_{n'_{ec},n_h} &= -\frac{2e_{3c}}{a-y_5}\sum_{n_h=0}^{\infty}\frac{n_h\pi}{a}\int_{y_5}^{a}\sin(\frac{n'_{ec}\pi}{a-y_5}y)\frac{\sin(\frac{n_h\pi}{a}y)}{\sqrt{1+\delta_{0n_h}}}\mathrm{d}y,\\
J^{\mathrm{II,III_c}}_{n'_{ec},n_e} &= \frac{2}{a-y_5}\sum_{n_e=1}^{\infty}\int_{y_5}^{a}\sin(\frac{n'_{ec}\pi}{a-y5}y)\sin(\frac{n_e\pi}{a}y)\mathrm{d}y,\\
e_{3c} &= \frac{k_z}{\omega\mu}\frac{\varepsilon_r^{\mathrm{II}}-\varepsilon_r^{\mathrm{III_c}}}{\varepsilon_r^{\mathrm{III_c}}-(k_z/k_0)^2}.
\end{aligned}
\tag{5.27}
$$

For z-direction magnetic fields at $x = x_2$ in Regions II and $\mathrm{III_a}$, according to Eq. 5.13, we have

$$\begin{aligned} \frac{\varepsilon_r^{\mathrm{II}} - (k_z/k_0)^2}{\varepsilon_r^{\mathrm{III_a}} - (k_z/k_0)^2} T_h^{\mathrm{II}} &= T_h^{\mathrm{III_a}}, \\ \left[J_{n'_{h\mathrm{a}}, n_h}^{\mathrm{II,III_a}}\right] \left[Q_{hm_h}^{\mathrm{II}}\right] &= \left[Q_{hm_{h\mathrm{a}}}^{\mathrm{III_a}}\right], \end{aligned} \tag{5.28}$$

where

$$\begin{aligned} J_{n'_{h\mathrm{a}}, n_h}^{\mathrm{II,III_a}} &= \frac{2e_{4\mathrm{a}}}{y_2} \sum_{n_h=0}^{\infty} \int_0^{y_2} \frac{\cos(\frac{n'_{h\mathrm{a}}\pi}{y_2} y)}{\sqrt{1+\delta_{0n'_{h\mathrm{a}}}}} \frac{\cos(\frac{n_h\pi}{a} y)}{\sqrt{1+\delta_{0n_h}}} \mathrm{d}y, \\ e_{4\mathrm{a}} &= \frac{\varepsilon_r^{\mathrm{II}} - (k_z/k_0)^2}{\varepsilon_r^{\mathrm{III_a}} - (k_z/k_0)^2}. \end{aligned} \tag{5.29}$$

For z-direction magnetic fields at $x = x_2$ in Region II and $\mathrm{III_b}$, we have

$$\begin{aligned} \frac{\varepsilon_r^{\mathrm{II}} - (k_z/k_0)^2}{\varepsilon_r^{\mathrm{III_b}} - (k_z/k_0)^2} T_h^{\mathrm{II}} &= T_h^{\mathrm{III_b}}, \\ \left[J_{n'_{h\mathrm{b}}, n_h}^{\mathrm{II,III_b}}\right] \left[Q_{hm_h}^{\mathrm{II}}\right] &= \left[Q_{hm_{h\mathrm{b}}}^{\mathrm{III_b}}\right], \end{aligned} \tag{5.30}$$

where

$$\begin{aligned} J_{n'_{h\mathrm{b}}, n_h}^{\mathrm{II,III_b}} &= \frac{2e_{4\mathrm{b}}}{y_4 - y_3} \sum_{n_h=0}^{\infty} \int_{y_3}^{y_4} \frac{\cos(\frac{n'_{h\mathrm{b}}\pi}{y_4 - y_3} y)}{\sqrt{1+\delta_{0n'_{h\mathrm{b}}}}} \frac{\cos(\frac{n_h\pi}{a} y)}{\sqrt{1+\delta_{0n_h}}} \mathrm{d}y, \\ e_{4\mathrm{b}} &= \frac{\varepsilon_r^{\mathrm{II}} - (k_z/k_0)^2}{\varepsilon_r^{\mathrm{III_b}} - (k_z/k_0)^2}. \end{aligned} \tag{5.31}$$

For z-direction magnetic fields at $x = x_2$ in Region II and $\mathrm{III_c}$, we have

$$\begin{aligned} \frac{\varepsilon_r^{\mathrm{II}} - (k_z/k_0)^2}{\varepsilon_r^{\mathrm{III_c}} - (k_z/k_0)^2} T_h^{\mathrm{II}} &= T_h^{\mathrm{III_c}}, \\ \left[J_{n'_{h\mathrm{c}}, n_h}^{\mathrm{II,III_c}}\right] \left[Q_{hm_h}^{\mathrm{II}}\right] &= \left[Q_{hm_{h\mathrm{c}}}^{\mathrm{III_c}}\right], \end{aligned} \tag{5.32}$$

where

$$\begin{aligned} J_{n'_{h\mathrm{c}}, n_h}^{\mathrm{II,III_c}} &= \frac{2e_{4\mathrm{c}}}{a - y_5} \sum_{n_h=0}^{\infty} \int_{y_5}^{a} \frac{\cos(\frac{n'_{h\mathrm{c}}\pi}{a - y_5} y)}{\sqrt{1+\delta_{0n'_{h\mathrm{c}}}}} \frac{\cos(\frac{n_h\pi}{a} y)}{\sqrt{1+\delta_{0n_h}}} \mathrm{d}y, \\ e_{4\mathrm{c}} &= \frac{\varepsilon_r^{\mathrm{II}} - (k_z/k_0)^2}{\varepsilon_r^{\mathrm{III_c}} - (k_z/k_0)^2}. \end{aligned} \tag{5.33}$$

Combining Eq. 5.22, 5.24, 5.26, 5.28, 5.30, and 5.32 into one matrix equation, we obtain

$$\begin{bmatrix} J^{\mathrm{II,III_a}}_{n'_{h\mathrm{a}},n_h} & 0 \\ J^{\mathrm{II,III_b}}_{n'_{h\mathrm{b}},n_h} & 0 \\ J^{\mathrm{II,III_c}}_{n'_{h\mathrm{c}},n_h} & 0 \\ J^{\mathrm{II,III_a}}_{n'_{e\mathrm{a}},n_h} & J^{\mathrm{II,III_a}}_{n'_{e\mathrm{a}},n_e} \\ J^{\mathrm{II,III_b}}_{n'_{e\mathrm{b}},n_h} & J^{\mathrm{II,III_b}}_{n'_{e\mathrm{b}},n_e} \\ J^{\mathrm{II,III_c}}_{n'_{e\mathrm{c}},n_h} & J^{\mathrm{II,III_c}}_{n'_{e\mathrm{c}},n_e} \end{bmatrix} \begin{bmatrix} \mathcal{Q}^{\mathrm{II}}_{hm_h} \\ \mathcal{Q}^{\mathrm{II}}_{em_e} \end{bmatrix} = \mathcal{C}_2^{\mathrm{II,III}} \begin{bmatrix} \mathcal{Q}^{\mathrm{II}}_{hm_h} \\ \mathcal{Q}^{\mathrm{II}}_{em_e} \end{bmatrix} = \begin{bmatrix} \mathcal{Q}^{\mathrm{III_a}}_{hm_{h\mathrm{a}}} \\ \mathcal{Q}^{\mathrm{III_b}}_{hm_{h\mathrm{b}}} \\ \mathcal{Q}^{\mathrm{III_c}}_{hm_{h\mathrm{c}}} \\ \mathcal{Q}^{\mathrm{III_a}}_{em_{e\mathrm{a}}} \\ \mathcal{Q}^{\mathrm{III_b}}_{em_{e\mathrm{b}}} \\ \mathcal{Q}^{\mathrm{III_c}}_{em_{e\mathrm{c}}} \end{bmatrix}, \tag{5.34}$$

where $\mathcal{C}_2^{\mathrm{II,III}}$ is the coupling matrix for y-direction and z-direction magnetic fields on interfaces between Regions II and III.

Furthermore, according to Eq. 5.21 and 5.34, another matrix equation for both the electric and magnetic fields can be obtained as the following

$$\begin{bmatrix} \mathcal{P}^{\mathrm{II}}_{hm_h} \\ \mathcal{P}^{\mathrm{II}}_{em_e} \\ \mathcal{Q}^{\mathrm{II}}_{hm_h} \\ \mathcal{Q}^{\mathrm{II}}_{em_e} \end{bmatrix} = \mathcal{C}^{\mathrm{II,III}} \begin{bmatrix} \mathcal{P}^{\mathrm{III}}_{hm_h} \\ \mathcal{P}^{\mathrm{III}}_{em_e} \\ \mathcal{Q}^{\mathrm{III}}_{hm_h} \\ \mathcal{Q}^{\mathrm{III}}_{em_e} \end{bmatrix} = \begin{bmatrix} \mathcal{C}_1^{\mathrm{II,III}} & 0 \\ 0 & \mathcal{C}_2^{\mathrm{II,III}} \end{bmatrix} \begin{bmatrix} \mathcal{P}^{\mathrm{III}}_{hm_h} \\ \mathcal{P}^{\mathrm{III}}_{em_e} \\ \mathcal{Q}^{\mathrm{III}}_{hm_h} \\ \mathcal{Q}^{\mathrm{III}}_{em_e} \end{bmatrix}, \tag{5.35}$$

where $\mathcal{C}^{\mathrm{II,III}}$ is the coupling matrix for y-direction and z-direction electric and magnetic fields on interfaces between Regions II and III, and $\mathcal{P}^{\mathrm{III}}_{hm_h}$, $\mathcal{P}^{\mathrm{III}}_{em_e}$, $\mathcal{Q}^{\mathrm{III}}_{hm_h}$, and $\mathcal{Q}^{\mathrm{III}}_{em_e}$ can be expressed as

$$\begin{aligned} \begin{bmatrix} \mathcal{P}^{\mathrm{III}}_{hm_h} \end{bmatrix} &= \begin{bmatrix} \mathcal{P}^{\mathrm{III_a}}_{hm_{h\mathrm{a}}} & \mathcal{P}^{\mathrm{III_b}}_{hm_{h\mathrm{b}}} & \mathcal{P}^{\mathrm{III_c}}_{hm_{h\mathrm{c}}} \end{bmatrix}^{tr}, \\ \begin{bmatrix} \mathcal{P}^{\mathrm{III}}_{em_e} \end{bmatrix} &= \begin{bmatrix} \mathcal{P}^{\mathrm{III_a}}_{em_{e\mathrm{a}}} & \mathcal{P}^{\mathrm{III_b}}_{em_{e\mathrm{b}}} & \mathcal{P}^{\mathrm{III_c}}_{em_{e\mathrm{c}}} \end{bmatrix}^{tr}, \\ \begin{bmatrix} \mathcal{Q}^{\mathrm{III}}_{hm_h} \end{bmatrix} &= \begin{bmatrix} \mathcal{Q}^{\mathrm{III_a}}_{hm_{h\mathrm{a}}} & \mathcal{Q}^{\mathrm{III_b}}_{hm_{h\mathrm{b}}} & \mathcal{Q}^{\mathrm{III_c}}_{hm_{h\mathrm{c}}} \end{bmatrix}^{tr}, \\ \begin{bmatrix} \mathcal{Q}^{\mathrm{III}}_{em_e} \end{bmatrix} &= \begin{bmatrix} \mathcal{Q}^{\mathrm{III_a}}_{em_{e\mathrm{a}}} & \mathcal{Q}^{\mathrm{III_b}}_{em_{e\mathrm{b}}} & \mathcal{Q}^{\mathrm{III_c}}_{em_{e\mathrm{c}}} \end{bmatrix}^{tr}. \end{aligned} \tag{5.36}$$

The transmission matrix $\mathcal{R}^i$ is able to transform the $\mathcal{P}^i_{hm_h}$, $\mathcal{P}^i_{em_e}$, $\mathcal{Q}^i_{hm_h}$, and $\mathcal{Q}^i_{em_e}$ from the bottom to the top boundary in regions or subregions, while the coupling matrix $\mathcal{C}^{i,i+1}$ can match the $\mathcal{P}^i_{hm_h}$, $\mathcal{P}^i_{em_e}$, $\mathcal{Q}^i_{hm_h}$, and $\mathcal{Q}^i_{em_e}$ on each interface between adjacent regions or subregions in the y-direction and z-direction. Therefore, the relationship between these elements on the lower ($x = 0$) and the upper ($x = b$) of the planar or quasi-planar

transmission line can be derived as

$$\begin{bmatrix} \mathcal{P}^{\mathrm{I}}_{hm_h}(0) \\ \mathcal{P}^{\mathrm{I}}_{em_e}(0) \\ \mathcal{Q}^{\mathrm{I}}_{hm_h}(0) \\ \mathcal{Q}^{\mathrm{I}}_{em_e}(0) \end{bmatrix} = \mathcal{RC} \begin{bmatrix} \mathcal{P}^{\mathrm{IV}}_{hm_h}(b) \\ \mathcal{P}^{\mathrm{IV}}_{em_e}(b) \\ \mathcal{Q}^{\mathrm{IV}}_{hm_h}(b) \\ \mathcal{Q}^{\mathrm{IV}}_{em_e}(b) \end{bmatrix} = \left[\begin{array}{cc:cc} \mathcal{RC}_{11} & \mathcal{RC}_{12} & \mathcal{RC}_{13} & \mathcal{RC}_{14} \\ \mathcal{RC}_{21} & \mathcal{RC}_{22} & \mathcal{RC}_{23} & \mathcal{RC}_{24} \\ \hdashline \mathcal{RC}_{31} & \mathcal{RC}_{32} & \mathcal{RC}_{33} & \mathcal{RC}_{34} \\ \mathcal{RC}_{41} & \mathcal{RC}_{42} & \mathcal{RC}_{43} & \mathcal{RC}_{44} \end{array}\right] \begin{bmatrix} \mathcal{P}^{\mathrm{IV}}_{hm_h}(b) \\ \mathcal{P}^{\mathrm{IV}}_{em_e}(b) \\ \mathcal{Q}^{\mathrm{IV}}_{hm_h}(b) \\ \mathcal{Q}^{\mathrm{IV}}_{em_e}(b) \end{bmatrix}, \tag{5.37}$$

where

$$\mathcal{RC} = \left[\mathcal{R}^{\mathrm{I}}\mathcal{C}^{\mathrm{I,II}}\mathcal{R}^{\mathrm{II}}\mathcal{C}^{\mathrm{II,III}}\mathcal{R}^{\mathrm{III}}\mathcal{C}^{\mathrm{III,IV}}\mathcal{R}^{\mathrm{IV}}\right]^{T}. \tag{5.38}$$

Utilising the remaining two electric wall conditions at $x = 0$ and $x = b$, which leads to $\mathcal{P}^{\mathrm{I}}_{hm_h}(0) = \mathcal{P}^{\mathrm{I}}_{em_e}(0) = \mathcal{P}^{\mathrm{IV}}_{hm_h}(b) = \mathcal{P}^{\mathrm{IV}}_{em_e}(b) = 0$, the size of Eq. 5.37 can be reduced as the following equation

$$\begin{bmatrix} 0 \\ 0 \end{bmatrix} = \left[\mathcal{RC}_{ur}\right] \begin{bmatrix} \mathcal{Q}^{\mathrm{IV}}_{hm_h}(b) \\ \mathcal{Q}^{\mathrm{IV}}_{em_e}(b) \end{bmatrix} = \begin{bmatrix} \mathcal{RC}_{13} & \mathcal{RC}_{14} \\ \mathcal{RC}_{23} & \mathcal{RC}_{24} \end{bmatrix} \begin{bmatrix} \mathcal{Q}^{\mathrm{IV}}_{hm_h}(b) \\ \mathcal{Q}^{\mathrm{IV}}_{em_e}(b) \end{bmatrix}, \tag{5.39}$$

where $\mathcal{RC}_{ur}$ is the upper right quarter of the matrix $\mathcal{RC}$.

Obviously, the determinant of $\mathcal{RC}_{ur}$ should satisfy the equation

$$\det(\mathcal{RC}_{ur}) = 0, \tag{5.40}$$

which is a transcendent function about the propagation constants k_z in the transmission line. It follows that, the desired propagation constants k_z for the hybrid modes can be obtained by solving the transcendent function.

5.3 Mode-Matching Analysis of Dimensions for Single-Mode Operation of Shielded Microstrip Lines

Shielded microstrip lines are widely used in microwave and millimetre-wave systems to connect devices while protecting circuits from environmental contaminants, preventing electromagnetic interference, and enhancing the mechanical strength. To avoid the influence of the metallic enclosures on the fundamental mode, the choice of dimensions for the housing is an important issue. In this section, the influence of those dimensions on the fundamental mode is investigated rigorously using the MMM explained in Section 5.2. In addition, the relationships between the cutoff frequency of the 2^{nd}-order mode and those geometrical variables of the cross-section of the shielded transmission line are presented. With these relationships, a reasonable geometry can be efficiently determined, which is important to prevent performance degradation through higher-order mode excitations, such as in waveguide transitions.

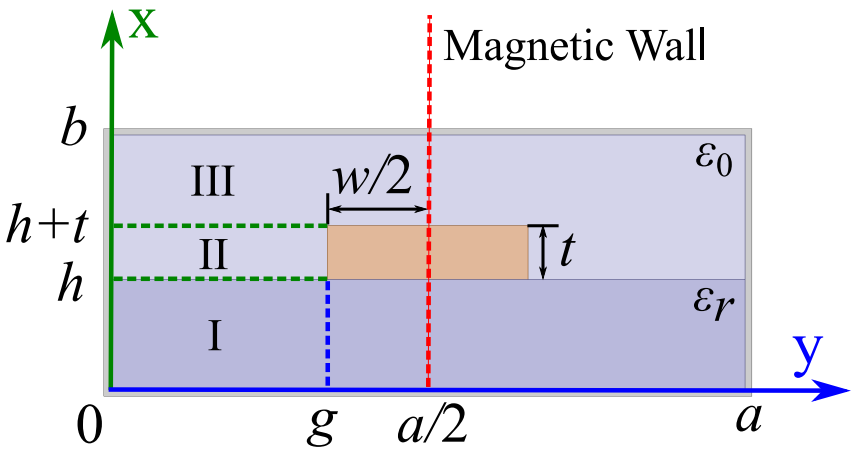

Figure 5.2. Cross-section of the shielded microstrip transmission line. This figure shows the cross-section of a shielded microstrip transmission line. In order to simplify the analysis, a magnetic wall is placed at the centre of the geometry. The half structure is then divided into three regions. Source: Self-created using Ansys HFSS and Matlab.

5.3.1 Eigenfunction in Shielded Microstrip Lines

The cross-section of a shielded microstrip transmission line is shown in Fig. 5.2. For a symmetric structure, in order to simplify the analysis, a magnetic wall or an electric wall can be placed on the centre geometrical symmetry axis to handle even modes or odd modes, respectively. Since both the fundamental quasi-TEM mode and the first higher-order mode (which resembles a quasi-TE_{10} mode in an inhomogeneously filled waveguide) in the shielded microstrip are even, a magnetic wall is employed in Fig. 5.2 and placed at $x = \frac{a}{2}$.

The half structure ($0 \leq x \leq \frac{a}{2}$) is then divided into three regions. Due to the magnetic wall assigned at the centre of the geometry, the boundary conditions for the half shielded transmission line are different from the example presented in Section 5.2. Thus, the electromagnetic fields in each region should be modified as the following

$$
\begin{aligned}
T_h^{\mathrm{I}} &= \sum_{n_h=0}^{\infty} \cos\left(\frac{(2n_h+1)\pi}{a}y\right)\left(A_{m_h}^{\mathrm{I}} e^{jk_{xm_h}^{\mathrm{I}}x} + B_{m_h}^{\mathrm{I}} e^{-jk_{xm_h}^{\mathrm{I}}x}\right), \\
T_h^{\mathrm{II}} &= \sum_{n_h=0}^{\infty} \frac{\cos\left(\frac{n_h\pi}{g}y\right)}{\sqrt{1+\delta_{0,n_h}}}\left(A_{m_h}^{\mathrm{II}} e^{jk_{xm_h}^{\mathrm{II}}x} + B_{m_h}^{\mathrm{II}} e^{-jk_{xm_h}^{\mathrm{II}}x}\right), \\
T_h^{\mathrm{III}} &= \sum_{n_h=0}^{\infty} \cos\left(\frac{(2n_h+1)\pi}{a}y\right)\left(A_{m_h}^{\mathrm{III}} e^{jk_{xm_h}^{\mathrm{III}}x} + B_{m_h}^{\mathrm{III}} e^{-jk_{xm_h}^{\mathrm{III}}x}\right),
\end{aligned}
\tag{5.41}
$$

$$
\begin{aligned}
T_e^{\mathrm{I}} &= \sum_{n_e=1}^{\infty} \sin\left(\frac{(2n_e-1)\pi}{a}y\right)\frac{1}{jk_{xm_e}^{\mathrm{I}}}\left(C_{m_e}^{\mathrm{I}}e^{jk_{xm_e}^{\mathrm{I}}x} - D_{m_e}^{\mathrm{I}}e^{-jk_{xm_e}^{\mathrm{I}}x}\right),\\
T_e^{\mathrm{II}} &= \sum_{n_e=1}^{\infty} \sin\left(\frac{n_e\pi}{g}y\right)\frac{1}{jk_{xm_e}^{\mathrm{II}}}\left(C_{m_e}^{\mathrm{II}}e^{jk_{xm_e}^{\mathrm{II}}x} - D_{m_e}^{\mathrm{II}}e^{-jk_{xm_e}^{\mathrm{II}}x}\right),\\
T_e^{\mathrm{III}} &= \sum_{n_e=1}^{\infty} \sin\left(\frac{(2n_e-1)\pi}{a}y\right)\frac{1}{jk_{xm_e}^{\mathrm{III}}}\left(C_{m_e}^{\mathrm{III}}e^{jk_{xm_e}^{\mathrm{III}}x} - D_{m_e}^{\mathrm{III}}e^{-jk_{xm_e}^{\mathrm{III}}x}\right),
\end{aligned}
\tag{5.42}
$$

where n_h, n_e, m_h, and m_e are the index of the modes, $k_{xm_h}^i$ and $k_{xm_e}^i$ are wavenumbers along the x-axis for different modes, δ_{0n} is the Kronecker delta, and $A_{m_h}^i$, $B_{m_h}^i$, $C_{m_e}^i$, $D_{m_e}^i$ are unknown amplitude coefficients.

By calculating the transmission matrices for the amplitude coefficients from the bottom to the top boundary in each region, computing the coupling matrices through matching the tangential fields at each interface, namely $x = h$ and $x = h + t$, and utilising the boundary conditions at $x = 0$ and $x = b$, a transcendent function of the propagation constant k_z can be obtained. Furthermore, the propagation constant k_z can be acquired by solving the transcendent equation. More detailed derivations are provided in Section 5.2.

5.3.2 Analysis of Fundamental Mode in Shielded Microstrip Lines

The modal analysis presented in Section 5.2 is especially relevant for millimetre-wave frequencies, where small dimensions result in larger tolerances. Millimetre-waves have a continuous attenuation because of the absorption by various atmospheric constituents such as water vapour, oxygen and, dust. However, there is a propagation window at 94 GHz where the attenuation is relatively modest (Yujiri *et al.* 2003). Due to the strong penetrability, numerous circuits operating at 94 GHz have been proposed and applied in low-visibility navigation, concealed weapons detection, and astronomy. Therefore, a shielded microstrip transmission line realised in GaAs technology is taken as an example here for the analysis of the influence of shield dimensions on the propagation characteristics in W-band (extending from 75 GHz to 110 GHz). The values of its variables are listed in Table 5.1.

In order to mitigate the influence of the shielding on the desired fundamental mode of the microstrip line, the dimensions of the shielding housing should be chosen reasonably. This is investigated numerically in the following based on the MMM. In the first case, the height b of the housing is fixed and the width a is varied from 500 µm to

Table 5.1. Parameters of a shielded microstrip transmission line. The table gives the dimensions, including the width a and height b of the housing, the width w and the thickness t of the microstrip, and the height h of the substrate as shown in Fig. 5.2. The relative permittivity of the dielectric is also provided.

a (µm)	b (µm)	h (µm)	t (µm)	w (µm)	ε_r
750	260	100	10	50	12.9

1250 µm. As shown in Fig. 5.3(a), with the increase of the width a, the phase constants first increase before stabilising to an asymptotic value when the width is 20 times of the width w of the microstrip. Similarly, for a fixed width a of the housing and variation of the height b from 200 µm to 600 µm, it is found that, as shown in Fig. 5.3(b), when the ratio of the housing height b to the substrate thickness h is larger than 4, the changes of the phase constants become negligible.

To illustrate this convergence, a test has been done to compare the phase constant of a microstrip line without housing and a shielded microstrip line at 94 GHz. As shown in Fig. 5.4(a), for a fixed height ratio $\frac{b}{h} = 4$, the phase constant for the quasi-TEM mode of the shielded transmission line converges to the value for the unshielded microstrip line when the width ratio $\frac{a}{w}$ reaches 20. Similarly, convergence of the results is confirmed for a fixed width ratio $\frac{a}{w} = 20$ in Fig. 5.4(b), when the varied height ratio $\frac{b}{h}$ reaches a value of 4. In both cases, the influence of the metallic enclosures becomes insignificant when the conditions $\frac{b}{h} \geq 4$ and $\frac{a}{w} \geq 20$ are satisfied.

5.3.3 Analysis of the 2^{nd}-Order Mode in Shielded Microstrip Lines

Higher-order modes in shielded microstrip lines should be taken into account in some cases, such as when potentially excited by a discontinuity. For example, the geometry of the cross-section of the shielded microstrip line for a W-band waveguide-to-microstrip transition should be decided suitably in order to allow the fundamental mode to propagate in the shielded microstrip line, while rejecting higher-order modes (Leong and Weinreb 1999, Shireen *et al.* 2010). Thus, the cutoff frequency of the next higher-order mode should be above 110 GHz.

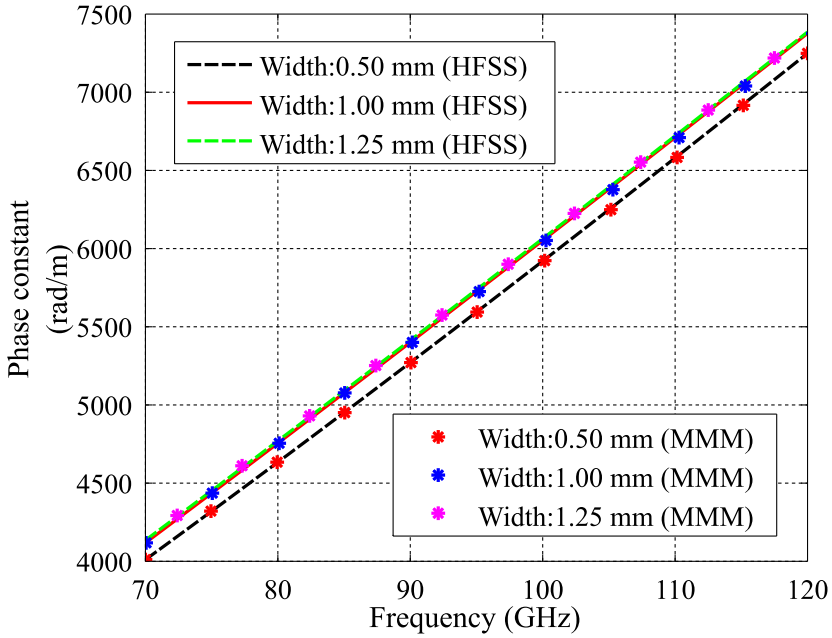

(a)

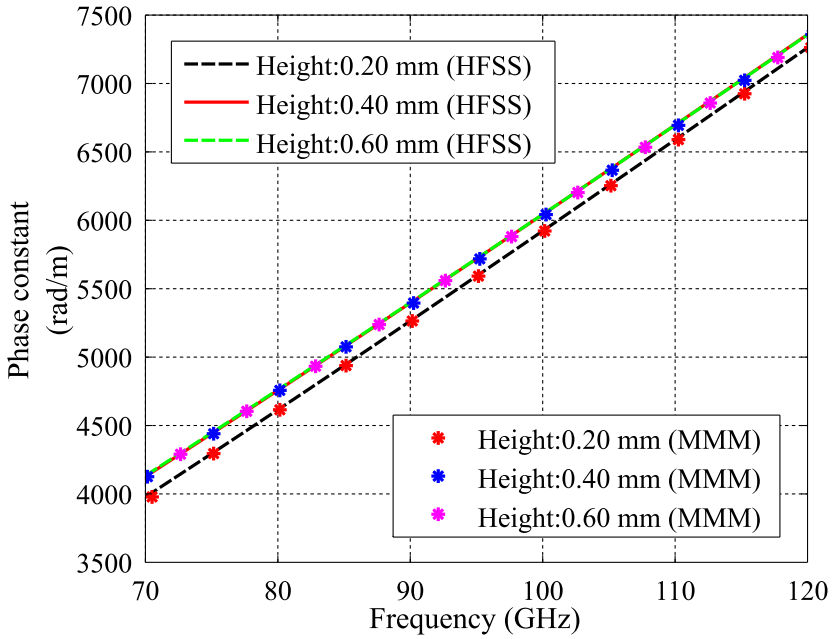

(b)

Figure 5.3. Influence on the fundamental mode of varying (a) the width a and (b) the height b of the shielding housing. These figures show how the fundamental mode is affected by changing the width a from 500 µm to 1250 µm, and varying the height b of the shielding housing from 200 µm to 600 µm. Source: Self-created using Ansys HFSS and Matlab.

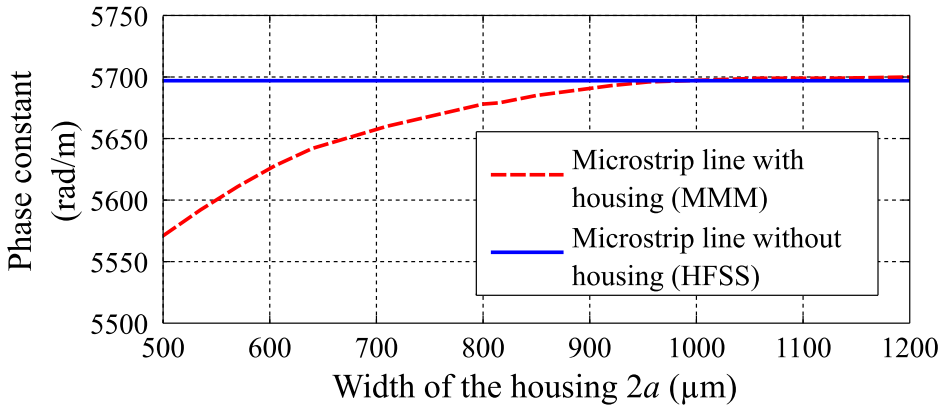

(a)

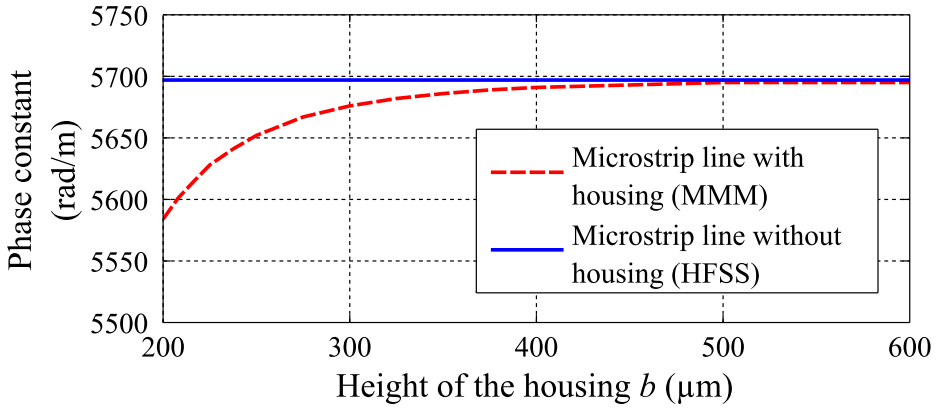

(b)

Figure 5.4. Comparison of the fundamental mode's phase constant at 94 GHz between a microstrip line without housing and a shielded microstrip line. These figures compare the phase constants of quasi-TEM modes for the microstrip line without housing and a shielded microstrip line. The first case sets the height b four times larger than the substrate thickness h and varies the width a from 500 μm to 1200 μm, while the second case sets the width a twenty times larger than the microstrip width w and changes the height b from 200 μm to 600 μm. Source: Self-created using Ansys HFSS and Matlab.

The cutoff frequency depends on the width a and the height b of the shielded microstrip line, the width w and the thickness t of the microstrip, and the thickness h and the relative permittivity ε_r of the substrate. By varying individually the value of one variable among them and fixing the other variables to the values given in Table 5.1, the relationships between the cutoff frequencies of the 2^{nd}-order modes and the variables have been obtained.

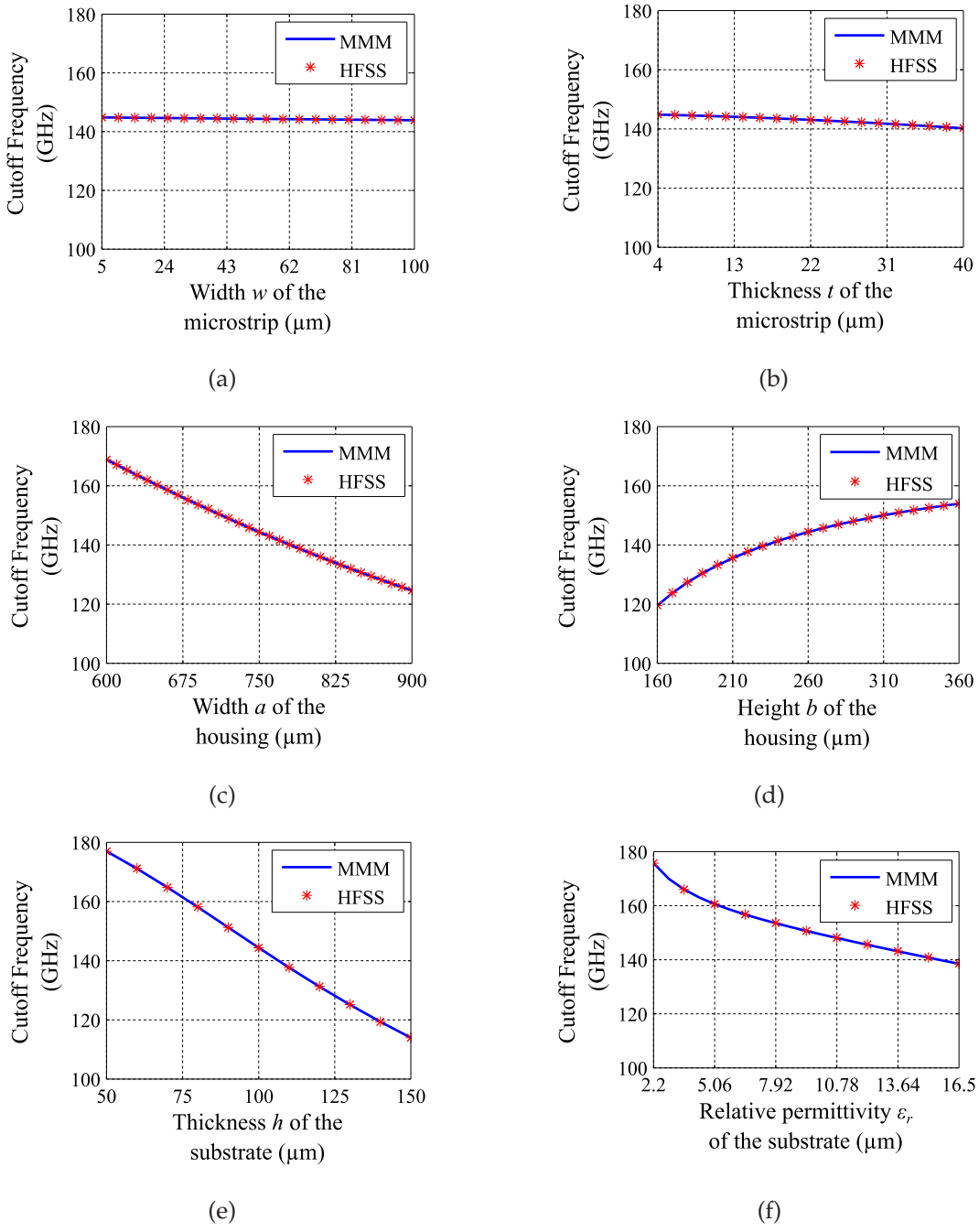

Figure 5.5. Influence on the cutoff frequency of the 2^{nd}-order mode caused by the geometry and the relative permittivity of the substrate. These figures show how the cutoff frequency of the 2^{nd}-order mode is affected by the variation of: (a) the width w of the microstrip, (b) the thickness t of the microstrip, (c) the width a of the shielded microstrip line housing, (d) the height b of the shielded microstrip line housing, (e) the thickness h of the substrate, (f) the relative permittivity ε_r of the substrate. Source: Self-created using Matlab.

Examining Fig. 5.5(a) and (b) reveals that the influence of the dimensions of the microstrip on the cutoff frequency is relatively limited. In contrast, the cutoff frequency is sensitive to the width and height of the shielded microstrip line housing and the thickness and the relative permittivity of the substrate. As shown in Fig. 5.5(c), with the increase of the width of the shielded microstrip line housing from 600 µm to 900 µm, the cutoff frequency of the second-order mode drops quickly from 168.8 GHz to 124.7 GHz. With the increase of the thickness or the relative permittivity of the substrate, the cutoff frequency has the similar changing trends as shown in Fig. 5.5(e) and (f). Conversely, as shown in Fig. 5.5(d), with the increase in the height of the shielded microstrip line housing from 160 µm to 360 µm, the cutoff frequency rises from 119.60 GHz to 153.95 GHz

According to the analysis above, it is obvious that large shielding dimensions are desired to avoid affecting the fundamental mode. However, by increasing dimensions, higher-order modes may be introduced into the working band. Thus, a trade-off should be made between the first two modes to maintain a single-mode operation system. The analysis results in this chapter provide guidance on the appropriate choice of shielded line parameters to satisfy this trade-off.

5.4 Folded Substrate-Integrated Waveguide and the Application in Band-Pass Post Filter

The application of microwave and millimetre-wave devices realised in rectangular waveguide technology is limited by their high cost, bulky volume, and difficult integration with other components. In order to overcome these shortcomings, the SIW has been proposed as planar dielectric-loaded rectangular waveguide equivalent. Nevertheless, despite the significant size reduction offered by realisation of devices in SIW technology, width reduction is still desirable for microwave and millimetre-wave systems.

The concept of FSIW is a viable option to reduce the size of devices in SIW technology. The characteristics of the FSIW have been analysed with the equivalent ridged waveguide method (Che *et al.* 2008b) and the variational method (Nguyen-Trong *et al.* 2015b). However, both methods only focus the two or three lowest-order modes in the FSIW. Based on the MMM, a more detailed analysis for the dispersion

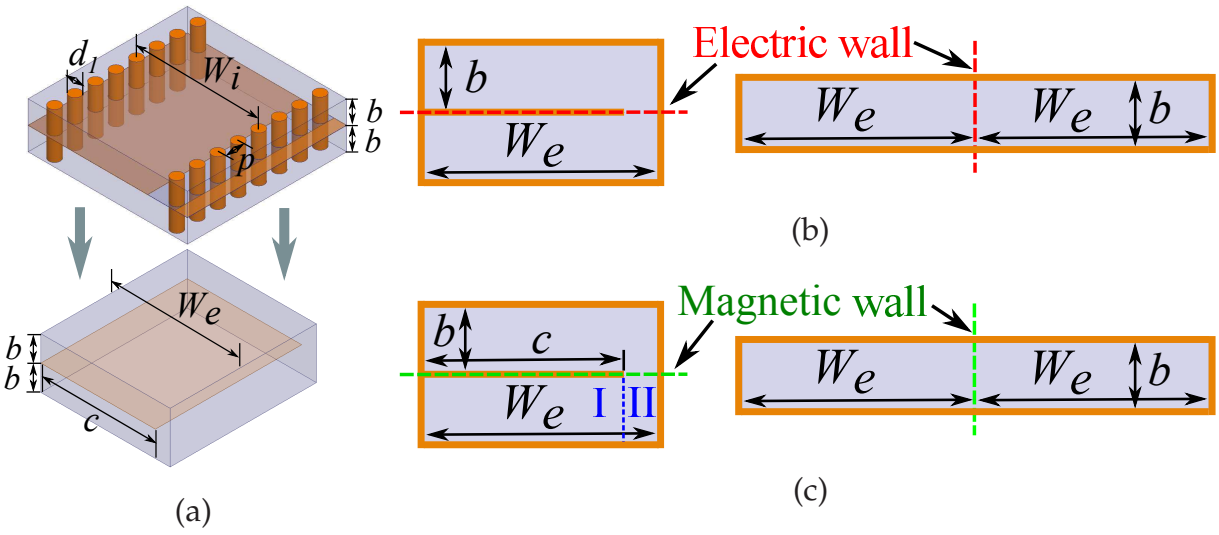

Figure 5.6. Structure of an E-type FSIW and its equivalent folded dielectric-loaded rectangular waveguide. These figures show the structure of an FSIW, and its equivalent configuration, which can be transformed with the equation introduced by Cassivi (Cassivi *et al.* 2002). In order to simplify the analysis, an electric wall and an magnetic wall are placed at the centre of the folded dielectric-loaded rectangular waveguide. Source: Self-created using Ansys HFSS and Inkscape.

characteristics is provided here and it shows that the FSIW can retain similar dispersion characteristics as the corresponding dielectric-loaded rectangular waveguide, but with half the size. According to this property, a novel concept of band-pass post filter in FSIW technology is presented in this section, together with an efficient and specific design procedure.

5.4.1 Dispersion Characteristics of Folded Substrate-Integrated Waveguide

To analyse the dispersion characteristics of a symmetric FSIW, it is firstly transformed into a dielectric-loaded folded rectangular waveguide as shown in Fig. 5.6(a). The equivalent width W_e can be accurately determined using the empirical equation Eq. 4.1 (Cassivi *et al.* 2002).

For the following analysis, we consider an example with a width W_e = 10.16 mm and thickness $2b$ = 1.524 mm for the folded rectangular waveguide, loaded by a dielectric with relative permittivity ε_r = 2.94. The width c of the middle vane will be varied to achieve the desired propagation characteristics. The odd and even modes are treated

respectively by placing an electric wall or a magnetic wall at the centre of the geometry, as explained in the following.

To investigate the dispersion characteristics of odd modes in a folded rectangular waveguide, an electric wall is placed at the centre of the geometry. Thus, the half structure of the folded rectangular waveguide becomes a standard rectangular waveguide as shown in Fig. 5.6(b). The corresponding modes are defined as odd modes whose phase constant β can be calculated through the classical equations below (Pozar 2011)

$$\begin{aligned} \beta &= \sqrt{\omega^2\mu\varepsilon - k_c^2}, \\ k_c^2 &= (\frac{m\pi}{W_e})^2 + (\frac{n\pi}{b})^2, \end{aligned} \tag{5.43}$$

where ω is the angle frequency, μ and ε are the permeability and permittivity of the dielectric respectively, k_c is the cutoff wavenumber, and m and n represent the index of the modes. Obviously, odd modes in the folded rectangular waveguide have the same phase constants as the $TE_{m,0}$ modes (m is positive even integer) in the unfolded rectangular waveguide with width $2W_e$.

Similarly, to explore the dispersion characteristics of even modes in a folded rectangular waveguide, a magnetic wall is placed at the centre of the geometry as shown in Fig. 5.6(c). The half structure is then divided into two regions. Region I contains three electric walls, while Region II consists of two electric walls and one magnetic wall. In this case, an analytical solution is not readily available, but the regular geometries can be handled conveniently with the MMM presented in Section 5.2.

Based on the MMM, the relationship between the length c of the middle vane and the cutoff frequency of the first even mode has been investigated. As shown in Fig. 5.7, while c increases from 0.01 mm to 10.15 mm, the cutoff frequency shifts to lower frequencies. The initial decrease of the cutoff frequency value is very rapid, but it settles soon to a relatively small rate of descent. It is observed that the first odd mode is replaced by the first even mode as the fundamental mode in the folded rectangular waveguide when c is larger than 4.74 mm. Meanwhile, as shown in Fig. 5.8, the electric fields for the first even mode at 10 GHz concentrate around the right edge of the middle vane, whereas for $c = 10.05$ mm, the electric fields has a maximum between the right edge of the middle vane and the right side of the folded rectangular waveguide.

Obviously, by adjusting the length c of the middle vane, the cutoff wavenumber of the fundamental mode in the folded rectangular waveguide can have the same value as that of the $TE_{1,0}$ mode in the corresponding unfolded rectangular waveguide. This

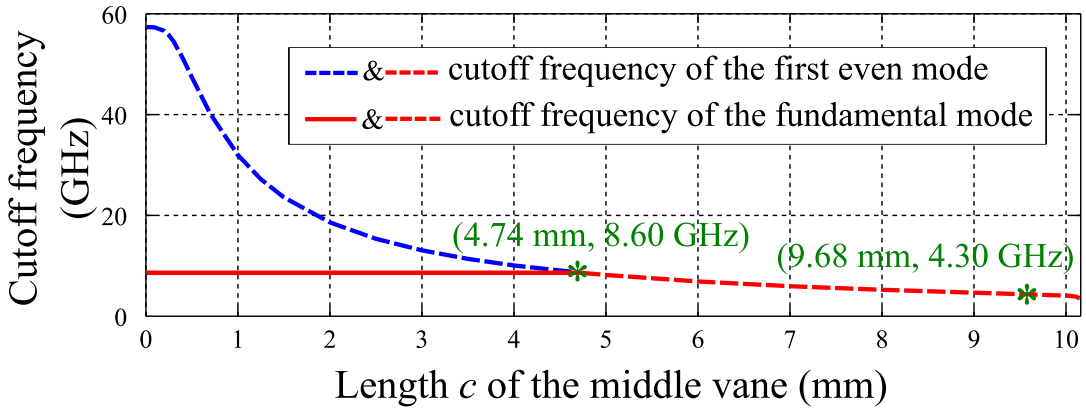

Figure 5.7. Relationship between the cutoff frequency of the first even mode in FSIW and the length of the middle vane. This figure shows how the cutoff frequency of the first even mode in FSIW is influenced by varying the length c of the middle metal vane. It also gives the length of the vane for which the fundamental mode is replaced by the first even mode. Source: Self-created using Matlab.

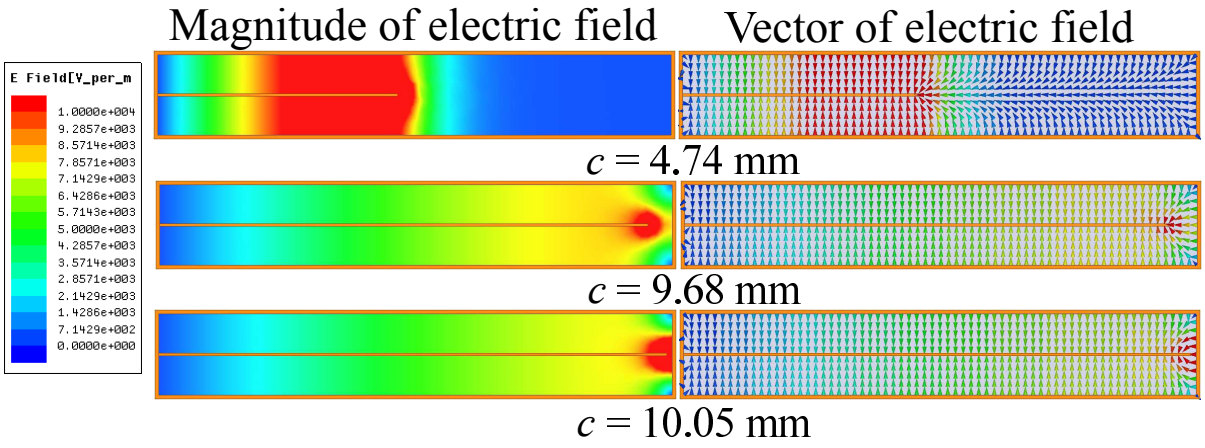

Figure 5.8. Electric fields of the first even mode at 10 GHz when the length c of the middle vane is 4.74 mm, 9.68 mm, and 10.05 mm. This figure shows the electric fields of the first even mode in an FSIW at 10 GHz. The electric fields concentrate around the right edge of the middle vane, whereas for $c = 10.05$ mm, the electric fields have a maximum between the right edge of the middle vane and the right side of the folded rectangular waveguide. Source: Self-created using Ansys HFSS and Inkscape.

value of c can be found easily using the bisection method or Newton's method. For the particular example handled here, when $c = 9.68$ mm, the same cutoff wavenumber can be achieved in the folded and unfolded waveguides. With this equivalent value

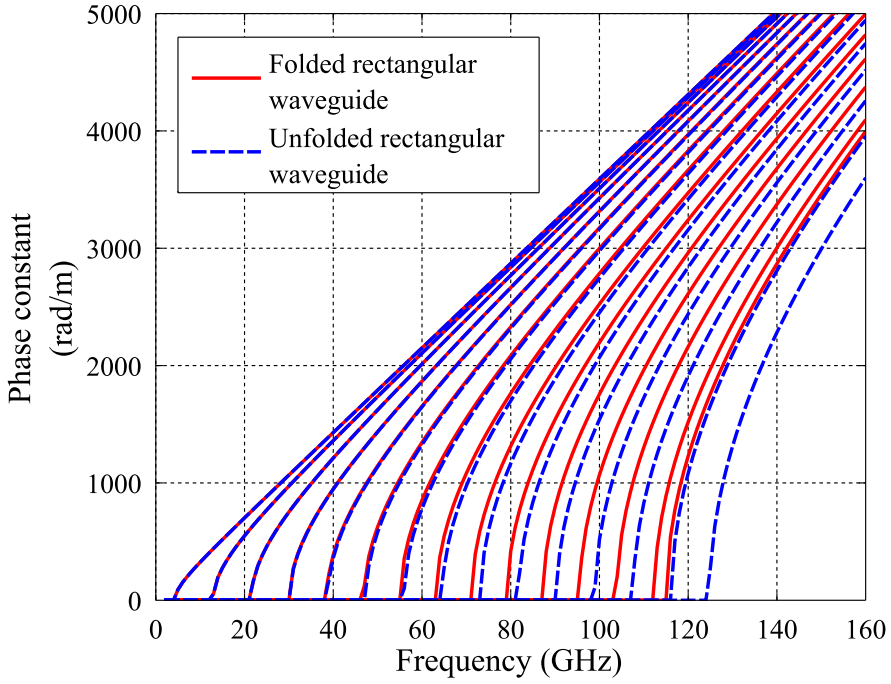

Figure 5.9. Comparison of the even modes' phase constants of the folded rectangular waveguide with corresponding modes of the unfolded rectangular waveguide when the length c of the middle vane is 9.68 mm. This figure compares the even modes' phase constants of the folded rectangular waveguide with corresponding modes of the unfolded rectangular waveguide when the length of the middle vane is fixed as 9.68 mm. It is found that the difference of the phase constant between even modes in the folded rectangular waveguide and the $TE_{m,0}$ modes (m is positive odd integer) in the corresponding dielectric-loaded rectangular waveguide can be considered small until about the 10^{th} even mode. Source: Self-created using Matlab.

of c in terms of the fundamental mode, the first fifteen even modes in the folded rectangular waveguide have also been compared with the first fifteen $TE_{m,0}$ modes (m is positive odd integer) in the unfolded rectangular waveguide. As shown in Fig. 5.9, the phase constants of the first six modes are nearly indistinguishable for both structures, whereas the differences become visible and gradually larger starting from the 7^{th} mode. Nevertheless, up to the 10^{th} mode, the difference of the cutoff wavenumber, that is, $\frac{\triangle k_c}{k_{c\_unfolded}}$, is about 3%, which still can be considered acceptable. Thus an appropriate choice of the width c allows the definition of a near-equivalence between the folded rectangular waveguide and an unfolded dielectric-loaded rectangular waveguide, with a validity in terms of propagation characteristics extending to around twenty modes, including odd and even modes.

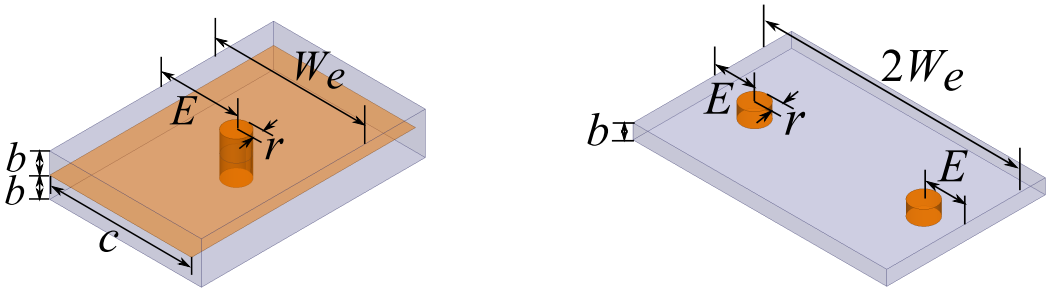

(a) (b)

Figure 5.10. Structures for posts placed in the cross-section of a folded and an unfolded rectangular waveguide. These figures show configurations for posts in a folded and an unfolded rectangular waveguides. Dimensions for these two waveguides are provided in Subsection 5.4.1, and the length c for the middle vane is set as 9.68 mm. The unfolded rectangular waveguides thus can be considered as the equivalent of the folded rectangular waveguide. Source: Self-created using Ansys HFSS and Inkscape.

5.4.2 Posts in Folded and Unfolded Rectangular Waveguide

To confirm this near-equivalence, the characteristic of posts placed in the cross-section of a folded rectangular waveguide has also been compared with that of post pairs placed symmetrically in the cross-section of a corresponding unfolded rectangular waveguide as shown in Fig. 5.10. For direct comparison of the physical structure with the equivalent model, the scattering parameters for the folded rectangular waveguide are obtained through full-wave simulations using Ansys HFSS, while the scattering parameters for the equivalent unfolded rectangular waveguide are calculated with the MMM considering only the first twenty modes. The results at 7 GHz (the intended filter centre frequency) are shown in Fig. 5.11 for posts with different radii r as a function of their location E in the waveguides. Both reflection and transmission coefficients show very similar behaviour for a large variety of parameters. This means that post pairs placed in the cross-section of an unfolded rectangular waveguide and computed with twenty modes can be considered as an equivalent structure to posts placed in the cross-section of a folded rectangular waveguide.

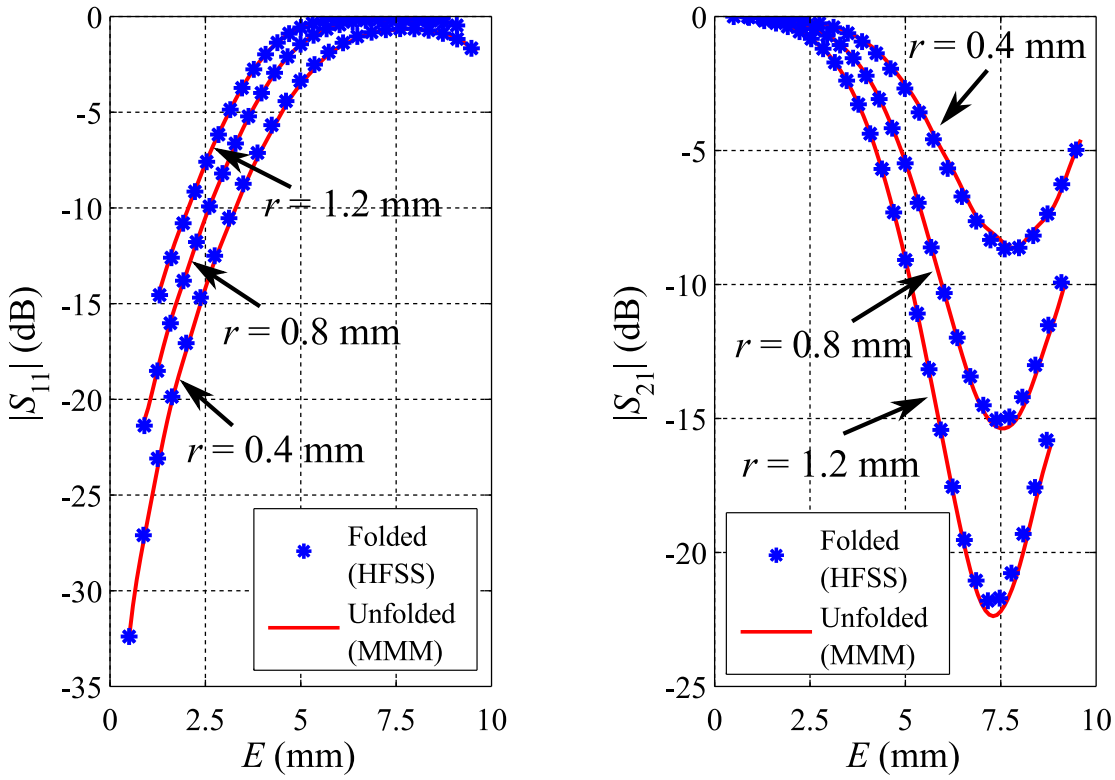

Figure 5.11. Comparison of (a) $|S_{11}|$ and (b) $|S_{21}|$ between posts with different radii r placed in the cross-section of a folded rectangular waveguide and the equivalent unfolded rectangular waveguide. These figures compare the scattering parameters (a) $|S_{11}|$ and (b) $|S_{21}|$ for posts with different radii r placed in the cross-section of a folded rectangular waveguide and the equivalent unfolded rectangular waveguide. It is found that both reflection and transmission coefficients show very similar behaviour for a large variety of parameters. Source: Self-created using Ansys HFSS and Matlab.

5.4.3 A Novel Band-Pass Post Folded Substrate-Integrated Waveguide Filter

According to the analyses in Sections 5.4.1 and 5.4.2, the geometry of a band-pass post filter with symmetric arrangement of posts in an unfolded SIW is perfectly adapted as equivalent problem for a band-pass FSIW filter as shown in Fig. 5.12, if the length c of the vane is chosen appropriately. The efficient mode-matching-based design method introduced in Chapter 4 can then be applied in this case. As a result, the dimensions of E_i and D_i for a 5^{th}-order Chebyshev band-pass post FSIW filter can be determined

Table 5.2. Sizes of an FSIW band-pass post filter (Units: mm). The table gives the dimensions, including the physical width W_i of the FSIW, the diameters d_1 and d_2 of the posts, interval p between adjacent posts, the gaps E between the posts and the FSIW wall, the length D of the resonant cavities formed by post pairs, the width W_t and length L_t of the taper for the FSIW-to-strip transition, and the width W_c and L_c of the slot for the strip-to-microstrip transition.

E_1,E_6	E_2,E_5	E_3,E_4	D_1,D_5	D_2,D_4	D_3	W_i	W_t
4.18	6.13	6.81	13.46	15.18	15.44	10.745	4.65

L_t	W_s	d_1	d_2	p	b	W_c	L_c
7.44	1.04	1.00	1.60	1.80	0.762	1.90	5.10

within 1 second by a standard computer with a 3.40 GHz i7-2600 CPU and 14.0 GB RAM. The resulting values for such a filter with centre frequency of 7 GHz and fractional band-width of 5.71% (passband extending from 6.8 GHz to 7.2 GHz) are listed in Table 5.2. As shown in Fig. 5.13, without considering the FSIW-to-stripline transition, the stripline-to-SMA transition and the losses, the simulation results for the FSIW band-pass filter obtained through Ansys HFSS agree well with the calculated results for its equivalent band-pass unfolded rectangular waveguide filter obtained through the MMM.

An FSIW-to-stripline transition has been designed with procedures which are similar to the method reported in (Deslandes 2010), while the width W_c and length L_c of the slot for a stripline-to-SMA transition have been optimised using the finite-element software Ansys HFSS, in order to test the band-pass filter. As shown in Fig. 5.13, the simulated reflection coefficient in the specified passband (6.8 GHz to 7.2 GHz) is below -23 dB. The transmission coefficient at the centre frequency (7 GHz) is -1.31 dB. A prototype of this FSIW band-pass filter has also been manufactured, as shown in Fig. 5.14, and tested. The measured reflection coefficient, also shown in Fig. 5.13, in the specified passband (extending from 6.8 GHz to 7.2 GHz) is below -17 dB. The transmission coefficient at the centre frequency (7 GHz) is -2.01 dB. The discrepancy between simulation and measurement insertion loss may be ascribed to the deviation of the loss tangent of the dielectric and the fabrication imperfections.

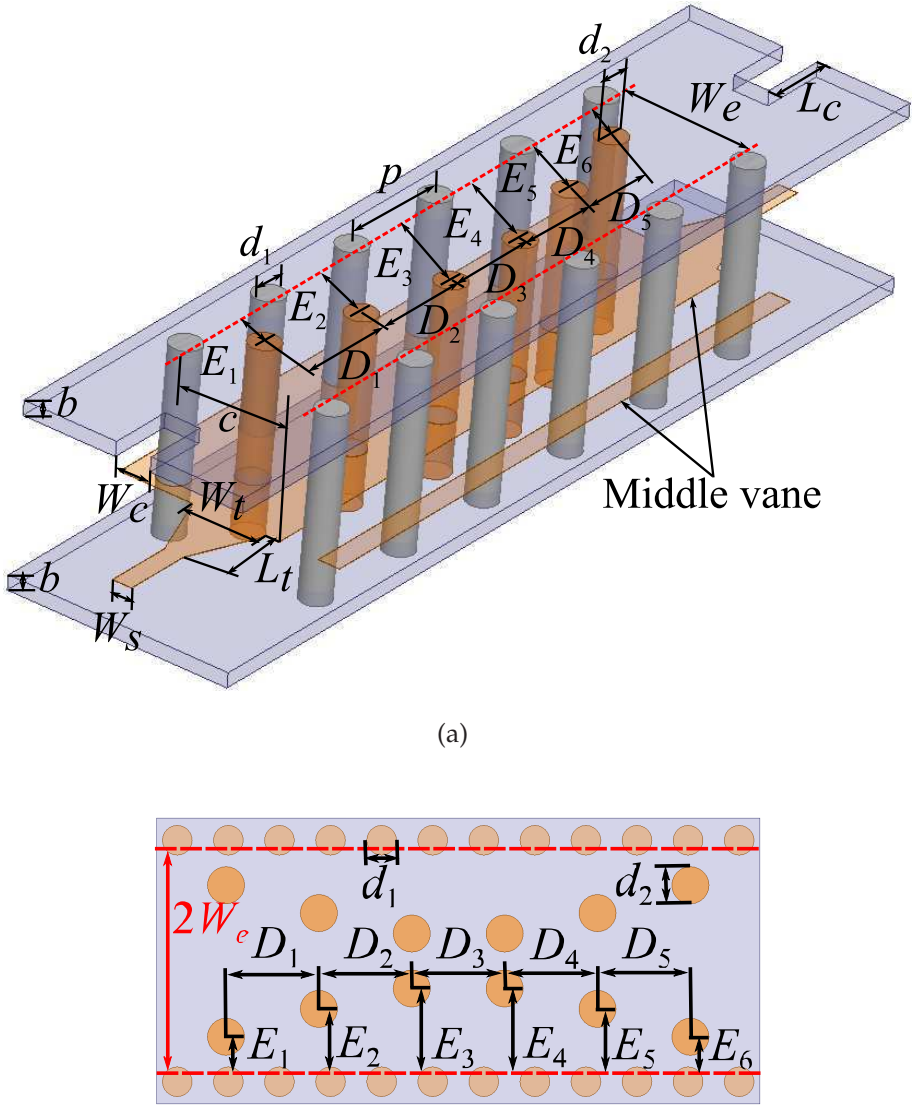

(a)

(b)

Figure 5.12. Structure of a 5-cavity Chebyshev band-pass post filter realised in: (a) FSIW technology, (b) and its equivalent structure in SIW technology. These figures show the structure of a 5-cavity Chebyshev band-pass post FSIW filter and its equivalent SIW structure. According to the analysis in Sections 5.4.1 and 5.4.2, the SIW band-pass filter can be considered as an equivalent problem for the band-pass FSIW filter with appropriate vane length c. Source: Self-created using Ansys HFSS and Inkscape.

To sum up, it has been demonstrated that the first twenty modes in an FSIW have nearly the same dispersion characteristics as an unfolded dielectric-loaded rectangular waveguide if the length of the middle vane for the FSIW is chosen appropriately.

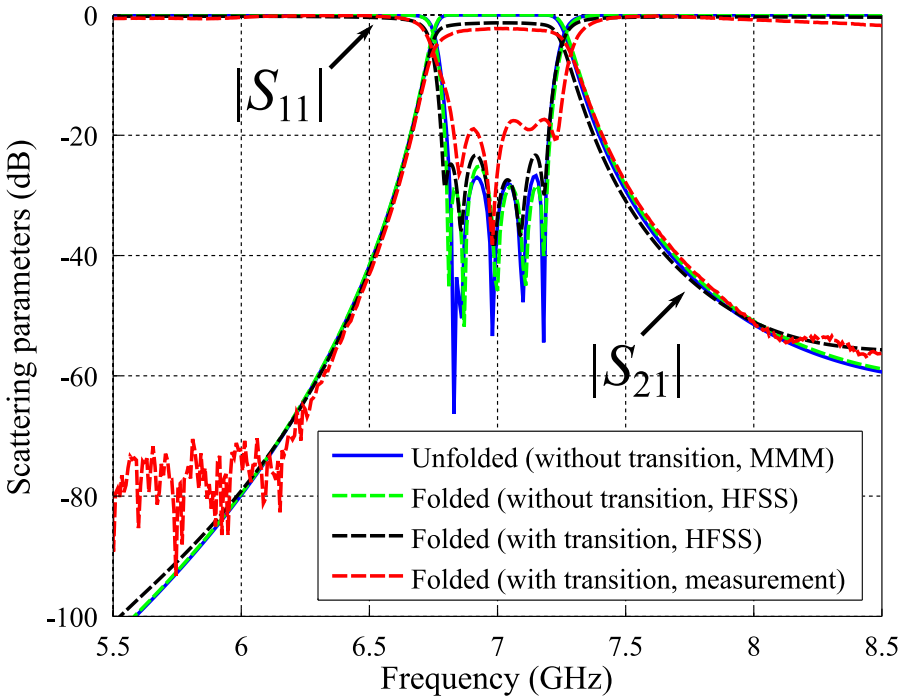

Figure 5.13. Comparison of scattering parameters between the band-pass post FSIW filter and its equivalent unfolded rectangular waveguide band-pass filter. This figure compares the scattering parameters between the band-pass post FSIW filter and its equivalent unfolded rectangular waveguide band-pass filter. Without considering the transitions and losses, the green dash lines and the blue lines represent the simulated Ansys HFSS and calculated mode-matching scattering parameters $|S_{11}|$ and $|S_{21}|$ for the FSIW filter and the unfolded rectangular waveguide filter. Considering the transitions and losses, the black dash lines and the red dash lines are the simulated and measured scattering parameters $|S_{11}|$ and $|S_{21}|$ for the FSIW filter. Source: Self-created using Ansys HFSS and Matlab.

The scattering parameters for posts placed in a folded rectangular waveguide and an equivalent unfolded rectangular waveguide have been compared, confirming that the two structures possess similar characteristics. Thus, the novel FSIW band-pass post filter structure introduced in this section can be conveniently designed by transforming it into an unfolded equivalent problem which can be handled with the MMM accurately and efficiently. The design method has been applied to realise a 5^{th}-order Chebyshev band-pass post FSIW filter with a centre frequency of 7 GHz and a fractional bandwidth of 5.71%. The viability and efficiency of the method has been successfully validated by full-wave finite-element simulations using Ansys HFSS and measurements on a fabricated prototype.

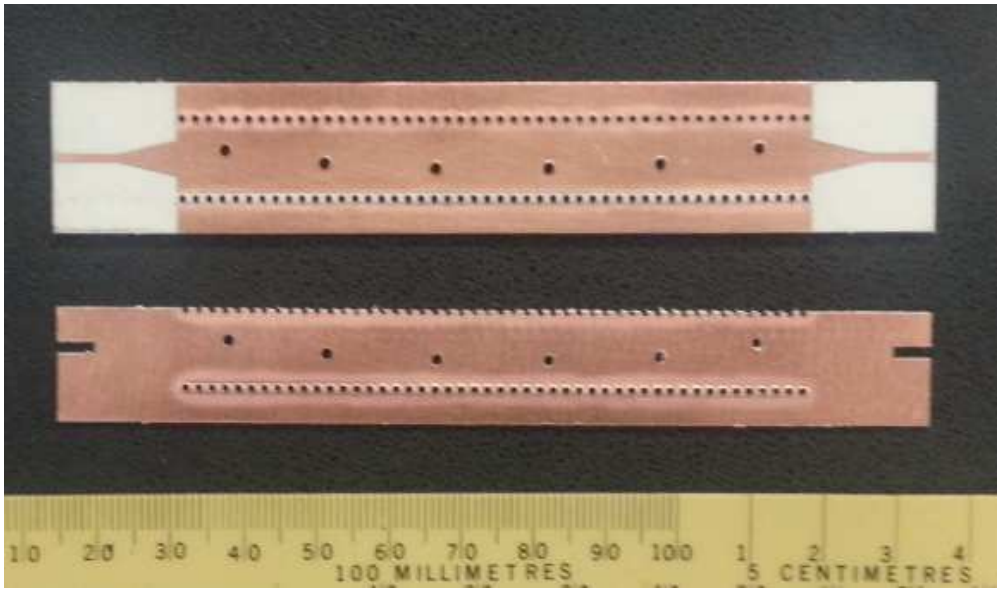

Figure 5.14. Fabricated FSIW band-pass post filter (bottom and top substrates). This figure shows the top and bottom layers of the fabricated FSIW band-pass post filter. The final filter is achieved by combining both layers together and inserting rivets into the corresponding holes. Source: Self-photographed.

5.5 Chapter Summary

In this chapter, the principle of the mode-matching method to analyse the characteristics of planar and quasi-planar transmission lines has been introduced. Applying this method to the single-mode operation of shielded microstrip lines, the influence of housing dimensions on the fundamental mode has been investigated rigorously. In particular, the relationships between the cutoff frequency of the 2^{nd}-order mode and the geometrical variables of the cross-section of the shielded transmission line have also been explored. In addition, the mode-matching method has also been utilised to analyse the characteristics of the folded substrate-integrated waveguide. It has been found that, if the length of the middle vane for the folded substrate-integrated waveguide is chosen appropriately, the first twenty modes in a folded substrate-integrated waveguide have nearly the same dispersion characteristics as a corresponding unfolded dielectric-loaded rectangular waveguide. According to this property, a novel band-pass post filter in folded substrate-integrated waveguide technology, together with an efficient and specific design procedure, has been presented. The viability and efficiency of the method has also been successfully validated by full-wave finite-element simulations using Ansys HFSS and measurements on a fabricated prototype.

In the next chapter, several three-port junctions will be introduced. Based on the various junctions, several diplexers will be presented, together with specific efficient design methods.

Chapter 6

Three-Port Junctions and Diplexers

THIS chapter starts by deriving the constraints to achieve optimum performance of diplexers employing symmetric three-port junctions. Such junctions are crucial components to be assembled with band-pass filters for the realisation of high-performance diplexers. Four types of novel three-port junctions, including two optimised Y-junctions in substrate-integrated waveguide technology, a double-layer junction in substrate-integrated waveguide technology, a Y-junction in T-type folded substrate-integrated waveguide technology, and a junction with stairs in T-type and E-type folded substrate-integrated waveguide technology, are then introduced in this chapter. Since these novel structures can satisfy the diplexer constraints well, some of them are utilised to develop specific diplexers. The viability of these designs is validated by the mode-matching method, the finite-element method, or measurements on fabricated prototypes.

6.1 Introduction

The ability to handle many channel signals is an essential requirement of efficient microwave and millimetre-wave communication systems. A diplexer is a device that separates a wider frequency band into two narrower bands, or combines frequency signals from two channels at one common port. Therefore, diplexers are often adopted in communication systems in order to reduce the manufacturing cost and minimise the dimensions. In addition, for the sake of improving the system performance, waveguide technology and substrate-integrated waveguide (SIW) technology are among the most commonly used for diplexers, as they present the advantages of low loss, low cost, and high power handling capability.

Typically, the structure of a diplexer consists of a three-port junction and two separately designed band-pass filters. Based on this configuration, several diplexers with E-plane and H-plane junctions in rectangular waveguide and SIW technology have been presented in (Dittloff and Arndt 1988, Shen *et al.* 2003, Hao *et al.* 2005). For illustration, a common rectangular waveguide diplexer, which is assembled with a T-junction, and two 6^{th}-order iris band-pass filters, is shown in Fig. 6.1.

This chapter is concerned with the designs and analysis of diplexers with three-port junctions. It is organised as follows. Section 6.2 derives the constraints for the optimum performance of diplexers which adopt symmetric three-port junctions. In Section 6.3, several junctions in SIW or folded substrate-integrated waveguide (FSIW) technology, which are able to reduce the dimensions of diplexers, are introduced. Meanwhile, all of these junctions can satisfy the derived optimal constraints well. Based on these junctions and combining with the band-pass filter design procedures introduced in Chapter 4 and 5, Section 6.4 develops corresponding diplexers with verification via full-wave simulations using Ansys High Frequency Structural Simulator (HFSS) or measurements on manufactured prototypes. The chapter ends in Section 6.5.

6.2 Constraints for the Optimum Performance of Diplexers with Symmetric Three-Port Junctions

A diplexer can be assembled with a three-port junction and two band-pass filters. Either the filter dimensions or the geometry of the junction and the distances between junction ports and the filters or both together should be considered in order for the

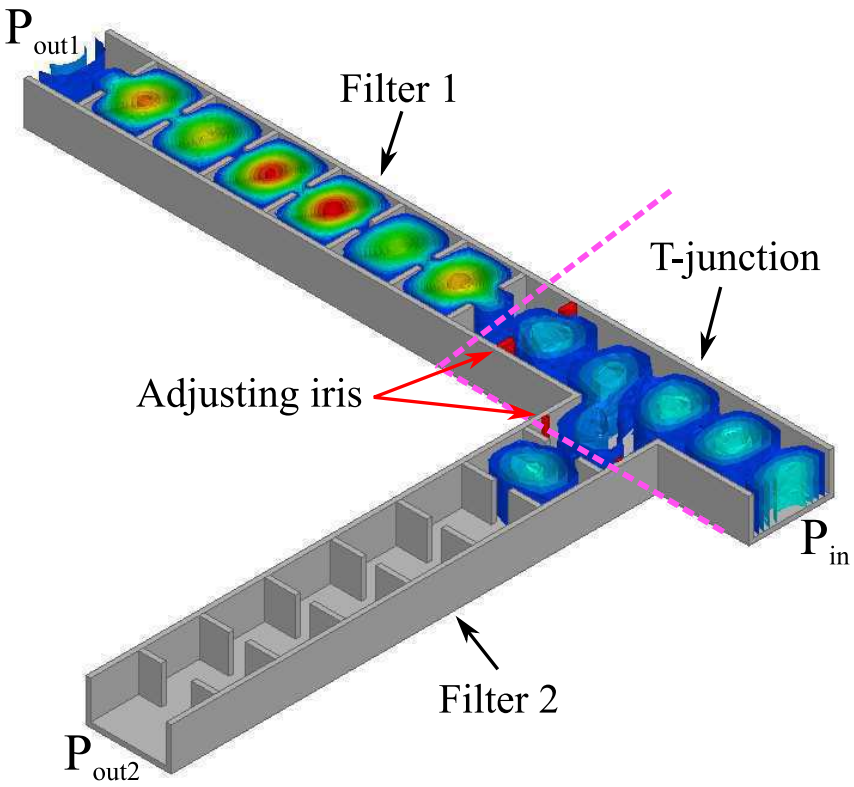

Figure 6.1. Structure of a common T-junction rectangular waveguide diplexer. This figure depicts a common rectangular waveguide diplexer which is designed with a T-junction structure and two 6^{th}-order iris band-pass filters. The red irises shown in the figure are utilised to adjust the scattering parameters of the diplexer in order to satisfy the required specifications. Source: Self-created using Ansys HFSS and Inkscape.

whole diplexer to achieve certain specified performance. The design procedure is iterative, and the optimisation process can be completed with various full-wave simulation methods, such as the finite-element method using commercial tools like Ansys HFSS or Microwave Studio from Computer Simulation Technology (CST). However, the finite-element solutions are time-consuming because of the high number of variables for the junction geometry, filter dimensions, and the distances between junction ports and filters, especially considering the requirement on mesh fineness in order to obtain results with sufficient precision.

To improve the design efficiency, the design of the junction and filters can be handled separately. For the optimisation of the three-port junction, some prescribed specifications for its characteristics and the analytical equations to compute the distances between the junction ports and the band-pass filters are briefly derived in the following. More detailed derivations are presented in (Morini and Rozzi 1996).

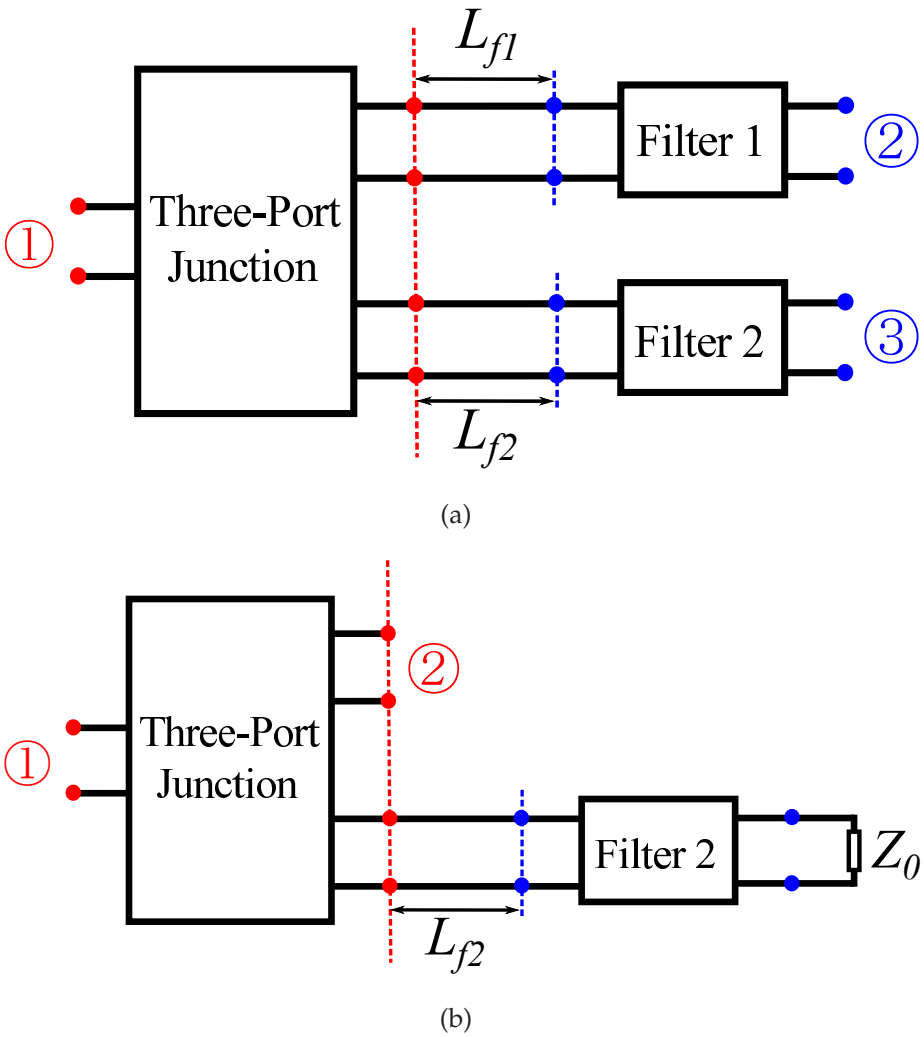

Figure 6.2. Configuration of a diplexer modelled as a lossless three-port junction and two band-pass filters. These figures show the structure of a diplexer modelled as a combination of a lossless symmetric three-port junction and two band-pass filters that are located at distance L_{f1} and L_{f2} from the junction ports, and the structure of the resulting two-port junction when Port 3 is terminated by a matched load. Source: Self-created using Inkscape.

As shown in Fig. 6.2(a), a lossless diplexer is modelled as a symmetric three-port junction and two band-pass filters which are placed at distances L_{f1} and L_{f2} from the junction ports. The passbands for the two filters are B_1 and B_2, while the centre frequencies for the two filters are f_1 and f_2 respectively.

Ideally, the propagation of electromagnetic waves in the diplexer shown in Fig. 6.2(a) requires a perfect transmission between Ports 1 and 2 over band B_1. Therefore, if Port 3 is terminated by a matched load, the resulting two-port junction should be lossless

and well matched over the band B_1, as shown in Fig. 6.2(b). Thus, the scattering matrix S for the resulting two-port structure can be expressed as below (Dobrowolski 2010)

$$S = \begin{bmatrix} S_{11} & S_{12} \\ S_{21} & S_{22} \end{bmatrix} = \begin{bmatrix} s_{11} & s_{12} \\ s_{21} & s_{22} \end{bmatrix} + \frac{1}{\frac{1}{\rho_{L_{f2}} e^{-j2\beta L_{f2}}} - s_{33}} \times \begin{bmatrix} s_{31}^2 & s_{31}s_{32} \\ s_{31}s_{32} & s_{32}^2 \end{bmatrix}, \tag{6.1}$$

where s_{ij} represents the parameters from scattering matrix s of the three-port junction, $\rho_{L_{f2}}$ represents the reflection coefficient of Filter 2, and β is the propagation constant of the fundamental mode of the waveguide feed.

A perfect transmission between Ports 1 and 2 gives $S_{22} = 0$ over the band B_1, while for a lossless junction, we have $s_{11}^* = \frac{s_{22}s_{33} - s_{32}^2}{\det(s)}$, where $\det(s)$ is the determinant of the scattering matrix s. Under the assumptions of perfect transmission and lossless junction, we can obtain from Eq. 6.1,

$$\rho_{L_{f2}} e^{-j2\beta L_{f2}} = \frac{s_{22}}{s_{22}s_{33} - s_{32}^2} = \frac{s_{22}}{\det(s) s_{11}^*}. \tag{6.2}$$

Band B_1 should be the stopband for Filter 2. Thus, the magnitude of the reflection coefficient of Filter 2 over band B_1 can be approximated as 1, that is, $|\rho_{L_{f2}}| \cong 1$. Meanwhile, for a lossless network, we can derive $|\det(s)| = 1$ from the unitary property (Pozar 2011). Therefore, according to Eq. 6.2, the condition below is required over the band B_1

$$|s_{11}| = |s_{22}|. \tag{6.3}$$

Secondly, the diplexer also requires a perfect transmission between Ports 1 and 3 over band B_2. Hence, in a similar way, the other requirement should be satisfied over the band B_2

$$|s_{11}| = |s_{33}|. \tag{6.4}$$

Hence, the combination of Eq. 6.3 and 6.4 implies that, in order to achieve the optimum performance of diplexers, the characteristics for a three-port junction should satisfy the following specification

$$|s_{11}| = |s_{22}| = |s_{33}|. \tag{6.5}$$

Furthermore, considering symmetric three-port waveguide junctions, such as T-junctions (Kordiboroujeni and Bornemann 2015b, Chen *et al.* 2015a), Y-junctions (Vanin *et al.* 2004, Vanin *et al.* 2010), and other junctions described in (Dittloff and Arndt 1989, Morini and Rozzi 1995, Kordiboroujeni and Bornemann 2015a), with

different excitation polarisation in reference to the symmetry plane, we have (Morini 1997)

$$\begin{aligned} s_{21} &= s_{31}, \qquad \text{or} \\ s_{21} &= -s_{31}, \end{aligned} \tag{6.6}$$

To continue the derivation, we consider the junctions whose $s_{21} = s_{31}$ first. The reflection coefficient for Port 2, which is corresponding to an even and an odd excitation at Ports 2 and 3, can be defined by Γ_{even} and Γ_{odd}. Thus, we obtain

$$\begin{aligned} s_{22} &= \frac{\Gamma_{even} + \Gamma_{odd}}{2}, \\ s_{23} &= \frac{\Gamma_{even} - \Gamma_{odd}}{2}. \end{aligned} \tag{6.7}$$

In addition, because of the lossless three-port junction and by utilising Eq. 6.3 and 6.7, we can further derive that

$$\begin{aligned} s_{11} &= -\frac{s_{21}}{s_{21}^*}(s_{22}^* + s_{23}^*), \\ |s_{11}| &= |\Gamma_{even}|, \\ |\Gamma_{even}| &= |\frac{\Gamma_{even} + \Gamma_{odd}}{2}|. \end{aligned} \tag{6.8}$$

Since the value for $|\Gamma_{odd}|$ can be demonstrated to be 1, and the minimum for s_{22} can be achieved when the phases for Γ_{even} and Γ_{odd} are opposite, it follows that

$$\begin{aligned} |\frac{\Gamma_{even} + \Gamma_{odd}}{2}| &\geq \frac{1 - |\Gamma_{even}|}{2}, \\ |s_{11}| = |\Gamma_{even}| &\geq \frac{1}{3}, \end{aligned} \tag{6.9}$$

which is a necessary condition to meet the specification expressed in Eq. 6.5. Besides, $|s_{11}| = \frac{1}{3}$ is preferable, because less reflection at Port 1 is desired.

For the junctions having $s_{21} = -s_{31}$, a similar method can be applied while exchanging Γ_{even} and Γ_{odd}, which yields the same result.

The distances L_{f1} and L_{f2} between the junction ports and the input location of the band-pass filters are two further variables that influence the performance of the diplexers. According to Eq. 6.2, to meet the requirements for perfect transmission between Ports 1 and 2 and Ports 1 and 3 at the frequencies f_2 and f_1, the distances L_{f1} and L_{f2}

can be derived as the following

$$\begin{aligned} L_{f1} &= -\frac{1}{2j\beta}\ln[\frac{s_{33}}{\Delta s s_{11}^{*}\rho_{L_{f1}}}], \quad f = f_2, \\ L_{f2} &= -\frac{1}{2j\beta}\ln[\frac{s_{22}}{\Delta s s_{11}^{*}\rho_{L_{f2}}}], \quad f = f_1. \end{aligned} \tag{6.10}$$

To sum up, in order for the designed diplexer to achieve optimum performance, the characteristics of the adopted three-port junction should satisfy Eq. 6.5 and 6.9 by adjusting the junction geometry. Meanwhile, Eq. 6.10 can be utilised to decide where the two band-pass filters should be positioned from the junction ports. It is noted that, for simplicity, the analysis above is based on a model which only considers the fundamental mode interaction. For the cases where the high order modes also play some role, the fundamental mode results can still be the initial points for an optimisation procedure.

6.3 Novel Three-Port Junctions

As mentioned, diplexers are an essential part of microwave and millimetre-wave systems and can be realised by assembling a three-port junction and two band-pass filters. Rectangular waveguide junctions, such as T-junctions, and Y-junctions, are often adopted to design diplexers, because of the advantages of low loss and high power handling capability. However, the application of these junctions is often limited by their high cost, bulky volume, and difficult integration with other components.

In order to overcome these shortcomings, the SIW has been developed because of the added advantages of low cost, significant reduction in size, and easy integration with other planar circuits. Moreover, the FSIW is another geometry option which can further reduce the dimensions, especially for applications in microwave and millimetre-wave systems whose volume is limited by system considerations.

Based on these technologies, several three-port SIW or FSIW junctions are developed in this section. In addition, it is shown that the characteristics of these junctions can satisfy the constraints for the optimum performance of diplexers.

6.3.1 Optimised Y-Junctions

The characteristics of a Y-junction can satisfy conveniently the constraints for optimum performance of diplexers (Morini and Rozzi 1996). Thus, the structure is often utilised

for designing diplexers (Shimonov *et al.* 2010, Vanin *et al.* 2010). To reduce the dimension of a Y-junction based diplexer, the two output branches of the junction can be configured in parallel by connecting them with two bends as shown in Fig. 6.3(a). To analyse efficiently the characteristics of the Y-junction with bends with the mode-matching method (MMM), the first step is to model the post walls as equivalent solid wall. Here, the empirical analytical equation Eq. 4.1 is employed again, which expresses the equivalent width W_e as

$$W_e = W_i - \frac{d_1^2}{0.95p}, \tag{6.11}$$

where d_1 is the via diameter, p is the interval between two adjacent vias, and W_i is the physical width of the SIW, measured as distance between the centres of the two via rows.

For the following analysis, as shown in Fig. 6.3(a), we consider an example with an equivalent width $W_e = 18\,\text{mm}$, a substrate with thickness $b = 0.762\,\text{mm}$ and relative permittivity $\varepsilon_r = 2.94$, and an angle $\varphi = 120^\circ$ between the output branches of the Y-junction. For efficient modelling, the junction can be considered as the combination of a series of symmetric H-plane steps and bifurcation steps in the dielectric-loaded rectangular waveguide as shown in Fig. 6.3(b). Based on the MMM reported in Chapter 3 and 4, the scattering matrices of the H-plane steps and the bifurcation steps in the dielectric-loaded rectangular waveguide can be calculated accurately and quickly. Thus, the scattering matrix of the three-port junction is obtained through cascading these matrices. As shown in Fig. 6.4, compared with the reflection coefficients of an original (unbent) Y-junction, the mode-matching calculated results show that the reflection coefficients for Y-junction with bends do not match well with the constraints to achieve the optimum performance of diplexers, that is, $|S_{11}| = |S_{22}| = |S_{33}|$ over the operation bands for the up and down channels. This can be understood considering that the three-way symmetry is broken in the bent structure. Besides, in the figure, it is observed that adjusting the length L_b of the branch before the bend from 3 mm to 8 mm cannot improve the performance.

In order to improve the characteristics of the bent Y-junction, two novel structures are proposed and given in Fig. 6.5(a) and (b). The first improved Y-junction includes a change of the output branch angle φ_1. As shown in Fig. 6.6(a), when adjusting the length $L_{b1} = 11.5\,\text{mm}$, and the angle $\varphi_1 = 100^\circ$, the characteristics of the Y-junction are improved, since the curves of $|S_{11}|$, $|S_{22}|$, and $|S_{33}|$ almost coincide from 7 GHz to

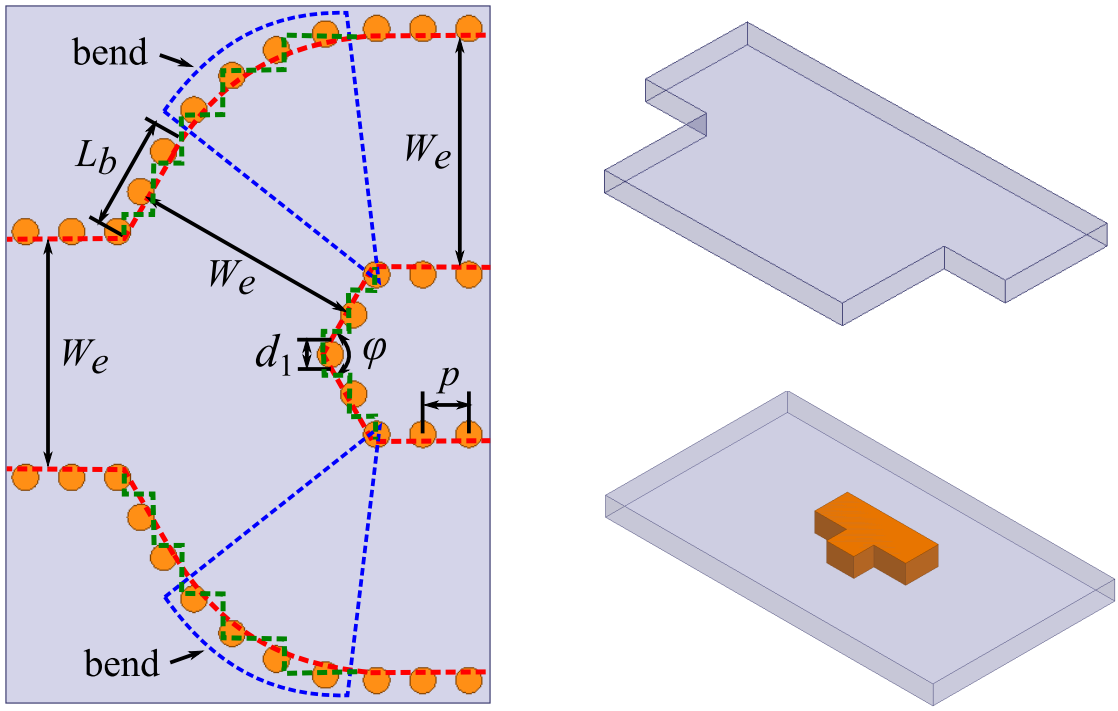

Figure 6.3. Structures of (a) a Y-junction with two bends, and (b) its approximation steps including an H-plane step and a bifurcation step in a dielectric-loaded rectangular waveguide. This figures show a Y-junction with two bends which can reduce the junction dimension, and the approximation elements including an H-plane step and a bifurcation step in a dielectric-loaded rectangular waveguide. The Y-junction with bends structure is realised in SIW technology using rivets with diameter d_1. Source: Self-created using Ansys HFSS and Inkscape.

8.5 GHz, that is, in a range which covers the required operation bands of the diplexer. The second improved Y-junction keeps the output branch angle $\varphi_2 = 120^\circ$ and adjusts the positions of two additional inserted vias with a diameter of d_2. As shown in Fig. 6.6(b), when the length $L_{b2} = 6.3\,\text{mm}$, the tuning via diameter $d_2 = 1\,\text{mm}$, the angle $\Theta = 56.2^\circ$, and the length $L_a = 16.95\,\text{mm}$, the mode-matching calculated $|S_{11}|$, $|S_{22}|$, and $|S_{33}|$ also meet the constraints for optimum performance of diplexer design well in the bands of operation.

In conclusion, the characteristics of Y-junction can meet the constraints for achieving optimum performance of diplexers. However, bends which are utilised to reduce the junction dimensions degrade the performance. In order to overcome the problems, two novel junctions have been proposed. With the dimensions listed in Table 6.1, both

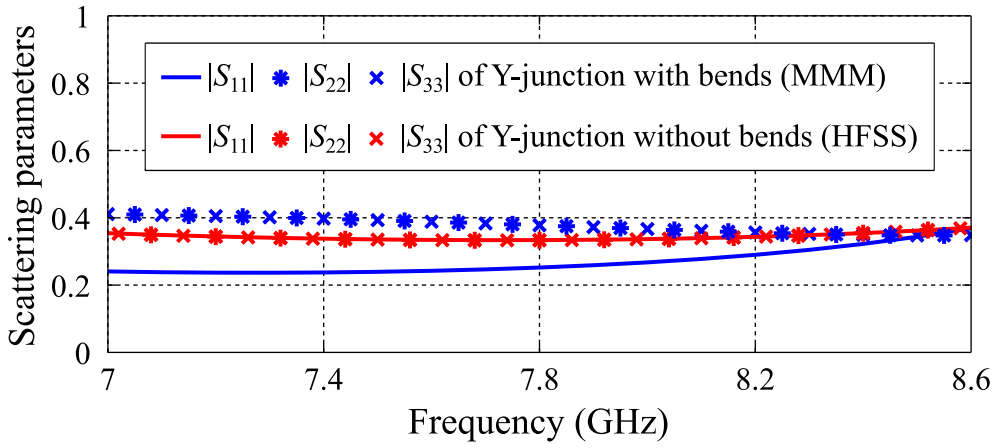

(a) $L_b = 3\,\text{mm}$

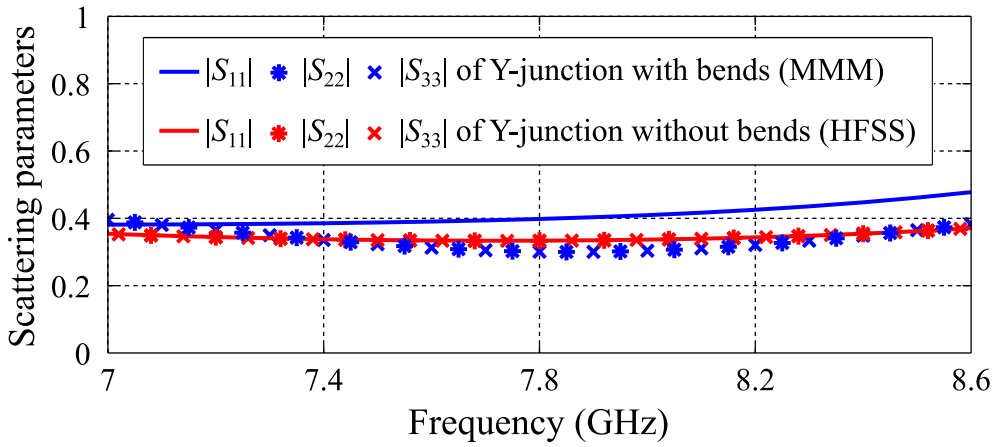

(b) $L_b = 8\,\text{mm}$

Figure 6.4. Comparison between scattering parameters ($|S_{11}|$, $|S_{22}|$, and $|S_{33}|$) of Y-junction with bends calculated using the MMM and those of Y-junction without bends obtained using Ansys HFSS when (a) $L_b = 3\,\text{mm}$, and (b) $L_b = 8\,\text{mm}$. These figures compare the characteristics of Y-junction with and without bends obtained using the MMM and the finite-element method using Ansys HFSS respectively. Obviously, the reflection coefficients for Y-junction with bends do not match well with the constraints for the optimum performance of diplexers. In addition, adjusting the length L_b of the branch before the bend from 3 mm to 8 mm cannot improve the performance. Source: Self-created using Matlab.

methods, including tuning the output branch angle and adjusting the positions of inserted vias, can improve the characteristics.

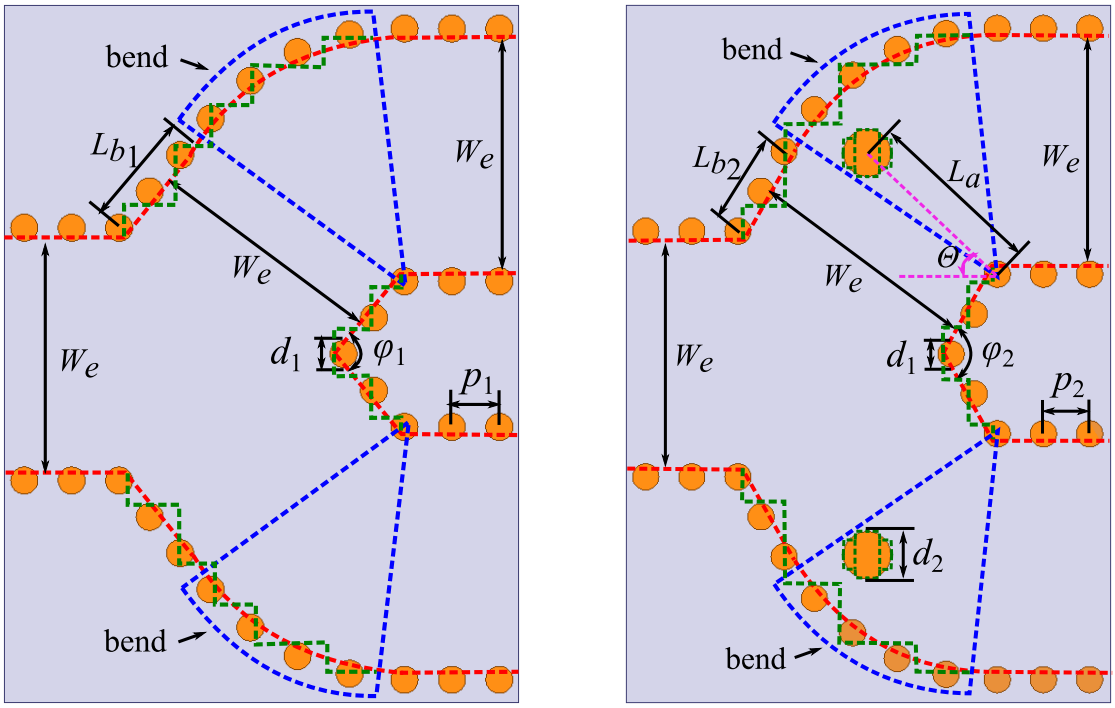

(a) Improved Y-junction 1 (b) Improved Y-junction 2

Figure 6.5. Structures of Y-junctions improved by (a) tuning the output branch angle φ_1 and (b) inserting vias into the junction. This figures show two novel Y-junction structures whose characteristics are improved by tuning the output branch angle φ_1 and adjusting the positions Θ, L_a for the two additional vias inserted into the junction. Source: Self-created using Ansys HFSS and Inkscape.

6.3.2 Double-Layer Junction

The double-layer three-port junction is another possible structure which can significantly decrease the dimension. This type of junction can be realised with two pieces of laminates, which are stacked and fixed together by inserting vias. As shown in Fig. 6.7(a), d is the rivet diameter, p is the interval between two adjacent vias, W_i is the physical width of the SIW, measured as the distance between the centres of the two via rows, b is the thickness of the substrates, and g_s is the width of the coupling slot between layers. Based on the empirical analytical equation (6.11), the double-layer three-port SIW junction can be transformed into its equivalent solid-wall model as shown in Fig. 6.7(b).

To analyse the characteristics of the converted junction shown in Fig. 6.7(b), we consider an example with an equivalent width $W_e = 18\,\text{mm}$, substrates with thickness $b = 0.762\,\text{mm}$ and relative permittivity $\varepsilon_r = 2.94$, and a metal vane of thickness

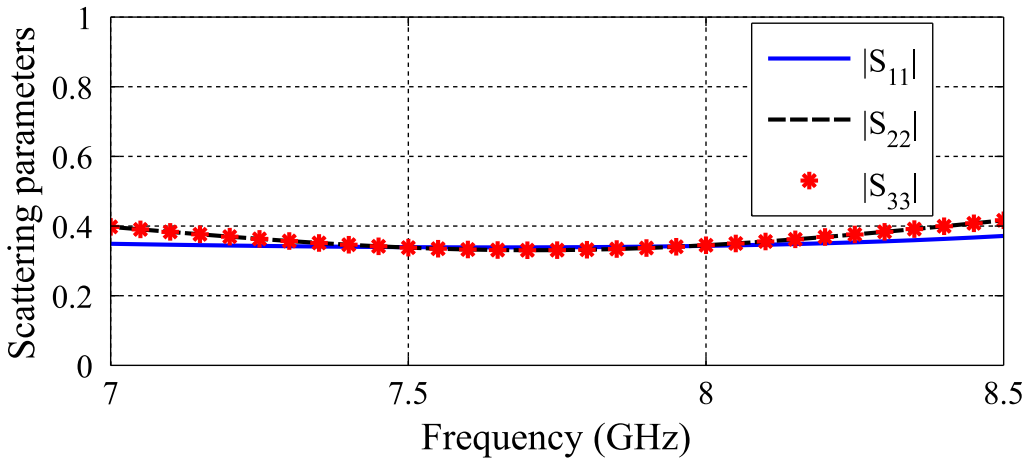

(a)

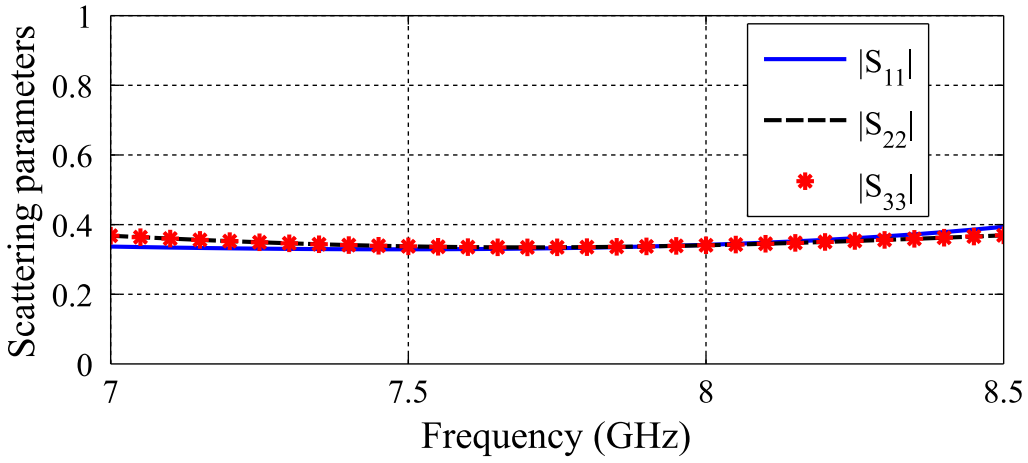

(b)

Figure 6.6. Scattering parameters obtained using the MMM for (a) improved Y-junction 1 and (b) improved Y-junction 2. These figures show the scattering parameters $|S_{11}|$, $|S_{22}|$, and $|S_{33}|$ for the two improved Y-junctions. Both methods are able to improve the junction performance, that is, the constraints for the optimum performance of diplexers can be satisfied. Source: Self-created using Matlab.

$t = 18\,\mu m$ that isolates the top and bottom layers. Thus, the width g_s of the coupling slot is the unique variable that can be adjusted so that the scattering parameters $|S_{11}|$, $|S_{22}|$, and $|S_{33}|$ of the junction are able to meet the constraints to achieve the optimum performance of diplexers.

For efficient modelling, the double-layer junction can be considered as the combination of an E-plane waveguide step, a normal rectangular waveguide, and an E-plane waveguide bifurcation as shown in Fig. 6.8. Based on the MMM reported in Chapter 3 and 4,

Table 6.1. Sizes of improved Y-junctions (Units: mm or degree). The table gives the dimensions for the two improved Y-junctions, including the equivalent width W_e for the SIW, the diameters d_1 and d_2 of the vias, the intervals p_1 and p_2 between adjacent vias, the output branch angles φ_1 and φ_2, and L_a and Θ which are utilised to define the positions of the tuning vias in the second Y-junction.

W_e	b	L_{b1}	L_{b2}	φ_1	φ_2	Θ	L_a	p_1	p_2	d_1	d_2
18.00	0.762	11.50	6.30	100	120	56.2	16.95	1.60	1.90	1.00	1.00

the scattering matrices of the three elements can be calculated accurately and quickly. Thus, the scattering matrix of the double-layer three-port junction can be obtained by cascading these matrices.

By varying the width g_s of the coupling slot in the middle of the junction from 0.1 mm and 2.0 mm, the scattering parameters $|S_{11}|$, $|S_{22}|$, and $|S_{33}|$ are investigated using the MMM. As shown in Fig. 6.9, for a prescribed width g_s of the coupling slot, as the frequency increases, the curves of the reflection coefficients gradually spread apart. In other words, the differences of $|S_{11}|$, $|S_{22}|$, and $|S_{33}|$ become larger. Meanwhile, for a given frequency (for example, 9.5 GHz), when the width g_s of the coupling slot is narrow (0.1 mm), the reflection coefficient $|S_{22}|$ was the same as $|S_{11}|$ initially. However, when progressively increasing the width g_s of the coupling slot, $|S_{22}|$ trends to be identical to $|S_{33}|$ instead. Importantly, as shown in Fig. 6.9(b), when the width of the coupling slot $g_s = 0.45$ mm, the characteristics of the double-plane three-port junction can satisfy well the constraints for achieving optimum performance of diplexers, that is, $|S_{11}| = |S_{22}| = |S_{33}|$ over a wide frequency band. Compared to the optimised Y-junction introduced in last subsection, the band with satisfactory performance is even wider. As a result, the flexibility in the choice for the bands of the up and down channels in diplexer design employing a double-plane junction can be increased greatly.

6.3.3 Y-junction in Folded Substrate-Integrated Waveguide Technology

As mentioned in Subsection 6.3.1, Y-junctions are often adopted to design diplexers, since the structures can satisfy easily the constraints for optimum performance of

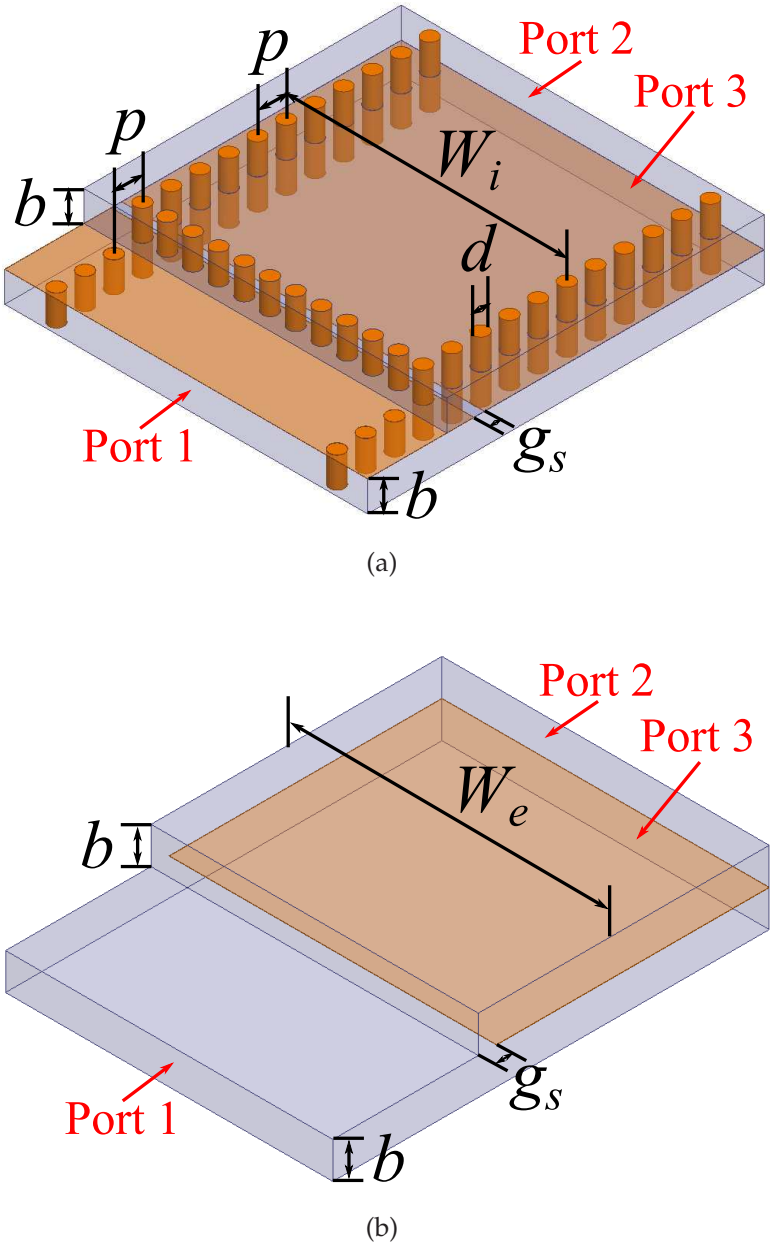

Figure 6.7. Structures of (a) a double-layer three-port SIW junction and (b) its equivalent model. The top figure (a) shows the structure of a double-layer three-port SIW junction which can be realised with two pieces of laminates and via walls. Base on the empirical analytical equation Eq. 6.11, the equivalent model of the junction is also obtained in the bottom figure (b). Source: Self-created using Ansys HFSS and Inkscape.

diplexers. Compared with diplexers in rectangular waveguide technology, although the size of diplexers can be greatly reduced by utilising SIW technology, further size reduction is still required in some microwave and millimetre-wave systems whose volume is restricted.

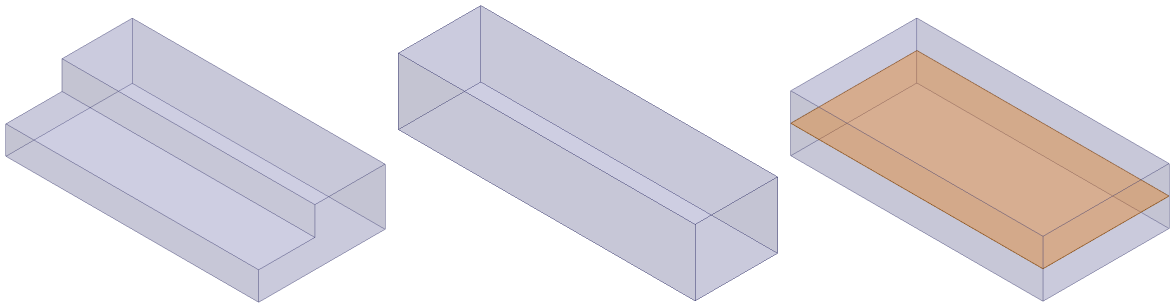

(a) (b) (c)

Figure 6.8. Elements used to form a double-layer three-port junction. These figures show the elements, including an (a) E-plane waveguide step, (b) a normal rectangular waveguide and (c) an E-plane waveguide bifurcation, that can be utilised to construct a double-layer three-port junction. Source: Self-created using Ansys HFSS.

In this perspective, a novel Y-junction that utilises FSIWs, is proposed in this subsection. As shown in Fig. 6.10(a), the junctions consists of three symmetric T-type FSIW branches which can be formed by folding the via walls to the centre of the SIW. Compared with the common SIW Y-junction shown in Fig. 6.10(b), obviously, the height is doubled, but the width is reduced significantly.

The characteristics of the Y-junctions in FSIW and SIW technology are analysed here with the finite-element method using Ansys HFSS. In order to investigate the characteristics efficiently, the first step is to model the post walls as equivalent solid walls through applying Eq. 6.11. Thus, the FSIWs and SIWs of the Y-junction can be transformed into equivalent dielectric-loaded folded rectangular waveguides and unfolded rectangular waveguides. The cross-sections of the equivalent waveguides are shown in Fig. 6.11(a) and (b).

For the following analysis, we first consider an unfolded rectangular waveguide Y-junction with dielectric loading corresponding to a substrate with thickness $b = 0.762\,\text{mm}$ and relative permittivity $\varepsilon_r = 2.94$. The cross-section of the waveguide is then chosen with a width of $W_e = 20.32\,\text{mm}$ corresponding to a cutoff frequency 4.30 GHz, which is the same as that of a standard C-band (extending from 5.85 GHz to 8.2 GHz) WR-137 waveguide. A folded rectangular waveguide Y-junction, whose middle metal vane has a thickness of 17.5 µm, is then considered. The width W'_{e1} and W'_{e2} of the cross-section for the folded rectangular waveguide Y-junction are chosen according to the relationship $W'_{e1} + 2W'_{e2} = W_e$. Importantly for convenient analysis of the folded structure, the width c of the middle vane can be selected in a parametric analysis so

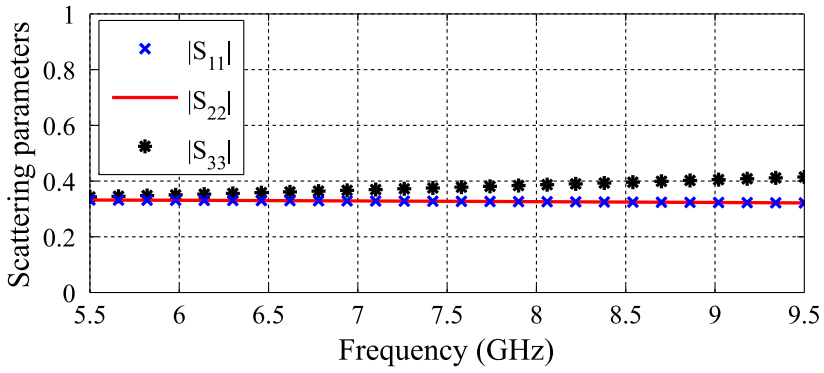

(a) $g_s = 0.1\,\text{mm}$

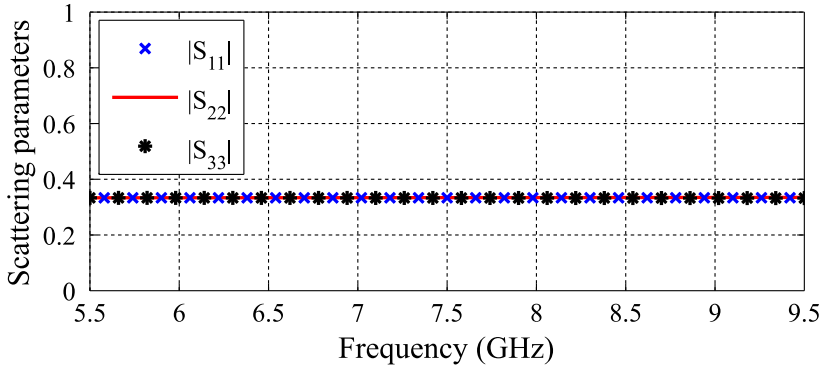

(b) $g_s = 0.45\,\text{mm}$

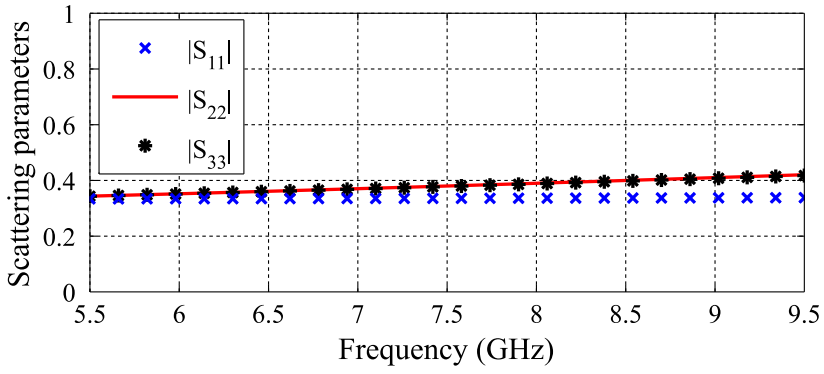

(c) $g_s = 2.0\,\text{mm}$

Figure 6.9. Characteristics of the double-layer three-port junction when the width g_s of the coupling slot is 0.1 mm, 0.45 mm, and 2.0 mm. These figures compare the characteristics of double-layer three-port junction when the width g_s of the coupling slot is 0.1 mm, 0.45 mm, and 2.0 mm respectively. It is found that, when the width $g_s = 0.45\,\text{mm}$, the scattering parameters $|S_{11}|$, $|S_{22}|$, and $|S_{33}|$ can satisfy the constraints for optimum performance of diplexers over a frequency band extending from 5.5 GHz to 9.5 GHz. Source: Self-created using Matlab.

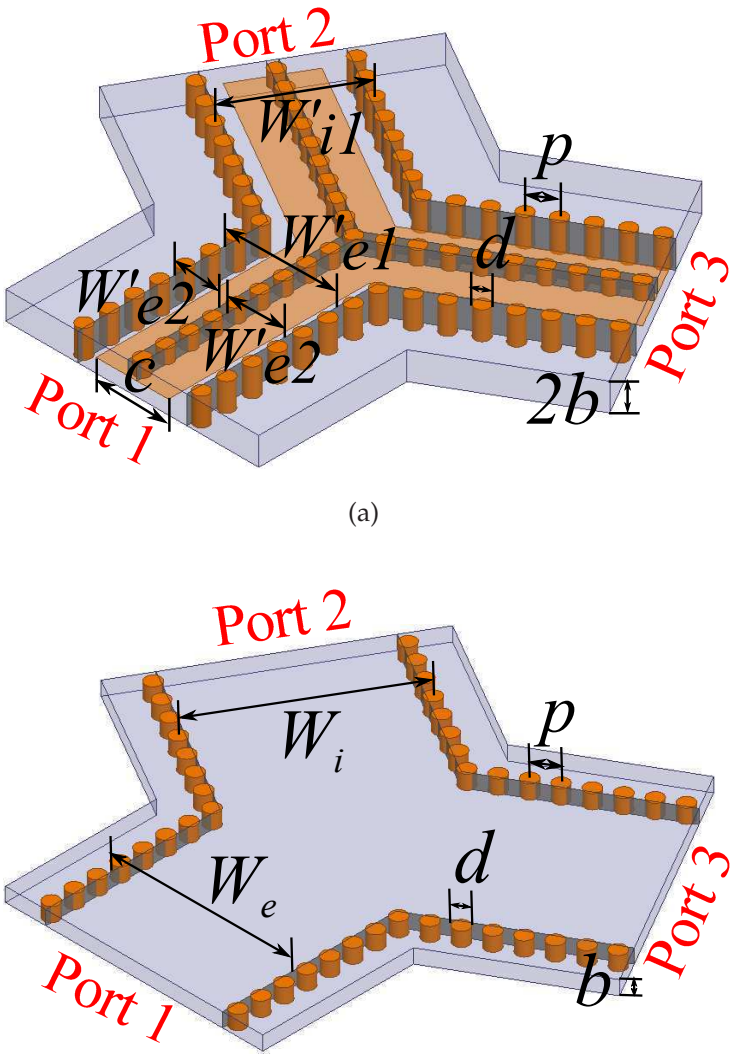

Figure 6.10. Structure of Y-junction realised in: (a) FSIW technology, and (b) SIW technology. The top figure (a) shows a novel Y-junction which is formed by three T-type FSIW branches. Compared with the common SIW Y-junction in the bottom figure (b), the height is doubled, while the width is reduced. Source: Self-created using Ansys HFSS and Inkscape.

that the phase constant of the fundamental mode in the folded rectangular waveguide matches that in the unfolded rectangular waveguide. From these considerations, the widths $W'_{e1} = 10.41\,\text{mm}$, $W'_{e2} = 4.955\,\text{mm}$, and $c = 9.45\,\text{mm}$ are then determined. It is noted that, with the dimensions provided above, the phase constants of the first 18 modes in both waveguides are nearly identical as shown in Fig. 6.12.

Based on those waveguide dimensions, the characteristics of the folded and unfolded Y-junctions with 120° branches are analysed with lossless simulations using Ansys

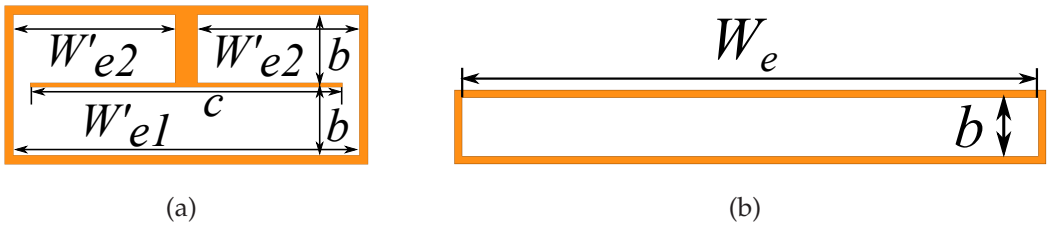

Figure 6.11. Cross-sections of equivalent solid-wall (a) folded waveguide and (b) unfolded waveguide. These figures show the cross-sections of a solid-wall folded waveguide and its equivalent unfolded waveguide, which can be utilised to form Y-junctions. Source: Self-created using Ansys HFSS and Inkscape.

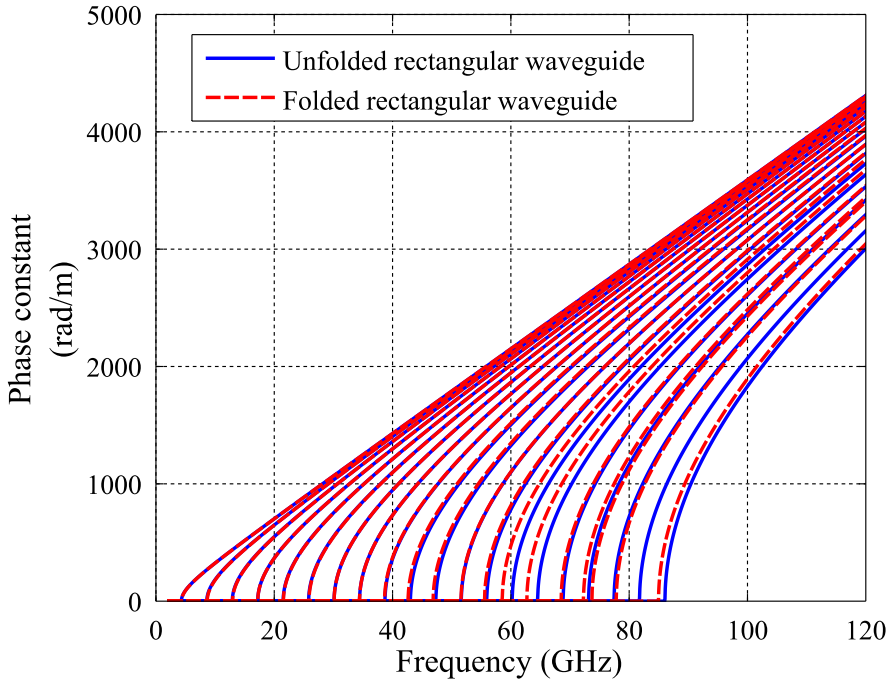

Figure 6.12. Comparison between the first twenty modes' phase constants of the folded rectangular waveguide and the corresponding modes of the unfolded rectangular waveguide. This figure compares the phase constants for the first twenty modes in a folded rectangular waveguide and the corresponding unfolded rectangular waveguide. It is found that, if the dimensions for the folded retangular waveguide are chosen reasonably, the phase constants of the first eighteen modes in both waveguides show similar characteristics. Source: Self-created using Ansys HFSS and Matlab.

HFSS. As shown in Fig. 6.13, the reflection coefficients of each branch port for an unfolded rectangular waveguide junction satisfy well the constraints for optimum performance of diplexers from 6 GHz to 7.5 GHz, that is, $|S_{11}| = |S_{22}| = |S_{33}|$, and $|S_{11}| \geq \frac{1}{3}$, preferably $|S_{11}| = \frac{1}{3}$. Compared with the characteristics of the unfolded Y-junction,

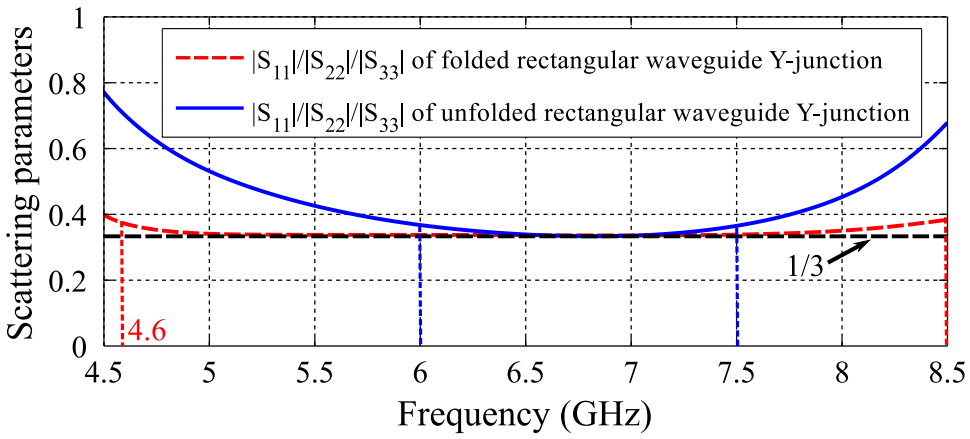

Figure 6.13. Scattering parameters of the folded and unfolded rectangular waveguide Y-junction with 120° angles. This figure shows reflection coefficients of each branch port for a unfolded Y-junction and a folded Y-junction. It is found that, compared with unfolded Y-junction, the folded Y-junction can meet the constraints to optimum performance of diplexers over a wider frequency band. Source: Self-created using Ansys HFSS and Matlab.

the folded Y-junction shows satisfactory performance over a wider frequency range. This maybe is because of the different central structures and the excited high-order modes (after the first eighteen modes) in the two Y-junctions. In the figure, the reflection coefficients of each branch port for the folded rectangular waveguide meet the diplexer constraints in a frequency band extending from 4.6 GHz to 8.5 GHz. This wider bandwidth adds flexibility into the selection of the up and down channel bands for a diplexer realised in a folded Y-junction with 120° angle.

The tolerance associated with the width and the thickness of the middle vane are investigated next, as these are specific to the folded geometry. As shown in Fig. 6.14(a), varying the width of the middle vane from 9.4 mm to 9.5 mm does not have a significant effect on the Y-junction performance. In contrast, the reflection coefficients are slightly more sensitive to the thickness of the middle vane. As show in Fig. 6.14(b), for the nominal width of the middle vane, a variation of the vane thickness from 17.5 µm to 70.0 µm, can have a measurable effect on the reflection coefficient. This needs to be considered in the choice of technology used in realisation of the device.

To sum up, this subsection presents a novel FSIW Y-junction. Compared with the unfolded Y-junction, the reflection coefficients of 120° branch ports for the folded Y-junction can satisfy the constraints for optimum performance of diplexers well over

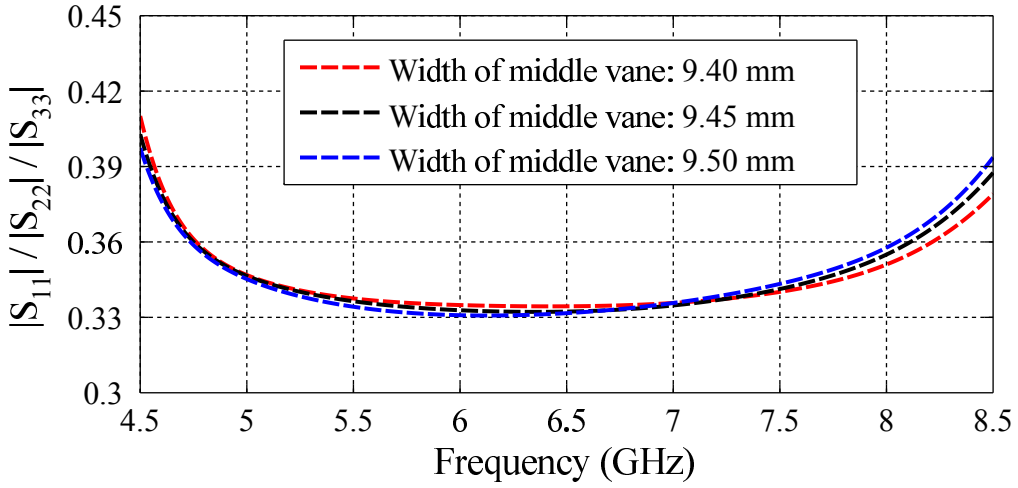

(a)

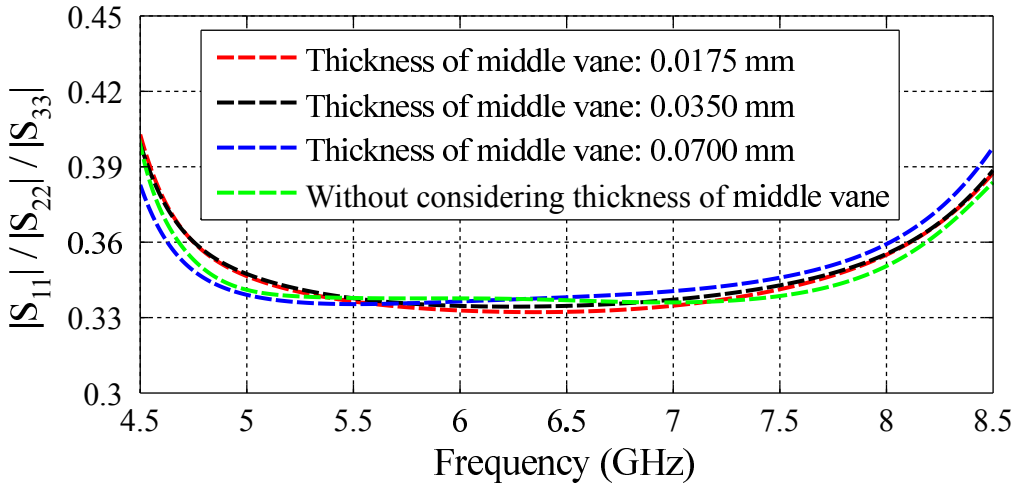

(b)

Figure 6.14. Influence on reflection coefficients caused by variations of (a) the width and (b) the thickness of the middle vane. These figures show the influence on reflection coefficients caused by variations of the width and the thickness of the middle vane. It is found that, compared with the influence caused by the width errors, the reflection coefficients are slightly more sensitive to the thickness variations. Source: Self-created using Ansys HFSS and Inkscape.

a wider frequency band. It means that, if the novel structure is applied in diplexer designs, the up and down channel bands can be chosen in a wider range.

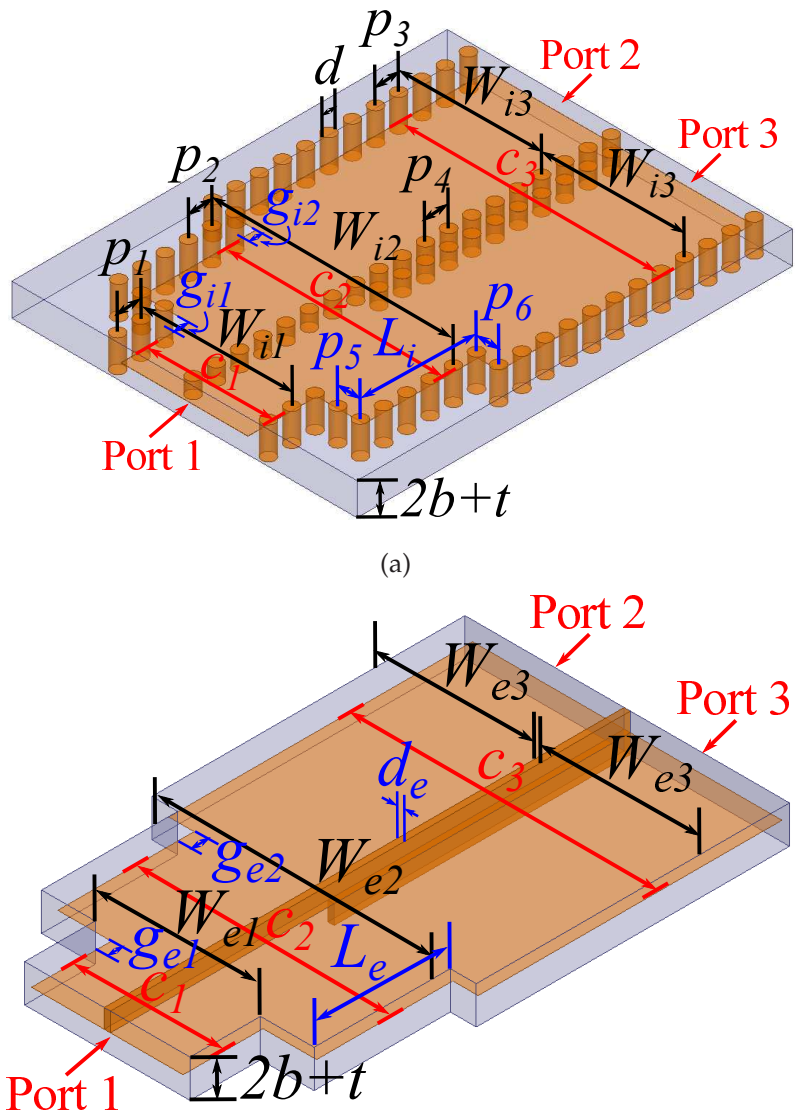

Figure 6.15. Structures of a symmetric three-port junction formed with T-type and E-type FSIWs and its equivalent model. The top figure (a) shows the structure of a symmetric three-port junction in T-type and E-type FSIW technology. By transforming the post walls in the structure into solid walls, its equivalent model can be obtained in the bottom figure (b). Source: Self-created using Ansys HFSS and Inkscape.

6.3.4 Junction with stairs in Folded Substrate-Integrated Waveguide Technology

A novel Y-junction in FSIW technology has been introduced in the last subsection. Compared to the common Y-junction in SIW technology, the dimensions of the structure have been significantly reduced because of the application of T-type FSIWs. Another symmetric three-port junction in FSIW technology can be formed with a T-type

FSIW and two E-type FSIWs (Fig. 5.6) whose characteristics have been analysed in Chapter 5. As shown in Fig. 6.15(a), a two-step T-type FSIW is set as the common feed port of the three-port junction, while the other two E-type FSIWs form the remaining output ports. In addition, in the figure, d is the diameter of the via, p_1, p_2, p_3, p_4, p_5, and p_6 are intervals between adjacent vias, W_{i1} and W_{i2} represent the physical widths for the first and second steps of T-type FSIWs, measured as distance between the centres of the two via rows, while W_{i3} is the physical width for the E-type FSIWs. The three-port junction is equally divided into top and bottom layers by the middle metal vane. The thickness of the top or bottom substrate is marked as b, while the thickness of the middle metal vane is defined as t. Moreover, c_1, c_2, and c_3 are used to represent the widths of the middle metal vane in T-type or E-type FSIWs. L_i is the length for the second step of T-type FSIW, while g_{i1} and g_{i2} are the distances between the edges of the middle metal vane and the centres of the vias.

The finite-element method using Ansys HFSS can again be employed here to analyse the characteristics of the proposed FSIW junction. However, this approach is time-consuming because of the high number of variables and the quantity of vias, especially when considering the requirement on mesh fineness in order to obtain results with sufficient precision. Thus, in order to improve the efficiency, the first step is to model the post walls as equivalent solid walls using Eq. 6.11. As shown in Fig. 6.15(b), W_{e1} and W_{e2} represent the equivalent widths for the first and second step of T-type dielectric-loaded folded rectangular waveguides, while W_{e3} is the equivalent width for the E-type dielectric-loaded folded rectangular waveguides. The variables c_1, c_2, and c_3 still represent the widths of the middle metal vane in T-type or E-type folded rectangular waveguides. The width d_e is the equivalent width of the post walls which are utilised to form T-type folded rectangular waveguides and isolate the two E-type folded rectangular waveguides. L_e is the equivalent length for the second step of the T-type folded rectangular waveguide. g_{e1} and g_{e2} denote the distances between the edges of the middle metal vane and the converted solid walls.

For the following analysis, as shown in Fig. 6.15(b), we consider an example with a middle metal vane with thickness $t = 18\,\mu\text{m}$, and substrates with thickness $b = 0.762\,\text{mm}$ and relative permittivity $\varepsilon_r = 2.94$. Because of the large number of variables, the dimensions for the first step of T-type folded rectangular waveguide and the E-type folded rectangular waveguides are first determined in order to simplify the adjusting process in the full-wave simulations using Ansys HFSS. According to the

approach presented in Subsection 6.3.3, for the first step of T-type folded rectangular waveguide, if the equivalent width d_e is chosen as 0.6 mm, the equivalent width W_{e1} for the folded rectangular waveguide and the width c_1 for the middle metal vane are determined as 10.76 mm and 9.88 mm respectively. Therefore, the fundamental mode is able to operate over frequency band extending from 4.5 GHz to 8.0 GHz, since with these dimensions the cutoff frequencies for the 1^{st}- and 2^{nd}-order modes are 4.16 GHz and 8.26 GHz respectively. Similarly, based on the method introduced in Subsection 5.4.1, for the E-type folded rectangular waveguide, the equivalent width W_{e3} for the rectangular waveguide and the width c_3 for the middle metal vane are chosen as 10.16 mm and 19.96 mm respectively. Therefore, the fundamental mode in the E-type folded rectangular waveguide also can work over the frequency band extending from 4.5 GHz to 8.0 GHz, because the cutoff frequencies for the first two modes are 4.30 GHz and 8.60 GHz.

Up to this point, the remaining variables shown in Fig. 6.15(b) that can influence the characteristics of the three-port FSIW junction include the equivalent length L_e for the second step of T-type folded rectangular waveguide, the width c_2 for the middle metal vane in the second step of T-type folded rectangular waveguide, and the gaps g_{e1} and g_{e2} between the edges of the middle metal vane and the converted solid walls. Adjusting these four variables with the finite-element method using Ansys HFSS, it is found that, when $L_e = 8.70$ mm, $c_2 = 16.92$ mm, $g_{e1} = 0.60$ mm, and $g_{e2} = 0.60$ mm, the reflection coefficients for the three junction ports can satisfy the constraints for the optimum performance of diplexers, that is, $|S_{11}| = |S_{22}| = |S_{33}|$, and $|S_{11}| \geq \frac{1}{3}$, preferably $|S_{11}| = \frac{1}{3}$, over the frequency band extending from 5.3 GHz to 6.8 GHz as shown in Fig. 6.16

Obviously, if the required up and down channels for a diplexer design can be included by the frequency band extending from 5.3 GHz to 6.8 GHz, the proposed FSIW junction example is a reasonable option to realise the diplexer. It is noted that the position and range of the frequency band that satisfies the constraints for optimum performance of diplexers can be modified by adjusting the four variables, that is, L_e, c_2, g_{e1}, and g_{e2}. Moreover, if necessary, more steps of a T-type folded rectangular waveguide can be applied in the junction structure. However, introducing more variables leads to more complicated design and thus longer time requirement for parameter adjustment.

In addition, a fine optimisation is still required with full-wave simulations, when the solid walls in the equivalent junction are reverted to post walls. This additional step

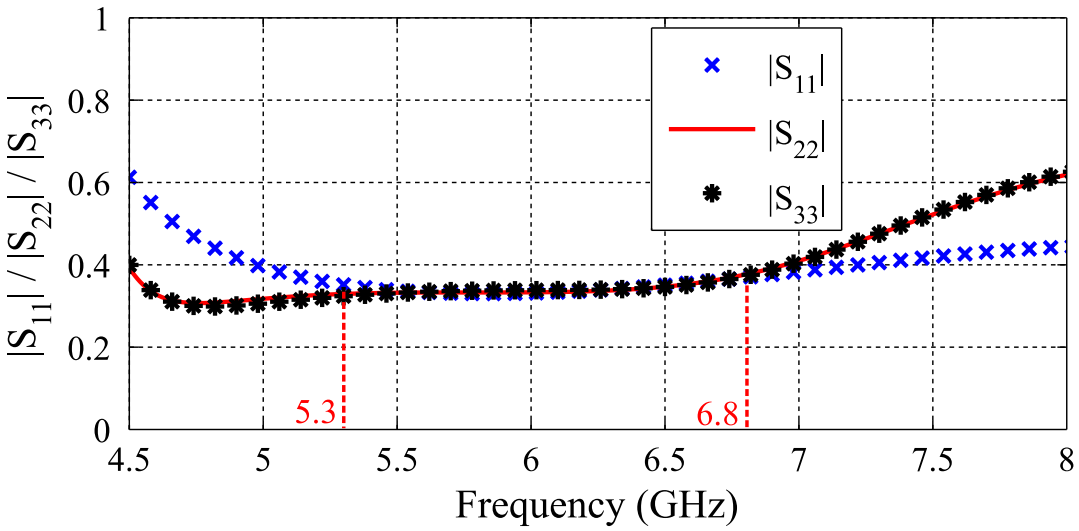

Figure 6.16. Scattering parameters of the three-port junction formed with T-type and E-type FSIWs. This figure depicts the reflection coefficients $|S_{11}|$, $|S_{22}|$, and $|S_{33}|$ for the three ports of the symmetric FSIW junction. It is found that, over the frequency band extending from 5.3 GHz to 6.8 GHz, the reflection coefficients meet the constraints for the optimum performance of diplexers, that is, $|S_{11}| = |S_{22}| = |S_{33}|$, and $|S_{11}| \geq \frac{1}{3}$, preferably $|S_{11}| = \frac{1}{3}$. Source: Self-created using Ansys HFSS and Matlab.

is required because the modelling for the gaps between the edges of the middle metal vane and the post walls, and the right angles which are formed by perpendicular post walls are actually not as perfect as described in the equivalent solid wall model. The optimised dimensions for the realistic structure shown in Fig. 6.15(a), are listed in Table 6.2. With the presented dimensions, similar characteristics of the three-port junction in T-type FSIW technology and E-type FSIW technology can be achieved.

6.4 Novel Diplexers

As mentioned above, diplexers are often realised by assembling a three-port junction and two band-pass filters. According to the analysis in Section 6.2, in order to make the diplexer achieve the optimum performance, the three-port junction should satisfy the reflection coefficient constraints, that is, $|S_{11}| = |S_{22}| = |S_{33}|$, and $|S_{11}| \geq \frac{1}{3}$, preferably $|S_{11}| = \frac{1}{3}$. Meanwhile, Eq. 6.10 presented in the same section can be utilised to determine the distance at which the two band-pass filters should be positioned from the junction ports.

Table 6.2. Dimensions of the junction with stairs in T-type and E-type FSIW technology (Units: mm). The table gives the dimensions for the junction with stairs in T-type and E-type FSIW technology, including the physical widths W_{i1}, W_{i2}, W_{i3} for the T-type or E-type FSIW, the widths c_1, c_2, and c_3 for the middle metal vane in the T-type or E-type FSIW, the intervals p_1, p_2, p_3, p_4, p_5, and p_6 between adjacent vias, the gaps g_{i1} and g_{i2} between the edges of the middle metal vane and the centres of the post walls, the diameter d of the vias, the thickness b of the substrate, and the thickness t of the middle metal vane.

W_{i1}	W_{i2}	W_{i3}	c_1	c_2	c_3	p_1, p_2, p_3, p_4
11.36	18.20	10.76	9.57	16.70	19.96	1.75

p_5	p_6	g_{i1}	g_{i2}	d	b	t
1.71	1.66	1.03	0.80	1.00	0.762	0.018

In Section 6.3, several novel three-port junctions have been introduced, including two optimised Y-junctions in SIW technology, a double-layer junction in SIW technology, a Y-junction in T-type FSIW technology, and a junction with stairs combining both T-type and E-type FSIW technology. All of these junction structures are able to meet the constraints to achieve optimum performance of diplexers over specific frequency bands. Thus, if the specified up and down channels for a diplexer can be included in the satisfactory frequency band of the junction, the required diplexer can be achieved with the corresponding three-port junctions.

In this section, based on some of the three-port junctions proposed in Section 6.3, relevant novel diplexers are designed and verified in the MMM, the finite-element method using Ansys HFSS or measurements.

6.4.1 Diplexers with Improved Y-junctions in Substrate-Integrated Waveguide Technology

The improvements for Y-junctions with bends that involve changing the output branch angle or adjusting the positions of the two additional inserted vias has been demonstrated in Subsection 6.3.1. With the given dimensions in that subsection for the two

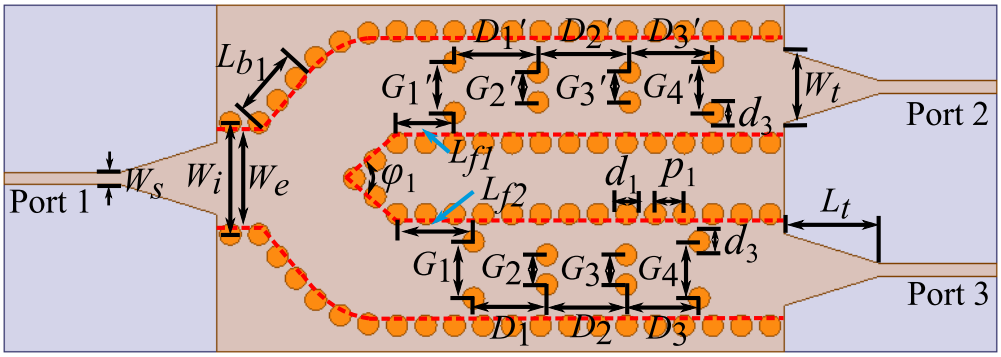

(a)

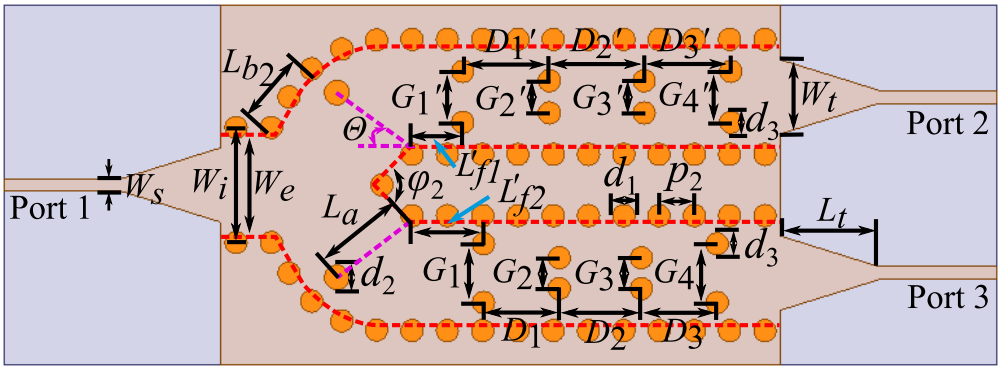

(b)

Figure 6.17. Structures of two diplexers with improved bent Y-junctions. These figures show the structures of two diplexers with bent Y-junctions that are improved through (a) tuning the angle φ_1 of the two output branches or (b) adjusting the locations of two additional vias inserted into the junction. For the Chebyshev 3^{rd}-order band-pass post filters, the bandwidths are all 200 MHz, while the centre frequencies are 7.4 GHz and 8.2 GHz. Source: Self-created using Ansys HFSS and Inkscape.

optimised Y-junctions, the characteristics of both structures were shown to satisfy the constraints of the optimum performance of diplexers over the frequency band extending from 7 GHz to 8.5 GHz. Thus, if the required up and down channels are located within this band, the diplexer can be designed with these two optimised Y-junctions. For illustration, two optimised Y-junction-based diplexers, whose structures are shown in Fig. 6.17, are developed. For each diplexer, the fractional bandwidths of operation for the up and down channels are 2.70% and 2.44% at 7.4 GHz and 8.2 GHz respectively. The viability of the design is validated by full-wave finite-element simulations using Ansys HFSS and measurements on the two fabricated diplexers, as presented later in this subsection.

Table 6.3. Synthesized parameters of the designed Chebyshev 3^{rd}-order band-pass SIW via filters (Units: mm). The table gives the dimensions of the Chebyshev 3^{rd}-order band-pass filters for up and down channels, including the distances G_i or G_i' between the via pairs, the lengths D_i or D_i' of the resonant cavities formed by via pairs, and the diameter d of the vias.

	G_1', G_4'	G_2', G_3'	D_1', D_3'	D_2'	d_3
Filter 1	10.43	6.80	14.00	15.31	1.6
	G_1, G_4	G_2, G_3	D_1, D_3	D_2	d_3
Filter 2	9.48	4.98	12.22	13.30	1.6

To realise the diplexing function after the junctions, two Chebyshev 3^{rd}-order band-pass via filters are designed. Their structures are shown in Fig. 6.17. The first filter has a centre frequency of 7.4 GHz and a fractional bandwidth of 2.70% (passband extending from 7.3 GHz to 7.5 GHz), while the second filter has a centre frequency of 8.2 GHz and a fractional bandwidth of 2.44% (passband extending from 8.1 GHz to 8.3 GHz). Based on the method presented in Chapter 4, adopting vias with a diameter of 1.6 mm, the distances G_i or G_i' between the via pairs and the lengths D_i or D_i' of the resonant cavities formed by via pairs can be calculated very efficiently (within 1 second for a standard computer with a 3.40 GHz i7-2600 CPU and 14.0 GB RAM, if 25 modes and 10-step approximation of the post are adopted). The resulting parameters are listed in Table 6.3, while the scattering parameters of the two Chebyshev 3^{rd}-order band-pass via filters are shown in Fig. 6.18. Obviously, the operation passbands for both synthesised filters satisfy the requirements well, and the $|S_{11}|$ in passbands are also better than -25 dB.

Up until now, both the scattering parameters for the the optimised Y-junctions and the reflection coefficients for the two Chebyshev 3^{rd}-order band-pass filters could be efficiently calculated with the MMM. Thus, according to Eq. 6.10, the distances L_{f1}', L_{f1}, L_{f2}', and L_{f2} between the filters and the ports of the junctions (as shown in Fig. 6.17) can be computed. In addition, according to the procedures reported by Deslandes (Deslandes 2010), the dimensions L_t and W_t for an SIW-to-microstrip transition are obtained in order to connect the diplexers to measurement apparatus. The obtained design dimensions are listed in Table 6.4.

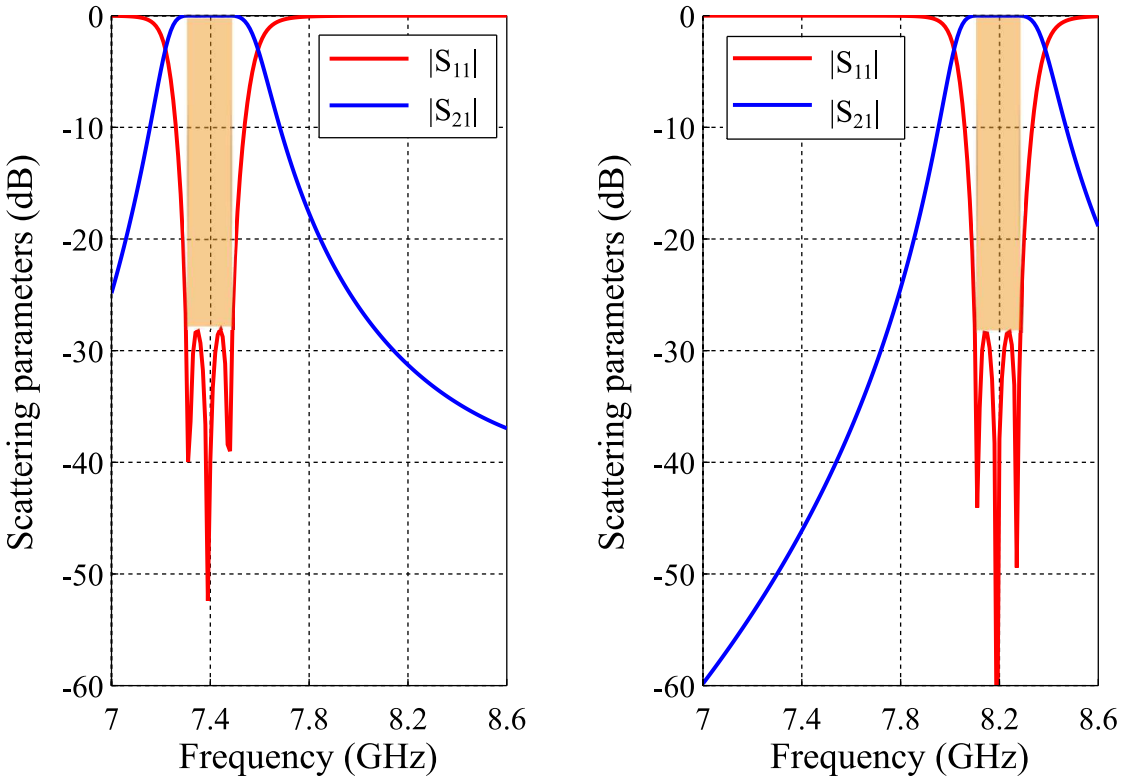

Figure 6.18. Scattering parameters calculated using the MMM for (a) Filter 1 and (b) Filter 2. These figures show the scattering parameters obtained using the MMM for the two band-pass filters required to achieve diplexers. According to the frequency response, both filters meet the requirements, that is, the first filter has a centre frequency of 7.4 GHz and a fractional bandwidth of 2.70%, while the second filter has a centre frequency of 8.2 GHz and a fractional bandwidth of 2.44%. Source: Self-created using Matlab.

The performance of the full structure can now be investigated with a self-written mode-matching code. The results obtained with this code do not take into account losses and the effect of the SIW-to-microstrip transitions, and thus they are first verified by the the full-wave simulations performed using Ansys HFSS. As shown in Fig. 6.19, the calculated results have a good match with the simulation results. Considering losses and transitions, the simulated return losses in the passbands for the up and down channels of both diplexers are better than 20 dB. The simulated insertion losses at 7.4 GHz and 8.2 GHz for Diplexer 1 are 1.62 dB and 1.77 dB respectively, while the corresponding simulated insertion losses for Diplexer 2 are 1.63 dB and 1.77 dB.

Table 6.4. Dimensions of an SIW-to-microstrip transition and the distances between filters and junction ports (Units: mm). The table gives the dimensions of an SIW-to-microstrip transition and the distances between filters and junction ports, where W_t and L_t are the width and length of the SIW-to-microstrip taper, while L'_{f1}, L_{f1}, L'_{f2} and L_{f2} are the distances between the filters and the ports of the junctions.

L_{f1}	L_{f2}	L'_{f1}	L'_{f2}	W_s	W_t	L_t
11.84	14.32	13.44	16.52	2.08	6.55	18.98

A second validation is provided by measurements on fabricated diplexers shown in Fig. 6.20. As shown in Fig. 6.19, the measured return losses in the passbands for the up and down channels of both diplexers are better than 16 dB. The measured insertion losses at 7.4 GHz and 8.2 GHz for Diplexer 1 are 1.92 dB and 2.14 dB respectively, while the corresponding simulated insertion losses for Diplexer 2 are 1.83 dB and 2.13 dB. The differences between simulation and measurement insertion losses may be attributed to the error of the loss tangent of the dielectric, the fabrication imperfections and losses in the SMA connectors.

To sum up, the novel Y-junctions, whose characteristics are improved through tuning the output branch angle or adjusting the positions of the two additional inserted vias, are found to be appropriate to handle the diplexer designs. By comparing the scattering parameters $|S_{11}|$, $|S_{21}|$, and $|S_{31}|$ obtained through the MMM (without considering losses and effect of transitions), the finite-element using Ansys HFSS (considering losses and effect of transitions) and the measurements on the two fabricated prototypes, the viability of the two designs is validated. Besides, the self-written mode-matching code also shows its advantage of high efficiency. For a standard computer with a 3.40 GHz i7-2600 CPU and 14.0 GB RAM, if 25 modes and a 10-step approximation of the post are adopted, it only takes 3.6 seconds for Diplexer 1 and 5.4 seconds for Diplexer 2 to calculate one frequency point (8.2 GHz). By contrast, under the same circumstances, Ansys HFSS spends 33 seconds for Diplexer 1 and 35 seconds for Diplexer 2 simulating one frequency point (8.2 GHz), when *maximum delta s*, *maximum number of passes*, and *mesh operations* are set as 0.01, 20, and default, respectively.

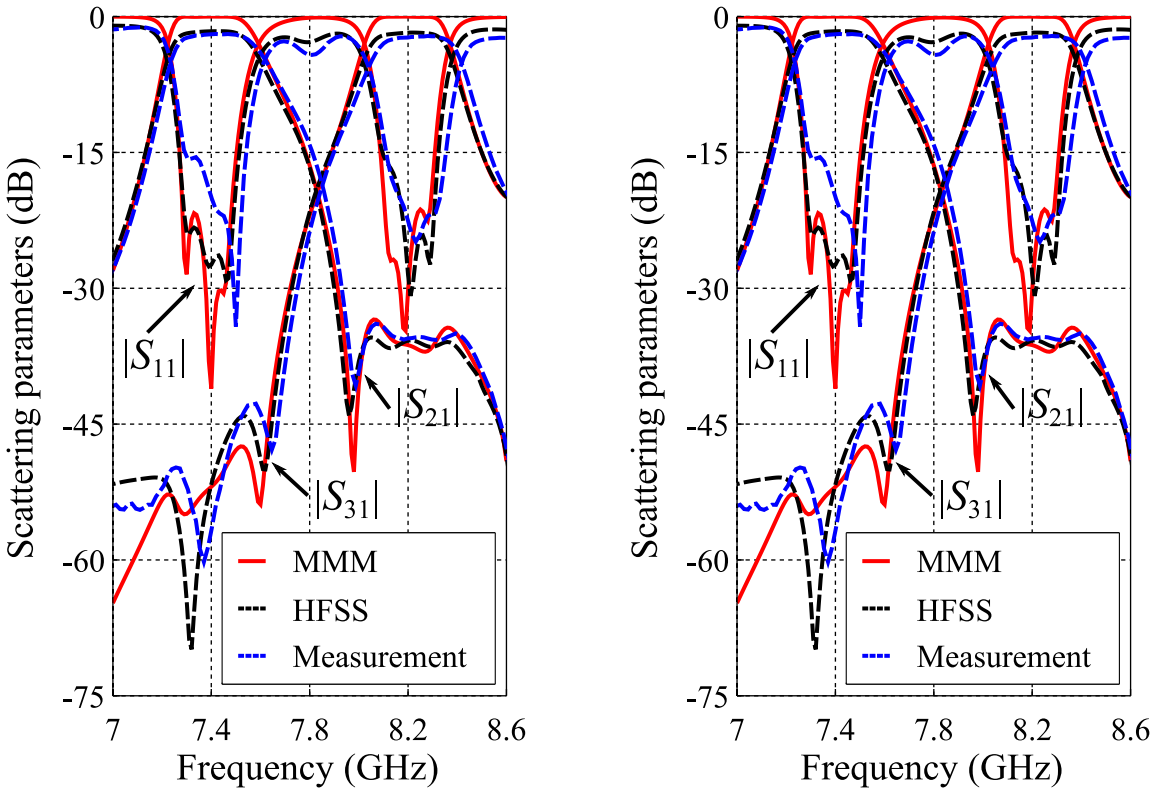

(a) Diplexer 1

(b) Diplexer 2

Figure 6.19. Comparison of scattering parameters obtained using the MMM (without considering losses and effect of transitions), the finite-element method Ansys HFSS and measurements for (a) Diplexer 1 and (b) Diplexer 2. These figures compare the scattering parameters obtained through the MMM (without considering losses and effect of transitions), the finite-element method using Ansys HFSS (considering losses and effect of transitions) and measurements on the two fabricated diplexers. Source: Self-created using Ansys HFSS and Matlab.

6.4.2 Diplexer with Double-Layer Junctions in Substrate-Integrated Waveguide Technology

In addition to the improved Y-junctions, the double-layer three-port structure is another option to realise diplexers. As shown in Fig. 6.7, the dimension of the double-layer junction structure is reduced significantly compared with the Y-junctions, because the two output ports are placed vertically.

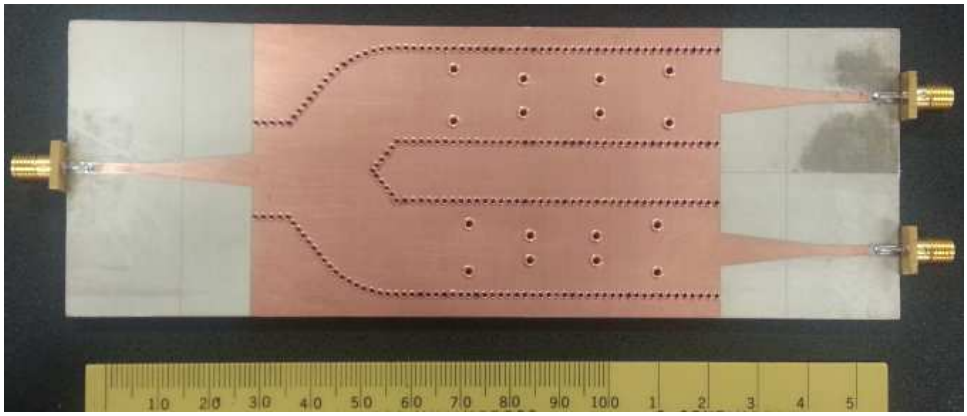

(a) Diplexer 1

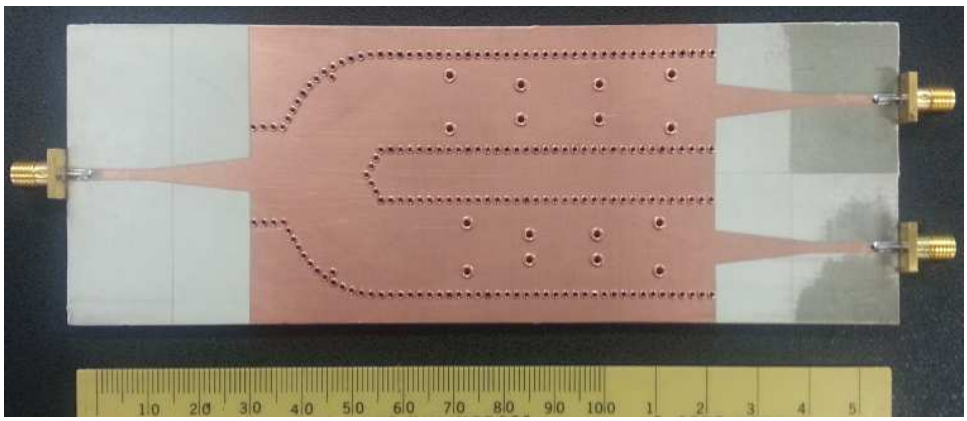

(b) Diplexer 2

Figure 6.20. Fabricated diplexers with improved Y-junctions. These figures show the two fabricated diplexers with Y-junctions which are improved through tuning the output branch angle and adjusting the positions of the two additional inserted vias. Source: Self-created by photographing.

According to the characteristic analysis performed with the MMM in Subsection 6.3.2, it is found that, the frequency band for the double-layer junction, in which the reflection coefficients satisfy well the constraints to achieve optimum performance of diplexers, is much wider than that for the improved Y-junctions. This means that the flexibility for the selection of the up and down channel bands for diplexers is increased. Moreover, if the physical width for the SIW is determined, the gap for the coupling slot between the top and the bottom layers is the unique variable that affects the reflection coefficients for the three junction ports. Therefore, the procedure for adjusting this single dimension can be very efficient.

With the given dimensions for the double-layer junction in Subsection 6.3.2, the characteristics for the three-port junction satisfy the constraints to the optimum performance of diplexers over the frequency band extending from 5.5 GHz to 9.5 GHz. Therefore, it is qualified to be utilised in a diplexer whose required up and down channels have fractional bandwidths of 2.86% and 2.50% at 7 GHz and 8 GHz, respectively. The whole structure of the proposed diplexer is shown in Fig. 6.21. The viability of the design is validated in this subsection by a set of full-wave finite-element simulations using Ansys HFSS.

To achieve the diplexing function after the double-layer three-port junctions, another two Chebyshev 3^{rd}-order band-pass via filters are designed with the configuration shown in Fig. 6.21. The first filter has a centre frequency of 7 GHz and a fractional bandwidth of 2.86%, that is, its passband extends from 6.9 GHz to 7.1 GHz, while the second filter has a centre frequency of 8 GHz and a fractional bandwidth of 2.50%, that is, its passband extends from 7.9 GHz to 8.1 GHz. Based on the method presented in Chapter 4, adopting vias with a diameter d_2 of 1.6 mm, the distances G_i or G_i' between the via pairs and the lengths D_i or D_i' of the resonant cavities formed by via pairs can be calculated accurately and quickly. The resulting parameters are listed in Table 6.5, while the scattering parameters $|S_{11}|$ and $|S_{21}|$ of the two Chebyshev 3^{rd}-order band-pass via filters are plotted in Fig. 6.22. Obviously, for the two operation passbands, both synthesised filters are able to satisfy the centre frequency and fractional bandwidth requirements. In addition, the return losses in the passbands are also better than 30 dB.

Till now, both the scattering parameters for the three-port double-layer junction and the reflection coefficients for the two Chebyshev 3^{rd}-order band-pass via filters were efficiently calculated with the self-written mode-matching code. Thus, according to Eq. 6.10 derived in Section 6.2, the distances L_{f1} and L_{f2} between the band-pass filters and the ports of the junctions (as shown in Fig. 6.21) can be computed. Furthermore here, in order to connect the diplexer to measurement apparatus, equations presented by Deslandes are employed again to determine the length L_t and width W_t of the taper for the SIW-to-microstrip transition (Deslandes 2010). Moreover, because of the double-layer structure, the two output ports for the diplexer need actually to be placed vertically to separate the outputs. Thus, the microstrip lines on the top and the bottom of the device should be bent in order to link with the SMA connectors. However, it is well-known that the characteristics of a microstrip line with a right angle corner

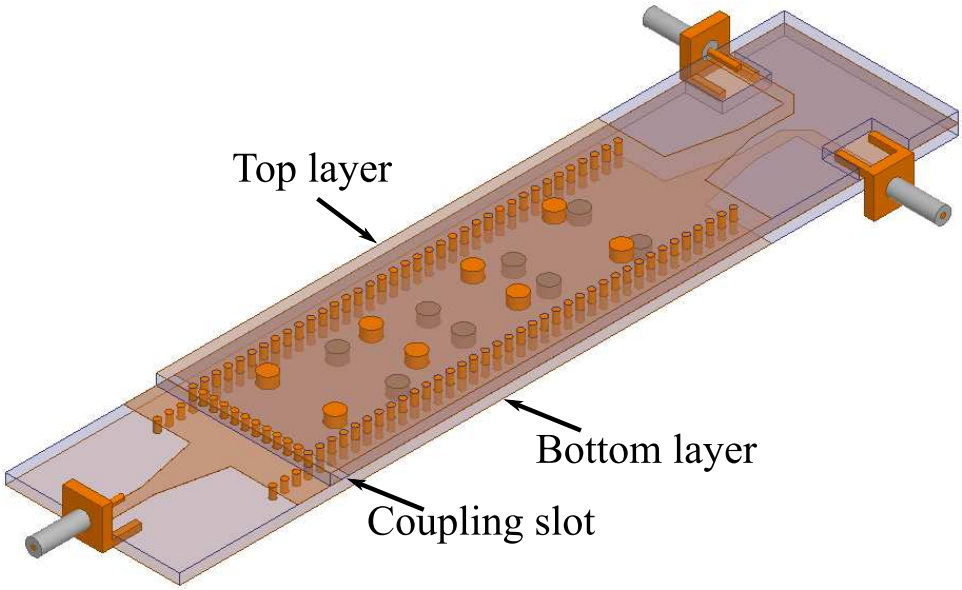

(a) Full structure

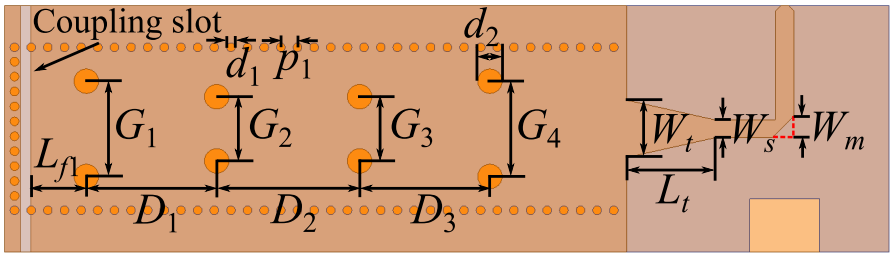

(b) Top layer

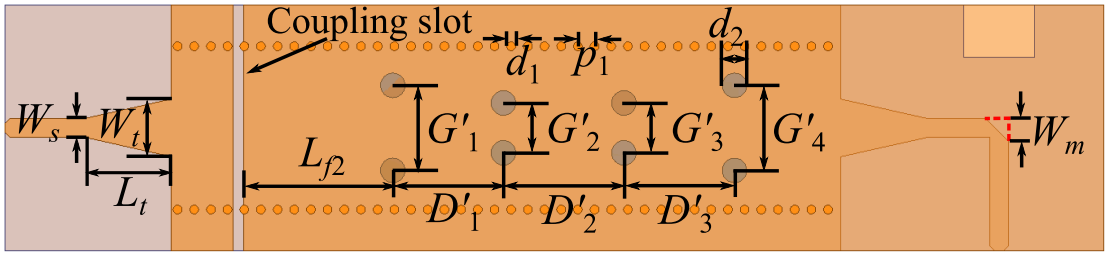

(c) Bottom layer

Figure 6.21. Structure of a diplexer realised in double-layer three-port junction. The top figure (a) shows the full structure of a diplexer realised in double-layer three-port junction which is formed with two pieces of substrates. The corresponding top and bottom layers are shown in (b) and (c). Source: Self-created by Ansys HFSS and Inkscape.

Table 6.5. Synthesized parameters of the designed Chebyshev 3^{rd}-order band-pass SIW via filters (Units: mm). The table gives the dimensions of the Chebyshev 3^{rd}-order band-pass filters for up and down channels, including the distances G_i or G_i' between the via pairs, the lengths D_i or D_i' of the resonant cavities formed by via pairs, and the diameter d of the vias.

	G_1, G_4	G_2, G_3	D_1, D_3	D_2	d_2
Filter 1	11.01	7.45	15.21	16.695	1.6
	G_1', G_4'	G_2', G_3'	D_1', D_3'	D_2'	d_2
Filter 2	9.66	5.52	12.60	13.728	1.6

Table 6.6. Dimensions of an SIW-to-microstrip transition, the side of the chamfered corner, and the distances between filters and junction ports (Units: mm). The table gives the width W_t and the length L_t of the transition taper, the width W_s of the microstrip line, the width W_m of the chamfered corner, and the distances L_{f1} and L_{f2} between filters and junction ports..

W_t	L_t	W_s	W_m	L_{f1}	L_{f2}
6.55	18.98	2.08	2.50	12.628	15.443

degrades gradually with increasing frequency. Hence, in order to improve the performance of the bent transmission line, two common approaches, as shown in Fig. 6.23, are considered here. One achieves the stated goal through connecting a round angle turn, while the other achieves the goal by making a 45° cut on the right angle corner, that is, chamfered corner. Here, the second method is adopted in the double-layer diplexer design. The side W_m of the chamfered corner is first calculated through the equation reported by Douville (Douville and James 1978), and then used as an initial value for the optimisation in Ansys HFSS. The obtained design dimensions are all listed in Table 6.6

The performance of the full structure is now ready for investigation. The results obtained with the self-written mode-matching code do not take into account losses, the

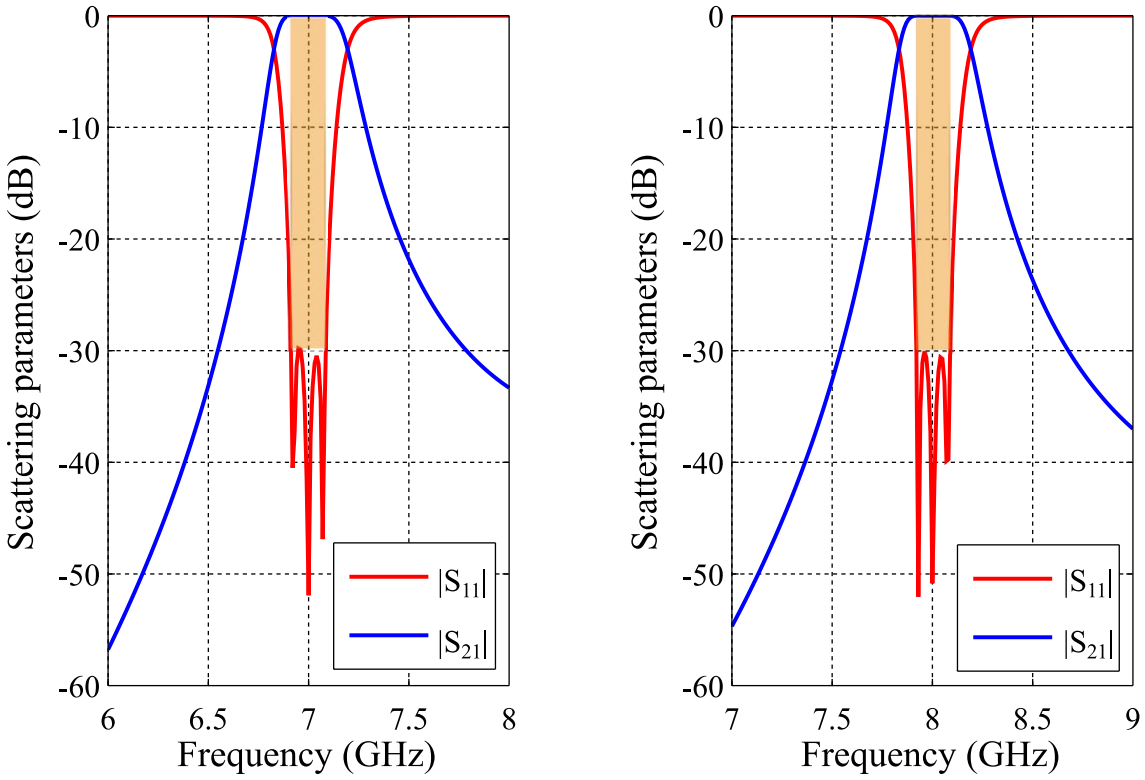

Figure 6.22. Scattering parameters calculated using the MMM for (a) Filter 1 and (b) Filter 2. These figures show the scattering parameters obtained using the MMM for the two band-pass filters required to achieve diplexers. According to the frequency response, both filters meet the requirements, that is, the first filter has a centre frequency of 7 GHz and a fractional bandwidth of 2.86%, while the second filter has a centre frequency of 8 GHz and a fractional bandwidth of 2.50%. Source: Self-created using Matlab.

effect of the SIW-to-microstrip transitions, and the influence of the SMA connectors, thus the full structure needs also to be verified by full-wave finite-element simulations performed using Ansys HFSS. As shown in Fig. 6.24, the calculated results have a good match with the simulation results. Considering losses, SIW-to-Microstrip transitions and SMA connectors, the simulated return losses in the passbands for the up and down channels of the double-layer diplexer are all better than 25 dB. The simulated insertion losses at 7 GHz and 8 GHz for the proposed diplexer are 1.56 dB and 1.79 dB respectively.

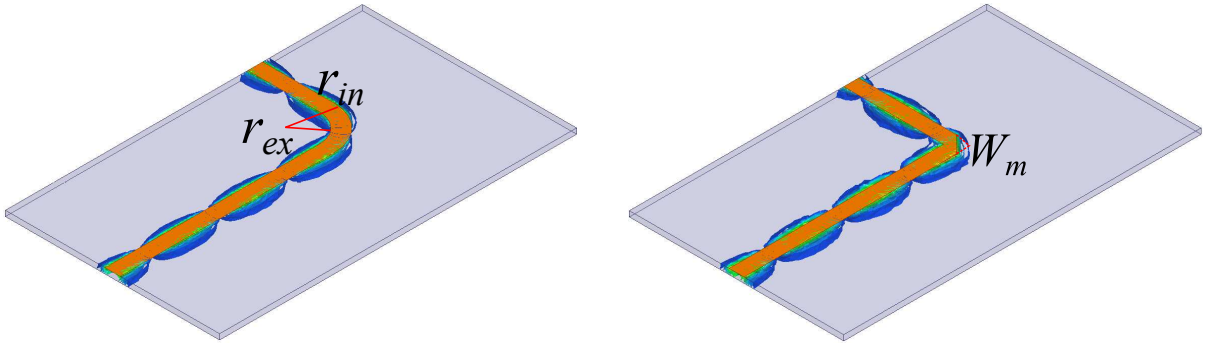

(a) (b)

Figure 6.23. Two common approaches to eliminate the unwanted bend discontinuity effect for transmission lines with (a) rounded corner (b) chamfered corner. These figures show two common approaches which can remove the undesired discontinuity effect caused by the transmission line bends. The first approach (a) achieves the goal through connecting a round angle turn, while the second approach (b) achieves the goal by making a 45° cut on the right angle corner. Source: Self-created using Ansys HFSS and Inkscape.

In conclusion, there exist important advantages in using the double-layer junction, these being a wide frequency band in which the reflection coefficients for junction ports satisfy the constraints for optimum performance of diplexers, and also a convenient design with a small number of variables that can influence the characteristics of three-port junction. The main design variable for the case where the width for the SIW is predefined is the gap of the coupling slot between the top and the bottom layers. Thus, the structure is very suitable for efficient design of compact diplexers.

To illustrate the approach, a double-layer diplexer based on this structure has been efficiently developed with the mode-matching code. According to the comparison of the scattering parameters $|S_{11}|$, $|S_{21}|$, and $|S_{31}|$ calculated through the MMM (without considering losses, effect of transitions, and SMA connectors), and simulated in the finite-element method using Ansys HFSS (considering losses, effect of transitions, and SMA connectors), the viability of the design has been successfully validated. In addition, the self-written code for the full diplexer structure also exhibits its advantage of high efficiency. For a standard computer with a 3.40 GHz i7-2600 CPU and 14.0 GB RAM, if 25 modes and 10-step approximation of the post are employed, it only takes 2.7 seconds to compute one frequency point (8 GHz), while under the same circumstances, Ansys HFSS spends 71 seconds, when *maximum delta s*, *maximum number of passes* and *mesh operations* are set as 0.01, 20 and default respectively.

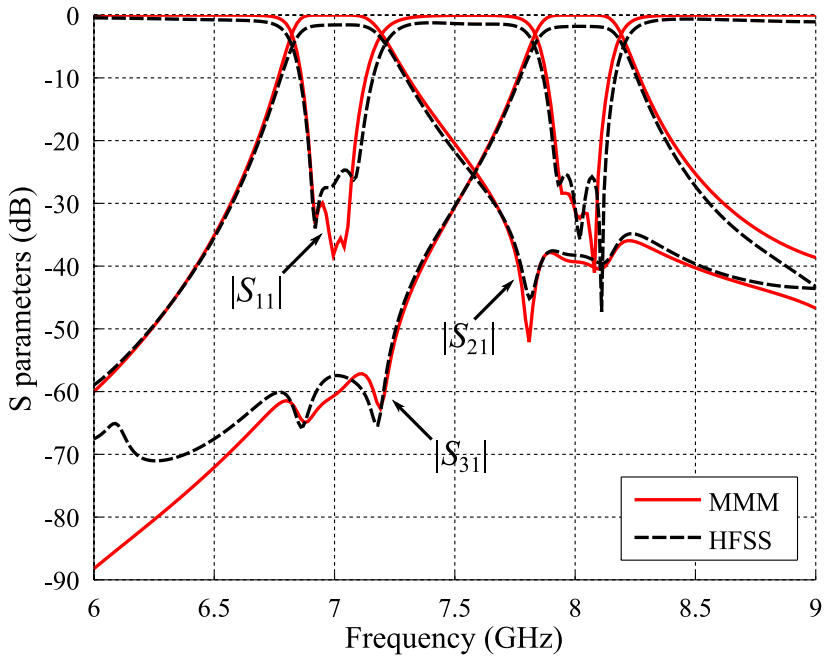

Figure 6.24. Comparison of scattering parameters obtained using the MMM (without considering losses, effect of transitions, and SMA connectors), and Ansys HFSS (considering losses, effect of transitions, and SMA connectors). This figure compares the scattering parameters obtained through the MMM (without considering losses and effect of transitions), and the finite-element method using Ansys HFSS (considering losses and effect of transitions). The calculated results using the MMM and the simulated results using Ansys HFSS match well. Source: Self-created using Matlab and Ansys HFSS.

6.4.3 Diplexer with Junction in T-type and E-type Folded Substrate-Integrated Waveguide Technology

Compared with an SIW, an FSIW is able to further reduce the lateral dimension. Thus, FSIW technology is often applied in designing filters, antennas, and other microwave passive components (Ding and Wu 2010, Yang *et al.* 2013, Bhowmik *et al.* 2014, Karimabadi and Attari 2015). However, to date, the technology has not been utilised in diplexer designs. Hence, in this subsection, the implementation for diplexer designs in FSIW technology is investigated.

According to the analysis in Subsections 5.4.1 and 6.3.3, it has been demonstrated that if the geometries for the cross-sections are chosen reasonably, the propagation and cutoff characteristics for both E-type and T-type FSIWs are nearly the same as those for SIWs.

Furthermore, based on the analysis presented in Subsections 6.3.3 and 6.3.4, both the Y-junction formed with three T-type FSIWs and the junction combined with a staircase T-type FSIW and two E-type FSIWs can be employed in diplexer designs. However, because of the comparative advantage for the latter one in dimension reduction, only the three-port junction with input T-type and output E-type FSIWs is adopted here to realise a specific diplexer whose full structure is shown in Fig. 6.25(a).

With the provided dimensions for the junction with T-type and E-type FSIWs in Subsection 6.3.4, the characteristics for the three-port junction have been shown to satisfy the constraints for the optimum performance of diplexers over the frequency band extending from 5.3 GHz to 6.8 GHz. Thus, for a diplexer whose up and down channel bands are located in this frequency band, the FSIW junction is a good option for the design. For instance, it is appropriate to design a diplexer with a 200 MHz up channel, whose centre frequency is 5.8 GHz, and a 200 MHz down channel, whose centre frequency is 6.2 GHz. The viability of the design is validated later in this subsection by full-wave finite-element simulations using Ansys HFSS.

After the three-port junction implemented in FSIW technology, another two Chebyshev 5^{th}-order band-pass FSIW via filters are designed to complete the diplexer design, as shown in Fig. 6.25(a). According to the diplexer requirements, the first filter should have a centre frequency of 5.8 GHz and a fractional bandwidth of 3.45%, that is, its passband extends from 5.7 GHz to 5.9 GHz, while the second one should have a centre frequency of 6.2 GHz and a fractional bandwidth of 3.23%, that is, its passband extends from 6.1 GHz to 6.3 GHz. Based on the method presented in Subsection 5.4.3, adopting vias with a diameter d_2 of 1.6 mm, the distances E_i or E_i' between the via centres and the FSIW walls, and the lengths D_i or D_i' of the resonant cavities formed by vias can be calculated within seconds for a standard computer with a 3.40 GHz i7-2600 CPU and 14.0 GB RAM, and the resulting values for the dimensions are all listed in Table 6.7. Moreover, as shown in Fig. 6.26, the finite-element simulated scattering parameters $|S_{11}|$ and $|S_{21}|$ for the two Chebyshev 5^{th}-order band-pass via FSIW filters, and the mode-matching results for their corresponding equivalent unfolded filters have a good agreement. In addition, for the two operation passbands, both filters are able to meet well the requirements for the centre frequency and fractional bandwidth, and the return losses in passbands are also better than 30 dB.

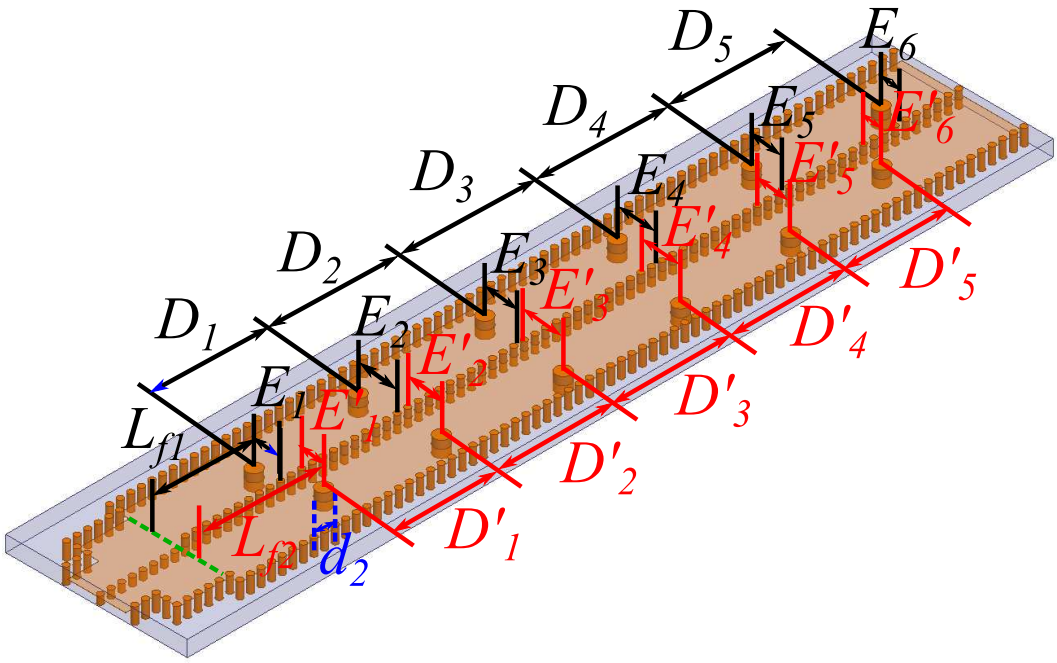

(a)

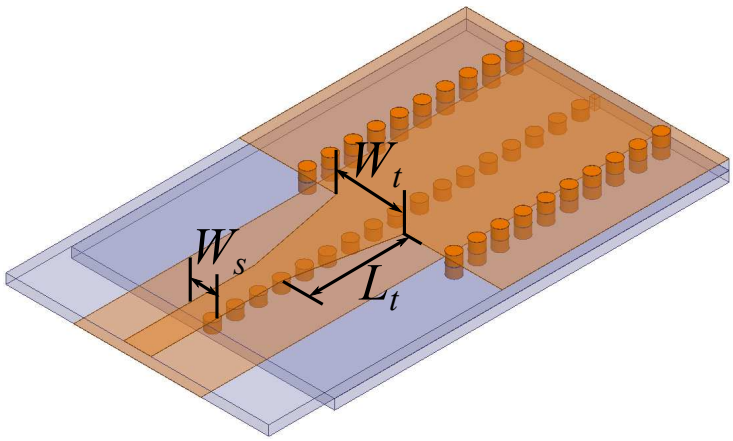

(b)

Figure 6.25. Structures of (a) the diplexer in FSIW technology and (b) the T-type FSIW-to-microstrip transimission. The top figure (a) shows the structure of the diplexer that is realised by assembling a three-port junction with T-type and E-type FSIWs, and two Chebyshev 5^{th}-order band-pass post filters. The up and down channels' bandwidths are both 200 MHz, while the centre frequencies are 7.4 GHz and 8.2 GHz respectively. In order to measure the diplexer, the E-type FSIW-to-strip transition and the strip-to-SMA connector transition introduced in Subsection 5.4.3 still can be used, while the structure for the T-type FSIW-to-microstrip transition is shown in the bottom figure (b). Source: Self-created using Ansys HFSS and Inkscape.

Table 6.7. Synthesized parameters of the designed Chebyshev 5^{th}-order band-pass via FSIW filters (Units: mm). The table gives the dimensions of the Chebyshev 5^{th}-order band-pass filters for up and down channels, including the distances E_i or E'_i between the via centres and the FSIW walls, the lengths D_i or D'_i of the resonant cavities formed by vias, and the diameter d_2 of the vias.

	E_1, E_6	E_2, E_5	E_3, E_4	D_1, D_5	D_2, D_4	D_3	d_2
Filter 1	3.70	5.80	6.42	19.29	21.56	21.86	1.6
	E'_1, E'_6	E'_2, E'_5	E'_3, E'_4	D'_1, D'_5	D'_2, D'_4	D'_3	d_2
Filter 2	4.19	6.40	7.37	17.26	19.16	19.40	1.6

Obviously, both the three-port junction realised in T-type and E-type FSIWs and the two band-pass via FSIW filters are ready to be assembled into a diplexer. Thus, according to Eq. 6.10 provided in Section 6.2, the distances L_{f1} and L_{f2} between the band-pass FSIW filters and the ports of the junctions (as shown in Fig. 6.25(a)) can then be calculated. Moreover, in order to connect the diplexer to measurement apparatus, the transition structures should be developed. For the two E-type FSIWs, the FSIW-to-strip transition and the strip-to-SMA connector transition introduced in Subsection 5.4.3 still can be applied in this design. For the T-type FSIW, a novel structure of the FSIW-to-microstrip transition is shown in Fig. 6.25(b), while the width W_t and the length L_t can be obtained through optimisation in full-wave finite-element simulations using Ansys HFSS. The obtained design dimensions are all listed in Table 6.8.

The performance of the designed complete diplexer in FSIW technology now can now be investigated. Without considering the effects of the T-type FSIW-to-microstrip and E-type FSIW-to-strip transitions, and the influence of the SMA connectors, the simulated results obtained from the finite-element method using Ansys HFSS show that the scattering parameters $|S_{11}|$, $|S_{21}|$, and $|S_{31}|$ can meet the required diplexer specifications well. As shown in Fig. 6.27, the simulated return losses in the passbands for the up and down channels of the diplexer in T-type and E-type FSIW technology are all better than 20 dB. The simulated insertion losses at 5.8 GHz and 6.2 GHz for the proposed diplexer are 1.56 dB and 1.79 dB respectively.

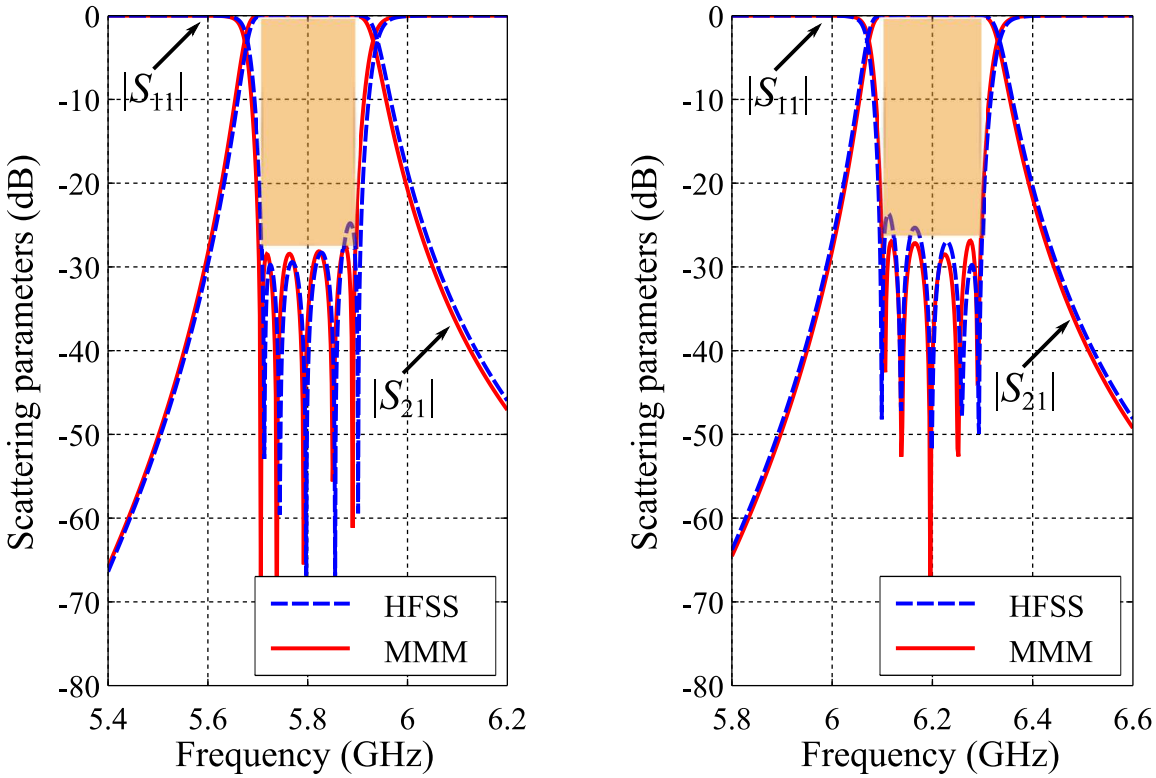

Figure 6.26. Comparison between scattering parameters simulated using Ansys HFSS for FSIW filters and that calculated using the MMM for the corresponding unfolded filters. These figures compare the scattering parameters simulated with the finite-element method using Ansys HFSS for FSIW filters and that calculated using the MMM for the corresponding unfolded filters. It is found that the simulated and calculated results match well. In addition, according to the frequency response, both filters meet the requirements, that is, the first filter (a) has a centre frequency of 5.8 GHz and a fractional bandwidth of 3.45%, while the second filter (b) has a centre frequency of 6.2 GHz and a fractional bandwidth of 3.23%. Source: Self-created using Matlab.

To sum up, in this subsection, the three-port junction realised with T-type and E-type FSIWs is employed in a diplexer design. According to the simulated results obtained with the finite-element method using Ansys HFSS, the scattering parameters $|S_{11}|$, $|S_{21}|$, and $|S_{31}|$ can satisfy the diplexer requirements well. It is noted that, although full-wave finite-element simulations using Ansys HFSS is very time-consuming, the efficiency for the diplexer development can be increased because the band-pass filter part can be completed within seconds by the self-written mode-matching code.

Table 6.8. Dimensions of a T-type FSIW-to-microstrip transition, and the distances between filters and the junction ports (Units: mm). The table gives the dimensions of the taper for a T-type FSIW-to-microstrip transition, and the distances between the two band-pass FSIW filters and the junction output ports, where W_t and L_t are the width and length of the FSIW-to-microstrip taper, while L_{f1} and L_{f2} are the distances between the filters and the ports of the junctions.

L_{f1}	L_{f2}	W_s	W_t	L_t
16.974	16.335	2.08	5.2	7.8

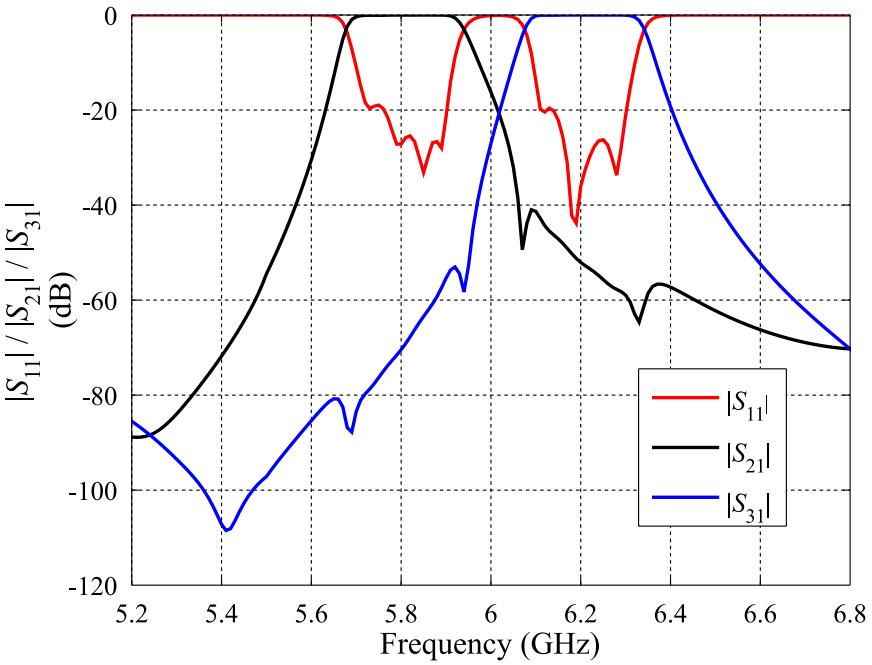

Figure 6.27. Scattering parameters for the diplexer in T-type and E-type FSIW technology obtained using Ansys HFSS. This figure gives the scattering parameters $|S_{11}|$, $|S_{21}|$, and $|S_{31}|$ obtained through the finite-element method using Ansys HFSS. The simulations consider losses, but the effects of the T-type FSIW-to-microstrip transition, the E-type FSIW-to-strip transition, and SMA connectors are not taken into account. Source: Self-created using Ansys HFSS and Matlab.

6.5 Chapter Summary

In the first part of this chapter, the constraints for optimum performance of diplexers employing symmetric three-port junctions have been derived. With these constraints, a diplexer that is composed of a three-port symmetric junction and two band-pass filters can be developed by an aided self-programmed mode-matching code much more efficiently than employing only the finite-element method using Ansys HFSS.

Four types of novel three-port junctions, including two optimised Y-junctions in substrate-integrated waveguide technology, a double-layer junction in substrate-integrated waveguide technology, a Y-junction in T-type folded substrate-integrated waveguide technology, and a junction with stairs in T-type and E-type folded substrate-integrated waveguide technology have been then proposed and explored. By adjusting the relative variables for these structures, the characteristics of all of these junctions have been demonstrated to successfully meet the constraints for the optimum performance of the diplexers in applicable bandwidths.

Based on some of these novel three-port junctions, three types of diplexers have been developed and investigated. According to the analysis results obtained through the mode-matching method, the finite-element method, or measurements on fabricated prototypes, the feasibility of these designs has been demonstrated.

Chapter 7

Conclusions and Future Work

THE research presented in this thesis has been described in two major parts. The first part of the thesis is relevant to band-pass filters and shielded microstrip lines. It has focused on efficient methods of analysis based on the mode-matching method. On that basis, a fast design method for band-pass post filters and a novel type of band-pass E-type folded substrate-integrated waveguide filter have been introduced. Additionally, the analysis of side aspects has been presented, such as a study of the negative influence of micro-machining errors and a modal analysis for shielded microstrip lines. The second part of the thesis, which is relevant to three-port junctions and diplexers, has introduced several novel junction structures which can satisfy the constraints to achieve optimum performance of diplexers over specific frequency bands. Based on the proposed junctions, three novel diplexers have been developed and verified using the mode-matching method, the finite-element method, or measurements. This chapter concludes this thesis and highlights the original contributions and the possible future work.

7.1 Introduction

Microwave and millimetre-wave systems are widely used in telecommunications, radar, remote sensing, and clinical medicine. As essential parts in these systems, band-pass filters are often utilised to remove undesired frequency components, while diplexers, are often adopted to handle more frequency channels, as they can separate a wider frequency band into a few narrower bands, or combines frequency signals from certain channels at one common port. This thesis has presented and validated approaches to improve the efficiency and accuracy of the computer-aided design (CAD) designs for band-pass filters, shielded microstrip lines, and diplexers. In addition, several novel structures for band-pass filters and diplexers have been discussed, with the aim of reducing overall dimensions. The original contributions mentioned above, together with the future work, are summarised in this chapter.

7.2 Band-Pass Filters and Shielded Microstrip Lines

As a first major part of this thesis, research work on efficient methods based on the mode-matching technique has been presented for band-pass filters in waveguide technology. This has allowed an investigation of the negative influence caused by machining errors and the formulation of efficient design methods for band-past post filters in Chapter 3 and 4. A novel band-pass filter structure with significant dimension reduction and a characteristic analysis for the shielded transmission line have been presented in Chapter 5.

7.2.1 Original Contributions

- With the rapid development of microwave and millimetre-wave technology, the performance requirements of band-pass filters and diplexers are steadily increasing. Band-pass filters are often realised in rectangular waveguide technology because of the advantages of high quality factor (Q factor), low loss, and good power handling capability. H-plane irises are able to be placed in the cross-section of a rectangular waveguide to realise a band-pass filter. However, limitations of micro-machining processes are a significant source of inaccuracies,

since the corners between waveguide walls and irises in a manufactured band-pass H-plane iris filter are curved instead of at right angles. These curved corners affect the performance, especially for high frequency bands. Based on the mode-matching method, for a band-pass H-plane iris filter such as the example provided in Subsection 3.4.1, it has been found that by increasing the radii of the round angles, the centre frequency of the band-pass filter shifts to higher frequencies while the 3 dB bandwidth varies slightly. Meanwhile, with the increase of the side lengths of the bevel angles for irises, the centre frequency of the band-pass filter shifts to lower frequencies, while the 3 dB bandwidth widens. In order to remove these negative influences, three methods have been proposed in Subsection 3.4.3, including a) revising the design parameters according to the estimated influence in order to compensate the frequency shift, b) designing the band-pass filter without considering the influence of fabrication and then introducing bevel angles selected to correct the offset of the centre frequency, and c) mapping the realised structure of irises and resonator cavities with the *K*-inverter and *LC* resonator network of a band-pass filter to compute the aperture sizes and resonator lengths accurately. According to the verification with the finite-element method using Ansys High Frequency Structural Simulator (HFSS), all of the three methods have been demonstrated to be effective (Zhao *et al.* 2014b).

- When creating a band-pass filter, assigning cylindrical posts in a rectangular waveguide appears to be a better option than placing irises, since circular apertures and cylindrical posts can be manufactured more easily and are less prone to machining errors. Thus, the characteristics of posts placed in the cross-section of a rectangular waveguide have been explored in Subsection 4.2.3. The scattering parameters of the post waveguide structure have been computed with three classes of approximation methods, including the equal width, arithmetic sequence thickness, and equal sector methods. Through comparing the differences between the calculated scattering parameters and the accurate values from a reference solution, as well as the rate of convergence for each method, the most efficient approximation approach has been recommended. The finite-element method using Ansys HFSS has then been successfully utilised to verify the suggested approximation approach (Zhao *et al.* 2014a).

- The applications in rectangular waveguide technology are limited by the high cost, bulky volume, and difficult integration with other components. In order to

overcome these shortcomings, the substrate-integrated waveguide has been proposed as a dielectric-loaded rectangular waveguide equivalent (Wu *et al.* 2003). In this perspective, Section 4.3 has handled the designs of the band-pass post rectangular waveguide filters and the band-pass via substrate-integrated waveguide filters as a single problem. This has allowed an efficient general design approach for this type of band-pass filters either in rectangular waveguide technology or substrate-integrated waveguide technology. With this technique, fast and accurate computations of the relationships for the K factors as a function of the post radii and the distances between posts have been demonstrated, which allows an in-depth analysis of the influence of machining tolerances on the filter performance. The computations can be used to choose reasonable posts for designing band-pass filters, while the error analysis helps to judge whether a given machining precision is sufficient. The approach has been applied to a Chebyshev band-pass post rectangular waveguide filter and a band-pass via substrate-integrated waveguide filter with a centre frequency of 10.5 GHz and a fractional bandwidth of 9.52% with verification via full-wave simulations using Ansys HFSS and measurements on manufactured prototypes (Zhao *et al.* 2015c).

- Insertion loss is a crucial specification to judge the quality of a substrate-integrated waveguide band-pass filter. In Section 4.5, six Chebyshev band-pass post filters in substrate-integrated waveguide technology have been designed with a self-written lossless mode-matching code. The considered filters have been designed with various orders for a centre frequency of 10.5 GHz and a fractional bandwidth of 9.52%. These filters have then been simulated with a full-wave electromagnetic solver in order to investigate the various contributions of ohmic and dielectric losses affecting the performance. In particular, the influence on the insertion loss due to the variations in the metal claddings and vias' conductivity, dielectric loss tangent, and substrate thickness has been quantitatively analysed. For validation, one prototype filter has been fabricated to compare the simulations to experimental results (Zhao *et al.* 2015a).

- Shielded microstrip lines are widely used in microwave and millimetre-wave systems to connect devices while protecting circuits from environmental contaminants, preventing electromagnetic interference, and enhancing the mechanical strength. To avoid the influence of the metallic enclosures on the fundamental mode, the dimensions for the housing is an important issue. In Section 5.3, the

influence of those dimensions on the fundamental mode has been investigated rigorously using the mode-matching method. In addition, the relationships between the cutoff frequency of the 2^{nd}-order mode and those geometrical variables of the cross-section of the shielded transmission line have been presented. With these relationships, a reasonable geometry can be efficiently determined, which is important to prevent performance degradation through higher-order mode excitations, such as in waveguide transitions. The analysis results have been verified with the finite-element simulations obtained with Ansys HFSS (Zhao *et al.* 2015b).

- Despite the significant size reduction offered by the realisation of filters in substrate-integrated waveguide technology, further width reduction is still desirable, especially in microwave or millimetre-wave systems whose volume is limited by system considerations. Thus the folded substrate-integrated waveguide is a viable option to further reduce the sizes of devices in substrate-integrated waveguide technology. Section 5.4 presented a novel concept of band-pass post filter in folded substrate-integrated waveguide technology, together with an efficient specific design procedure. The approach is based on a rigorous mode-matching analysis of the dispersion characteristics for the odd and even modes in the folded substrate-integrated waveguide, which allows the definition of an accurate unfolded equivalent problem for a suitably chosen middle vane dimension. A direct comparison of the posts placed in the folded substrate-integrated waveguide and in the equivalent unfolded dielectric-loaded rectangular waveguide has confirmed their similar characteristics. For illustration, the method has been applied to realise a 5-order Chebyshev band-pass post folded substrate-integrated waveguide filter with a centre frequency of 7 GHz and a fractional bandwidth of 5.71%. The viability and efficiency of the design approach has been successfully validated by the finite-element simulations and the measurements on a fabricated prototype (Zhao *et al.* n.d.).

7.2.2 Future Work

- Chapters 3 to 5 have focused on band-pass filters, but in microwave and millimetre-wave systems, low-pass and band-stop filters are also indispensable elements. Thus, generalising the proposed efficient procedures based on the mode-matching method to design these types of filters can be future work.

- With a demonstrated equivalent model, Chapter 5 has introduced an efficient design procedure for a novel concept of band-pass post filter in folded substrate-integrated waveguide technology. In order to describe the new structure more accurately, a mode-matching algorithm that can directly analyse the characteristics of the posts placed in the cross-section of a folded substrate-integrated waveguide will be developed in the future.

7.3 New Junctions and Diplexers

As the second major part of this thesis, Chapter 6 has proposed several three-port junctions that can satisfy the constraints to achieve optimum performance of diplexers over specific frequency bands with the goal of improving the performance or reducing the dimensions of diplexers. Based on these new junctions, some diplexers have been designed, while their corresponding characteristics have also been investigated. The original contributions and possible future work for this aspect are summarised below.

7.3.1 Original Contributions

- Y-junctions are often adopted to design diplexers since their characteristics can conveniently satisfy the constraints for optimum performance of diplexer designs. To decrease the dimension of the Y-junction diplexer, the two output branches can be bent to yield parallel ports. However, doing so degrades the characteristics of the parallel configuration junction. In order to achieve the best performance for a diplexer, two improved novel configurations of Y-junctions have been introduced and analysed with an efficient mode-matching method in Subsection 6.3.1. Through varying the angle between the two output branches or adjusting the positions of the two inserted vias, both improved junctions can satisfy the constraints for optimum performance of diplexers over the frequency band extending from 7 GHz to 8.5 GHz (Zhao *et al.* 2016b).

- In Subsection 6.3.2, a double-layer structure has been introduced to realise a three-port junction for the dimension reduction of diplexers. With the proposed structure, the characteristics can meet the constraints to achieve optimum performance of diplexers conveniently, because only one variable can influence the reflection coefficients of the junction ports. Additionally, the developed mode-matching code can improve the efficiency of parameter adjustment significantly.

According to the analysis, the junction can satisfy the diplexer constraints from 5.5 GHz to 9.5 GHz. The wider frequency band translates into flexibility for the selection of a diplexer's up and down channels.

- A novel Y-junction realised in T-type folded substrate-integrated waveguide technology has been introduced in Subsection 6.3.3. Similar propagation characteristics of the first eighteen modes for the folded substrate-integrated waveguide and the corresponding equivalent unfolded dielectric-loaded rectangular waveguide has been demonstrated when a particular width of the middle metal vane is chosen. In addition, it has also been found that the characteristics of the proposed Y-junction structure can satisfy the constraints to achieve optimum performance of diplexers over the frequency band extending from 4.6 GHz to 8.5 GHz. Hence, diplexers using the novel Y-junction in T-type folded substrate-integrated waveguide technology can accommodate the up and down channels in a much wider frequency band compared with common Y-junction diplexers (Zhao *et al.* 2016a).

- To further decrease the dimensions of diplexers, a three-port junction with stairs realised in both T-type and E-type folded substrate-integrated waveguide technology has been introduced in Subsection 6.3.4. Based on the finite-element method using Ansys HFSS, the reflection coefficients for the junction ports can satisfy the constraints for optimum performance of diplexers over a frequency band from 5.3 GHz to 6.8 GHz.

- All the proposed novel three-port junctions can be readily utilised in diplexer designs, while with the self-written mode-matching code, the dimensions of the band-pass filters required for the up and down channels can be calculated accurately and quickly. Thus, three types of diplexers realised with two improved Y-junctions, one double-layer junction, and one junction with stairs in T-type and E-type folded substrate-integrated waveguide technology have been designed efficiently and presented in Section 6.4. According to the analysis results obtained with the mode-matching method, the finite-element method, or measurements, it has been found that the three diplexer designs perform well and the specifications can be satisfied over the operation bands.

7.3.2 Future Work

- Subsections 6.4.2 and 6.4.3 have presented two diplexers employing a double-layer junction in substrate-integrated waveguide technology and a junction with stairs in T-type and E-type folded substrate-integrated waveguide technology. On account of the time constraints, as well as the processing difficulty of the double-layer structures, both of them have not been manufactured and experimentally tested yet. Thus, the fabrication and measurement of the two realised diplexers can be future work.

- As demonstrated, the three-port Y-junction in T-type folded substrate-integrated waveguide technology offers the advantage of a wide frequency band to satisfy the constraints for optimum performance of diplexers. This property allows large flexibility in the selection of up and down channels for diplexers. However, because of the time constraints, this junction has not been utilised to design diplexers. Hence, a diplexer using the T-type folded substrate-integrated waveguide Y-junction will be developed in the future.

- In Chapter 6, the analyses for the Y-junction in T-type folded substrate-integrated waveguide technology, the junction with stairs in T-type and E-type folded substrate-integrated waveguide technology, and the diplexer employing a junction with stairs have been obtained with the finite-element method using Ansys HFSS. However, the simulations are quite time-consuming because of the large amount of variables, especially considering the mesh fineness required to obtain results with sufficient precision. Thus, the mode-matching-based codes, which can directly handle T-type and E-type folded substrate-integrated waveguide and discontinuities in them, will be developed in order to improve the efficiency.

7.4 Closing Comments

This thesis has presented validated design procedures for band-pass filters, shielded transmission lines, and diplexers by combining the usage of the lossless mode-matching method and the finite-element commercial software Ansys HFSS. A large improvement in the design reliability and a great reduction in the design cycle have then been demonstrated, because

a) the mode-matching method can quickly and accurately determine the dimensions for these passive components (for example, a Chebyshev 5^{th}-order band-pass post filter can be completed within 1 second), as well as gather data about tolerances and fabrication inaccuracies (for instance, negative influence on a band-pass H-plane iris filter introduced by micro-machining errors can be analysed efficiently);

b) before the prototype fabrication, a small number of finite-element simulations using Ansys HFSS plays the other important role of confirming the specifications of the designed components, such as insertion loss and bandwidth.

The combination of these two methods can be extended to other device designs in order to satisfy the increasing requirements for microwave and millimetre-wave systems.

Importantly, the application of the introduced equivalent models and efficient design procedures has allowed the rapid development of novel structures. In this context, this thesis has also aimed to reduce the dimensions of band-pass filters and diplexers. A novel concept of band-pass post filter in folded substrate-integrated waveguide technology has been introduced, together with an efficient specific design procedure using its equivalent model. Meanwhile, four types of novel three-port junctions have been presented for dimension reduction of diplexers. It is noted that, the proposed junction structures can also be utilised in other passive component designs, such as power dividers and slot array antennas.

Bibliography

ABELE-T. A. (1967). Transmission Line Filters Approximating a Constant Delay in a Maximally Flat Sense, *IEEE Transactions on Circuit Theory*, **14**(3), pp. 298–306.

ACCATINO-L., AND BERTIN-G. (1994). Design of Coupling Irises between Circular Cavities by Modal Analysis, *IEEE Transactions on Microwave Theory and Techniques*, **42**(7), pp. 1307–1313.

ALESSANDRI-F., BARTOLUCCI-G., AND SORRENTINO-R. (1988). Admittance Matrix Formulation of Waveguide Discontinuity Problems: Computer-Aided Design of Branch Guide Directional Couplers, *IEEE Transactions on Microwave Theory and Techniques*, **36**(2), pp. 394–403.

ARNDT-F., AHRENS-I., PAPZINER-U., WIECHMANN-U., AND WILKEIT-R. (1987). Optimized E-Plane T-Junction Series Power Dividers, *IEEE Transactions on Microwave Theory and Techniques*, **35**(11), pp. 1052–1059.

ARNDT-F., BORNEMANN-J., HECKMANN-D., PIONTEK-C., SEMMEROW-H., AND SCHUELER-H. (1986). Modal S-Matrix Method for the Optimum Design of Inductively Direct-Coupled Cavity Filters, *IEE Proceedings H - Microwaves, Antennas and Propagation*, **133**(5), pp. 341–350.

ARNDT-F., KOCH-B., ORLOK-H. J., AND SCHRODER-N. (1985). Field Theory Design of Rectangular Waveguide Broad-Wall Metal-Insert Slot Coulplers for Millimeter-Wave Applications, *IEEE Transactions on Microwave Theory and Techniques*, **33**(2), pp. 95–104.

ATIA-A. E., AND WILLIAMS-A. E. (1972). Narrow-Bandpass Waveguide Filters, *IEEE Transactions on Microwave Theory and Techniques*, **20**(4), pp. 258–265.

ATIA-A. E., AND WILLIAMS-A. E. (1973). Non-Minimum Phase, Optimum Amplitude, Bandpass Waveguide Filters, *Microwave Symposium, 1973 IEEE G-MTT International*, pp. 210–212.

ATIA-A. E., WILLIAMS-A. E., AND NEWCOMB-R. W. (1974). Narrow-Band Multiple-Coupled Cavity Synthesis, *IEEE Transactions on Circuits and Systems*, **21**(5), pp. 649–655.

BARRETT-R. M. (1984). Microwave Printed Circuits - The Early Years, *IEEE Transactions on Microwave Theory and Techniques*, **32**(9), pp. 983–990.

BELENGUER-A., ESTEBAN-H., BORIA-V. E., BACHILLER-C., AND MORRO-J. V. (2010). Hybrid Mode Matching and Method of Moments Method for the Full-Wave Analysis of Arbitrarily Shaped Structures Fed Through Canonical Waveguides Using Only Electric Currents, *IEEE Transactions on Microwave Theory and Techniques*, **58**(3), pp. 537–544.

BELEVITCH-V. (1962). Summary of the History of Circuit Theory, *Proceedings of the IRE*, **50**(5), pp. 848–855.

BHOWMIK-W., SRIVASTAVA-S., AND PRASAD-L. (2014). Design of Multiple Beam Forming Antenna System Using Substrate Integrated Folded Waveguide (SIFW) Technology, *Progress in Electromagnetics Research B*, **60**, pp. 15–34.

BORNEMANN-J. (2001). Design of Waveguide Filters without Tuning Elements for Production-Efficient Fabrication by Milling, *2001 Asia-Pacific Microwave Conference (APMC)*, Vol. 2, pp. 759–762 vol.2.

BORNEMANN-J., AND ARNDT-F. (1987). Modal-S-Matrix Design of Optimum Stepped Ridged and Finned Waveguide Transformers, *IEEE Transactions on Microwave Theory and Techniques*, **35**(6), pp. 561–567.

BORNEMANN-J., ROSENBERG-U., AMARI-S., AND VAHLDIECK-R. (2005). Tolerance Analysis of Bypass-, Cross- and Direct-Coupled Rectangular Waveguide Band-Pass Filters, *IEE Proceedings - Microwaves, Antennas and Propagation*, **152**(3), pp. 167–170.

BORNEMANN-J., TARINGOU-F., AND KORDIBOROUJENI-Z. (2011). A Mode-Matching Approach for the Analysis and Design of Substrate-Integrated Waveguide Components, *Frequenz*, **65**(9-10), pp. 287–292.

BRAY-J. (2002). *Innovation and the Communications Revolution: from the Victorian Pioneers to Broadband Internet*, The Institution of Engineering and Technology, London, UK.

BURDEN-R. L., FAIRES-J. D., AND BURDEN-A. M. (2015). *Numerical Analysis*, 10th edn, Cengage Learning, Boston, Massachusetts, USA.

CABALLERO-E. D., MARTINEZ-A. B., GONZALEZ-H. E., BELDA-O. M., AND ESBERT-V. B. (2013). A Novel Transition from Microstrip to a Substrate Integrated Waveguide with Higher Characteristic Impedance, *2013 IEEE MTT-S International Microwave Symposium Digest (IMS)*, pp. 1–4.

CAMERON-R. J. (1999). General Coupling Matrix Synthesis Methods for Chebyshev Filtering Functions, *IEEE Transactions on Microwave Theory and Techniques*, **47**(4), pp. 433–442.

CAMERON-R. J. (2003). Advanced Coupling Matrix Synthesis Techniques for Microwave Filters, *IEEE Transactions on Microwave Theory and Techniques*, **51**(1), pp. 1–10.

CAMERON-R. J., MANSOUR-R., AND KUDSIA-C. M. (2007). *Microwave Filters for Communication Systems: Fundamentals, Design and Applications*, Wiley-Interscience, Hoboken, New Jersey, USA.

CAMPBELL-G. A. (1917). Electric Wave-Filter. US Patent 1,227,113.

CASSIVI-Y., PERREGRINI-L., ARCIONI-P., BRESSAN-M., WU-K., AND CONCIAURO-G. (2002). Dispersion Characteristics of Substrate Integrated Rectangular Waveguide, *IEEE Microwave and Wireless Components Letters*, **12**(9), pp. 333–335.

CHANG-S. (2010). *Academic Genealogy of Mathematicians*, World Scientific Publishing Company, Singapore.

CHEN-M.-H., CHENG-H.-S., CHOU-P.-J., AND CHANG-C.-Y. (2015a). W-Band T-Junction and Bifurcated Substrate Integrated Waveguide Diplexers, *Electromagnetics: Applications and Student Innovation Competition (iWEM), 2015 International Workshop on*, pp. 1–2.

CHEN-R. S., WONG-S. W., ZHU-L., AND CHU-Q. X. (2015b). Wideband Bandpass Filter Using U-Slotted Substrate Integrated Waveguide (SIW) Cavities, *IEEE Microwave and Wireless Components Letters*, **25**(1), pp. 1–3.

CHEN-S., VAHLDIECK-R., AND HUANG-J. (1996). Rigorous Analysis of Mode Propagation and Field Scattering in Silicon-Based Coplanar MIS Slow Wave Structures with Abrupt Transitions to Transmission Lines on Normal Substrate, *IEEE Transactions on Microwave Theory and Techniques*, **44**(12), pp. 2487–2494.

CHE-W., DENG-K., WANG-D., AND CHOW-Y. L. (2008a). Analytical Equivalence between Substrate-Integrated Waveguide and Rectangular Waveguide, *IET Microwaves, Antennas Propagation*, **2**(1), pp. 35–41.

CHE-W., GENG-L., DENG-K., AND CHOW-Y. L. (2008b). Analysis and Experiments of Compact Folded Substrate-Integrated Waveguide, *IEEE Transactions on Microwave Theory and Techniques*, **56**(1), pp. 88–93.

CHU-H., GUO-Y. X., SONG-Y. L., AND WANG-Z. L. (2011). 40/50 GHz Diplexer Design in LTCC Technology, *Electronics Letters*, **47**(4), pp. 260–262.

CLOUGH-R. W. (1960). The Finite Element Method in Plane Stress Analysis, *Second ASCE Conference on Electronic Computation*.

COHN-S. B. (1957). Direct-Coupled-Resonator Filters, *Proceedings of the IRE*, **45**(2), pp. 187–196.

COHN-S. B. (1965). Microwave Filters Containing High-Q Dielectric Resonators, *G-MTT Symposium Digest, 1965*, Vol. 65, pp. 49–54.

COLLIN-R. (1991). *Field Theory of Guided Waves*, 2nd edn, IEEE Press, New York, USA.

COURANT-R. (1943). Variational Methods for the Solution of Problems of Equilibrium and Vibrations, *Bulletin of the American Mathematical Society*, **49**(1), pp. 1–23.

CRISTAL-E. G., AND MATTHAEI-G. L. (1964). A Technique for the Design of Multiplexers Having Contiguous Channels, *IEEE Transactions on Microwave Theory and Techniques*, **12**(1), pp. 88–93.

DAVIES-J. B., AND MUILWYK-C. A. (1966). Numerical Solution of Uniform Hollow Waveguides with Boundaries of Arbitrary Shape, *Proceedings of the Institution of Electrical Engineers*, **113**(2), pp. 277–284.

DESLANDES-D. (2010). Design Equations for Tapered Microstrip-to-Substrate Integrated Waveguide Transitions, *2010 IEEE MTT-S International Microwave Symposium Digest (MTT)*, pp. 704–707.

DESLANDES-D., AND WU-K. (2002). Design Consideration and Performance Analysis of Substrate Integrated Waveguide Components, *2002 32nd European Microwave Conference*, pp. 1–4.

DESLANDES-D., AND WU-K. (2006). Accurate Modeling, Wave Mechanisms, and Design Considerations of A Substrate Integrated Waveguide, *IEEE Transactions on Microwave Theory and Techniques*, **54**(6), pp. 2516–2526.

DHATT-G., LEFRANÇOIS-E., AND TOUZOT-G. (2012). *Finite Element Method*, Wiley-ISTE, Hoboken, New Jersey, USA.

DING-Y., AND WU-K. (2007). Substrate Integrated Waveguide-to-Microstrip Transition in Multilayer Substrate, *IEEE Transactions on Microwave Theory and Techniques*, **55**(12), pp. 2839–2844.

DING-Y., AND WU-K. (2010). T-Type Folded Substrate Integrated Waveguide (TFSIW) Slot Array Antenna, *IEEE Transactions on Antennas and Propagation*, **58**(5), pp. 1792–1795.

DITTLOFF-J., AND ARNDT-F. (1988). Computer-Aided Design of Slit-Coupled H-Plane T-Junction Diplexers with E-Plane Metal-Insert Filters, *IEEE Transactions on Microwave Theory and Techniques*, **36**(12), pp. 1833–1840.

DITTLOFF-J., AND ARNDT-F. (1989). Rigorous Field Theory Design of Millimeter-Wave E-Plane Integrated Circuit Multiplexers, *IEEE Transactions on Microwave Theory and Techniques*, **37**(2), pp. 340–350.

DOBROWOLSKI-J. A. (2010). *Microwave Network Design Using the Scattering Matrix*, Artech House, Norwood, Massachusetts, USA.

DOUVILLE-R. J. P., AND JAMES-D. S. (1978). Experimental Study of Symmetric Microstrip Bends and Their Compensation, *IEEE Transactions on Microwave Theory and Techniques*, **26**(3), pp. 175–182.

GRIEG-D. D., AND ENGELMANN-H. F. (1952). Microstrip - A New Transmission Technique for the Klilomegacycle Range, *Proceedings of the IRE*, **40**(12), pp. 1644–1650.

GRIGOROPOULOS-N., SANZ-IZQUIERDO-B., AND YOUNG-P. R. (2005). Substrate Integrated Folded Waveguides (SIFW) and Filters, *IEEE Microwave and Wireless Components Letters*, **15**(12), pp. 829–831.

GUHA-D., AND SAHA-P. K. (1997). Some Characteristics of Ridge-Trough Waveguide, *IEEE Transactions on Microwave Theory and Techniques*, **45**(3), pp. 449–453.

GUSTRAU-F. (2012). *RF and Microwave Engineering: Fundamentals of Wireless Communications*, John Wiley & Sons, Hoboken, New Jersey, USA.

HAN-S., WANG-X.-L., FAN-Y., YANG-Z., AND HE-Z. (2007). The Generalized Chebyshev Substrate Integrated Waveguide Diplexer, *Progress In Electromagnetics Research*, **73**, pp. 29–38.

HAO-Z. C., HONG-W., CHEN-J. X., CHEN-X. P., AND WU-K. (2005). Planar Diplexer for Microwave Integrated Circuits, *IEE Proceedings - Microwaves, Antennas and Propagation*, **152**(6), pp. 455–459.

HARRINGTON-R. F. (1993). *Field Computation by Moment Methods*, Wiley-IEEE Press.

HONG-J.-S., AND LANCASTER-M. J. (2011). *Microstrip Filters for RF/Microwave Applications*, 2nd edn, John Wiley & Sons, Singapore.

HONG-W., LIU-B., WANG-Y., LAI-Q., TANG-H., YIN-X. X., DONG-Y. D., ZHANG-Y., AND WU-K. (2006). Half Mode Substrate Integrated Waveguide: A New Guided Wave Structure for Microwave and Millimeter Wave Application, *Infrared Millimeter Waves and 14th International Conference on Teraherz Electronics, 2006. IRMMW-THz 2006. Joint 31st International Conference on*, pp. 219–219.

HRENNIKOFF-A. (1941). Solution of Problems of Elasticity by the Framework Method, *Journal of applied mechanics*, **8**(4), pp. 169–175.

HUNT-B. J. (1994). *The Maxwellians*, Cornell University Press.

Itoh, T.. (ed.) (1989a). *Numerical Techniques for Microwave and Millimeter-Wave Passive Structures*, Wiley-Interscience.

ITOH-T. (1989b). Overview of Quasi-Planar Transmission Lines, *IEEE Transactions on Microwave Theory and Techniques*, **37**(2), pp. 275–280.

JARRY-P., AND BENEAT-J. (2008). *Advanced Design Techniques and Realizations of Microwave and RF Filters*, Wiley-IEEE Press, Hoboken, New Jersey, USA.

JOHNSON-E. C. (1964). New Developments in Designing Bandpass Filters, *Electronic Industries*, pp. 87–90.

JOHNS-P. B., AND BEURLE-R. L. (1971). Numerical Solution of 2-Dimensional Scattering Problems Using A Transmission-Line Matrix, *Proceedings of the Institution of Electrical Engineers*, **118**(9), pp. 1203–1208.

KARIMABADI-S. S., AND ATTARI-A. (2015). X-Band Multi-Hole Directional Coupler with Folded Substrate-Integrated Waveguide, *Electromagnetics*, **35**(6), pp. 404–414.

KIANG-J.-F. (1996). Quasi-TEM Analysis of Coplanar Waveguides with An Inhomogeneous Semiconductor Substrate, *IEEE Transactions on Microwave Theory and Techniques*, **44**(9), pp. 1586–1589.

KORDIBOROUJENI-Z., AND BORNEMANN-J. (2015a). K-Band Backward Diplexer in Substrate Integrated Waveguide Technology, *Electronics Letters*, **51**(18), pp. 1428–1429.

KORDIBOROUJENI-Z., AND BORNEMANN-J. (2015b). Mode-Matching Analysis and Design of Substrate Integrated Waveguide T-Junction Diplexer and Corner Filter, *International Journal of Numerical Modelling: Electronic Networks, Devices and Fields*, **28**(5), pp. 497–507.

KORDIBOROUJENI-Z., BORNEMANN-J., AND SIEVERDING-T. (2014). K-band Substrate Integrated Waveguide T-junction diplexer design by Mode-Matching Techniques, *2014 Asia-Pacific Microwave Conference (APMC)*, pp. 1297–1299.

KÖRNER-T. W. (1989). *Fourier Analysis*, Cambridge University Press.

KUCERA-J. J., AND GUTMANN-R. J. (1997). Effect of Finite Metallization and Inhomogeneous Dopings on Slow-Wave-Mode Propagation, *IEEE Transactions on Microwave Theory and Techniques*, **45**(10), pp. 1807–1810.

KURZROK-R. M. (1966). General Four-Resonator Filters at Microwave Frequencies, *IEEE Transactions on Microwave Theory and Techniques*, **14**(6), pp. 295–296.

LAI-Q., FUMEAUX-C., HONG-W., AND VAHLDIECK-R. (2009). Characterization of the Propagation Properties of the Half-Mode Substrate Integrated Waveguide, *IEEE Transactions on Microwave Theory and Techniques*, **57**(8), pp. 1996–2004.

LEONG-Y.-C., AND WEINREB-S. (1999). Full Band Waveguide-to-Microstrip Probe Transitions, *1999 IEEE MTT-S International Microwave Symposium Digest*, Vol. 4, pp. 1435–1438 vol.4.

LEROY-M. (1983). On the Convergence of Numerical Results in Modal Analysis, *IEEE Transactions on Antennas and Propagation*, **31**(4), pp. 655–659.

LEVY-R. (1967). Theory of Direct-Coupled-Cavity Filters, *IEEE Transactions on Microwave Theory and Techniques*, **15**(6), pp. 340–348.

LEVY-R., AND COHN-S. B. (1984). A History of Microwave Filter Research, Design, and Development, *IEEE Transactions on Microwave Theory and Techniques*, **32**(9), pp. 1055–1067.

LIANG-X. P., ZAKI-K. A., AND ATIA-A. E. (1991). A Rigorous Three Plane Mode-Matching Technique for Characterizing Waveguide T-Junctions, and Its Application in Multiplexer Design, *IEEE Transactions on Microwave Theory and Techniques*, **39**(12), pp. 2138–2147.

MALORATSKY-L. G. (2000). Reviewing the Basics of Microstrip, *Microwaves RF*, **39**, pp. 79–88.

MANSOUR-R. R., AND MACPHIE-R. H. (1986). An Improved Transmission Matrix Formulation of Cascaded Discontinuities and its Application to E-Plane Circuits, *1986 IEEE MTT-S International Microwave Symposium Digest*, pp. 785–788.

MASON-W. P. (1930). Wave Filter. US Patent 1,781,469.

MASON-W. P., AND SYKES-R. A. (1937). The Use of Coaxial and Balanced Transmission Lines in Filters and Wide-Band Transformers for High Radio Frequencies, *Bell System Technical Journal*, **16**(3), pp. 275–302.

MASSÉ-D. J., AND PUCEL-R. A. (1972). A Temperature-Stable Bandpass Filter Using Dielectric Resonators, *Proceedings of the IEEE*, **60**(6), pp. 730–731.

MATTHAEI-G. L., AND CRISTAL-E. G. (1967). Theory and Design of Diplexers and Multiplexers, *Advances in microwaves*, **2**, pp. 237–324.

MATTHAEI-G. L., YOUNG-L., AND JONES-E. (1980). *Microwave Filters, Impedance-Matching Networks, and Coupling Structures (Artech Microwave Library)*, Artech House.

MATTHEWS-P. C. (2000). *Vector Calculus*, 3rd edn, Springer.

MIRALLES-E., ESTEBAN-H., BACHILLER-C., BELENGUER-A., AND BORIA-V. E. (2011). Improvement for the Design Equations for Tapered Microstrip-to-Substrate Integrated Waveguide Transitions, *2011 International Conference on Electromagnetics in Advanced Applications (ICEAA)*, pp. 652–655.

MORINI-A. (1997). Correction to "Constraints To The Optimum Performance And Bandwidth Limitations Of Diplexers Employing Three-port Junctions", *IEEE Transactions on Microwave Theory and Techniques*, **45**(5), pp. 704–704.

MORINI-A., AND ROZZI-T. (1995). Analysis of Compact E-Plane Diplexers in Rectangular Waveguide, *IEEE Transactions on Microwave Theory and Techniques*, **43**(8), pp. 1834–1839.

MORINI-A., AND ROZZI-T. (1996). Constraints to the Optimum Performance and Bandwidth Limitations of Diplexers Employing Symmetric Three-Port Junctions, *IEEE Transactions on Microwave Theory and Techniques*, **44**(2), pp. 242–248.

NAHIN-P. J. (2002). *Oliver Heaviside: The Life, Work, and Times of an Electrical Genius of the Victorian Age*, johns hopkins paperback ed edn, Johns Hopkins University Press.

NAM-H., YUN-T.-S., KIM-K.-B., YOON-K.-C., AND LEE-J.-C. (2005). Ku-Band Transition between Microstrip and Substrate Integrated Waveguide (SIW), *2005 Asia-Pacific Microwave Conference (APMC)*, Vol. 1, pp. 4 pp.–.

NGUYEN-TRONG-N., KAUFMANN-T., HALL-L., AND FUMEAUX-C. (2015a). Variational Analysis of Folded Substrate-Integrated Waveguides, *IEEE Microwave and Wireless Components Letters*, **25**(6), pp. 352–354.

NGUYEN-TRONG-N., KAUFMANN-T., HALL-L., AND FUMEAUX-C. (2015b). Variational Analysis of Folded Substrate-Integrated Waveguides, *IEEE Microwave and Wireless Components Letters*, **25**(6), pp. 352–354.

OFLI-E., VAHLDIECK-R., AND AMARI-S. (2005). Novel E-Plane Filters and Diplexers with Elliptic Response for Millimeter-Wave Applications, *IEEE Transactions on Microwave Theory and Techniques*, **53**(3), pp. 843–851.

OHM-G. S. (1827). *Die Galvanische Kette, Mathematisch Bearbeitet*, Riemann.

OZAKI-H., AND ISHII-J. (1958). Synthesis of A Class of Strip-Line Filters, *IRE Transactions on Circuit Theory*, **5**(2), pp. 104–109.

PAPZINER-U., AND ARNDT-F. (1993). Field Theoretical Computer-Aided Design of Rectangular and Circular Iris Coupled Rectangular or Circular Waveguide Cavity Filters, *IEEE Transactions on Microwave Theory and Techniques*, **41**(3), pp. 462–471.

PARK-S. S., HAN-S. T., CHO-Y. M., JE-D. H., KIM-K. D., AND PARK-D. C. (2003). Design of 40 GHz-Band Iris-Type Waveguide Bandpass Filter, *International Journal of Infrared and Millimeter Waves*, **24**(6), pp. 941–951.

PATZELT-H., AND ARNDT-F. (1982). Double-Plane Steps in Rectangular Waveguides and Their Application for Transformers, Irises, and Filters, *IEEE Transactions on Microwave Theory and Techniques*, **30**(5), pp. 771–776.

PELLEGRINI-A., MONORCHIO-A., MANARA-G., AND MITTRA-R. (2014). A Hybrid Mode Matching-Finite Element Method and Spectral Decomposition Approach for the Analysis of Large Finite Phased Arrays of Waveguides, *IEEE Transactions on Antennas and Propagation*, **62**(5), pp. 2553–2561.

PIERCE-J. R. (1949). Paralleled-Resonator Filters, *Proceedings of the IRE*, **37**(2), pp. 152–155.

PIERCE-J. R. (1953). Guided Wave Frequency Range Transducer. US Patent 2,626,990.

POLYANIN-A. D., AND MANZHIROV-A. V. (2006). *Handbook of Mathematics for Engineers and Scientists*, Chapman and Hall/CRC, Boca Raton, Florida, USA.

POTELON-B., FAVENNEC-J. F., QUENDO-C., RIUS-E., PERSON-C., AND BOHORQUEZ-J. C. (2008). Design of a Substrate Integrated Waveguide (SIW) Filter Using a Novel Topology of Coupling, *IEEE Microwave and Wireless Components Letters*, **18**(9), pp. 596–598.

POZAR-D. (2011). *Microwave Engineering*, 4th edn, John Wiley & Sons, Hoboken, New Jersey, USA.

QIU-P., ZHANG-Y., AND YAN-B. (2008). A Novel Millimeter-Wave Substrate Integrated Waveguide (SIW) Filter Buried in LTCC, *2008 Asia-Pacific Microwave Conference (APMC)*, pp. 1–4.

Ragan, G. L.. (ed.) (1948). *Microwave Transmission Circuits*, McGraw-Hill Book Company.

RASHID-A. K., SHEN-Z., AND LI-B. (2012). An Elliptical Bandpass Frequency Selective Structure Based on Microstrip Lines, *IEEE Transactions on Antennas and Propagation*, **60**(10), pp. 4661–4669.

REN-C.-L. (1969). On the Analysis of General Parallel Coupled TEM Structures Including Nonadjacent Couplings, *IEEE Transactions on Microwave Theory and Techniques*, **17**(5), pp. 242–249.

Reynolds, T. S.. (ed.) (1991). *The Engineer in America: A Historical Anthology from Technology and Culture*, University of Chicago Press Journals.

RHODES-J. D. (1976). Direct Design of Symmetrical Interacting Bandpass Channel Diplexers, *IEE Journal on Microwaves, Optics and Acoustics*, **1**(1), pp. 34–40.

RHODES-J. D., AND LEVY-R. (1979). A Generalized Multiplexer Theory, *IEEE Transactions on Microwave Theory and Techniques*, **27**(2), pp. 99–111.

RICHARDS-P. I. (1948). Resistor-Transmission-Line Circuits, *Proceedings of the IRE*, **36**(2), pp. 217–220.

ROGERS CORPORATION. (2015). RT/duroid 6002 High Frequency Laminates.

ROTHWELL-E. J., AND CLOUD-M. J. (2008). *Electromagnetics*, 2nd edn, CRC Press, Boca Raton, Florida, USA.

SALEHI-M., AND MEHRSHAHI-E. (2011). A Closed-Form Formula for Dispersion Characteristics of Fundamental SIW Mode, *IEEE Microwave and Wireless Components Letters*, **21**(1), pp. 4–6.

SCHMIDT-L. P. (1981). A Comprehensive Analysis of Quasiplanar Waveguides for Millimeter-Wave Application, *11th European Microwave Conference*, pp. 315–320.

SHEN-T., ZAKI-K., AND DOLAN-T. (2003). Rectangular Waveguide Diplexers with a Circular Waveguide Common Port, *IEEE Transactions on Microwave Theory and Techniques*, **51**(2), pp. 578–582.

SHEN-W., YIN-W. Y., AND SUN-X. W. (2011). Compact Substrate Integrated Waveguide (SIW) Filter With Defected Ground Structure, *IEEE Microwave and Wireless Components Letters*, **21**(2), pp. 83–85.

SHIH-Y. C., AND GRAY-K. G. (1983). Convergence of Numerical Solutions of Step-Type Waveguide Discontinuity Problems by Modal Analysis, *1983 IEEE MTT-S International Microwave Symposium Digest*, pp. 233–235.

SHIH-Y. C., CHU-T. S., AND ITOH-T. (1985). Comparative Study of Mode Matching Formulations for Microstrip Discontinuity Problems, *1985 IEEE MTT-S International Microwave Symposium Digest*, pp. 435–438.

SHIMONOV-G., GARB-K., AND KASTNER-R. (2010). Mode Matching Analysis and Design of Waveguide E-Plane Filters and Diplexers, *Antenna Technology (iWAT), 2010 International Workshop on*, pp. 1–4.

SHIREEN-R., SHI-S., AND PRATHER-D. W. (2010). W-Band Microstrip-to-Waveguide Transition Using Via Fences, *Progress in Electromagnetics Research Letters*, **16**, pp. 151–160.

SIEVERDING-T., PAPZINER-U., AND ARNDT-F. (1997). Mode-Matching CAD of Rectangular or Circular Multiaperture Narrow-Wall Couplers, *IEEE Transactions on Microwave Theory and Techniques*, **45**(7), pp. 1034–1040.

SILVESTER-P. P., AND FERRARI-R. L. (1996). *Finite Elements for Electrical Engineers*, 3rd edn, Cambridge University Press.

SIRCI-S., MARTNEZ-J. D., VAGUE-J., AND BORIA-V. E. (2015). Substrate Integrated Waveguide Diplexer Based on Circular Triplet Combline Filters, *IEEE Microwave and Wireless Components Letters*, **25**(7), pp. 430–432.

Sorrentino, R.. (ed.) (1989). *Numerical Methods for Passive Microwave and Millimeter Wave Structures*, IEEE.

SORRENTINO-R., AND BIANCHI-G. (2010). *Microwave and RF Engineering*, John Wiley & Sons, Chichester, West Sussex, U.K. Hoboken, New Jersey, USA.

SUBRAMANYAM-A. V. G., SIVAREDDY-D., SRINIVASAN-V. V., AND HARIHARAN-V. K. (2014). Realization and Qualification of Waveguide Iris Filters for Space Applications, *2014 IEEE International Microwave and RF Conference (IMaRC)*, pp. 334–337.

TANG-H. J., HONG-W., CHEN-J. X., LUO-G. Q., AND WU-K. (2007). Development of Millimeter-Wave Planar Diplexers Based on Complementary Characters of Dual-Mode Substrate Integrated Waveguide Filters With Circular and Elliptic Cavities, *IEEE Transactions on Microwave Theory and Techniques*, **55**(4), pp. 776–782.

TRANS-TECH. (2015). 7300 Series: Temperature-Stable Dielectric Material.

TURNER-M. J., CLOUGH-R. W., MARTIN-H. C., AND TOPP-L. J. (1956). Stiffness and Deflection Analysis of Complex Structures, *Journal of the Aeronautical Sciences*.

UHER-J., AND BORNEMANN-J. (1993). *Waveguide Components for Antenna Feed Systems: Theory and CAD*, Artech House, Norwood, Massachusetts, USA.

UMAR-A. (2004). *Mobile Computing And Wireless Communications: Applications, Networks, Platforms, Architectures and Security*, NGE Solutions.

VAHLDIECK-R., AND BORNEMANN-J. (1985). A Modified Mode-Matching Technique and its Application to a Class of Quasi-Planar Transmission Lines, *IEEE Transactions on Microwave Theory and Techniques*, **33**(10), pp. 916–926.

VAHLDIECK-R., BORNEMANN-J., ARNDT-F., AND GRAUERHOLZ-D. (1983). Optimized Waveguide E-plane Metal Insert Filters For Millimeter-wave Applications, *IEEE Transactions on Microwave Theory and Techniques*, **31**(1), pp. 65–69.

VANIN-F. M., FREZZA-F., AND SCHMITT-D. (2010). Computer-Aided Design of Y-Junction Waveguide Diplexers, *Progress In Electromagnetics Research C*, **17**, pp. 203–218.

VANIN-F. M., SCHMITT-D., AND LEVY-R. (2004). Dimensional Synthesis for Wide-Band Waveguide Filters and Diplexers, *IEEE Transactions on Microwave Theory and Techniques*, **52**(11), pp. 2488–2495.

WANG-R., WU-L.-S., AND ZHOU-X.-L. (2008). Compact Folded Substrate Integrated Waveguide Cavities and Bandpass Filter, *Progress In Electromagnetics Research*, **84**, pp. 135–147.

WANG-Z., JIN-Y., XU-R., YAN-B., AND LIN-W. (2010a). Substrate Integrated Folded Waveguide (SIFW) Partial H-plane Filter with Quarter Wavelength Resonators, *Journal of Electromagnetic Waves and Applications*, **24**(5-6), pp. 607–617.

WANG-Z., LI-X., ZHOU-S., YAN-B., XU-R.-M., AND LIN-W. (2010b). Half Mode Substrate Integrated Folded Waveguide (HMSIFW) and Partial H-Plane Bandpass Filter, *Progress In Electromagnetics Research*, **101**, pp. 203–216.

WELLS-J. (2010). *Multi-Gigabit Microwave and Millimeter-Wave Wireless Communications*, Artech House, Norwood, Massachusetts, USA.

WEXLER-A. (1967). Solution of Waveguide Discontinuities by Modal Analysis, *IEEE Transactions on Microwave Theory and Techniques*, **15**(9), pp. 508–517.

WU-K., DESLANDES-D., AND CASSIVI-Y. (2003). The Substrate Integrated Circuits - A New Concept for High-Frequency Electronics and Optoelectronics, *6th International Conference on Telecommunications in Modern Satellite, Cable and Broadcasting Service, 2003. TELSIKS 2003.*, Vol. 1, pp. P–III–P–X vol.1.

WU-L. S., ZHOU-X. L., AND YIN-W. Y. (2009). A Novel Multilayer Partial H-Plane Filter Implemented With Folded Substrate Integrated Waveguide (FSIW), *IEEE Microwave and Wireless Components Letters*, **19**(8), pp. 494–496.

XU-F., AND WU-K. (2005). Guided-Wave and Leakage Characteristics of Substrate Integrated Waveguide, *IEEE Transactions on Microwave Theory and Techniques*, **53**(1), pp. 66–73.

YANG-T., CHI-P. L., XU-R., AND LIN-W. (2013). Folded Substrate Integrated Waveguide Based Composite Right/Left-Handed Transmission Line and Its Application to Partial H-Plane Filters, *IEEE Transactions on Microwave Theory and Techniques*, **61**(2), pp. 789–799.

YAN-L., HONG-W., HUA-G., CHEN-J., WU-K., AND CUI-T. J. (2004). Simulation and Experiment on SIW Slot Array Antennas, *IEEE Microwave and Wireless Components Letters*, **14**(9), pp. 446–448.

YAO-H.-W., AND ZAKI-K. A. (1995). Modeling Generalized Coaxial Probes in Rectangular Waveguides, *1995 IEEE MTT-S International Microwave Symposium Digest*, pp. 979–982 vol.2.

YEE-K. S. (1966). Numerical Solution of Initial Boundary Value Problems Involving Maxwell's Equations in Isotropic Media, *IEEE Transactions on Antennas and Propagation*, **14**(3), pp. 302–307.

YOUNG-L. (1963). Direct-Coupled Cavity Filters for Wide and Narrow Bandwidths, *IEEE Transactions on Microwave Theory and Techniques*, **11**(3), pp. 162–178.

YUJIRI-L., SHOUCRI-M., AND MOFFA-P. (2003). Passive Millimeter Wave Imaging, *Microwave Magazine, IEEE*, **4**(3), pp. 39–50.

ZHANG-Q. F., AND LU-Y. L. (2010). Dimensional Synthesis Method for Wide-Band waveguide Iris Filters, *IET Microwaves, Antennas Propagation*, **4**(9), pp. 1256–1263.

ZHANG-Q. L., YIN-W. Y., HE-S., AND WU-L. S. (2010a). Compact Substrate Integrated Waveguide (SIW) Bandpass Filter With Complementary Split-Ring Resonators (CSRRs), *IEEE Microwave and Wireless Components Letters*, **20**(8), pp. 426–428.

ZHANG-W. T., F. YE-L., Y. ZHAO-H., AND L. CHAI-S. (2010b). Design of Waveguide E-Plane Hybrid Metal Insert Filters for Millimeter-Wave Application, *2010 International Conference on Wireless Communications and Signal Processing (WCSP)*, pp. 1–4.

ZHANG-Y. L., HONG-W., WU-K., CHEN-J. X., AND TANG-H. J. (2005). Novel Substrate Integrated Waveguide Cavity Filter with Defected Ground Structure, *IEEE Transactions on Microwave Theory and Techniques*, **53**(4), pp. 1280–1287.

ZHAO-C., FUMEAUX-C., AND LIM-C. C. (2015a). Losses in Substrate Integrated Waveguide Band-Pass Post Filters, *2015 Asia-Pacific Microwave Conference (APMC)*, Vol. 2, pp. 1–3.

ZHAO-C., FUMEAUX-C., AND LIM-C. C. (2016a). Folded Y-junction in Substrate-Integrated Waveguide Technology, *The 2nd Australian Microwave Symposium*.

ZHAO-C., FUMEAUX-C., AND LIM-C. C. (2016b). Substrate-Integrated Waveguide (SIW) Diplexers with Improved Y-junctions, *Microwave and Optical Technology Letters*, **58**(6), pp. 1384–1388.

ZHAO-C., FUMEAUX-C., AND LIM-C. C. (n.d.). Folded Substrate-Integrated Waveguide Band-pass Post Filter, *IEEE Microwave and Wireless Components Letters*. Accepted on 1 July 2016, Subject to revision.

ZHAO-C., FUMEAUX-C., KAUFMANN-T., ZHU-Y., AND LIM-C. C. (2015b). Mode Matching Analysis of Dimension for Single-Mode Operation of Shielded Microstrip Lines, *2015 Asia-Pacific Microwave Conference (APMC)*, Vol. 2, pp. 1–3.

ZHAO-C., FUMEAUX-C., KAUFMANN-T., ZHU-Y., HORESTANI-A. K., AND LIM-C. C. (2015c). General Design Method for Band-pass Post Filters in Rectangular Waveguide and Substrate Integrated Waveguide, *International Symposium on Antennas and Propagation (ISAP2015)*, pp. 946–949.

ZHAO-C., KAUFMANN-T., ZHU-Y., AND LIM-C. C. (2014a). Approximation Methods for Cylindrical Posts in Rectangular Waveguides with Mode Matching Technique, *2014 IEEE Asia-Pacific Conference on Applied Electromagnetics (APACE)*, pp. 179–182.

ZHAO-C., KAUFMANN-T., ZHU-Y., AND LIM-C. C. (2014b). Efficient Approaches to Eliminate Influence Caused by Micro-Machining in Fabricating H-Plane Iris Band-Pass Filters, *2014 Asia-Pacific Microwave Conference (APMC)*, pp. 1306–1308.

ZHAO-M., AND FAN-Y. (2011). A Ka Band Low Loss Wideband E-Plane Waveguide Filter, *2011 IEEE 4th International Symposium on Microwave, Antenna, Propagation, and EMC Technologies for Wireless Communications (MAPE)*, pp. 802–804.

ZIENKIEWICZ-O. C. (1995). Origins, Milestones and Directions of the Finite Element Method A Personal View, *Archives of Computational Methods in Engineering*, **2**(1), pp. 1–48.

ZOBEL-O. J. (1932). Electrical Wave Filter. US Patent 1,850,146.

ZOU-X., MING TONG-C., AND WANG YU-D. (2011). Design of An X-Band Symmetrical Window Band-pass Filter Based on Substrate Integrated Waveguide, *2011 Cross Strait Quad-Regional Radio Science and Wireless Technology Conference (CSQRWC)*, Vol. 1, pp. 571–574.

List of Acronyms

BEM Boundary Element Method

CAD Computer-Aided Design

CST Computer Simulation Technology

FDM Finite-Difference Method

FDTD Finite-Difference Time-Domain

FEM Finite-Element Method

FSIW Folded Substrate-Integrated Waveguide

FSS Frequency Selective Structure

GAM General Admittance Matrix

GSM Generalised Scattering Matrix

GTM General Transmission Matrix

HFSS High Frequency Structural Simulator

HMSIW Half-Mode Substrate-Integrated Waveguide

MIS Metal-Insulator-Semiconductor

MMIC Monolithic Microwave Integrated Circuit

MMM Mode-Matching Method

MMT Mode-Matching Technique

MoM Method of Moments

OEIC Optoelectronic Integrated Circuit

SDM Spectral Domain Method

SIW Substrate-Integrated Waveguide

TLM Transmission Line Matrix

VSWR Voltage Standing Wave Ratio

List of Symbols

R	Resistance
L	Inductance
C	Capacitance
$\vec{E}$	Electric field existing in a rectangular waveguide
$\vec{H}$	Magnetic field existing in a rectangular waveguide
ω	Radian frequency
ε	Permittivity of a dielectric medium
ε_0	Permittivity of free space
ε_r	Relative permittivity of a dielectric medium
μ	Permeability of a dielectric medium
A_h	Magnitude of z-directed magnetic vector potential
A_e	Magnitude of z-directed electric vector potential
Q_h	Amplitude coefficient for TE mode
Q_e	Amplitude coefficient for TM mode
Γ_h	Propagation constant for TE mode with the notation for complex numbers
Γ_e	Propagation constant for TM mode with the notation for complex numbers
k_{hx}	Wavenumber along the x-axis for TE mode
k_{hy}	Wavenumber along the y-axis for TE mode

k_{ex}	Wavenumber along the x-axis for TM mode
k_{ey}	Wavenumber along the y-axis for TM mode
k_c	Cutoff wavenumber
T_h	Eigenfunction for TE mode
T_e	Eigenfunction for TM mode
m, n	Index of TE or TM mode
a	Rectangular waveguide width
b	Rectangular waveguide height Substrate thickness
c	Thickness of iris Width of the middle vane of folded substrate-integrated waveguide
P_h	Power carried by TE mode
P_e	Power carried by TM mode
$\mathcal{S}$	Closed cross-section surface of the rectangular waveguide
$\mathcal{L}$	Closed contour enclosing surface
G_h	Normalised coefficient for TE mode
G_e	Normalised coefficient for TM mode
Z_h	Wave impedance for TE mode
Y_e	Wave admittance for TM mode
J	Coupling coefficients between hybrid modes in different regions
S, s	Scattering parameters

U	Unit matrix
$\mathcal{M}$	Coupling coefficient matrix
P_{inc}	Power available from source
P_{load}	Power delivered to load
P_{LR}	Power loss ratio
ω_c	Cutoff radian frequency
ϵ	Ripple constant
F_N	Filtering function
N	Order of a filter Number of bifurcations in waveguide
IL	Insertion loss for a filter
A_r	Passband ripple
$\mathcal{T}_N$	Chebyshev function
g	Normalised values for electronic elements in filter network
FBW	Fractional bandwidth
ω_1'	Higher passband edge radian frequency for a band-pass filter
ω_2'	Lower passband edge radian frequency for a band-pass filter
ω_0'	Centre radian frequency for a band-pass filter
ϑ	Impedance scaling factor
k	Impedance inverter factor
X	Reactance of the distributed resonator

λ_{g1}	Guide wavelengths at the higher passband edge frequency
λ_{g2}	Guide wavelengths at the lower passband edge frequency
λ_{g0}	Guide wavelengths at the centre frequency
FGW	Fractional guide wavelength
G	Gap between the iris plates Gap between the post pair
D	Length of the resonant cavity
θ	Electrical length
X_s, X_p	Element values of an impedance inverter
r	Radius of a rounded corner Radius of a post/via
ls	Side of a bevel angle
M	Number of steps to approximate a rounded corner or a post/via
W_i	Physical width of a substrate-integrated waveguide
W_e	Equivalent width of a substrate-integrated waveguide
d	Diameter of a post/via
p	Interval between two adjacent Posts/vias
H	Thicknesses of the N-furcations to approximate a post/via
W	Widths of the N-furcations to approximate a post/via
ti	Computation time
W_s	Width of a microstrip line

W_t	Width of a taper of a transition structure
L_t	length of a taper of a transition structure
δ	Dielectric loss angle
A, B	Amplitude coefficients for TE modes
C, D	Amplitude coefficients for TM modes
$\mathcal{R}$	Transmission matrix
k_z	Propagation constant
$\mathcal{C}$	Coupling matrix for planar and quasi-planar transmission lines
w	Width of the microstrip line in a shielded transmission line
t	Thickness of the microstrip line in a shielded transmission line Thickness of metal claddings electroplated onto the substrates surfaces
h	Thickness of the dielectric in a shielded transmission line
β	Phase constant
E	Gap between the centre of the post and the FSIW wall
W_c	Width of the slot for a strip-to-microstrip transition
L_c	Length of the slot for a strip-to-microstrip transition
$\rho_{L_{f1}}$	Reflection coefficient of the first filter in a diplexer
$\rho_{L_{f2}}$	Reflection coefficient of the second filter in a diplexer
L_{f1}	Distance between the first filter and the junction port of a diplexer
L_{f2}	Distance between the second filter and the junction port of a diplexer
φ	Angle between the output branches of the Y-junction

L_b	Length of the branch before the bend of an improved Y-junction
L_a, Θ	Dimensions used to determine the positions of the two adjusting vias
g_s	Width of the coupling slot in the double-layer junction
L_i	Length for the second step of T-type FSIW in a three-port junction combining T-type and E-type FSIW technology
g_{i1}, g_{i2}	Distances between the edges of the middle metal vane and the centres of the vias in the three-port junction in T-type and E-type FSIW technology
L_e	Equivalent length for L_i
g_{e1}, g_{e2}	Equivalent distances for g_{i1}, g_{i2}
W_m	Side of the chamfered corner
r_{ex}	External radius of a round angle turn
r_{in}	Inner radius of a round angle turn

Biography

Cheng Zhao was born in Yangzhou City, Jiangsu Province, China. He received his bachelor's degree from the School of Information Science & Engineering, Southeast University, China in 2007, and his master's degree from the School of Electrical & Electronic Engineering, the University of Adelaide in 2011. In 2012, he was awarded the Australian Postgraduate Award (APA) to pursue his PhD research in the School of Electrical & Electronic Engineering, the University of Adelaide. He is studying in the field of microwave and millimetre-wave circuit design under the supervision of Assoc Prof Cheng-Chew Lim, Prof Christophe Fumeaux and Dr Thomas Kaufmann.

During his PhD candidature, he has focussed his research on computational electromagnetics, especially on the mode-matching method which can efficiently handle certain types of microwave, millimetre-wave, or even optical components. Based on the combination of the mode-matching method, equivalent models and the finite-element simulations, he proposed several novel band-pass filters and diplexers with dimension reductions, as well as demonstrated a large improvement in the design reliability and a great reduction in the design cycle. His research interests also include Monolithic Microwave Integrated Circuits for wireless communications and sensor applications, and numerical methods for the analysis and optimisation for printed microwave and millimetre-wave circuits such as antennas and reflectarrays.

Cheng Zhao is a student member of the Institute of Electrical and Electronics Engineers.

Cheng Zhao
c.zhao@adelaide.edu.au